

The University of Sheffield



Combustion Visualization Monitoring Using High Speed Imaging

By

Miss. Lukai Zheng

Combustion and Flow Diagnostics Research Group

Department of Mechanical Engineering

This thesis is submitted to the University of Sheffield for the degree of Doctor of

Philosophy, February 2018

UNIVERSITY OF SHEFFIELD

RESEARCH AND INNOVATION SERVICES

The undersigned certify that they have read, and recommend to Research and Innovation Services for acceptance, a thesis entitled " Combustion Visualization Monitoring Using High Speed Imaging " submitted by Lukai Zheng in partial fulfilment of the requirements of the degree of "Doctor of Philosophy".

Supervisor, Professor Yang Zhang, Mechanical Engineering

Second Supervisor, Dr. Jem Rongong, Mechanical Engineering

04/02/2018

Publications

Journal:

1. **L. Zheng** and Y. Zhang, “High Speed Digital Imaging for Flame Studies: Potentials and Limitations,” *Energy Procedia*, 2015, vol. 66, pp. 237–240.
2. Y. Wang, **L. Zheng**, R. Woolley, and Y. Zhang, “Investigation of ignition process from visible to infrared by a high-speed colour camera,” *Fuel*, vol. 185, pp. 500–507, 2016.
3. **L. Zheng**, S. Ji, and Y. Zhang, Laminar Premixed Flame Structure and Dilution Behaviour under External Acoustic Excitation Base on Digital Colour Imaging Analysis, [*Experimental Thermal and Fluid Science*], Under Review.
4. **L. Zheng**, S. Ji, and Y. Zhang, Lifted and reattached behaviour of laminar Premixed flame under external acoustic excitation, [*Experimental Thermal and Fluid Science*], Under Review.
5. A.M.E. Faik, Z. Ma, **L. Zheng**, Y. Zhang, Quantitative Investigation of Flame Characteristics during the Combustion of a Single Diesel-in-water Emulsion Droplet, [*International Journal of Multiphase Flow*], Under Review.
6. **L. Zheng**, J. Cronly, E. Ubogu, I. Ahmed, Y. Zhang and B. Khandelwal, Effects of Fuel Properties and compositions on the combustion performance of a Gas Turbine Combustor, [*Applied energy*], Under Review.
7. **L. Zheng**, J. Cronly, E. Ubogu, I. Ahmed, Y. Zhang and B. Khandelwal, The Combined Investigation of Aromatics Impact on Flame Soot Propensity in a Gas

- Turbine Using PM Measurement and Flame Visualisation, [*Applied energy*], Under Review.
8. **L. Zheng**, J. Cronly, C. Ling, E. Ubogu, I. Ahmed, Y. Zhang and B. Khandelwal, The Effect of Fuel Properties on Soot Formation, [*Fuel*], Under Review.
 9. **L. Zheng**, J. Cronly, C. Ling, E. Ubogu, I. Ahmed, Y. Zhang and B. Khandelwal, The Effect of Fuel Properties on Lean Blowout, [*Fuel*], Under Review.
 10. J. Cronly, **L. Zheng**, E. Ubogu, I. Ahmed, Y. Zhang and B. Khandelwal, The Impact of Aromatic Type and Proportion on the Combustion Emission of Gas Turbine, [*Fuel*], Under Review.

Conference:

1. **L. Zheng**, A. Faik, and Y. Zhang, “Flame colour analysis for the droplet combustion of water-in-diesel emulsions,” in 12th International Conference on Heat Transferr, Fluid Mechanics and Thermodynamics, 2016, pp. 212–217, Malaga, Spain, Oral Presentation.
2. **L. Zheng**, S. Ji, and Y. Zhang, “Experimental Investigation on the Flame Wrinkle Fluctuation under External Acoustic Excitation,” in 26th International Colloquium on the Dynamics of Explosions and Reactive Systems (26th ICDERS), Boston, US, 2017. Oral Presentation.
3. **L. Zheng**, S. Ji, and Y. Zhang, “Impact of Acoustic Excitation Frequency on Laminar Premixed Flame,” in 26th International Colloquium on the Dynamics of Explosions and Reactive Systems (26th ICDERS), Boston, US, 2017. Oral Presentation.
4. **L. Zheng**, I. Ahmed, Y. Zhang, and B. Khandelwal, “Evaluation of impact on Lean Blowout Limit while using alternative fuels on gas turbine combustor,” in The

International Society of Air Breathing Engines (23th ISABE), Manchester, UK, 2017.
Oral Presentation.

5. T. Gill, **L. Zheng**, E. Ubogu, I. Ahmed and B. Khandelwal, ‘The Effect of the Sample Line Length on Gas Turbine Emission Measurement’ 5th ASME Gas Turbine India Conference, 2017. Oral Presentation.
6. Ahmed, **L. Zheng**, and B. Khandelwal, Evaluation of impact on Lean Blowout Limit and ignition delay while using alternative fuels on gas turbine combustor, Turbomachinery Technical Conference & Exposition (ASME Turbo Expo 2018), Accepted

Report:

1. **L. Zheng**, E.A. Ubogu, I. Ahmed, J. Cronly, J.N. Knapton, B. Khandelwal, Test and Analysis of Alternative Jet Fuel Combustion Performance, (Project Number R/152069), 2017

Acknowledgments

The author wishes to express recognition to following people for their help, support company and generosity during this research.

Firstly, nothing would have been possible, without the love of my family, parents, husband, parents-in-law, who unconditionally supported me whenever I need.

I'll always appreciate my supervisor, Prof. Yang Zhang, for his continuous guidance, encouragement, and respected advices throughout the research period. I am extremely grateful for everything he taught me in work and life. I have benefited greatly from his outstanding knowledge in research. Then I would like to thank my second supervisor, Dr. Jem Rongong for his additional support.

I would like to express my sincere gratitude to Dr. Bhupendra Khandelwal for the opportunity to let me participate the FAA project. Not only did this opportunity broaden my horizons, I also met those skilful and friendly colleagues in this team, Ihab S Ahmed, Emamode A Ubogu, Jonathan Knapton etc. I would also like to acknowledge the Low Carbon Combustion Centre (LCCC) technicians team, who made a contribution to this research through the manufacturing and troubleshooting of experimental platforms.

To my colleagues in my group, Paco, Yiran Wang, Shuaida Ji, Zhen Ma, Songyang Yu, Houshi Jiang, Ahmad Faik, Ahmad Fuad, Yufeng Lai, Xiao Wang, Muyi Pan, thank you for making my time in UK a more enjoyable experience.

EPSRC and US Federal Aviation Administration (FAA) Office of Environment and Energy have funded some research works. Some of the fuels for this work were funded by the US FAA Office of Environment and Energy as a part of the NJFCP Program. University of Sheffield's Low Carbon Combustion Centre have supported part of this work.

Abstract

Optical visualisation of flames plays an important role in the in-depth understanding of complex combustion phenomena. In particular, a high-speed camera can provide nonintrusive and continuous monitoring of flames. Through the recorded images, further analysis on colour, temperature, flame dynamics, and a variety of other information can be achieved, which is essential for physical study and numerical modelling. The main objectives of the present work are to apply visualisation monitoring to different combustion conditions, quantitatively analyse the combustion performance, and integrate these analyses with their inherent nature to achieve physical insights into these combustion phenomena.

First, with the rapid development and popularisation of computer and multimedia technology, digital image processing technology has received unprecedented attention, and many new application fields and processing methods have emerged. In the present work, suitable methods for combustion diagnostics, including schlieren, digital flame colour discrimination method, a self-developed de-noising method, boundary detection methods, and a flame chemiluminescence measurement method are introduced and compared with the general methods. Then, a complementary analysis on the limitations and the validation of the flame chemiluminescence measuring method are experimentally examined. The relationship between the chemiluminescence and equivalence ratio is discussed from the effects of the flame region, fuels types, and camera sensors via two measuring methods.

Second, in the visualisation application on acoustically perturbed gaseous fuel

combustion study, the nonlinear coupling interaction effect between a variation of external excitation and the vortex structure of a lifted jet flame under acoustic excitation is investigated utilising a high-speed optical system combined with the image processing approaches in this experiment. The results of the flame structure and dilution behaviour show how the flame responds to hydrodynamic instability. The harmonics and coupling frequency peaks of the flame flicking are observed for the combustion instability under an external forcing frequency. In addition, the turbulent stretching at the shear layer generated by the excitation lead to flame lift-off. Kelvin–Helmholtz vortices in the unburnt part play a key role in preventing flame lift-off.

Third, in the visualisation application on gas turbine liquid fuel combustion study, a range of tests were conducted on a Rolls–Royce Tay combustor test rig. Visual images of the flame at lean blowout (LBO) were captured by a high-speed camera and analysed to develop a new model for the evaluation of the LBO performance of alternative fuels. The results show that the LBO equivalence ratio and soot formation always exhibit opposite responses, whereby low LBO equivalence ratios and low soot content cannot be achieved at the same time. The fuel’s derived cetane number (DCN) was observed to have a considerable effect on the optimisation of the LBO equivalence ratio and was shown to induce the formation of soot in an acceptable manner. Meanwhile, the particulate emission results support the hypotheses that not all aromatic species produce the same levels of smoke and emissions.

Overall, this work improves the understanding of combustion, and contributes towards the development of tools for flame performance analysis and evaluation. These benefits could be crucial for future fuels and engines.

Content

PUBLICATIONS.....	III
ACKNOWLEDGMENTS	VI
ABSTRACT	VII
CONTENT	IX
LIST OF FIGURES	XV
LIST OF TABLES.....	XXI
NOMENCLATURE	XXII
1. INTRODUCTION.....	1
1.1. Motivation.....	1
1.2. Objectives.....	2
1.3. Outline of the Thesis	4
2. BASIC BACKGROUND KNOWLEDGE	6
2.1. General Concept of Hydrocarbon Combustion	6
2.1.1. Types of Hydrocarbons	7
2.1.1.1. Saturated Hydrocarbons	8
2.1.1.2. Unsaturated Hydrocarbons.....	9
2.1.1.3. Alicyclic.....	9
2.1.1.4. Aromatic	10
2.1.2. Gaseous Combustion.....	11
2.1.2.1. Diffusion Flames.....	11

2.1.2.2.	<i>Premixed Flames</i>	13
2.1.2.3.	<i>Partially Premixed Flame</i>	14
2.1.3.	Liquid Combustion.....	15
2.1.3.1.	<i>Liquid Fuel Spray Combustion</i>	16
2.1.3.2.	<i>Droplet Combustion</i>	18
2.1.4.	Fuel–Air Ratio.....	19
2.1.5.	Flame Colour.....	21
2.1.6.	Emission.....	26
2.2.	General Optical Methods for Combustion Research.....	27
2.2.1.	Shadowgraphy.....	27
2.2.2.	Schlieren.....	28
2.2.3.	Backlighting Imaging.....	30
2.2.4.	Self-illuminated Direct Imaging.....	31
2.2.5.	Particle Image Velocimetry (PIV).....	32
2.2.6.	Laser Induced Fluorescence.....	33
2.2.7.	Others	34
2.3.	General Concept of Vision Systems	34
2.3.1.	Camera Evolution.....	34
2.3.2.	Digital Vision System.....	36
2.3.2.1.	<i>Image Sensors</i>	36
2.3.2.2.	<i>Camera Sensor Response to the Spectrum</i>	39
2.3.2.3.	<i>Colour Model</i>	40
2.3.2.4.	<i>Shutter Speed</i>	44
2.3.2.5.	<i>Camera Noise</i>	46
3.	IMAGE PROCESSING METHODOLOGY.....	50
3.1.	Denoising Processing.....	50
3.1.1.	Averaging Filter.....	52
3.1.2.	Median Filter.....	52

3.1.3.	Adaptive Filter	52
3.1.4.	Wiener Filter	53
3.1.5.	Gaussian filter	53
3.1.6.	Centre Point Denoise.....	53
3.2.	Boundary Detection	55
3.3.	Image Colour Selection and Enhancement.....	57
3.4.	Flame Chemiluminescence Measurements	60
4.	VALIDATION OF FLAME CHEMILUMINESCENCE MEASUREMENTS	64
4.1.	Introduction	64
4.2.	Camera Parameters Calibration	65
4.3.	Experimental Setup.....	71
4.4.	Conventional Method Comparison	72
4.5.	Result and Discussion	75
4.5.1.	Results Comparison	81
4.5.2.	Validated Range	84
4.6.	Summary	86
5.	ACOUSTIC IMPACT ON FLAME IN AN EXTERNAL EXCITED	88
	CHAMBER.....	88
5.1.	Introduction	88
5.2.	Background Knowledge.....	90
5.2.1.	Acoustic.....	90
5.2.2.	Standing Wave.....	91
5.2.3.	Reynolds Number.....	95

5.2.4.	Flame Lifted Off.....	95
5.2.5.	Principle of Microphone.....	98
5.3.	Experiment Setup.....	99
5.3.1.	Burner System.....	100
5.3.2.	Sound Generating and Data Acquisition System	100
5.3.3.	Standing Wave Measurement.....	101
5.3.4.	Colour Imaging Setup	102
5.3.5.	Single Schlieren System.....	104
5.4.	Results	105
5.4.1.	Flame Flicking	105
5.4.2.	Flame Configuration	107
5.4.2.1.	<i>Fluctuation of Single Point on Flame Wrinkle</i>	<i>109</i>
5.4.2.2.	<i>Fluctuation of Flame Wrinkle Line.....</i>	<i>111</i>
5.4.2.3.	<i>Flame Surface Area to Volume Ratio</i>	<i>114</i>
5.4.3.	Flame Lifted Behaviour	118
5.4.3.1.	<i>Hysteresis Behaviour.....</i>	<i>119</i>
5.4.3.2.	<i>Nonlinear Coupling of Lifted Flame and Acoustic Wave</i>	<i>124</i>
5.4.4.	Flame Chemiluminescent Radiations Measurement	128
5.5.	Conclusion.....	137
6.	GAS TURBINE COMBUSTION OF FUELS EVALUATION.....	140
6.1.	Introduction	140
6.2.	Background Knowledge.....	141
6.2.1.	Flame Stability in Jet Engine	141
6.2.2.	Lean Blowout Detection Method	143
6.2.3.	Alternative Fuels	145
6.2.4.	Fuel Physical Properties.....	147

6.2.5.	Chemical Composition.....	151
6.3.	Experiment Setup.....	153
6.3.1.	Combustor Rig and Alternative Fuels Test Campaign	153
6.3.2.	Tay Combustor Experimental Apparatus	154
6.3.3.	Experimental Procedures.....	157
6.3.4.	Fuels Matrix	160
6.4.	Results and Discussion.....	163
6.3.5.	Fuel Physical Property Effect on LBO Performance	163
6.3.5.1.	<i>LBO Equivalence Ratio</i>	<i>163</i>
6.3.5.2.	<i>LBO Sooty Flame Concentration.....</i>	<i>166</i>
6.3.5.3.	<i>Summery.....</i>	<i>172</i>
6.3.6.	Fuel Composition Effect on LBO Performance	174
6.3.7.	Air Flow Rate Effect	178
6.3.8.	Cetane Additives Effect.....	181
6.5.	Conclusion.....	184
7.	SUMMARY AND FUTURE WORK.....	186
7.1.	Summary.....	186
7.1.1.	Visualisation Monitoring Techniques.....	186
7.1.2.	Application on Acoustic Induced Gaseous Fuel Monitoring	187
7.1.3.	Application on Gas Turbine Liquid Fuel Monitoring	189
7.2.	Future Work	190
APPENDIX	194
Appendix I:	Microphone Specification.....	194
Appendix II:	LBO Images for All the Fuels.....	195

**Appendix III: Sample LBO Images for Seven Fuels Burning at Three
Operating Conditions..... 196**

REFERENCE 198

List of Figures

Figure 1 Structure of the thesis	4
Figure 2. Main categories of hydrocarbons	7
Figure 3 Flame categories: diffusion, premixed, and partial premixed flame	11
Figure 4 Schematic of Bunsen burner flames: (a) diffusion flames and (b) premixed flames.....	13
Figure 5 Structure of propane premixed flame	13
Figure 6 The structure of partially premixed flame [3].....	14
Figure 7 Spray images at different injection pressures [7]	17
Figure 8. Scheme of spray structure for different atomisation regimes [8]	18
Figure 9 Visible light spectrum [16]	22
Figure 10 Hydrocarbon fire typical emission spectrum [17]	23
Figure 11 Photons of light are emitted as an electron drops back to its ground state after being excited	24
Figure 12 Chemiluminescence spectra of premixed atmospheric methane–air flames at different measured equivalence ratios [18]	25
Figure 13 (a) Light shadowgraph setup; (b) sample shadowgraph of a bullet moving in stagnant air [36].....	27
Figure 14 A standard Z-configuration parallel-light schlieren system [40]	29
Figure 15 Comparison of the droplet microexplosion images obtained by shadowgraph and schlieren methods	30
Figure 16 Different nucleation sites inside burning water and diesel emulsions droplet	31
Figure 17 Sample of combustion visualization in cylinder.....	32

Figure 18 PIV system setup	33
Figure 19 Camera development history	35
Figure 20 CCD Sensor	37
Figure 21 CMOS Sensor	38
Figure 22 Colour filter arrangement for film (a) and digital (b).....	39
Figure 23 3D display model of the RGB colour.	41
Figure 24 HSV colour model	42
Figure 25 Result of the flame picture after enhancement	45
Figure 26 Sample of intensity feather	48
Figure 27 Sample of a raw image of blue flame	51
Figure 28 3×3 averaging kernel often used in centre point denoise filtering	54
Figure 29 Denoising result with different methods.....	54
Figure 30 Boundary detection the results of processing by each operator	56
Figure 31 Refined smooth boundary of flame	57
Figure 32 Sample of the flame image without adjustment	58
Figure 33 Colour distribution histograms in hue space.	59
Figure 34 (a) the orange sooty flame region; (b) the infrared soot emission enhanced with 30 times enhancement; (c) the chemiluminescence-induced blue flame with 50 times enhancement; (d) the entire image after selective image enhancement	60
Figure 35 Relationship between image colour and radiation emission [65].....	61
Figure 36 Calibration equipment: (a) monochromator, (b) convex lens, (c) fibre optic illuminator.	65
Figure 37 (a) Dimensions and (b) internal structure of the Newport manual mini monochromator	66
Figure 38 Calibrated cameras: Photron SA-4 high-speed camera (left) and Sony α77 (right).....	67
Figure 39 Double insurance of dark condition setup for calibration	67

Figure 40 Experimental setup for the camera sensor calibration.....	68
Figure 41 Sensor spectral responses for different cameras	70
Figure 42 Schematic diagram of the flame measurement experimental setup.....	71
Figure 43 Principle and function of camera with the stereo adapter imaging system ..	74
Figure 44 Samples of CH ₄ and C ₃ H ₈ premixed flame observed via different cameras and methods in the measured equivalence range.....	76
Figure 45 (a) Whole flame of propane and the separated inner flame and outer flame, (b) colour model chemiluminescence CH*/C2* ratio map for the different regions of the flame, (c) comparison of calculated CH*/C2* ratio from different flame sections to equivalence ratio	78
Figure 46 Analysis results of the CH*/C2* based on colour-modelled and filter with two cameras;.....	82
Figure 47 Relationship between the CH*/C2* intensity ratio and the equivalence ratio from lean premixed to partially premixed flame.....	85
Figure 48 Two opposing waves combine to form a standing wave.	93
Figure 49. Standing sound waves in one end closed and one end open tube.....	94
Figure 50. Principle of Microphone	98
Figure 51. Layout of the test rig arrangement.....	99
Figure 52 Experimental measurement of pressure response to position and frequency	101
Figure 53 The schematic layout of the Colour imaging experimental apparatus setup	102
Figure 54. Shutter speed selection	103
Figure 55 Experimental setup of schlieren system	104
Figure 56. The sample of series images under various excitation groups.....	105
Figure 57 Intensity frequency under the four harmonic frequencies and three sound pressures.....	106

Figure 58 Samples of boundary lines of the instantaneous flame.....	108
Figure 59. Schematic of the single-point displacement on the flame wrinkle.....	109
Figure 60 Amplitude of the point displacement along the tube under various excitation frequencies	111
Figure 61. Schematic of the flame front configuration (a) and the wrinkle coordinates (b)	112
Figure 62. Instantaneous fluctuation magnitude of the sample flame front from each excitation group along the normalized \mathbf{i} -axis.....	113
Figure 63. Fluctuation magnitude on downstream direction at different excitation cases	114
Figure 64 The refine perimeter of the excited flame front.....	115
Figure 65. Surface area per unit volume along the tube under various excited frequencies	117
Figure 66 Surface area to volume ratio FFT	118
Figure 67 (a) Sequence of photographs from the single-mirror schlieren at shutter speed 1/50 s; (b) The samples of series colour images in successive 4/2000 s; (c) Three sequential samples of the flame front contour lines with 1/2000 s interval.....	120
Figure 68 Variation of flame height H_f and lift-off height H_l of acoustically excited flame.....	122
Figure 69 Sample schlieren pictures for three perturbation conditions.....	123
Figure 70 (a) Colour images for cycle of attachment, lift-off and reattachment; (b) The trajectories of the flame lifted height	125
Figure 71 Frequency of the lifted height for various acoustic excitation conditions..	126
Figure 72 (a) Schlieren images for flame and jet flow structure during the lifted and reattached process; (b) Instantaneous calculated CH^*/C_2^* ratio colour map.....	130
Figure 73 CH^*/C_2^* ratio along the tube under various excited frequencies.....	132
Figure 74 Sample of post-processed images to give CH^*/C_2^* ratio distribution at the	

various sound intensities condition of each frequency group	133
Figure 75 6 th order polynomial curve fit Gaussian distribution CH*/C ₂ * ratio for various acoustic excitations	134
Figure 76 Comparison of the average CH*/C ₂ * ratio	135
Figure 77 CH*/C ₂ * ratio FFT	136
Figure 78. Basic components of a gas turbine engine.....	142
Figure 79. Diagram of air flow paths in a gas turbine combustor[146].....	142
Figure 80 Derived cetane number against equivalence ratio at LBO[183].....	150
Figure 81 Chemical compositions of C-7	152
Figure 82. Tay Combustor experimental apparatus	154
Figure 83. Overview of the combustor test rig	155
Figure 84 Fuel supply system	156
Figure 85. NI SCXI chassis and control PC.....	157
Figure 86 Equivalence ratio of candidate fuels at LBO.....	163
Figure 87 Equivalence ratio of candidate fuels at LBO.....	164
Figure 88 Plot of the normalised equivalence ratio against normalised fuel properties	165
Figure 89 Feature importance for LBO.....	166
Figure 90 (a) Flame visualisation and (b) soot concentration contour plot of different types of sample fuels at last 0.1s of LBO;	167
Figure 91 Sooty flame concentration ratio of candidate fuels at LBO condition	169
Figure 92 Sooty flame concentration ratio of the candidate fuels comparing with the A2	170
Figure 93 Plot of the normalised sooty area ratio against normalised fuel properties.	171
Figure 94 Feature importance for SCR.....	172
Figure 95 Incorporated effects index of fuel properties on the combustion performance	

at LBO condition.....	173
Figure 96 Ternary diagram for fuel composition effect on combustion performance	175
Figure 97 Aromatics composition effect on sooty flame concentration ratio	177
Figure 98. Sample images for seven fuels burning in the last 50/2000s at LBO.....	179
Figure 99 Sooty flame concentration ratio for seven fuels at three air flow conditions	179
Figure 100 Equivalence ratio for seven fuels at three air flow conditions.....	180
Figure 101 Sooty flame concentration ratio vs the LBO equivalence ratio at three flow rate conditions	181
Figure 102 DCN result of the Fuels with DTBP	182
Figure 103 LBO Fuel/Air Ratio results for two fuels with different proportions of DTBP	183
Figure 104 Sooty flame concentration ratio results for the two fuels with different proportions of DTBP	184
Figure 105 Suggested setup for the acoustic perturbation effect on the flame propagation in open/close tube.....	192
Figure 106 Deal sample instrument for side combustion chamber optical monitoring	193

List of Tables

Table. 1: Saturated hydrocarbon naming convention and formulae.....	8
Table. 2 Unsaturated Hydrocarbon bonds.....	9
Table. 3 Camera operation parameters.....	75
Table 4 Typical Chemical Families in Aviation Fuel	151
Table. 5 Operating parameters for the LBO condition.....	156
Table. 6 Operating conditions and measurement uncertainty during LBO.....	158
Table 7 Conventional Fuel Selection	160
Table 8 Conventional Fuel Properties Matrix	161
Table 9 Data of the Fuels with Cetane additives.....	162
Table 10 Aromatics groups description.....	176
Table 11 Aromatic types content of each candidate fuel.....	177

Nomenclature

LBO	Lean Blow-out Limit
N_2	Nitrogen gas
H_2O	Water
CO_2	Carbon Dioxide
CO	Carbon monoxide
NO_x	Nitrogen oxides
PM	Particulate matter
ρ	The density of the fluid in gas phase (kg/m ³)
v_l, v_g	The velocity of liquid and gas phase (m/s)
d_l	Its characteristic length, typically the droplet diameter (m)
σ	The surface tension (N/m)
μ	The viscosity of the liquid
ρ_l	The density of the liquid.
Oh_d	Ohnesorge number
We	Weber Number
D_t	Temporal droplet size
D_0	Initial droplet size
K	Burning rate constant (mm ² /s)
t	Burning time
m_{air}	Mass ratio of air
m_{fuel}	Mass ratio of fuel
FAR	fuel-air ratio
ϕ	Equivalence ratio

st	stoichiometric
E	A photon energy
h	Planck's constant
λ	The wavelength
c	The speed of light
f	Frequency
OH*	OH radical chemiluminescence
CH*	CH radical chemiluminescence
C ₂ *	C ₂ radical chemiluminescence
CCD	Charge-coupled Device
CMOS	Complementary Metal-Oxide-Semiconductor
RGB	Red, Green, Blue
I	Intensity of light
HSV	Hue, Saturation and Value
fps	Frame per Second
m	The total number of pixels in the template.
C	Colour
α	The light conversion rates
PIV	Particle image velocimetry
T	Temperature
V	Speed of sound in air
I _s	Intensity of a sound wave
P	The sound power
r	The distance from the sound source
A(r)	The area of a sphere of radius r
β	The sound intensity level in dB
I ₀	The reference sound intensity;

A	The wave amplitude
ω	Angular frequency
x	Longitudinal position
L	The length of the tube
V (in Eq 33)	velocity of the mixture gas at the nozzle
D	inside diameter of the nozzle
μ_m	The dynamic viscosity of the mixture gas
ρ_m	The density of the mixture gas,
H_L	Lift-off height
D_f	Diameter of the fuel tube
U_f	Fuel jet velocity
f_e	Acoustic excitation frequency
f_L	Flame lifted off frequency
ξ_i^\pm	The displacement of perturbation of the flame front to the steady position
σ_{ξ_i}	The average flame fluctuation amplitude
A	Flame area
V	Flame volume
a_{unit}	The flame surface area per unit volume
H_f	The visible flame length
Re	Reynolds number
LCCC	Low Carbon Combustion Centre
NJFCP	National Jet Fuels Combustion Program
FAA	Federal Aviation Administration
DFCD	Digital flame colour discrimination
DCN	Derived Cetane Number
GtL	Gas to liquid

FM	Coriolis mass flow meter
ATJ	Alcohol-to-jet
R	Coefficient of determination
SCR	Sooty flame concentration ratio
AFR	Air flow rate
k	The gradient of the slope
DTBP	Di-tert-butyl peroxide

1. Introduction

1.1. Motivation

Although the exploitation and utilisation of renewable energy is on the rise and developing, a large portion of the global energy requirements still rely on combustion. In particular, in the transportation sector, increasing population and economic growth have boosted traffic levels markedly. The tremendous expansion in global energy demand combined with the energy crisis and the stringent limitations on environmental pollution has been the challenge and the driving force for combustion research. In addition to developing new energy sources, using fuel effectively and reducing emissions are the primary objectives of such research. A thorough understanding of the mechanism of combustion, comprehensive monitoring, and integrated assessment are essential for the improvement of combustion performance.

Combustion has been a fundamental research topic in recent centuries. Since Mallard and LeChatelier first applied the photographic method to flame measurements in 1883, optical equipment has become indispensable in various fields of combustion research. The modality of the camera application developed from film to digital and the recorded image data progressed from generalised to quantitative.

Optical visualisation of flames plays an important role in the in-depth understanding of complex combustion phenomena. In particular, a high-speed camera can provide nonintrusive and continuous monitoring of flames. Through the recorded images, further analysis on colour, temperature, flame dynamics, and a tremendous variety of other

information can be achieved, which is essential for physical study and numerical modelling.

In terms of practical applications, consider the endoscope of the engine as an example. Diagnosis can be performed without demolition through the recording of images on the ignition states, gas dynamic characteristic, and flame oscillation, which also enables the detection, recognition, and quantitative assessment of the occurring damage and material defects. However, each diagnostic technique has its drawbacks. For example, the borescope is a useful tool for the engine chamber detection. But the flame images are always blurry due to the violent vibration, the flame fast oscillation. The selection of the frame rate and shutter speed has a significant effect on the accuracy of the flame measurement. Low frame rates cause a loss in detail, whereas high frame rates may lead to signal drop-out. The balancing of these two factors is of importance during recording.

Therefore, the aim of the research work is to provide instructions on how to effectively apply the visualisation technique to different combustion conditions and obtain valuable combustion knowledge with the aid of optical monitoring.

1.2. Objectives

According to the motivations in the previous section, the main objective of the present work is to apply the visualisation monitoring to different combustion conditions and acquire new combustion phenomena, integrate these findings with their inherent nature, and achieve new combustion knowledge. The sub-objectives of the research carried out in this study are listed below:

- To develop a suitable imaging processing method for combustion diagnostics,

Chapter 1 Introduction

including noise removal, boundary detection, colour selection, and chemiluminescence measuring.

- To explore the relationships between the chemiluminescence and equivalence ratio with the effects of flame regions, different fuels, camera sensor sensitivity, and measurement methods.
- To compare the accuracy of novel and conventional measurement methods.
- To identify the experimental validation of equivalence ratio range for the different measurement methods, fuels, and cameras.

Apply the visualisation monitoring to gaseous fuel combustion under acoustic excitation condition:

- To investigate the response of flame features to acoustic excitation, from the perspective of flame flicking and configuration.
- To explore the principle of acoustically induced dilution behaviour.
- To study the cause and consequences of the acoustically induced lift-off phenomenon.

Apply the visualisation monitoring to liquid fuel combustion in a gas turbine:

- To evaluate the fuel performance in the transient lean blowout (LBO) and stable combustion condition on a small spray gas turbine combustor.
- To characterise effects of the physical and chemical fuel properties on the LBO equivalence ratio and soot formation.
- To examine the air flow rate effect on the LBO performance of the different fuels.
- To propose a potential method to optimise fuel LBO performance, such as by blending additives.

1.3. Outline of the Thesis

The thesis includes three main sections, pertaining to the knowledge and methodology of the visualisation monitoring, and the application of these methods to gaseous fuel and liquid fuel combustion. The main structure is shown in the flow chart Figure 1. Each of the three main chapters includes an introduction, background knowledge, main body, and conclusion.

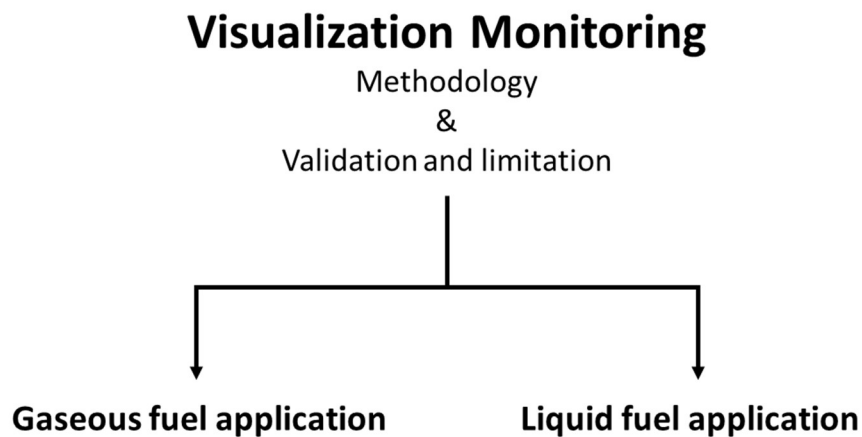


Figure 1 Structure of the thesis

The thesis consists of seven chapters:

Chapter 1 introduces the motivation and objectives of the research and outlines the structure of the thesis.

Chapter 2 provides the basic knowledge of combustion and cameras.

Chapter 3 presents the imaging processing methodology for combustion purposes. It also compares the suitable self-developed flame diagnostic methods with the generally applied conventional methods.

Chapter 1 Introduction

Chapter 4 presents a complementary analysis to experimentally examine the methods introduced in the previous chapter. It proves the validation of the colour modelled chemiluminescence measuring method and limited the validation range.

Chapter 5 applies the visualisation approaches to observe the flame/acoustic interaction on the premixed flame front dynamic structure. It combines the schlieren and other image processing techniques to understand the perturbation effect on fuel/air mixing, particularly the dynamic character of the dilution behaviour.

Chapter 6 applies the visualisation approaches to characterise the effects of the physical and chemical fuel properties on the LBO equivalence ratio and soot formation. Furthermore, it evaluates the combustion performance of the alternative fuels from the aspects of LBO, soot emission, different operating conditions, and blending with additives.

Chapter 7 concludes the methods and applications of visualisation monitoring on combustion and presents perspectives of further work that could or should be carried out in the future.

2. Basic Background Knowledge

Combustion is a vast and complex topic and has penetrated into every corner of our daily life, including energy, transportation, environment, safety, and so on. Moreover, with the rapid development of digital and computational techniques, many complicated optical diagnostic systems have been exploited to provide monitoring for combustion researches. Even only in terms of optical combustion diagnostic, the applications, flame types, operating conditions, and monitoring purposes are diverse from each other and it's impossible to mention all the details in one chapter.

As in this work, the main discussion is the application the visualisation monitoring to gaseous fuel and liquid fuel combustion and acquire new combustion phenomena. Therefore, in the section, only basic concept of combustion and optical diagnostic will be introduced. More details of literature review for each application will be discussed in its relative chapter.

2.1. General Concept of Hydrocarbon Combustion

Combustion is a chemical reaction between fuels and an oxidant at high temperature. The final products of ideally complete combustion are water and CO₂, but this is hardly

practical. The instantaneous reaction includes complex procedures. During the reaction, atoms and free radicals are generated, and electromagnetic radiation and other active intermediates are released in the forms of light and heat. After the reaction, taking the most common fuel, hydrocarbon combustion, as an example, the exhaust gas contains nontoxic gas (N_2 , H_2O , and CO_2) and toxic substances (CO , C_xH_y , $C_xH_yO_z$, NO_x , etc.).

2.1.1. Types of Hydrocarbons

Pure hydrocarbon fuels are compounds of carbon and hydrogen only. They can be solid, liquid, or gaseous at normal pressure and temperature. The state of these hydrocarbons is mainly dependent on the number of carbon atoms and their molecular structure. The gaseous hydrocarbons have fewer than four carbon atoms. Those with a range between five and nineteen carbon atoms are liquid, while those with twenty or more are solid. Hydrocarbons have been divided into three main categories: Saturated, Unsaturated hydrocarbons and Aromatic hydrocarbons, shown in Figure 2.

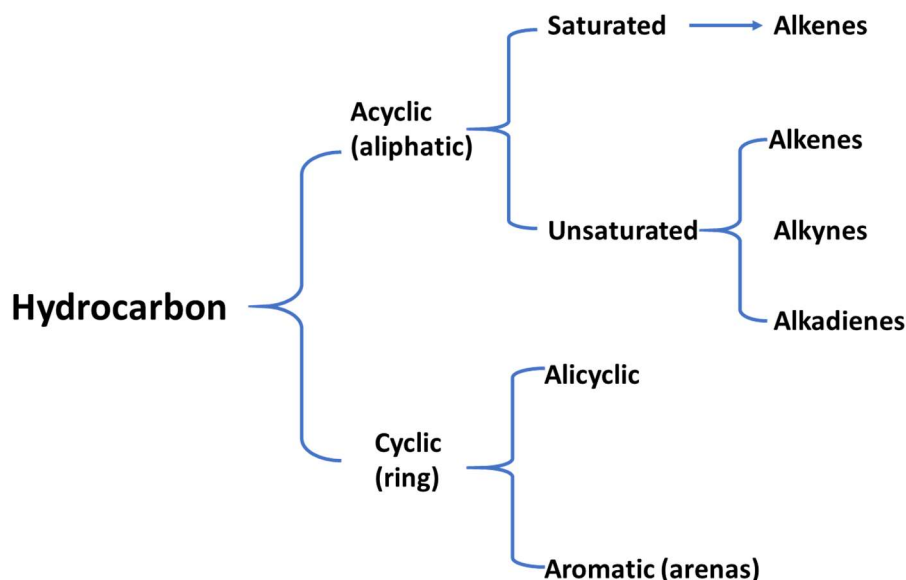


Figure 2. Main categories of hydrocarbons

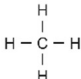
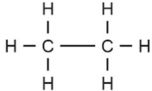
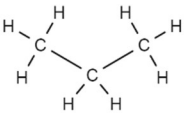
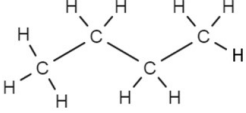
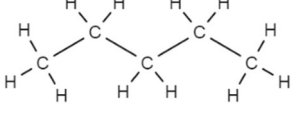
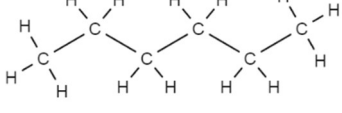
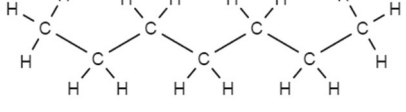
Chapter 2 Basic Background Knowledge

2.1.1.1. Saturated Hydrocarbons

Saturated hydrocarbons are also called alkanes, the molecules which contain pure single carbon-carbon bonds. No additional atoms can be incorporated into their structure. Hence, these saturated molecules are stable and not very reactive.

Table 1 shows the samples of alkanes. The general formula of an alkane is defined as C_nH_{2n+2} , in which the subscript n represents the number of carbon atoms in the molecule.

Table. 1: Saturated hydrocarbon naming convention and formulae.

Carbons	Name	Molecular Formula	Formula Structural
1	Methane	CH_4	
2	Ethane	C_2H_6	
3	Propane	C_3H_8	
4	Butane	C_4H_{10}	
5	Pentane	C_5H_{12}	
6	Hexane	C_6H_{14}	
7	Heptane	C_7H_{16}	

Chapter 2 Basic Background Knowledge

n	C_nH_{2n+2}
---	---------------

2.1.1.2. Unsaturated Hydrocarbons

The molecules of unsaturated hydrocarbons, such as alkenes and alkynes, contain double or triple carbon-carbon bond(s) in their structure. These molecules are highly reactive to incorporate other atoms into their structure.

The alkenes and alkynes share a similar general pattern. However, alkenes (C_nH_{2n}) have a double bond between two carbon atoms, whereas alkynes (C_nH_{2n-2}) contain a triple bond instead. The different bonding structures of ethane (saturated hydrocarbon), ethene, and ethyne (unsaturated hydrocarbons) are shown in Table 2.

Table. 2 Unsaturated hydrocarbon bonds.

Ethane	Ethene	Ethyne
CH_3-CH_3	$CH_2=CH_2$	$CH\equiv CH$

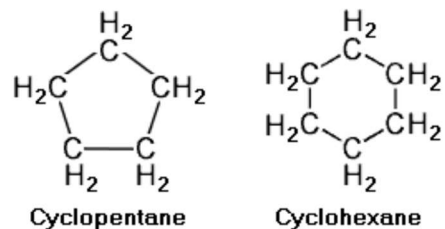
2.1.1.3. Alicyclic

An alicyclic compound is an organic compound that is both aliphatic and cyclic. Alicyclic compounds can be attached with one or more aliphatic side chains. They contain one or several pure carbon rings, which may be either saturated or unsaturated, but do not have aromatic character.

Cycloparaffins, or naphthenes, are saturated hydrocarbons, in which the carbon atoms are linked to form rings instead of chains as in the case of paraffin. They have the same base names as paraffins of the same number of carbon atoms but with the addition

Chapter 2 Basic Background Knowledge

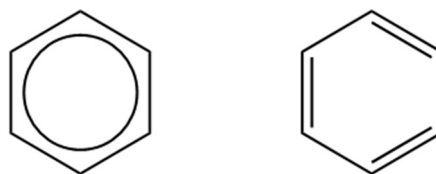
of the prefix 'cyclo' as below:



Usually jet fuels contain 25–35% of naphthenes. These are close to paraffins in their chemical stability, soot-forming tendencies, and high heat of combustion

2.1.1.4. Aromatic

In organic chemistry, the term aromaticity is used to describe a cyclic (ring-shaped), planar (flat) molecule with a ring of resonance bonds. Compared with the other geometric or connective arrangements with the same set of atoms, aromatic molecules have a very stable structure, and hardly break apart to react with other substances. Certain organic compounds with cyclic structure are classified as aliphatic compounds. An aromatic hydrocarbon is a cyclic hydrocarbon with alternating double and single bonds and $(4n + 2) \pi$ electrons, which have special stability and low reactivity. Benzene is the most common example ($n = 1$).



Aromatic hydrocarbons are much more stable than their noncyclic counterparts. The carbon–carbon bonds in aromatic hydrocarbons are equivalent. They are not alternating

double and single bonds with different lengths. They are all the same length and equivalent to each other. To show this symmetry, the formulas of aromatic hydrocarbons often use a circle to represent the π electrons.

2.1.2. Gaseous Combustion

Flames can be classified into three categories: premixed, partial premixed, and diffusion, depending on whether the fuel and oxidiser have been mixed or not and the level of mixture prior to the reaction.

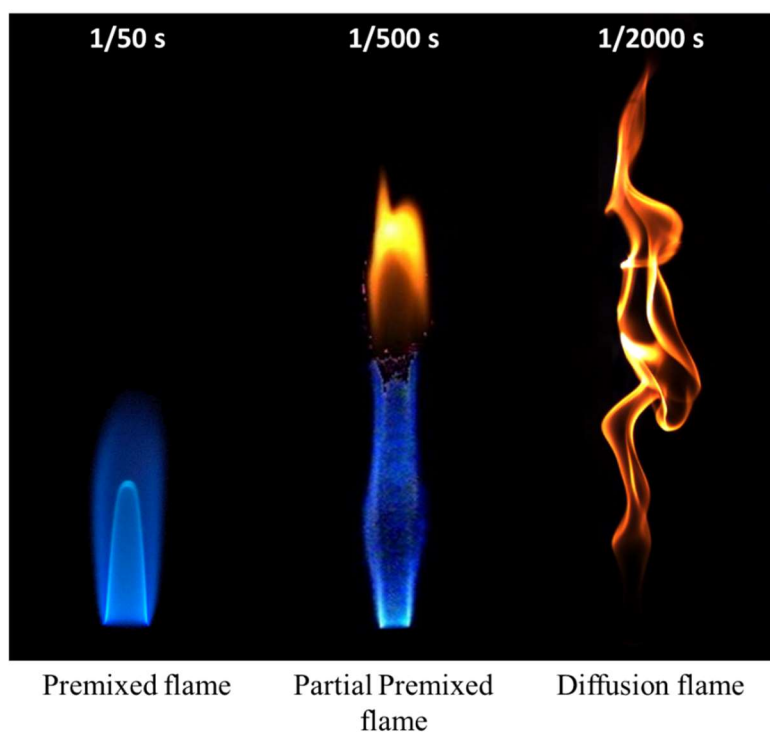


Figure 3 Flame categories: diffusion, premixed, and partial premixed flame

2.1.2.1. Diffusion Flames

For a diffusion flame, the fuel and oxidant are not mixed homogeneously before the

Chapter 2 Basic Background Knowledge

combustion. Normally, the burning of pure fuel directly reacts with the surrounding air. In this situation, the mixing rate is far lower than the chemical stoichiometric reaction rate [1]. Thus, mixing rate controls the combustion process and limits the flame speed. Generally, due to the insufficient oxidiser, the diffusion flame generates soot and burns slower than a premixed flame. The soot particles are heated to high temperature and exhibit an orange-yellow colour. A candle flame is a classic example of a diffusion flame.

The Bunsen burner, invented by Robert Bunsen in 1855 [1], is a common piece of lab equipment to heat up, sterilize, and burn [2]. It can produce both diffusion and premixed flames by adjusting the amount of the input air and the fuel rate. A schematic of a Bunsen burner is shown in Figure 4. The left subfigure (a) illustrates a diffusion flame with a closed air hole, which means only fuel flow is available, as indicated by the red arrow. The flame colour in the luminous reaction zone is bright orange-yellow owing to the incandescent soot particles.

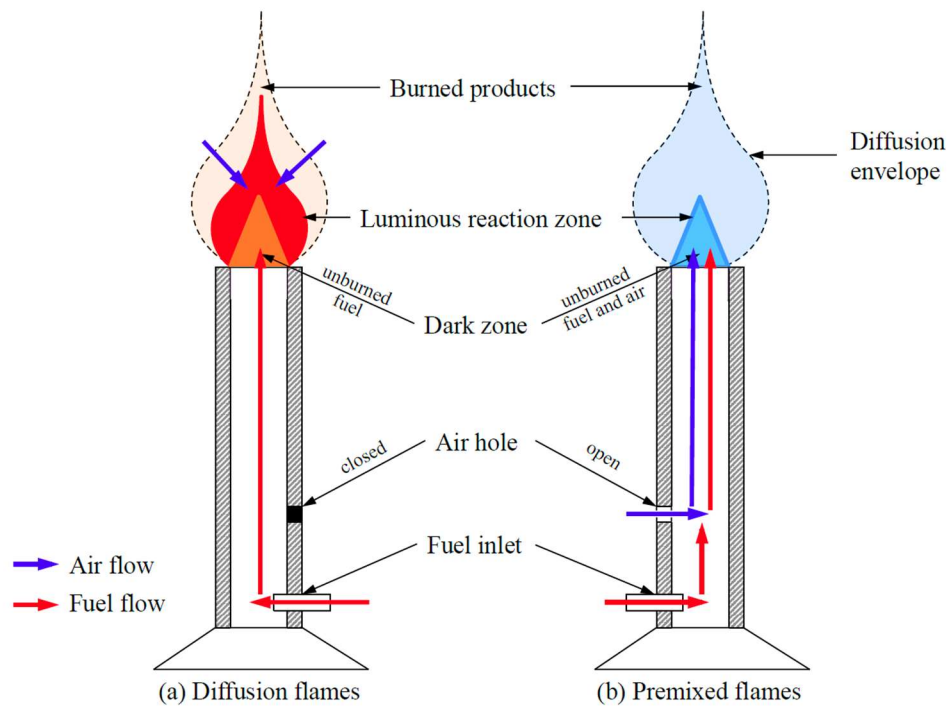


Figure 4 Schematic of Bunsen burner flames: (a) diffusion flames and (b) premixed flames

2.1.2.2. Premixed Flames

To produce a premixed flame, the fuel and air are homogeneously mixed in advance of combustion. The reaction mainly occurs at the interfacial layer between the unburned and the burned gases. The chemical reaction dominates the reaction rate. The flame speed is equal to premixed flame propagation speed, which is determined by the balance of the convection-diffusion-reaction. Figure 4(b) shows a schematic premixed flame in a Bunsen burner with the addition of the air flow (blue line). The air enters the pipe of the burner and mixes with the fuel. The flame colour in the luminous reaction zone is blue-green owing to the chemiluminescence. The details of the chemical reaction structure and products are shown in Figure 5.

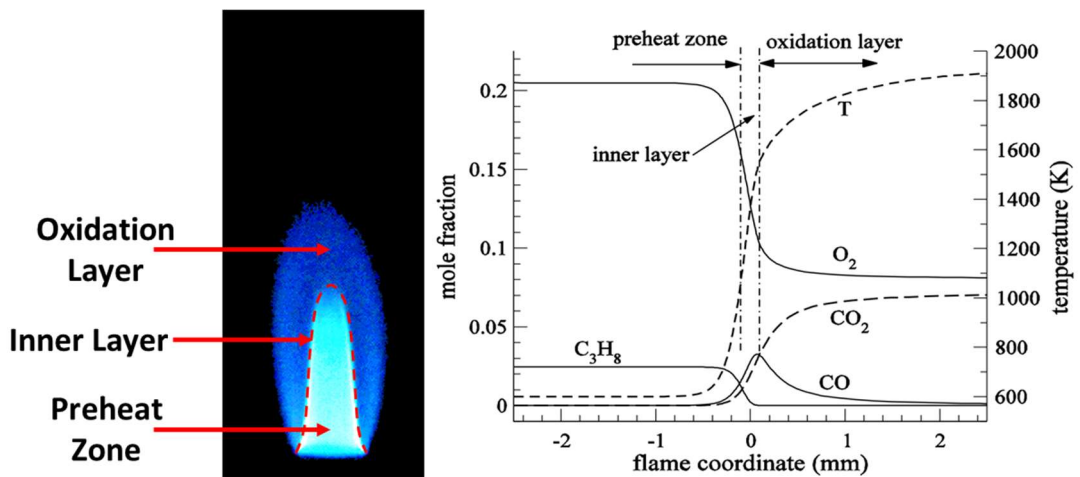


Figure 5 Structure of propane premixed flame

- Preheat zone: heating up the reactants
- Inner-layer: radical formation

- Oxidation-layer: finishing the remaining reactions

2.1.2.3. Partially Premixed Flame

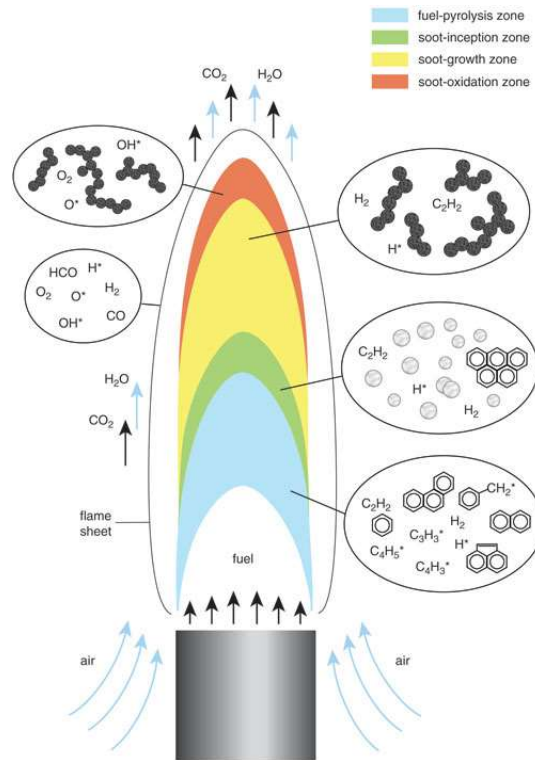


Figure 6 The structure of partially premixed flame [3]

Before burning at the nozzle, the fuel and part of the stoichiometrically required oxidiser have been mixed. However, the supplied oxidiser is insufficient to support the completed reaction; thus, the further reaction of the residual unburned fuel and the intermediates of the oxidation reaction will rely on surrounding air in the space and continuously burn as a diffusion flame. That will cause the combustion to generate a flame with the characteristic of both premixed and diffusion flame features, as shown in Figure 6. This flame is a so-called partially premixed flame.

2.1.3. Liquid Combustion

Liquid fuel is considered as the life blood of the industry. Modern vehicles such as cars, diesel locomotives, airplanes, and ships use liquid fuel to generate the driving power. The ubiquity of liquid fuels is due to their many advantages. For example, for a given mass of fuel, the volume of liquid and solid fuels is similar, which is far smaller than that of gas. However, liquid fuel has double the calorific value of coal. In addition, the liquid fuel has the characteristics of fast burning, easy control of combustion process, sufficient burning, and no residuals.

Liquid fuel combustion is mainly carried out in the gaseous state. Namely, the liquid fuel needs to vaporise to form a fuel vapor, then mixes with oxygen in the air to burn. Liquid fuel combustion is also a type of gaseous combustion, with the difference being the additional evaporation gasification process. Obviously, the burning time of liquid fuel consists of three parts: evaporation, diffusion mixing, and chemical reaction. The chemical reaction is very rapid, whereas the evaporation process is the slowest part. Therefore, the burning rate of liquid fuel mainly depends on the evaporation rate, which is called the volatility.

In general, the rate of evaporation of a liquid fuel depends on factors such as the contact surface area between it and the surrounding air, temperature differences, concentration differences, and fuel diffusion coefficients. Among these factors, increasing the contact surface area with air is a key factor. Atomisation devices are used to atomise the droplets into a fine droplet group, which is an important method to increase the evaporation surface area and improve the burning rate. It has been found that smaller droplets can burn with a premixed flame, owing to complete evaporation and burning [4]. In addition, this sufficient burning performance leads to reductions in

the NO_x and particulate matter (PM) [5].

Atomising combustion is a complex process involving simultaneous exchange of heat, mass, and momentum, and chemical reactions. Owing to the complexity of the process, it is difficult to obtain detailed and accurate information on the combustion of liquid fuels by studying atomisation combustion. Therefore, two research methods are commonly used for liquid fuel combustion: single droplet combustion and spray combustion.

2.1.3.1. Liquid Fuel Spray Combustion

The basic principle of droplet separation is to use external forces to increase the surface of the liquid until it becomes unstable and broken. The process of droplet generation from a liquid depends on the flow properties (laminar or turbulent flow) of the liquid in the atomising nozzle, the method for adding energy to the liquid, the physical properties of the liquid, and the properties of the surrounding atmosphere. The liquid jet itself is subjected to the initial turbulence and the action of the surrounding gas on the jet (pulsation, friction, etc.), which causes the surface of the liquid to fluctuate, wrinkle, and eventually separate into liquid fragments or filaments. Then, under the influence of surface tension, liquid fragments or filaments shrink into spherical droplets [6].

Pressure atomisation uses a pressure decrease at the nozzle inlet to achieve the separation of liquid droplets from the liquid jet. Air blast atomisation uses air as an atomising medium to separate droplets from the liquid fuel.

There are two important parameters that affect the atomisation process. One is the relative velocity gradient between the liquid fuel jet and the surrounding gas. The other

Chapter 2 Basic Background Knowledge

is the pressure difference before and after the atomising nozzle. The size of the droplet group will be finer with a larger pressure difference, higher relative speed, and faster atomisation process.

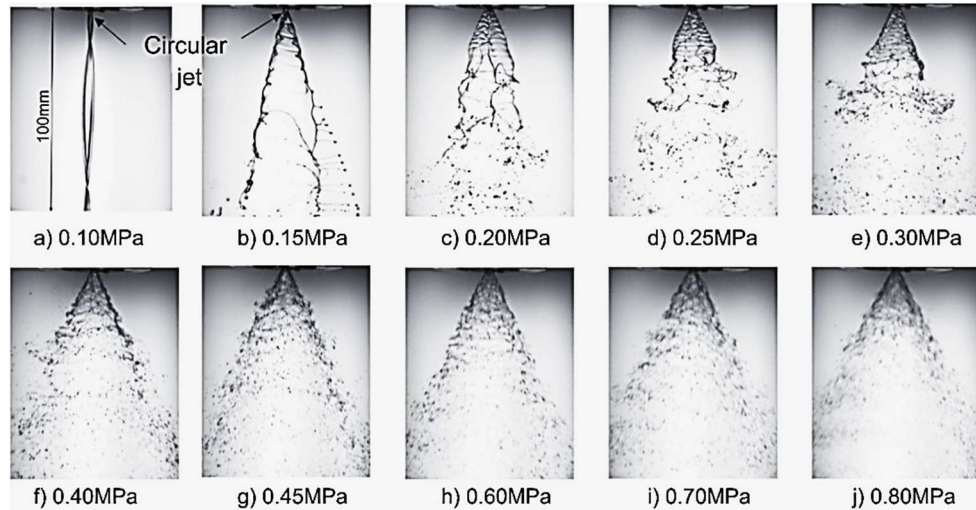


Figure 7 Spray images at different injection pressures [7]

Several mechanisms have evolved into the fuel jet break-up process. Two dimensionless numbers, Weber number and Ohnesorge number, are used to characterize these mechanisms.

The Weber number is the ratio of the inertial force to the surface tension force. It determines which is dominant between the kinetic and surface tension energy. It can be expressed as:

$$We_g = \frac{\rho_g(v_l - v_g)^2 d_l}{\sigma} \quad \text{Equation 1}$$

where, ρ : the density of the fluid in gas phase (kg/m^3).

v_l, v_g : the velocities of liquid and gas phase (m/s).

d_l : the characteristic length, typically the droplet diameter (m).

σ : the surface tension (N/m).

The Ohnesorge number is a dimensionless number used in fluid mechanics to measure the relationship among the viscous forces, inertial forces, and surface tensions.

$$Oh_d = \frac{\mu_l}{\sqrt{\rho_1 d_1 \sigma}}$$

Equation 2

where μ_l : the viscosity of the liquid.

ρ_1 : the density of the liquid.

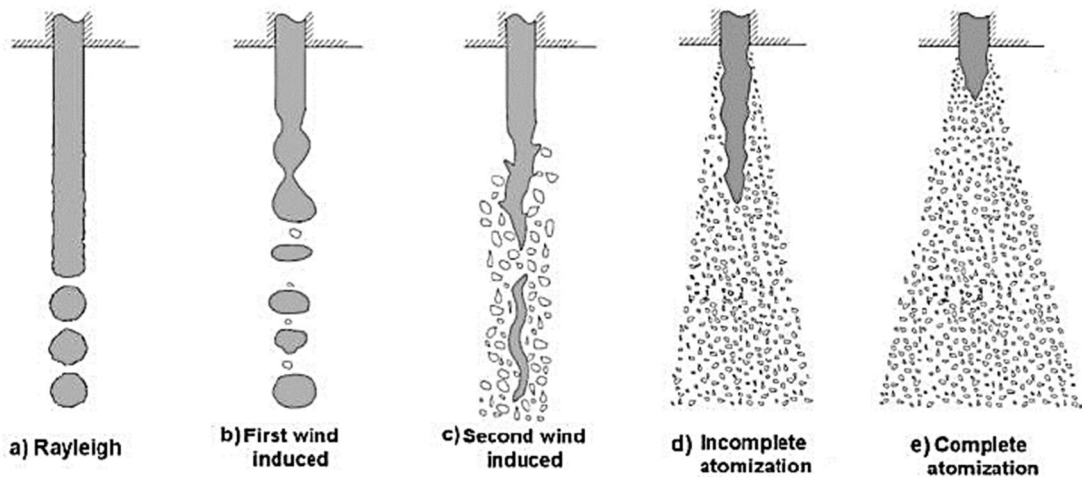


Figure 8. Scheme of spray structure for different atomisation regimes [8]

At the low velocity of the fluid condition, the break-up process is dominated by Rayleigh mechanism, which is the competition between the surface tension and inertia. With the increase in the jet velocity, the mechanism transitions to the first wind-induced regime, where We is nearly 1. For high Weber number from 10 to 40, the jet can be atomised completely right out of the nozzle.

2.1.3.2. Droplet Combustion

Chapter 2 Basic Background Knowledge

The complex liquid spray combustion is assisted with multidimensional fluid dynamics, diffusive processes, heat transfer, and combustion/emissions chemistry. Droplet combustion is a simplified and basic sub-subject with the features of unidimensionality, time-dependence, and easy manipulability, which is critical to understanding, developing, testing, and validating the spray combustion performance.

The droplet combustion also reveals further details of the fuel burning performance. The first droplet study dates back to the 1950s by Godsave [9][10], Kumagai [11] and Spalding [12]. They presented the D^2 -law which is the classical theory to describe the droplet evaporation and combustion, shown in Equation 3.

$$D_t^2 = D_0^2 - Kt \quad \text{Equation 3}$$

where D_t : temporal droplet size;

D_0 : initial droplet size;

K : burning rate constant (mm^2/s);

t : burning time.

Currently, with the development in experimental and numerical technology, our understanding has deepened and more phenomena during the transient droplet burning process have been tracked [13,14], especially for the optical diagnostic methods. Further descriptions of these techniques are introduced below.

2.1.4. Fuel–Air Ratio

The fuel-air ratio (FAR) is the mass ratio of fuel to air in a combustible mixture and commonly used in the gas turbine combustion.

$$FAR = \frac{m_{air}}{m_{fuel}} \quad \text{Equation 4}$$

The FAR is an important parameter in the engine running. It has a great influence on exhaust emissions, engine power, and economy. In the ideal situation, the supplied air can be consumed completely by the available fuel, with a so-called stoichiometric mixture. However, it can be hardly achieved in practical engine applications, which will be affected by the atomisation degree, burning duration, pressure, dilution condition, etc. The equivalence ratio is a dimensionless parameter defined to express the mixture degree of the fuel and air. It is the ratio of the actual FAR to the stoichiometric FAR, as mathematically described in Equation 5.

$$\phi = \frac{FAR_{actual}}{FAR_{stoichiometric}} = \frac{(m_{fuel}/m_{air})_{actual}}{(m_{fuel}/m_{air})_{st}} = \frac{(n_{fuel}/n_{air})_{actual}}{(n_{fuel}/n_{air})_{st}} \quad \text{Equation 5}$$

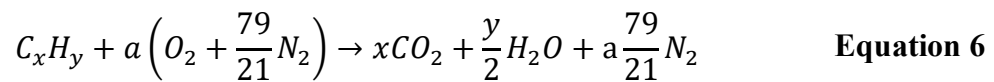
where m is the mass and n is the number of moles, the st is short for ‘stoichiometric’.

The value of the equivalence ratio is regarded as an indicator to determine the combustion condition is fuel rich or fuel lean.

$\phi > 1$: fuel rich

$\phi < 1$: fuel lean

The most common way to determine the stoichiometric ratio for the different fuel-to-air combustion is through the balancing of the chemical equation to convert reactants to exhaust products. For mixtures of hydrocarbon fuel and air constituents, the chemical reaction can be balanced via [15]:



Thus, the stoichiometric ratio can be defined as:

$$\left(\frac{m_f}{m_o} \right) = \left(\frac{m_{C_xH_y}}{a \times m_o} \right) \quad \text{Equation 7}$$

For example, when methane (CH₄) reacts with oxygen (O₂), the stoichiometric chemical balance equation is given by:



which means 1 mole of propane consumes 2 moles of oxygen stoichiometrically

$$n_{CH_4} : n_{O_2} = 1 : 2 \quad \text{Equation 9}$$

Dry air contains 20.95% oxygen and rest of other gases, hence,

$$V_{CH_4} : V_{air} = 1 : \frac{2}{\frac{V_{O_2}}{V_{air}}} = 1 : \frac{2}{20.95\%} = 1 : 9.55 \quad \text{Equation 10}$$

2.1.5. Flame Colour

Experimental spectroscopy is concerned with characterising the absorption, emission, and/or scattering of electromagnetic radiation by atoms or molecules. The most well-known region is associated with the wavelength range sensitive to human vision. The human eye is sensitive to a broad band of wavelengths with the approximate range 350–750 nm (see Figure 9). The visible spectrum represents only a small fraction of the full electromagnetic spectrum. Within the visible spectrum certain wavelengths give rise to certain visual sensations. For example, the shorter wavelengths are perceived to be violet and blue, and the longer wavelengths are perceived as red. The shorter-wavelength photons with higher frequency carry higher energy.

Chapter 2 Basic Background Knowledge

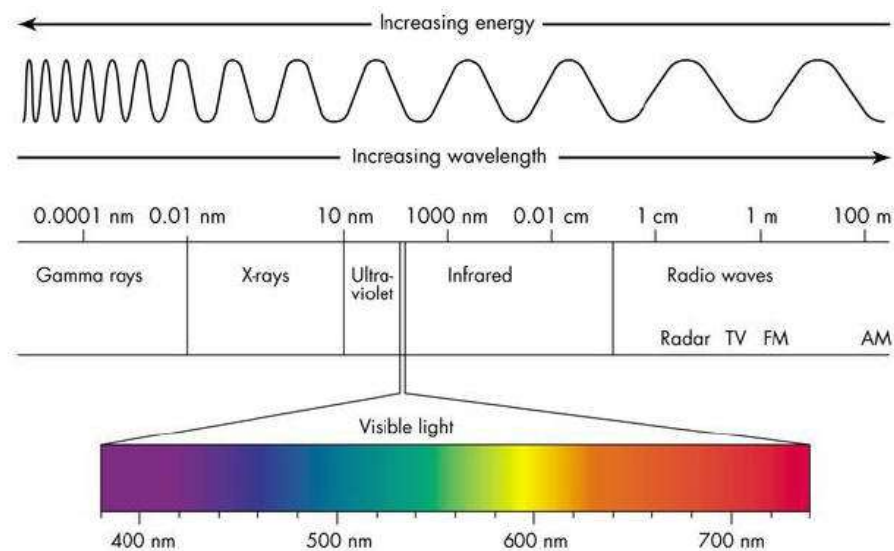


Figure 9 Visible light spectrum [16]

For the hydrocarbon flame, the oxygen supply and the pre-mixture level is the dominant factor for flame colour, because they determine the combustion rate, temperature, and reaction path, which lead to different colour generation.

The Bunsen burner diffusion flame consists of hot incompletely burned soot particles at approximately 1000 °C. These particles produce a continuous band of light with a peak dependent on the temperature, in accordance with the black-body radiation spectrum. With the increase in the temperature, the diffusion flame colour changes from red, transitioning through orange and yellow to white.

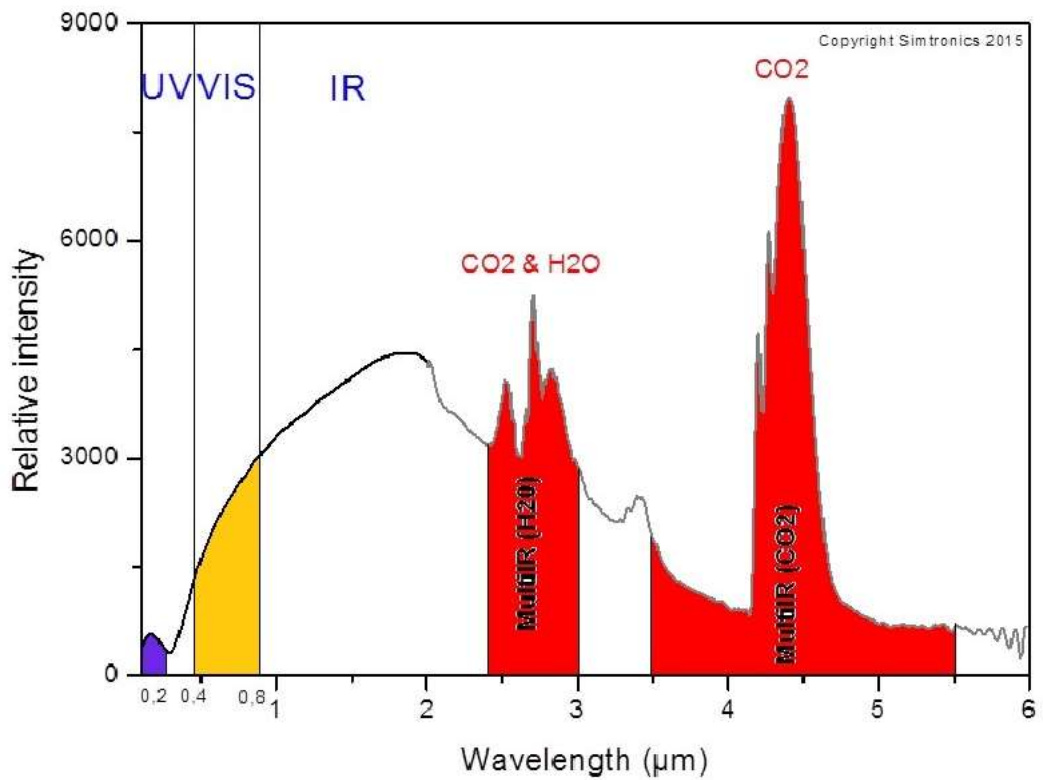


Figure 10 Hydrocarbon fire typical emission spectrum [17]

With the increase in the oxygen supply, sufficient burning releases higher energy to excite the molecules. When the atoms of a gas or vapor are excited, by heating or by applying an electrical field, their electrons are able to move from their ground state to higher energy levels. As they return to their ground state, they emit photons of very specific energy, as represented by the schematic of the procedure shown in Figure 11. These energies correspond to particular wavelengths of light, and thus produce particular colours of light.

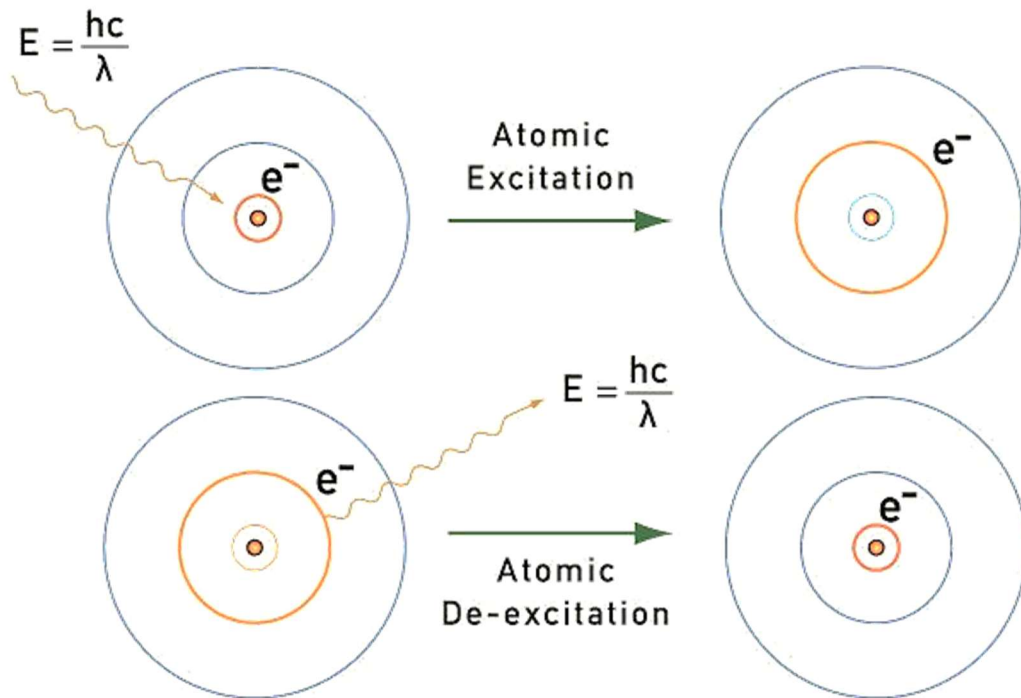


Figure 11 Photons of light are emitted as an electron drops back to its ground state after being excited

As mentioned in Chapter 1, the reaction mechanism for converting reactants to products during combustion does not happen in a single step. Instead, it involves the formation of many short-lived intermediate chemical species that carry the reaction from one process to another. In combustion studies, the accompanied emission of photons as excited species drop back to their stationary states is known as chemiluminescence. The wavelength of radiation emitted is a characteristic of the particular fuel type and its chemical transition process. Usually, the band spectral emissions from excited OH^* , CH^* , and C_2^* , in the UV–VIS spectrum are dominant emissive features in premixed hydrocarbon–air flames.

Consequently, our perception of flame colour is based on this emissivity in the

visible wavelength. For hydrocarbon flames, the visible emanating energy can be attributed to the spectra of electronically excited combustion radicals of CH^* (430 nm), C_2^* (C_2^* Swan system, dominant emissive band head at 473.71 nm and 516.52 nm), and the continuous spectrum from solid carbon/soot.

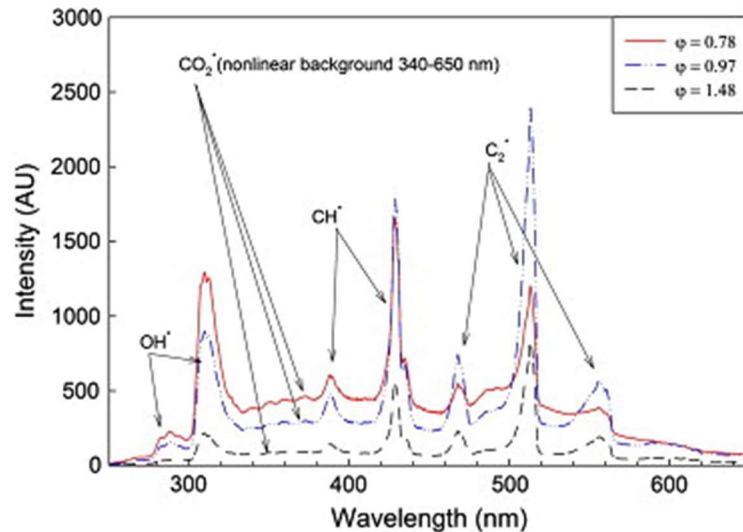


Figure 12 Chemiluminescence spectra of premixed atmospheric methane–air flames at different measured equivalence ratios [18]

Figure 12 illustrates a sample flame emission of a premixed flame in the *UV–VIS* spectrum. Three main emissive systems are observable for the CH^* , out of which, the 431 nm system is one of the most prominent with a characteristic degradation profile towards the shorter wavelength. The other of the most dominant emissions is C_2^* with prominent band heads at 474, 516, and 563 nm. For both CH^* and C_2^* , their production is known to be limited to the primary and secondary reaction zone. However, OH^* emission can be observed from both the primary and secondary reaction zone of the flame, with the strongest emission from the 306 nm system. In terms of visual flame colour perception, it is this mixing of chemiluminescent emissions in the VIS spectrum that contributed to the classical human visual association of a ‘green-blue’ premixed

flame colouration.

The intensity of the energy released by these spectra is related to a number of factors, such as burning condition, fuel composition, and fuel-to-oxidiser ratio. Such variation would consequently affect the colour perceived from a given flame. Thus, the colour of a flame can be used to obtain information on its general spectrometric composition.

2.1.6. Emission

There are a wide range of gaseous pollutants, but with the increasing number of vehicles and high demand for transportation, the fuel combustion is considered as the most influential the source of pollutants. For hydrocarbon fuels, the main exhaust gas contains nontoxic gases (N_2 , H_2O , and CO_2) and toxic substances (CO , C_xH_y , NO_x , etc.). Of these, CO_2 is also termed a greenhouse gas, which leads to global warming and NO_x comes from excessive temperature and smoke emission, normally known as PM. CO_2 and PM have attracted extensive societal attention, because they are not only harmful for human health, but also detrimental to the environment. CO_2 is an unavoidable product of sufficient burning, but PM is produced by incomplete combustion, which is mostly made up of soot particles with irregular shapes, size, chemical compositions [19,20].

PM can be easily controlled for gaseous fuels, but the elimination of residual insufficient fuel particles in fossil fuels is still a challenging research goal. Soot exhibits a bright yellowish sooty flame during combustion, owing the hot temperature. After cooling down, it becomes very refined small black particles, suspended in the air or settling on surfaces [21].

The statistics show [22–24], that there is a close relationship between the yearly

increase in the morbidity and mortality of respiratory diseases and the PM emissions. PM has been regarded as the one of the most serious respiratory health risks, leading to cardiopulmonary complications [25,26] in both the short term and long term. Kelly's study [27] revealed that the effects of inhaled PM deposition on lung function are depending on its toxic chemical properties and exposure duration. Heyder [28] reported that the size, shape, and density of the particles also play an important role.

2.2. General Optical Methods for Combustion Research

2.2.1. Shadowgraphy

The shadowgraph method was developed by Robert Hooke [29] and applied to flow dynamics research by Vincenz Dvorak [30]. Since then, this method has been extensively implemented in fluid dynamics [31–34], thermal dynamics, acoustic[35] and combustion experimental research. Typical parallel shadowgraph setup and sample image are shown in Figure 13.

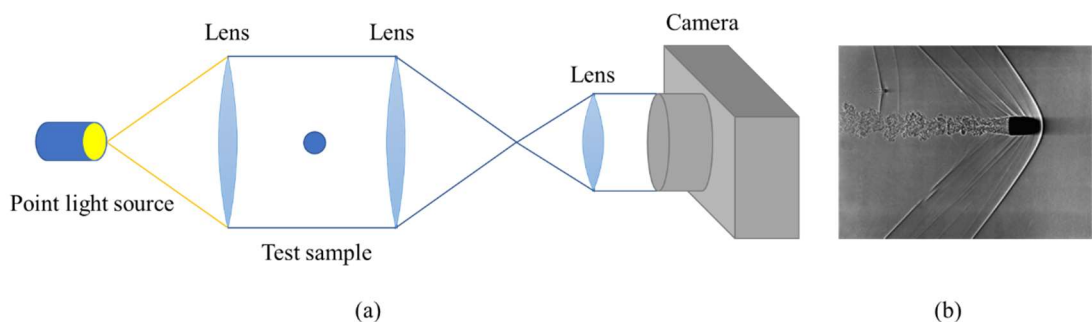


Figure 13 (a) Light shadowgraph setup; (b) sample shadowgraph of a bullet moving in stagnant air [36]

With the help of the shadowgraph tracking method, Kobayasi [37] calculated the

burning rate of different fuel blends. Ahmad observed different nucleation size and location inside a burning water and diesel emulsion. Many other experimental works on droplet evaporation and combustion have been carried out with the aid of shadowgraph imaging for tracking droplet size and appearance [38].

2.2.2. Schlieren

Refraction occurred when the light rays travel through inhomogeneous media. The original path of the rays is bent which led to Schlieren. Schlieren imaging relies on deflection of light by a refractive index gradient. The refractive index gradient is related to flow density gradient. The flow density gradient is vertical to the knife edge. The knife edges which block some of the undisturbed light, then contribute to different degrees on screen illumination [39]. In 1665, the first Schlieren system was composed of a convex lens and two candles and observed by Robert Hooke. The candles were used to provide a light source and air flow [40]. After improvement, schlieren systems are widely utilized to explore the invisible phenomena and objective by hundred years. Until today, schlieren are exerted in military field. Stealth planes are manufactured by the advanced technique, reduced radar reflected waves. Even so, the air vortex path is non-removable with existing technology. As a consequence, schlieren cameras are used as anti-stealthy technology [41].

In physics, schlieren imaging was widely applied on fluid dynamics study. A standard Z-configuration parallel-light schlieren system is a common setup in the laboratory. It is composed of a point light source, two spherical concave mirrors in parallel direction, a high-speed digital camera and a knife-edge placing ahead the camera Figure 14. Generally, a condenser lens and a board with a small hole are exerted to provide a bright slit of light source. The light source is placed one focal length away

Chapter 2 Basic Background Knowledge

from the first mirror A. Then the light is bent by mirror A, the refracted ray passed through the region of interest. Finally, the mirror B collimated the ray towards the direction of the camera and knife-edge which will block some light. The knife-edge which is placed at the focal point in order to view a light or dark area on the screen [40].

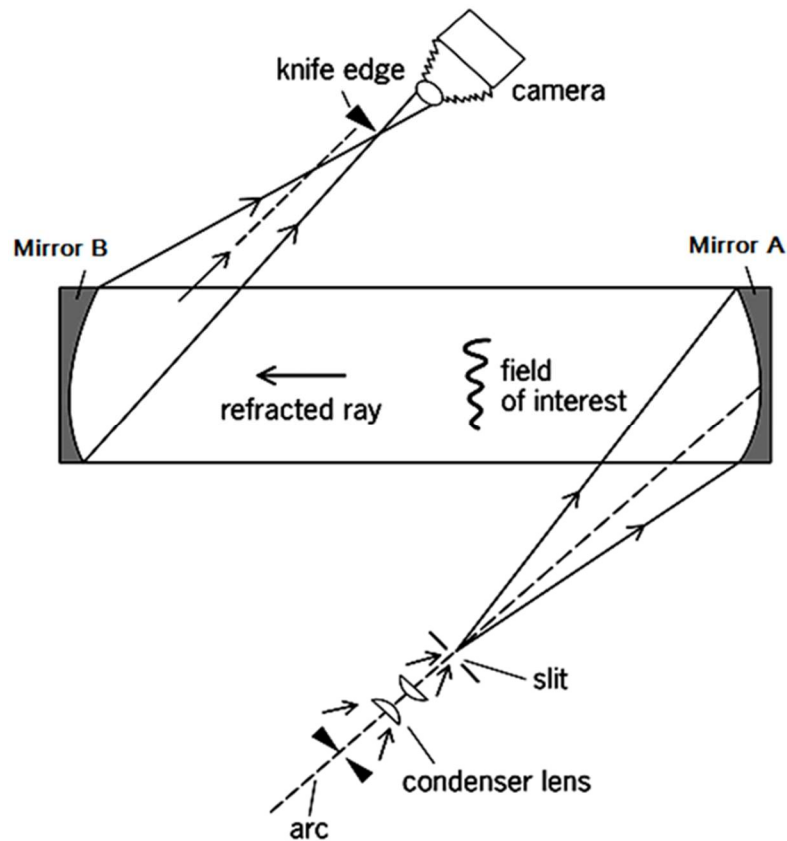


Figure 14 A standard Z-configuration parallel-light schlieren system [40]

Schlieren imaging is sensitive to the density gradient change; hence, it is frequently used aerodynamics and thermodynamics. Similar to shadowgraphy, it uses a point-light and the convex lens to generate the parallel light rays passing through the test region. The difference between schlieren and shadowgraphy are listed below:

Shadowgraphy	Schlieren
Displays a mere shadow	Displays a focused image
Shows light ray displacement	Shows ray refraction angle, ϵ
No knife edge used	No knife edge used
Second derivative of density	First derivative of density

This technique was applied to study droplets by Kumagai et al. [42]. However, they claimed the schlieren method was not suitable for droplet and flame boundary detection. Later on, Reichenbach et al. [43] published experimental work on droplet ignition and flame propagation based on a schlieren optical setup. Okajima and Kumagai [44] used the schlieren method to observe the hot gas zone of the droplet under zero-gravity condition. Recently, Ahmad released his study on emulsion droplet microexplosion with schlieren imaging and shadowgraphy, as shown in Figure 15.

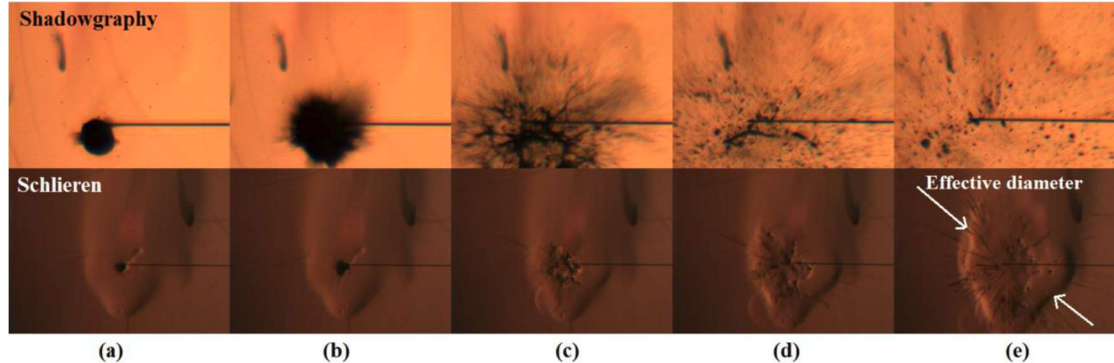


Figure 15 Comparison of the droplet microexplosion images obtained by shadowgraph and schlieren methods

2.2.3. Backlighting Imaging

Backlighting imaging is now the most widely used droplet tracking method. This is not only because the test platform is easy to set up, but also because it can detect very

pronounced changes inside and outside the droplet with sharp boundary. Examples of backlighting images are shown in Figure 16. Furthermore, the zoom in degrees can be easily controlled, which means it can provide the most suitable magnification and maximally yield the expected results.

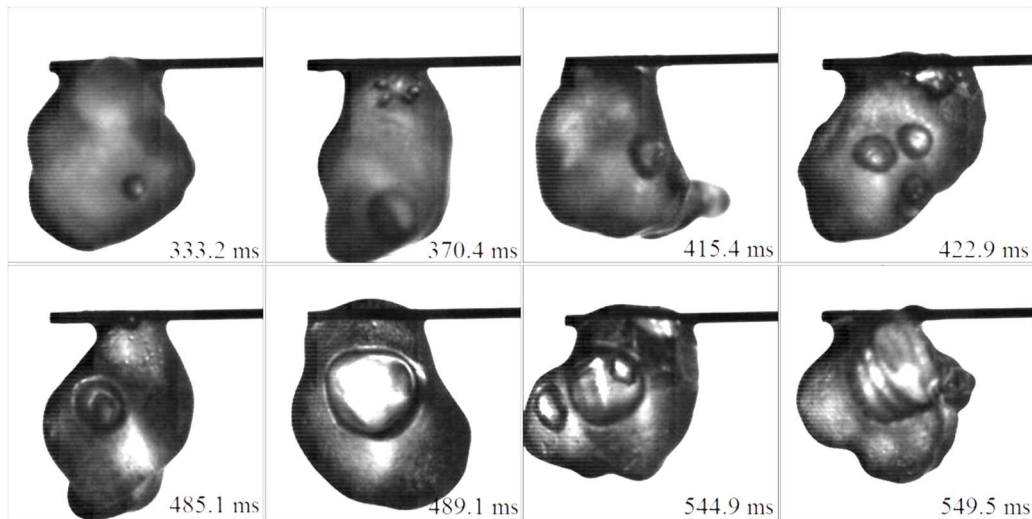


Figure 16 Different nucleation sites inside burning water and diesel emulsions droplet

Jain et al. observed the droplet breakup pattern at different Weber numbers [45], Cheng [46] combined the direct imaging and backlighting to study the effect of initial droplet diameter on combustion. Ahmad recently studies the bubble burst and puffing behaviour with backlight imaging.

2.2.4. Self-illuminated Direct Imaging

Different from the methods introduced above, which focus on the study of the droplet, self-illuminated direct imaging is mainly focussed on the flame region when the droplet burns. In this method, the light of the flame is the only illumination. In addition, it is best carried out in total darkness to avoid the background noise effect. Mikami et al.

[47] implemented direct imaging to track the flame propagation and Marchese et al. studied the emission of radicals. The intensity of the droplet flame have been studied by Ambekar et al. [48]. The following studies in this work are based on this method applied to water and diesel emulsion ignition, burning, and puffing performance. The bore scope system is one of the self-illuminated direct imaging method has been used on combustion chamber monitoring, samples [49] shown in Figure 17. It can give a direct observation of combustion for further the spatial flame temperature and sooting profile analysis [50].

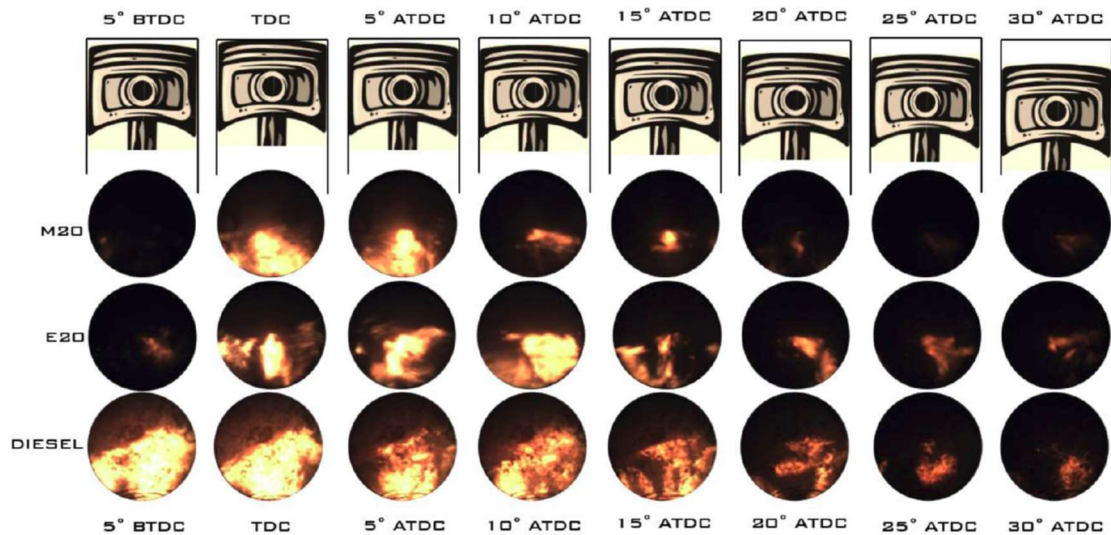


Figure 17 Sample of combustion visualization in cylinder

2.2.5. Particle Image Velocimetry (PIV)

PIV has been applied to measure the velocity distribution of the flow with or without the vortices. The principle of PIV measurement is to capture a moving object from two photographs which the time between these two photos are measured. So, the speed and direction of this object can be identified. The flow field is measured by a PIV system which consists of a laser sheet generator, a laser pulse synchroniser, a seeding generator,

a data acquisition system and data analysis software, as shown in Figure 18. Practically, the tiny particles are applied in the measuring area represent as the moving object. These particles are extremely fined, small, and light, they can easily follow the motion in the flow velocity field. These tiny particles also can scatter the laser light. The camera can easily capture the successional photos of these particles within a short time interval. The camera and the laser pulse are synchronised. The flow trace of these particles in the two successional images can be analysed by data post processing.

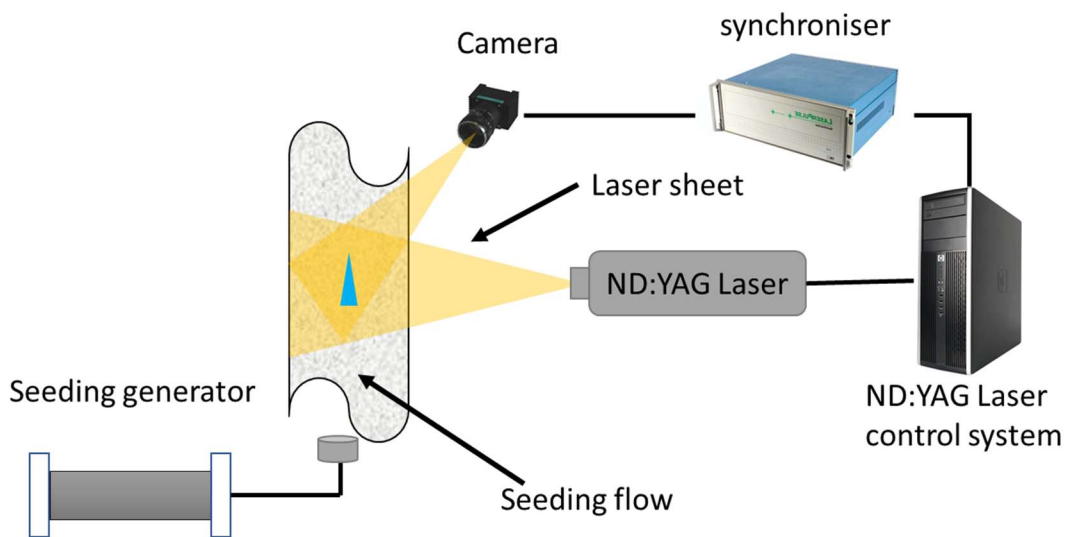


Figure 18 PIV system setup

2.2.6. Laser Induced Fluorescence

The laser induced fluorescence (LIF) was first implemented on flow measurement was in 1982 and it has widely applied technically in flow dynamics research areas. LIF techniques is based on the fluorescence the principle, in which the atoms or molecules being excited to a higher energy level when absorb the specific electromagnetic radiation form the laser light. The different number and types of the atoms and molecules exhibit different level of fluorescence intensity. Therefore, the intensity variation can be utilised

to measure the concentration, temperature, velocity and pressure distribution of the flow. The Planar LIF is successfully implemented in combustion study to provide two-dimensional radiations concentration and distribution.

2.2.7. Others

There are many other methods for different diagnostic purpose. Stereoscopic imaging technique or it combined with other optical system can used for flame 3-D reconstruction [51–53]. Tomographic PIV provides a cross-sectional structure and velocity field of flame [54–56]. Mie scattering images is used to estimate fuel/air mixing behaviours based on the mass fraction parameter [57,58].

2.3. General Concept of Vision Systems

2.3.1. Camera Evolution

Cameras evolved from the camera obscura and continued to change through many generations of photographic technology, including daguerreotypes, calotypes, dry plates, film, and digital cameras.



Daguerreotype camera, 1839



Dry plates, 1871



Brownie box film camera, 1910



Sony digital camera, 1981

Figure 19 Camera development history

The camera has become an indispensable part of people's modern lives. It can be utilised to record memorable moments, describe the little drops of life, help police solve cases, and it also is a very powerful scientific research tool. Compared with tedious written descriptions, images are more attractive, spreadable, and contain extensive detailed evidences.

For photographic film, each film includes two basic components: a single or multiple emulsion layer and a photosensitive emulsion layer support (substrate). The photosensitive material suspended in gelatine is a silver halide grain. The particles are so fine that they can only be observed under high magnification. An area of one square inch of typical emulsion film contains approximately 40 billion silver halide crystals. The film sensitivity is lower with smaller silver halide particles, but the resolution and texture are better.

When the photosensitive layer of the film is exposed, a photon of energy $h\nu$ acts on the silver halide crystal. Halide ions first absorb the light quantum, release a free electron, and become halogen atoms. The halogen atoms make up the halogen molecules and leave the crystal, and the lattice structure is absorbed by the gelatine. The free electrons move to the photo centre and are fixed quickly. Thus, the photo concentration centre has become a charged body with many negative electrons. Silver ions in the

crystal lattice are driven to the electrons by the electric field, and silver ions in turn capture the electrons gathered in the light-sensing centre. As consequence, the silver ions are reduced to silver atoms. The reduced metal silver atoms are also fixed in the photosensitive centre, and thus the photosensitive centre further expands the enlarged photosensitive centre and continues to capture the photolysed electrons. As the cycle repeats, the photographic centre continues to grow up to a certain extent until the exposure is appropriate. Then, the photographic centre formed by the imaging centre of the imaging core. The latent image is constituted by numerous developing centres and undergoes a post-chemical development and the fixing process to form the required images [59].

In 1975, Steven Sasson at Eastman Kodak invented digital camera. The photosensitive element is based on electronic transfer instead of a chemical reaction. This gives more opportunity to manipulate picture and acquire the optical information under the appearance.

2.3.2. Digital Vision System

For digital image systems, the principal types of sensor are the charge-coupled device (CCD) and complementary metal–oxide–semiconductor (CMOS). There are four primary functions for the image sensor: photon conversion, charge accumulation/collection/storage, charge transfer/readout, and signal measurement.

2.3.2.1. Image Sensors

In the late 1960s, Bell Laboratories in the United States proposed the concept of solid-state imaging devices. Since then, it has developed rapidly and has become an

Chapter 2 Basic Background Knowledge

important branch of sensing technology. It is an indispensable peripheral for PC multimedia, but also a core device in monitoring.

The image sensor is the core system of a camera. For both CCD and CMOS image sensors, the principle of the silicon photoelectric effect is used for the optical detection. The photodiode structure receives incident light and converts it to an electrical signal. The major differentiator is the pixel photo-induced charge readout method.

CCD

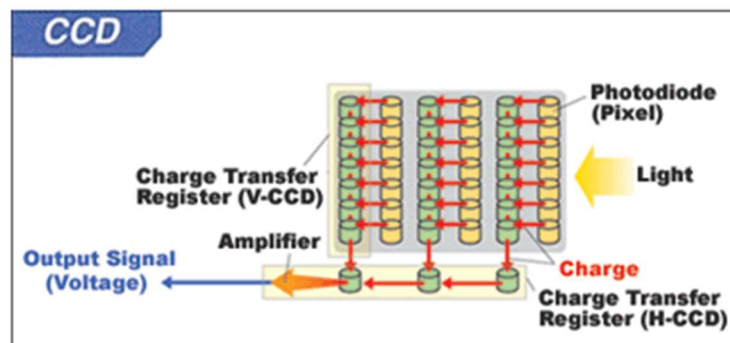


Figure 20 CCD Sensor

After receiving light, the photosensitive element produces a corresponding current. The power of the current corresponds to the light intensity, such that the photosensitive element directly outputs the analogue electrical signal. In the CCD sensor, the photosensitive elements do not further process the signal, but it is directly outputted to the next photosensitive element of the storage unit, combined with the analogue signal generated by the element and then outputted to the third photosensitive element, and so on, until the last combined signal of a photosensitive element to form a unified output. As the light-sensitive components of the electrical signal are too weak and cannot be directly converted from analogue to digital. These output data require unified amplification. After the amplifier processing, the electrical signal intensity of each pixel is increased by the same amplitude.

CMOS

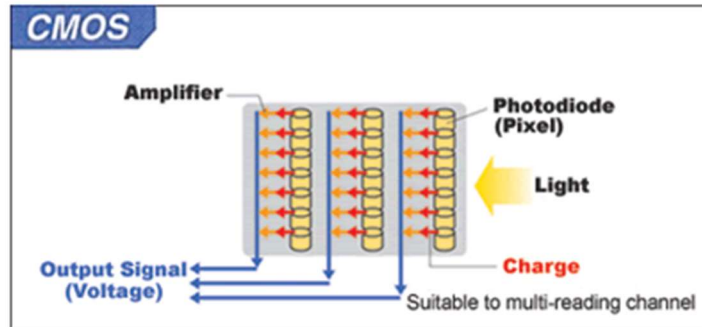


Figure 21 CMOS Sensor

In most CMOS devices, each pixel has several transistors, which can individually function to amplify and convert the charges from the photodiode to digital signals. Signal amplification in CMOS sensors is processed on the basis of each pixel. This method can prevent invalid transfer operations. Therefore, CMOS can perform fast data scanning with low energy consumption while reducing noise.

The characteristic of CCD is to keep the signal intact during the transmission (exclusive channel design), and to maintain the integrity of the data through collection from each pixel to a single amplifier for unified processing. The CMOS process is relatively simple; there is no dedicated channel design, and thus the signal must be amplified first before the various pixel data are integrated. Because CMOS has an amplifier next to each photodiode, millions of pixels require more than a million amplifiers, and even though they are made under uniform manufacturing, each amplifier shows slight difference. Therefore, it is difficult to achieve synchronized amplification; compared to a single-amplifier CCD, CMOS generates more noise.

The light sensitivity of a CMOS chip is relatively low, because each pixel is accompanied by several transistors. Hence, when the photons hit the chip, some of them hit the transistors instead of the photodiode.

Chapter 2 Basic Background Knowledge

The main advantage of CMOS is its lower power consumption. Unlike CCDs, which are composed of diodes, CMOS circuits have almost no static power consumption and only consume power when the circuit is on. This makes the CMOS power consumption only approximately 1/3 of that of a normal CCD, which helps to improve people's bad impression on the digital camera.

In the study of combustion with visualisation, flame is a fast-moving process. A high shutter speed is required to capture its instantaneous behaviour. A high resolution and good sensitivity can yield a finer quality of images. The charge information stored in a CCD needs to be transferred under the control of the synchronisation signal before being read. The charge information transfer and read output require the cooperation between the circuit and three different power supplies. Hence, the entire circuit is more complex and slower. A CMOS photoelectric sensor generates a voltage signal directly after the photoelectric conversion. The signal reading is very simple, and it can simultaneously process the image information of each unit. The working process is much faster than that of the CCD. Thus, the CMOS sensor is more suitable than the CCD for this research.

2.3.2.2. Camera Sensor Response to the Spectrum

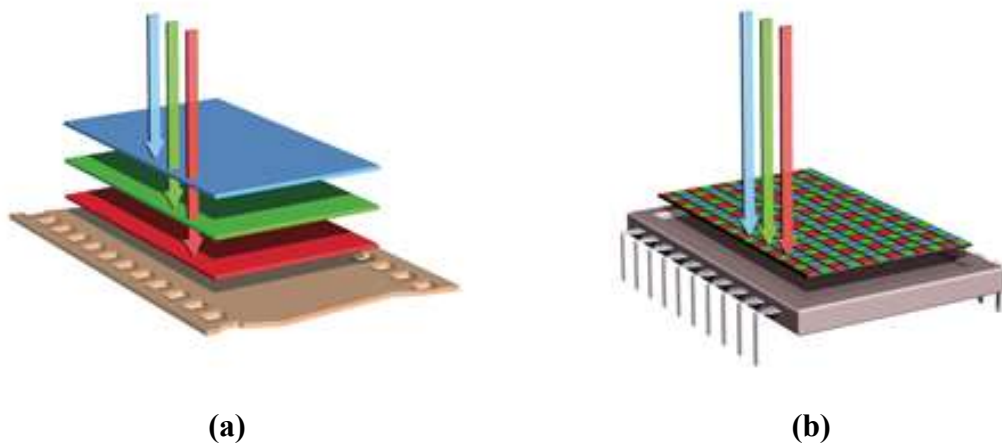


Figure 22 Colour filter arrangement for film (a) and digital (b)

The film colour sensor uses a three-layer structure. Their colours from top to bottom are blue, green, and red, and each layer records one homologous colour. The layer position arrangement is based on the principle that silicon absorbs different wavelengths of light to different depths.

Most digital colour sensors use a Bayer filter mosaic, which is a colour filter array for arranging RGB colour filters on a square grid of photosensors. Each pixel is covered with a filter and records just one colour; four pixels are in one group including one red, one blue, and two greens. Hence, it is also named a BGGR filter. The reason for the uneven primary colour filter distribution is to match the human spectral sensitivity by sampling the G signal at a higher rate than the other primary colours. The incoming light beam is passed through the beam-splitters and the three filters. Each sensor gets an identical image, but only responds to one of the primary colours according to its particular filter.

2.3.2.3. Colour Model

RGB colour model

RGB colour space is based on three primary colours: red (R), green (G), and blue (B), with different degrees of superimposition to produce rich and extensive colours, with a so-called three-color model. RGB space is the most commonly used colour model, with most televisions and CRT monitors using this model. Any colour in nature can be represented by a mixture of red, green, and blue light components. In nature, there are infinitely many different colours, but the human eye can only distinguish a limited number of different colours. The RGB model can represent more than 16 million different colours and is very close to nature's colour. It is also known as the natural colour

model.

For image processing, RGB is the most important and common colour model. The RGB colour model can be presented in a cartesian coordinate system with RGB as the three axes, as shown in Figure 23. Eight common colours, black, blue, green, purple, red, yellow, and white, are represented by the eight vertices of the cube. Black is usually placed at the origin of the three-dimensional Cartesian coordinate system. The primary colours red, green, and blue are along the x, y and z-axes, and the entire cube placed within the first quadrant.

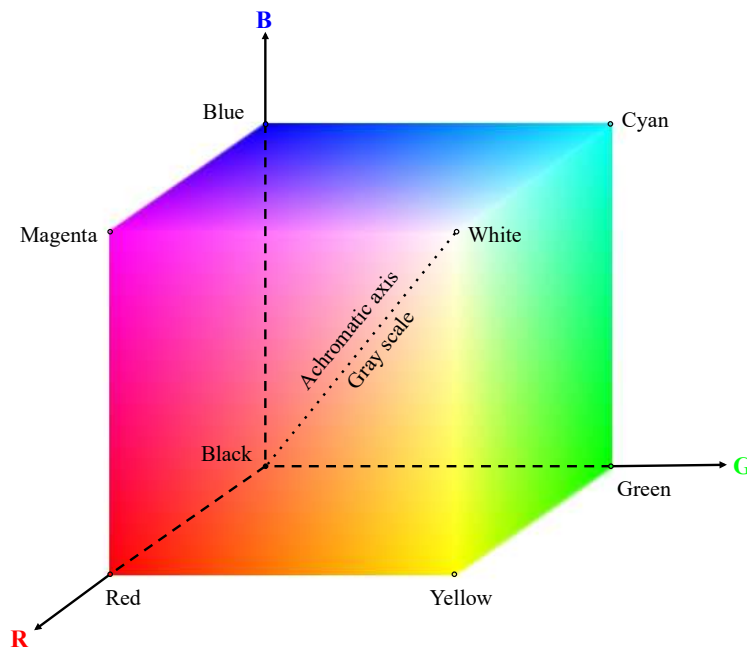


Figure 23 3D display model of the RGB colour.

All the other colours can be presented by different combinations of these three primary colours, as shown in Equation 11.

$$\text{Colour} = [I_R, I_G, I_B] \quad \text{Equation 11}$$

Chapter 2 Basic Background Knowledge

where I refers to the value from darkness to brightness of each primary colour. The range of each parameter follows the grey scale: R: 0–255; G: 0–255; B: 0–255 from black to white. If value of three primary colours intensities are the same, the output colour is along this grey scale axis.

HSV colour model

Whereas RGB is defined in relation to primary colours, which is hard to describe colour, HSV is a more understandable model to represent colour, as it is defined similarly to how humans perceive colour [60]. HSV is an acronym for three components: hue, saturation, and value, which stand for colour, brightness, and intensity, respectively. The HSV colour model space describes colours in terms of their shade and brightness value, and the colours are specified in a conical coordinate system, as depicted in Figure 24.

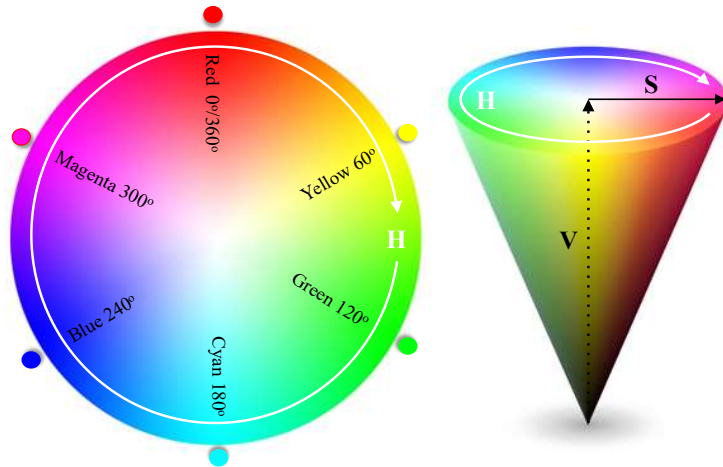


Figure 24 HSV colour model

Within the colour wheel, the colour in the hue coordinates is expressed as the angular degree from 0 to 360. For instance, reddish colour is in the angle range of 0°–60°, greenish are located at 120°–180° and blueish are near 240°–300°. Saturation refers

Chapter 2 Basic Background Knowledge

to the colour vividness, also known as colour purity. The degree of saturation depends on the proportion of the colour-removing component (white or grey) in the colour. The colour gradually fades out as its saturation decreases. The saturation is defined in the range of 0 to 1 from the white centre of the panel to the primary colour at the panel edge along the radial axis. The value is given as the depth along the achromatic line to describe the brightness or intensity of the colour, from 0%–100%, where 0% at the bottom means completely black and 100% is the brightest. Therefore, the HSV colour space is a convenient model for colour selection by picking the range of the colour spaces and adjusting the shape and brightness value for a certain hue range [61].

By take advantage of this, Smith [62] presented the standard transformation algorithms to convert a colour from the RGB model into the HSV model:

$$H' = \begin{cases} \frac{G - B}{Max - Min} & \text{if } R = Max \\ 2 + \frac{B - R}{Max - Min} & \text{if } G = Max \\ 4 + \frac{R - G}{Max - Min} & \text{if } B = Max \end{cases} \quad \text{Equation 12}$$

$$H' = \frac{H'}{6} \times 360 \quad \text{Equation 13}$$

$$H = \begin{cases} H' & \text{if } H' > 0 \\ H' + 360 & \text{if } H' < 0 \end{cases} \quad \text{Equation 14}$$

$$S = \begin{cases} 0 & \text{if } Max = 0 \\ 1 - \frac{Min(R, G, B)}{Max(R, G, B)} & \text{Otherwise} \end{cases} \quad \text{Equation 15}$$

$$V = Max(R, G, B) \quad \text{Equation 16}$$

2.3.2.4. Shutter Speed

In photography, shutter speed defined as the length of time the camera's shutter is open to let the sensor 'see' the scene. The amount of light that reaches the film or image sensor is proportional to the exposure time. If the shutter speed is lower, more light will enter into the camera with longer exposure time, and with higher shutter speed less light will get through.

In addition to its effect on exposure, shutter speed can have a dramatic impact on the appearance of moving objects. Very short shutter speeds can be used to freeze the moment of fast-moving subjects, such as a flying bird. Very long shutter speeds are used in very-low-light situations or intentionally to record the blurry trace of a moving subject.

For flame observation, fast shutter speeds can record more detail of the movement of the flame dynamic. However, high shutter speed causes signal drop-out. In this experiment, the effect of shutter speed has been tested against the V-shape premixed flame. The results were compared qualitatively and quantitatively with the aid of image processing, such as boundary tracking and intensity calculation.

Figure 25, the first column shows the results of a high-speed camera with different frame rates from 50 fps to 5000 fps. It is obvious that with the increase in the frame rate, the blue colour gradually fades out. The horizontal axis shows the times of enhancement processing. Each image has been enhanced to the limit of overexposure. From the results, the blue stains in each picture have been effectively selected and strengthened, even for the image in the high-frame-rate condition, in which the blue stain cannot be recognised by the naked eye in the original picture.

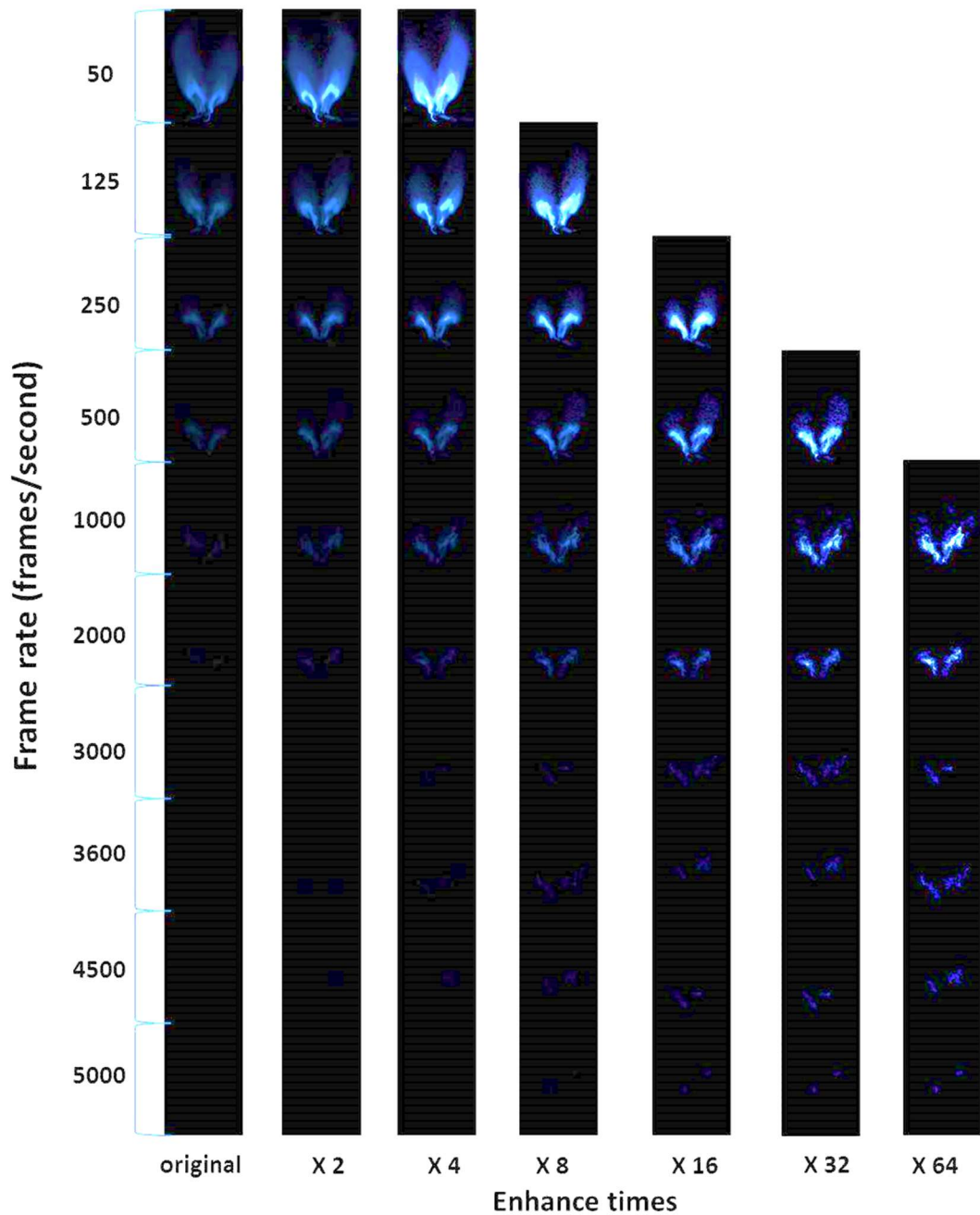


Figure 25 Result of the flame picture after enhancement

Figure 25 presents one selected example of images in each time series taken at different frame rate. It can be seen that with the increase in the frame rate, the visibility of the flame is gradually weakened owing to the shortened exposure time. The flame is

nearly invisible by naked eyes at a frame rate of 500 fps. After the enhancement by an innovative digital imaging processing program, the entire flame is clearly shown in the picture. At 50 fps, the flame is bright and smooth, which means the flame has a time-averaged appearance. To enhance the image at shorter exposure time, the blue colour flame pixels are identified and extracted. Then, these classified pixels will be selectively enhanced for easy observation and analysis. By careful observation, it can be seen that in the images taken at 500 fps, there are many black 'holes' in the image, although the pattern of the flame is clear. The observability of details has decreased owing to signal drop-out. From a frame rate of 1000 fps and higher, the whole flame cannot be visualised with confidence, even after enhancement. At 3000 fps, the boundary of the flame is obscured, and only the brightest part of the flame can be seen. At 4000 fps, the flame fades into a flickering light spot.

The processing provides a great advantage of using a conventional camera for monitoring flame properties based on the colour spectrum. It is easy to interface with a computer, is cost-efficient, and has particular spatial resolution. Furthermore, it has been demonstrated that a conventional digital camera can image flames not only in the visible spectrum but also in the infrared.

2.3.2.5. Camera Noise

The noise of the digital camera mainly refers to the rough part of the image produced by the CCD (CMOS) receiving and outputting the light as the received signal, and also refers to the redundant erroneous pixel colour that should not appear in the image, which are usually generated by electronic interference. The image appears to be corrupted and covered with small rough spots. This seriously affects not only the beauty of images, but also the image data validity.

Chapter 2 Basic Background Knowledge

Svensson et al. [63] have classified the causes of noise in digital imaging into four groups: read noise, shot noise, thermal dark noise, and fixed pattern noise. Payri et al. claimed that for a scientific-grade camera, the read noise and fixed pattern noise can be ignored.

The shot noise is derived from the statistical nature of light and the photoelectric conversion process in the image sensor, especially in the low-light condition. To achieve proper exposure, lower shutter speed and higher ISO sensitivity are required. However, this operation renders the camera's sensor pixels unable to function properly and enhances the false colour to complement the underexposure. In this case, a random variable with Poisson's density distribution is used as a model of photoelectric noise.

Thermal noise, caused by the thermal shock of electrons in a conductor, is present in all electronics and transmission media. It is the result of temperature changes, but not affected by frequency changes. Thermal noise is distributed in the same form in all frequency spectra and cannot be eliminated. Therefore, maintaining the validation and cooling of a camera is an effective way to restrain the noise level.

In contrast to the dark condition, in over-exposure and high-contrast situations, the signal drop-out and excessive noise can be observed simultaneously. Zhao and Ladommatos [64] attributed this phenomenon to dust and soot deposition on the optical window. Apart from these, the innate imperfection of the CMOS sensor workflow cannot be ignored.

After the CMOS exposure, a pixel transferring procedure will be performed; a signal of the amplified charge of each pixel will be sequentially sent to a charge storage row by row. The calculation of the amplification, transmission, and storage in this row will be different from other rows. Therefore, in certain high-contrast shooting conditions, the

Chapter 2 Basic Background Knowledge

uneven intensity amplification degrees can be notice in the row direction. An example of this phenomenon is shown in Figure 26 (a).

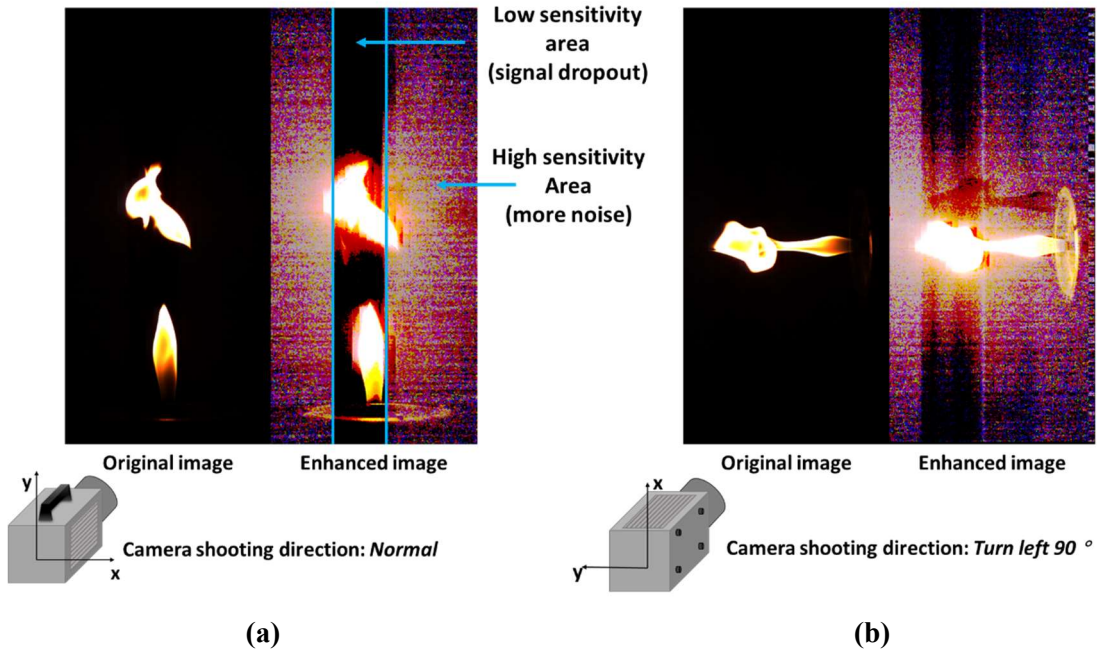


Figure 26 Sample of intensity feather

The signal of the row with high-intensity flame pixels has been barely amplified. On the contrary, for the low intensity region, the sensitivity for those rows has been adjusted to a very high level and the redundant noise signals have been amplified. The noise can be removed by post processing, but the lost signals cannot be recovered. Therefore, in order to acquire as much data from the image as possible, especially for the information at the tail of the flame front, it can be addressed by physically changing the camera shooting direction, as shown in Figure 26 (b). Although the problem of uneven amplification cannot be completely solved, the signal information around the flame can be preserved.

Based on experience, the image file format is an additional factor to generate noise, owing to the compression. Different file types have their specialties and applications.

Chapter 2 Basic Background Knowledge

The table below lists the common image file formats and their special suitability.

	Characteristic	Applicability
JPEG	Lossy 8×8 pixels compression High level of noise Very small file The artefacts degrade and detract from the original	Ideal for web and nonprofessional prints Limited space storage Very fast read and write
PNG	Lossless compression 8/16/24/48 bits and indexed colour Transparency and small distortion	Slower to read or write Suitable for web images
TIF	No compression No image quality or information loss Larger file sizes The most versatile 8/16/24/48 bits and RGB, CMYK, LAB, or indexed colour	High quality prints Professional publications Image data research analysis Not incompatible with most of software
RAW	Directly stores uncompressed data captured from a camera's sensor Is not directly viewable and usable, and requires an editing step first	Saves metadata, unprocessed raw information Offers substantial benefits for image manipulation the image (exposure and white balance)

According to these statements, all the analysed image data in this work are in the TIF format.

3. Image Processing Methodology

With the rapid development and popularisation of computer and multimedia technology, digital image processing technology has received unprecedented attention, and many new application fields and processing methods have emerged.

3.1. Denoising Processing

Images are often disturbed and influenced by various types of noise in the of generation and transmission processes. The noise deteriorates the image quality and makes the image blurred, even without image features, which brings difficulties for the following image segmentation, analysis, and diagnosis. Therefore, removing noise and restoring the original image in the image pre-processing stage are important steps in image processing. For flame monitoring, the yellow soot is bright and always overexposed, whereas the blue flame is dim, often exhibits signal drop-out, or is occasionally even removed as noise. Hence, it is necessary to find a suitable method for flame image denoising.

Figure 27 presents a sample of a raw image of blue flame recorded by a high-speed camera at a shutter speed of 1/2000 s. The original image is too dim to see the flame in detail, but after improving the brightness, the noise also has been enhanced. Therefore,

the procedure of denoising is essential before further analysis on the flame.

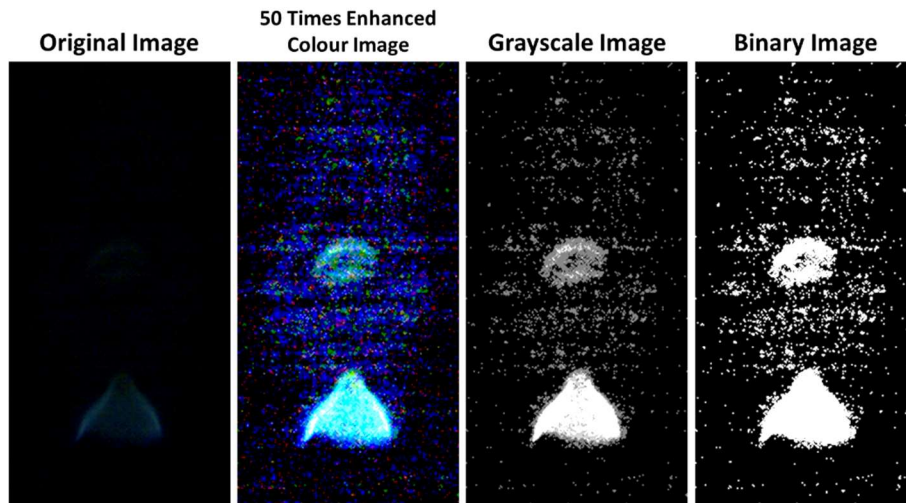


Figure 27 Sample of a raw image of blue flame

This section first introduces four image denoising functions in the Matlab image processing toolbox: median filter, Wiener filter, adaptive filter, and averaging filter. Next, I compare their advantages and disadvantages in an actual application of flame image processing, which provided a theoretical basis for further image processing. Based on the above research, I introduce two self-developed denoise programs (Gaussian filter and centre point denoise) for flame research.

A good image denoising method should remove the noise without blurring the edges and lines of the image. In the spatial domain, one of methods for noise removal is to first determine whether a pixel is noise. If it is noise, it will be reassigned; if it is not, the output keeps the original value. The other method is averaging, which averages the entire image without relying on the identification and removal of noise.

3.1.1. Averaging Filter

Averaging filter, also known as linear filtering, uses the neighbourhood averaging method. The basic principle is to replace each pixel value in the original image with the average value. In simpler terms, consider that the current pixel is (x, y) . A template needs to be selected which is composed of several pixels in its neighbourhood and the average of all the pixels in this template is determined. The mean assigned to the current pixel is the grayscale $g(x, y)$ of the processed image at that point.

$$g(x, y) = \frac{1}{m} \sum f(x, y) \quad \text{Equation 17}$$

where m is the total number of pixels in the template.

3.1.2. Median Filter

The median filter is a commonly used nonlinear noise filter, the principle of which is similar to that of the average filter. The difference between these two is that the output pixel value of the median filter is determined by the median of the neighbouring pixels instead of the average value.

3.1.3. Adaptive Filter

Adaptive filter refers to the use of adaptive algorithms to change the filter parameters and structure of the filter according to changes in the environment. The adaptive filter coefficients are time-varying coefficients, updated by the adaptive algorithm. In other words, its coefficients automatically and continuously adapt to a given signal to obtain the desired response. The most important feature of an adaptive

filter is that it can work effectively in an unknown environment and track the time-varying signature of the input signal.

3.1.4. Wiener Filter

Wiener filtering is an optimal estimator of stationary processes based on the least mean square error criterion. The mean square error between the output and the desired output is minimised, and thus it can be regarded as an optimal filtering system. It can be used to extract signals that are contaminated by stationary noise.

3.1.5. Gaussian filter

Gaussian filter is a process of finding the weighted average of the entire image; the value of each pixel value is obtained by the weighted average of itself and other pixels in the neighbourhood. The specific operation of Gaussian filtering is to scan each pixel in the image with a template (or convolution, mask) and replace the value of the pixel in the centre of the template with the weighted average grey value of pixels in the neighbourhood, as determined by the template.

3.1.6. Centre Point Denoise

Centre point denoise uses a 3×3 square kernel to determine whether the point in the middle is noise or not. For example, setting the threshold as 3 means if more than three out of the eight neighbours have a value of '1', the pixel will be kept, otherwise the pixel will be removed as noise. In the example shown in Figure 28, both 'a' and 'b' are noise and they will be reassigned as '0'.

0	0	0
0	a	0
0	0	0

1	1	1
0	b	0
0	0	0

1	0	0
1	c	1
0	0	1

Figure 28 3×3 averaging kernel often used in centre point denoise filtering

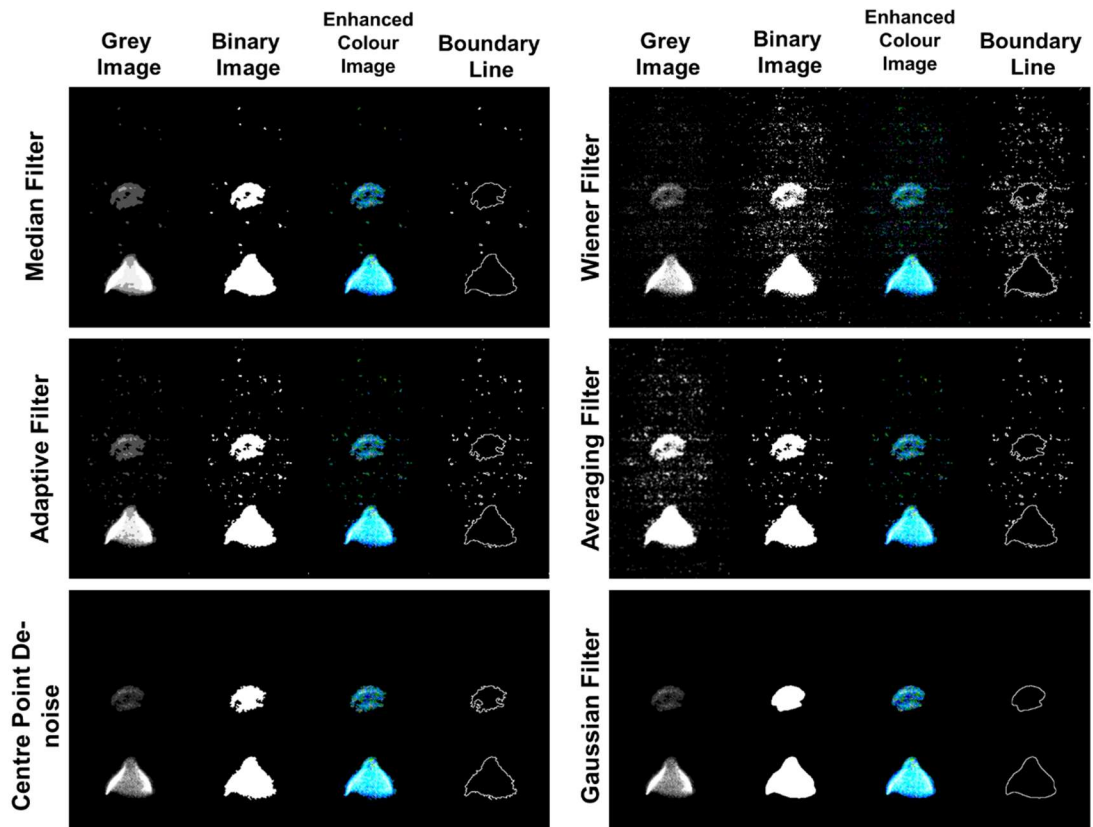


Figure 29 Denoising result with different methods

Applying the denoising methods mentioned above to a raw flame image yields a number of different results, as shown in Figure 29.

Wiener filter and averaging filter did not exhibit good performance for high-noise level flame denoising, because they are prone to keeping too much redundant signals

and blurring the boundary. Adaptive filter and median filter removed more noise and maintained the boundary shaper, but some unwanted parts are still left and some of the main body has been eliminated. The centre point denoise method and Gaussian filter are the most suitable noise removal filters for flame diagnostics. They can effectively remove the noise and preserve the integrity of the flame. This is especially true of the Gaussian filter, which provides a very clear and sharp boundary for further studies.

3.2. Boundary Detection

Edges are the most important features of an image. The edge refers to the set of pixels with step changes in pixel grey level. Edge detection mainly relies on the measurement, detection, and positioning of grey-scale changes. There are many different methods of edge detection, and individual methods can even apply different filters. In the Matlab image processing toolbox, the edge function provides several operations to detect the edges of a grayscale image.

To determine which operator gives the best performance for flame edge detection, five operators have been examined on the greyscale flame image, which has been denoised with Gaussian filter, as discussed in last section. In Figure 30, the top image is the original greyscale flame image, and the results of processing by each operator are shown in the bottom row.

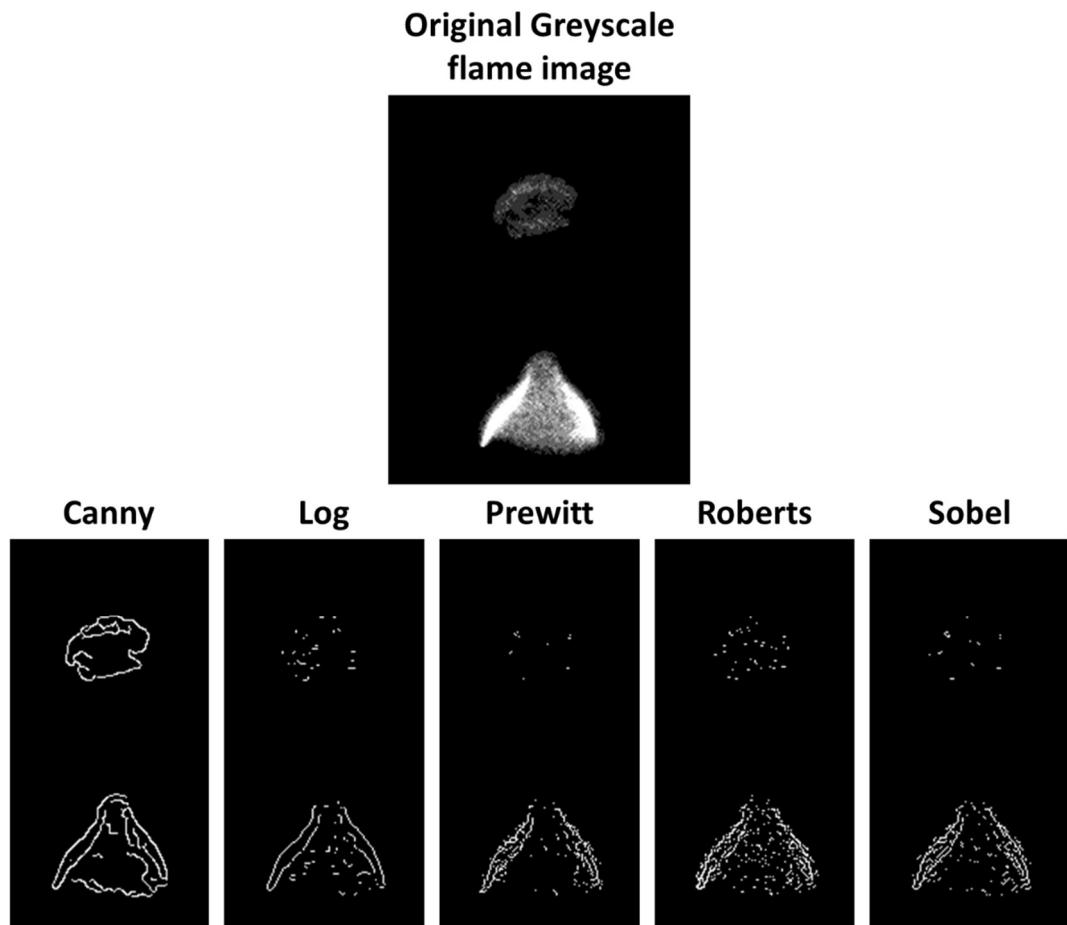


Figure 30 Boundary detection the results of processing by each operator

As the results show, the Canny method is less susceptible to noise and can detect true weak edges. The advantage is that two different thresholds are used to detect the strong and the weak edges. Weak edges are included in the output image only when they are connected to strong edges. The Prewitt operator detection method is more effective on image processing with more grey gradients and noise, but the edge is wide and intermittent. The Roberts operator detection method is better for processing with sharp and low-noise images. The extracted edge by applying Roberts operator is thick, such that the location of the edge is not very accurate. The Sobel operator detection method has good effect on grayscale gradation and noise with more image processing. However, it is not very accurate for edge location, and the edge is represented by more than one

pixel.

The boundary line is arranged by successive pixels; when zooming in, the dislocation between the pixels appears a stair-step shape. For certain research needs, sometimes more accurate and smoother boundary curves are required. The refinement, characterised by a smoothing of the boundary, gained through the application of the 10-point interpolation principle is clearly evident for the smooth boundary. Figure 31 shows the refined perimeter of a complex wrinkled flame front and the discrepancy between the tentative and refined perimeters.

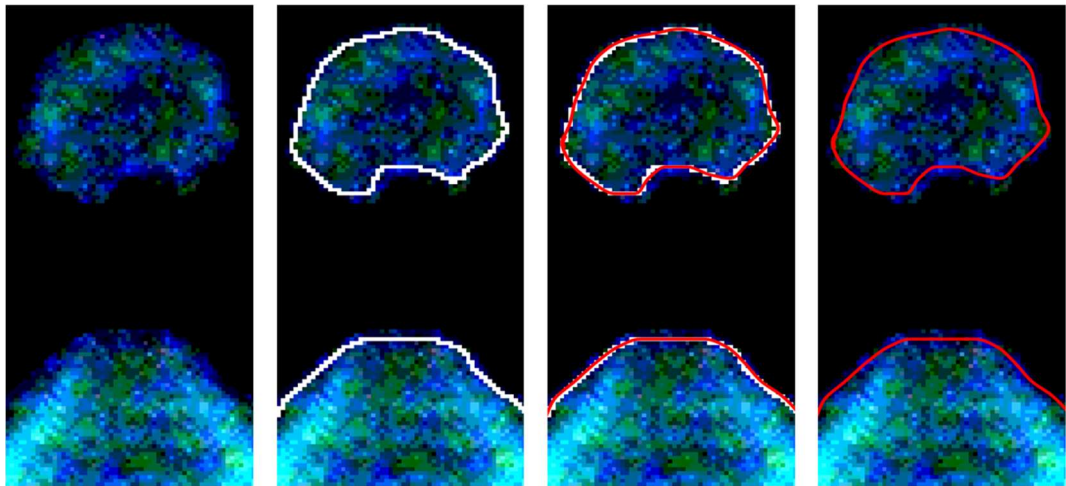


Figure 31 Refined smooth boundary of flame

3.3. Image Colour Selection and Enhancement

As discussed earlier, by shooting at high shutter speeds, the obtained pictures are always dim, and the objects cannot be seen evidently owing to the short exposure time. Therefore, the picture needs to be properly adjusted and enhanced. A sample of a flame

image at a shutter speed of 1/2000 s is shown in Figure 32. Without adjustment, only the bright orange area can be seen by the naked eye. After an overall enhancement of 50 times, the structure and more colour areas of the whole flame show up. As shown in the enhanced image, the dominant three colour sections of the hydrocarbon flame can be clearly seen, including the orange sooty flame, the pinkish infrared emission, and the chemiluminescence-induced blue flame. However, arbitrary enhancement not only makes the noise appear, but also makes the original bright part overexposed and loses its research value. Hence, to acquire a valid and visualised flame image, image segmentation and colour-selective enhancement is inevitable.

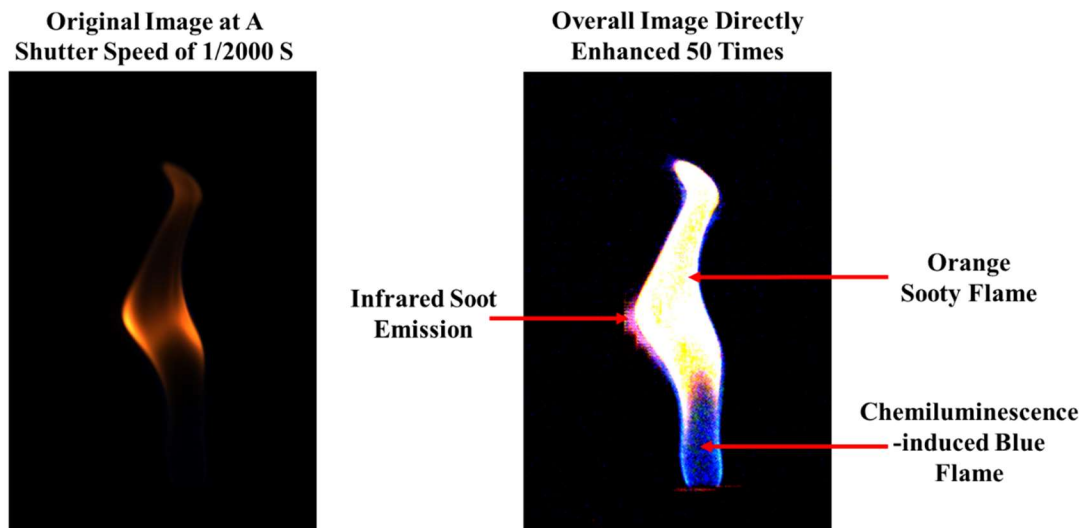


Figure 32 Sample of the flame image without adjustment

Generally, image segmentation refers to the division of an image into several nonoverlapping regions, according to the characteristics of grayscale, colour, texture, and shape. These features in the same region show similarities, but in different regions show obvious differences. The segmentation method used in this work is based on colour, the principle of which is described as follows.

Figure 33 presents the distribution of flame in the hue model. In the coordinates, the X-axis of the histogram gives the range of the hue from 0° to 360° , which has been divided into 16 bars corresponding to the chart listed on the right. The four rows in the Y-axis represent the saturation degrees, which have been divided into four sections within the range from 0 to 1. The Z-axis illustrates the statistical average pixel count in each colour blocks.

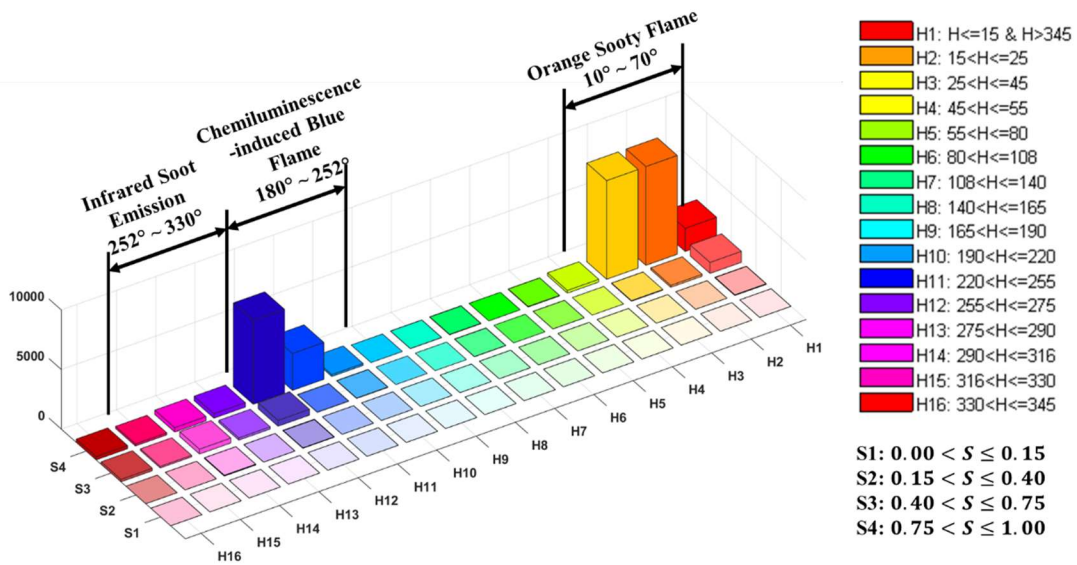


Figure 33 Colour distribution histograms in hue space.

According to the colour distribution plot shown in Figure 33, the orange sooty flame dominates from H1 to H3 (10° – 70°) in hue space, whereas the weak blue flame dominates from H10 to H12 (180° – 252°). In addition, there is emission captured from H13 to H15 (252° – 330°) which corresponds to the infrared. Therefore, the selection of a specific hue value range can help to segment the image according to the colour region and manipulate these regions individually.

Figure 34 shows the segmented colour sections enhanced by different degrees according to its intrinsic visibility. The soot section has been enhanced five times and

the barely visible infrared and chemiluminescence flame areas have been enhanced 30 and 50 times, respectively.

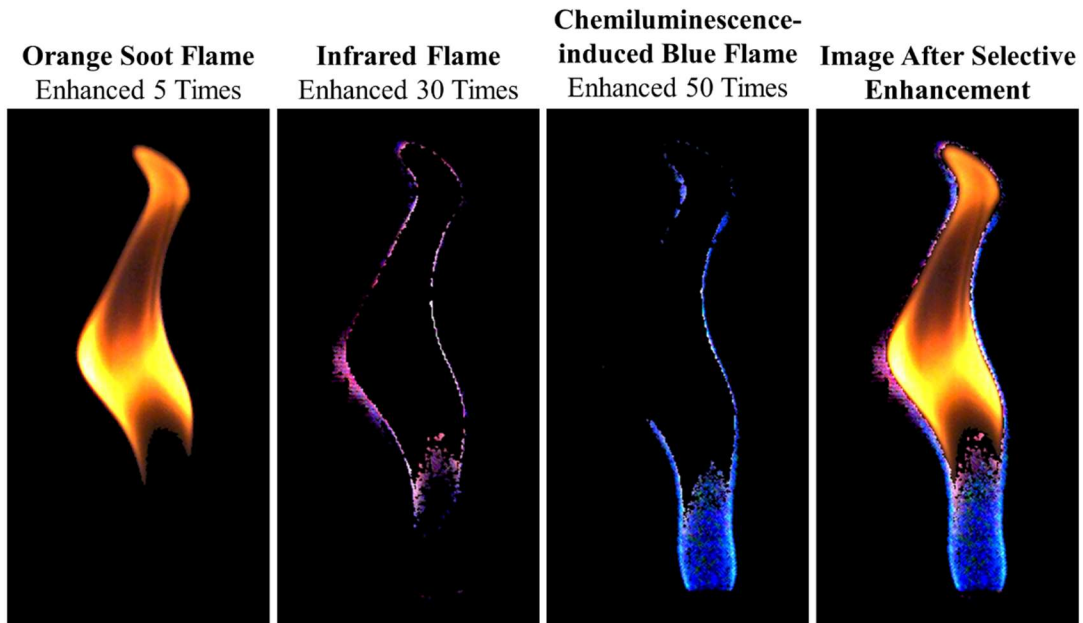


Figure 34 (a) the orange sooty flame region; (b) the infrared soot emission enhanced with 30 times enhancement; (c) the chemiluminescence-induced blue flame with 50 times enhancement; (d) the entire image after selective image enhancement

3.4. Flame Chemiluminescence Measurements

As in the RGB colour model, all colours are a combination of these three primary colours. Thus, the colour information of visible light in each of the pixels is defined as $C = [I_R, I_G, I_B]$, which was introduced in Section 2.3.2.3 by Equation 11.

The intensity of the R, G, and B colours can be derived from the integration of the radiation over their respective wavelength ranges. Therefore, I_R , I_G , and I_B can be

expressed as:

$$\begin{cases} I_R = \sum_{R\lambda_{min}}^{R\lambda_{max}} I_{R\lambda} \\ I_G = \sum_{G\lambda_{min}}^{G\lambda_{max}} I_{G\lambda} \\ I_B = \sum_{B\lambda_{min}}^{B\lambda_{max}} I_{B\lambda} \end{cases} \quad \text{Equation 18}$$

where λ refers to the wavelength and the subscripts max and min indicate the maximum and minimum sensitive wavelength range in that channel, respectively.

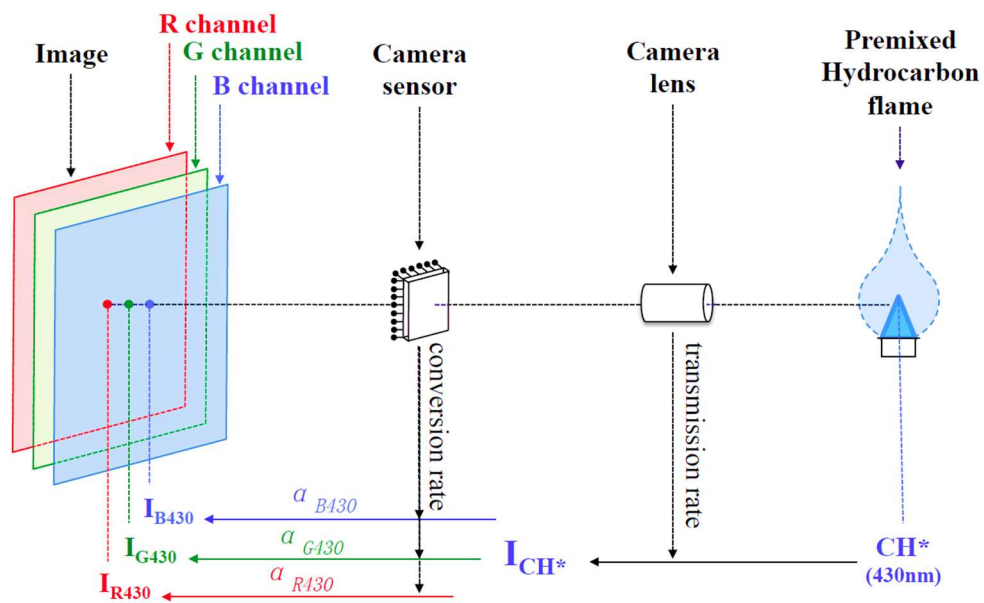


Figure 35 Relationship between image colour and radiation emission [65]

The flame colour of a premixed hydrocarbon flame, which has been detailed in Section 1.1.5, is mainly attributed to the radical emissions of CH^* and C_2^* . Although these two radicals are distributed over many wavelengths, various works have confirmed that the dominated intensity of CH^* and C_2^* emissions peak at wavelengths of 430 and 516 nm, respectively. For conventional chemiluminescence measurements, the narrow

Chapter 3 Experimental Techniques and Methodology

bandpass filters employed in research works are always based on these two wavelength bands. The principle of intensity in each colour channel responding to the radiation at a certain wavelength is illustrated in Figure 35. Therefore, the colour model based the chemiluminescence measurement method will only consider the emission at these two wavelengths for further analysis. Thus, Equation 18 can be simplified as:

$$\begin{cases} I_R = I_{R_{430}} + I_{R_{516}} \\ I_G = I_{G_{430}} + I_{G_{516}} \\ I_B = I_{B_{430}} + I_{B_{516}} \end{cases} \quad \text{Equation 19}$$

As mentioned in the previous section, for each channel, the light conversion rates α at certain wavelength are different and they have been calculated by the calibration. At the same incident intensity condition, the intensity value of each channel is:

$$I_{R\lambda} = I \times \alpha_{R\lambda}; \quad I_{G\lambda} = I \times \alpha_{G\lambda}; \quad I_{B\lambda} = I \times \alpha_{B\lambda} \quad \text{Equation 20}$$

where, α_λ is the spectral colour sensitivity rate of R, G and B at a specific wavelength. Therefore, the following relationship exists between channels,

$$I = \frac{I_{R\lambda}}{\alpha_{R\lambda}} = \frac{I_{G\lambda}}{\alpha_{G\lambda}} = \frac{I_{B\lambda}}{\alpha_{B\lambda}} \quad \text{Equation 21}$$

Applying the incident light only at the wavelength of 430 nm for CH* and 516 nm for C₂*, Equation 21 can be written as:

$$\begin{cases} I_{CH^*} = \frac{I_{R_{430}}}{\alpha_{R_{430}}} = \frac{I_{G_{430}}}{\alpha_{G_{430}}} = \frac{I_{B_{430}}}{\alpha_{B_{430}}} \\ I_{C_2^*} = \frac{I_{R_{516}}}{\alpha_{R_{516}}} = \frac{I_{G_{516}}}{\alpha_{G_{516}}} = \frac{I_{B_{516}}}{\alpha_{B_{516}}} \end{cases} \quad \text{Equation 22}$$

Combining Equation 19 and Equation 22 yields

$$\begin{cases} I_G = I_{CH^*}\alpha_{G430} + I_{C_2^*}\alpha_{G516} \\ I_B = I_{CH^*}\alpha_{B430} + I_{C_2^*}\alpha_{B516} \end{cases} \quad \text{Equation 23}$$

I_G and I_B are the intensities in the G and B channels from the recorded flame image; the values of α_{G430} , α_{G516} , α_{B430} , and α_{B516} have been determined by a calibration procedure. Only I_{CH^*} and $I_{C_2^*}$ are unknown quantities. Thus, after solving the binary quadratic system, the relationship between CH^* and C_2^* emissions and colour intensity can be established, expressed as:

$$\begin{cases} I_{C_2^*} = \frac{I_B\alpha_{G430} - I_G\alpha_{B430}}{\alpha_{G516}\alpha_{G430} - \alpha_{G516}\alpha_{B430}} \\ I_{CH^*} = \frac{I_B\alpha_{G516} - I_G\alpha_{B516}}{\alpha_{B430}\alpha_{G516} - \alpha_{G430}\alpha_{B516}} \end{cases} \quad \text{Equation 24}$$

Compared with the equation given by Yang and Zhang [65], this is the generalised equation that can be used for any calibrated camera. The intensity ratio of $I_{CH^*}/I_{C_2^*}$ is the final obtained colour mode CH^*/C_2^* ratio expression, which will be used for following study of flame chemiluminescence measurements of methane and propane premixed flames.

4. Validation of Flame Chemiluminescence Measurements

4.1. Introduction

Flame chemiluminescence refers to the process in which the excited chemical radicals return to steady state, thereby releasing energy and emitting photons, which is widely exploited for combustion monitoring and diagnostics. For flame produced by hydrocarbon fuel premixed with air, CO^* , OH^* , CH^* , and C_2^* are the main radicals in the visible and ultraviolet emission spectrum [66]. Since 1958, these radicals have been employed to detect the FAR [67], flame position [68], shape [69], structure and heat release [70–72] for both gaseous and liquid fuel combustion [73–75].

H^* emission responds in the UV spectrum, which cannot be captured by normal digital cameras. Hence, for the camera visualisation measurement, only the radicals in the visible wavelength band, CH^* and C_2^* , are discussed in this work. Kojima et al. [76] have linked the chemiluminescence emission of CH^* and C_2^* with the equivalence ratio in methane–air premixed flames. Later on, the linear relationship between the CH^*/C_2^* ratio and equivalence ratio was confirmed by Huang [77] and Yang [78]. The chemiluminescence-based equivalence ratio method has been applied to various flame

monitoring conditions [79–85].

4.2. Camera Parameters Calibration

In general, digital images are stored and displayed in the RGB colour model. The sensors of different cameras have different sensitivities to the colour spectral range. Therefore, the camera parameter calibration is an essential procedure for determining the relationship between image colour and flame chemiluminescence.

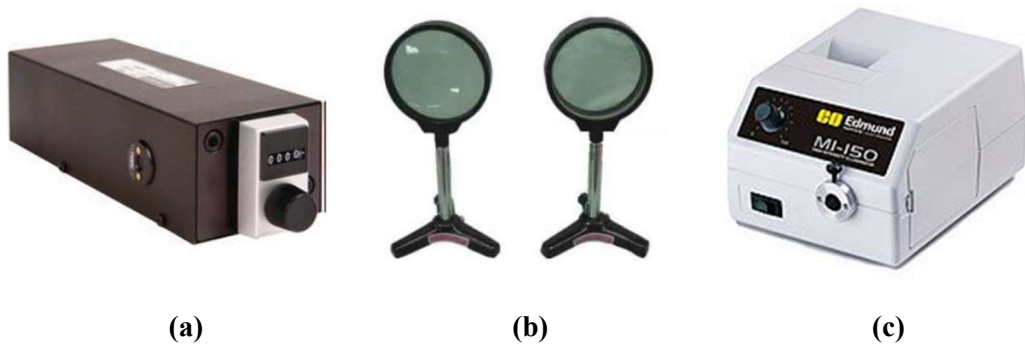


Figure 36 Calibration equipment: (a) monochromator, (b) convex lens, (c) fibre optic illuminator.

The principle of the calibration procedure was introduced by Takeuchi et al. [86] and Simonini et al. [87]. The general colour spectrum response of the digital camera was plotted by capturing the monochromatic light. Monochromatic light consists primarily of photons of a single frequency, which indicates that only a single colour is emitted. The calibration setup includes a monochromator, convex lens, and fibre optic Illuminator, as shown in Figure 36.

The MI-150 fibre optic illuminator is a light source with a 150 W EKE bulb. It can generate light covering the entire wavelength range and the colour temperature is 3200 K, performing as a blackbody calibration source. The intensity of the illuminator can be

adjusted, but it needs to be kept at a constant level throughout the calibration process to ensure the uniform incident light intensity.

The convex lens is used to focus the dispersed light from the illuminator to the entrance slit of the monochromator. A Newport manual mini monochromator is an optical device that can produce a monotonic spectral range. The outer dimension and inner construction are shown in Figure 37. It consists of a diffraction grating, slits, and spherical mirrors. The diffraction grating can be adjusted to allow a specific wavelength of light to exit the slit. The incident light via the entrance slit is scattered to all colours over the wavelength range by the rotatable diffraction grating. The rotation angle of the grating determines the particular wavelength to be reflected to the exit slit. After the light is separated, it passes through a slit to narrow the light beam and transmit the selected narrow wavelength band of the light. The monochromatic light emerges from the exit slit and is captured by a digital camera.

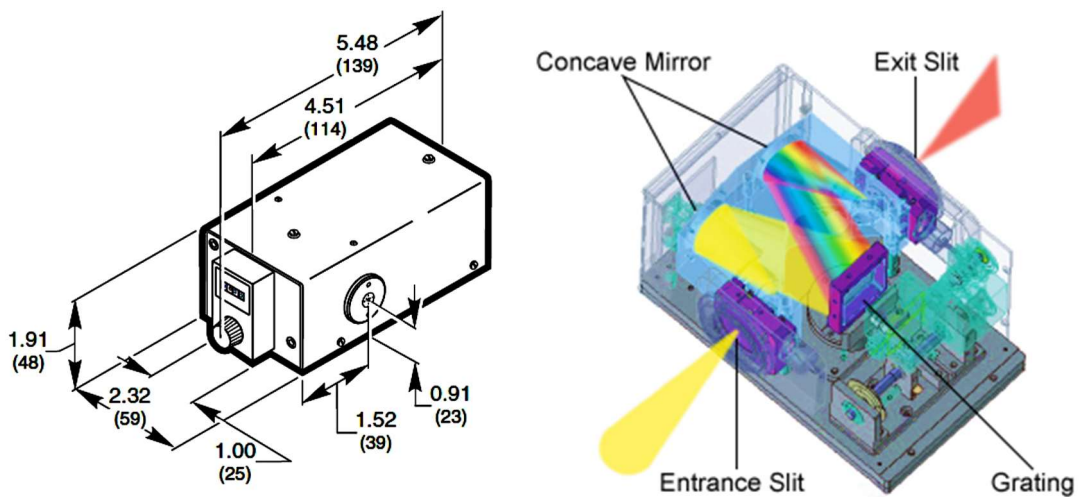


Figure 37 (a) Dimensions and (b) internal structure of the Newport manual mini monochromator

Two types of cameras are calibrated in this work, a scientific-grade camera (Photron

Chapter 4 Flame Chemiluminescence Measurements

SA-4 high-speed camera) and domestic camera (Sony $\alpha 77$). Both cameras are equipped with a CMOS sensor. The Photron high-speed camera setting default is ISO 4500 sensitivity, whereas the Sony $\alpha 77$ is set to its lowest setting of ISO 100 sensitivity to avoid noise.



Figure 38 Calibrated cameras: Photron SA-4 high-speed camera (left) and Sony $\alpha 77$ (right)

The experiment was carried out in a dark room. To avoid unexpected light interference with the experiment accuracy, a non-transparent black card board was used to cover the entire light beam path, as shown in Figure 39.

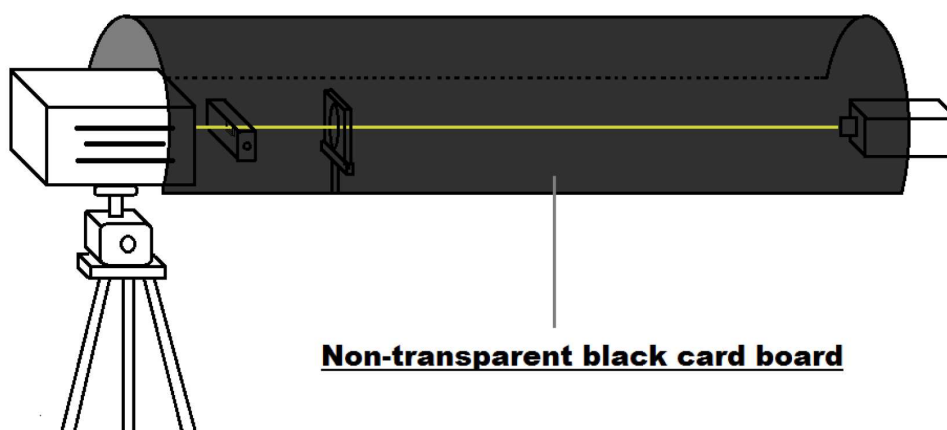


Figure 39 Double insurance of dark condition setup for calibration

The overall experimental setup is shown in Figure 40. During the experiment, the illuminator was maintained at a constant intensity level. The convex lens was fixed once it reached the position to focus the light beam to a point exactly at the entrance slit of the

Chapter 4 Flame Chemiluminescence Measurements

monochromator. The monochromator was adjusted through the wavelength range from 350 nm to 750 nm with 5-nm intervals to cover the entire the range of the visible spectrum. The light was captured directly from the slit and the camera recorded 50 images for each wavelength test point.

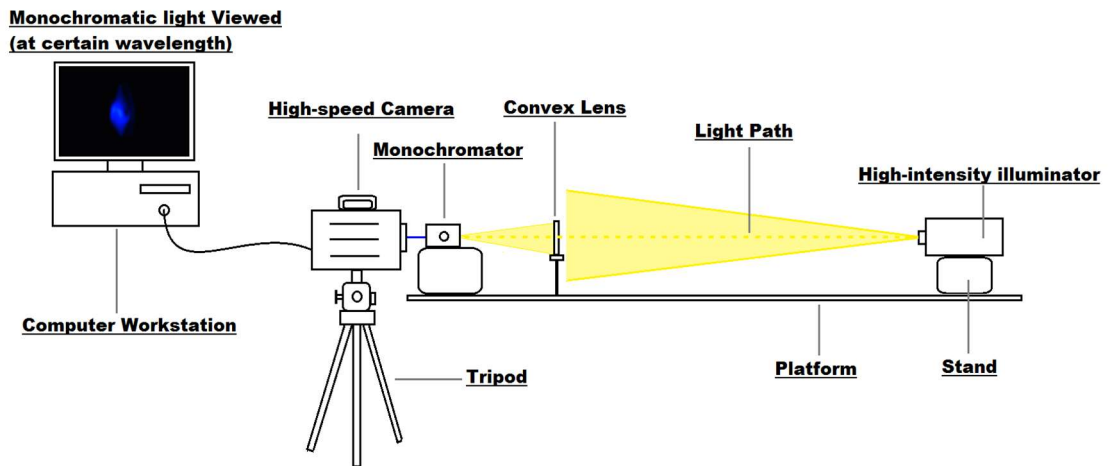


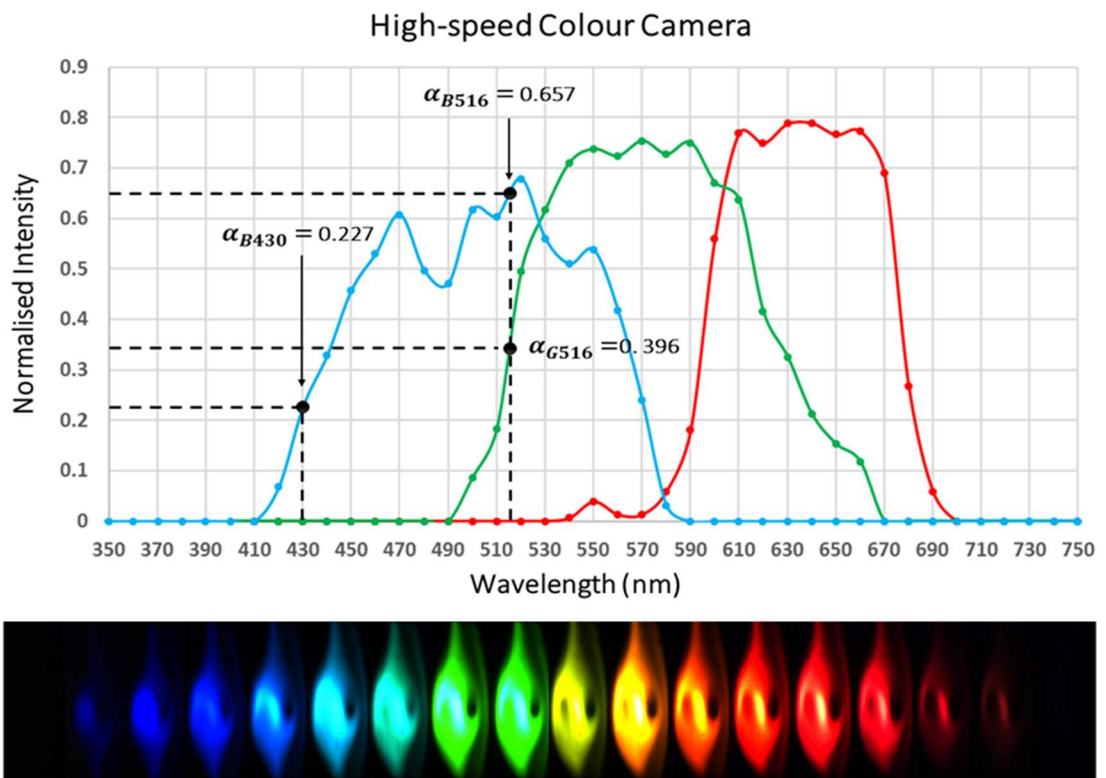
Figure 40 Experimental setup for the camera sensor calibration

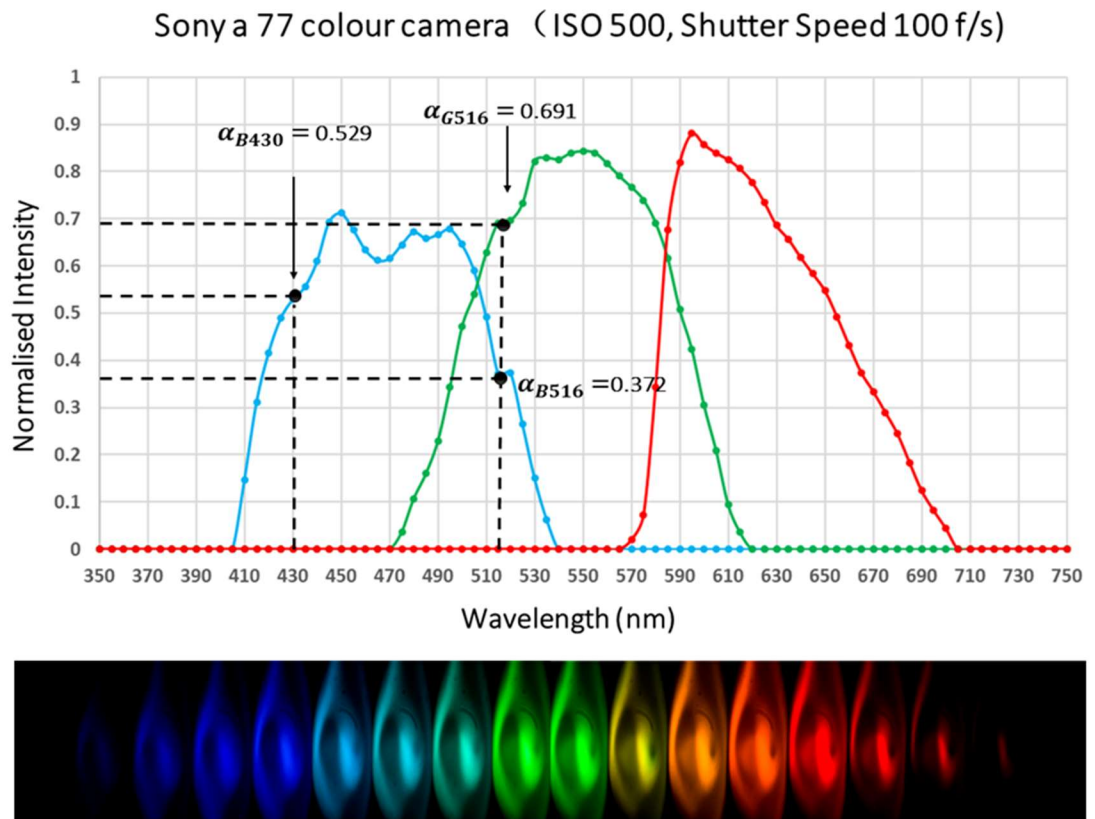
The captured image data for both camera are saved as 8-bit TIFF format. The images were processed using Matlab. The average value of the RGB intensities was calculated from the effective pixels for all 50 images. The average intensity of each colour channel was plotted against the wavelength, yielding the colour response curves.

In Figure 41, the samples of colour images over the measured wavelength range are shown below each plot of the results. In the plot, the intensities in the y-axis have been normalised by dividing by the maximum pixel intensity value (2^8-1). The red, blue, and green lines represent the spectral sensitivities for their corresponding colour channels. As shown from the results, for both cameras, the overall spectral sensitivity ranges are similar from 410 nm to 700 nm, but they show slightly different ranges in each channel. The B and G channels of the high-speed camera are sensitive to the wavelength range of 410–590 nm and 490–670 nm, respectively, whereas the ranges are

Chapter 4 Flame Chemiluminescence Measurements

slightly narrower for the Sony, with 405–540 nm and 470–620 nm. For the R channel, the sensitivity ranges for the two cameras are similar, but for the Sony *a77*, the intensity reaches the peak point at 595 nm and gradually decays with increasing wavelength. For Photron camera, the intensity value is highly equalized, which is closer to the ideal theoretical model. The camera sensor light conversion rates α at certain wavelengths, 430 nm and 516 nm, have been marked in the figures, which are used to link the colour to the chemiluminescence parameters. This will be further discussed in the following methodology section.





(b)

Figure 41 Sensor spectral responses for different cameras

4.3. Experimental Setup

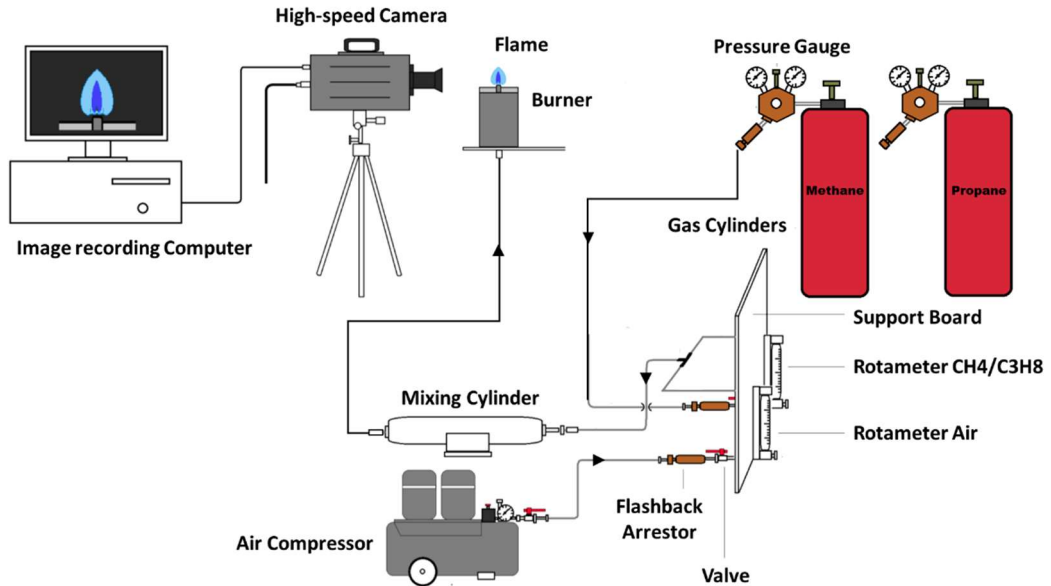


Figure 42 Schematic diagram of the flame measurement experimental setup

Figure 42 demonstrates the overview of the experimental setup, which consists of three parts. Two different fuels, methane and propane, were used in this work to compare the effect of fuels on the colour-modelled chemiluminescence measurement. The fuel was supplied from cylinders on the roof and the air was supplied by an in-door air compressor. The flow rates were adjusted by rotameters. Measured amounts of fuel and air were mixed in a mixing chamber before the burner to ensure they were fully premixed. The measured equivalence ratio range was from 0.8 to 1.55 with 0.05 intervals for both fuels. The details of the fuel and air flow rates with their corresponding equivalence ratios are shown in Table 1.

Table 1 Fuel and air flow rate for different equivalence ratios of CH4 and C3H8

	CH4		C3H8	
Equivalence Ratio(Φ)	Air(l/min)	CH4(L/min)	Air(l/min)	C3H8(L/min)
0.80	3.581	0.3	2.984	0.1

0.85	3.371	0.3	2.809	0.1
0.90	3.183	0.3	2.653	0.1
0.95	3.016	0.3	2.513	0.1
1.00	2.865	0.3	2.388	0.1
1.05	2.729	0.3	2.274	0.1
1.10	2.605	0.3	2.170	0.1
1.15	2.491	0.3	2.076	0.1
1.20	2.388	0.3	1.990	0.1
1.25	2.292	0.3	1.910	0.1
1.30	2.204	0.3	1.837	0.1
1.35	2.122	0.3	1.769	0.1
1.40	2.046	0.3	1.705	0.1
1.45	1.976	0.3	1.647	0.1
1.50	1.910	0.3	1.592	0.1
1.55	1.848	0.3	1.540	0.1

Two tested cameras, a high-speed camera and Sony domestic camera, were employed to record the flame images. Five-hundred images were captured at each equivalence ratio for the high-speed camera, with a shutter speed 125 1/s and 10 images for the Sony camera with a shutter speed 50 1/s. All the operation and sensor settings were the same as those used in the calibration procedure to ensure the validity of the measurements. The image data in this experiment were post-processed and analysed using Matlab.

4.4. Conventional Method Comparison

In conventional flame chemiluminescence measurements, researchers employed narrow-bandpass filters to achieve certain wavelength images. Migloirini [88] used the CH* filter (420–440 nm) and C2* filter (505–525 nm) to analyse the flame spectral band features. However, images with different filters cannot be taken at the same time, which is only suitable for very stable and continuous flame burning conditions. For certain instantaneous flame features, this method would not be effective. To improve the

synchronicity of the filter measuring, recently, Jin et al. [89] implemented a customised double-channel bandpass filter to record the chemiluminescence emission intensities of CH* and C2* with one shoot and conducted a post-processing algorithm to separate the two wavelengths. However, the validity of the post-processing algorithm has not yet been proven.

With the help of a stereo adapter, a new approach of simultaneously recording CH* and C2* emission has been implemented in this work. The same experimental settings and procedures were conducted using the conventional method with adding filters mounted on the camera lens. The stereo adapter can optically split the physical high-speed camera into two virtual cameras; the principle of the stereo function is illustrated in Figure 43.

The stereo adapter is made up of four mirrors in two (left and right) regions. In each imaging region, the inner mirror is placed at the adapter centre at a 45° angle to the centre line. The parallel inner mirror and outer mirror are fixed with a discrepancy angle of 3.5°. The outer mirror receives the incident light and reflects it to the inner mirrors. Then, the camera sensor receives the reflected light from the inner mirrors. Consequently, imaginary cameras get a pair views of the object, stereo vision 1 and 2, with a variation angle. The adapter is typically used to establish a 3D construction [90], which may demand elaborate calculations of the dimension and other parameters. However, for this experiment, the objectives are focussed on the colour analysis. Hence, the details of the position accuracy derivation are not described here.

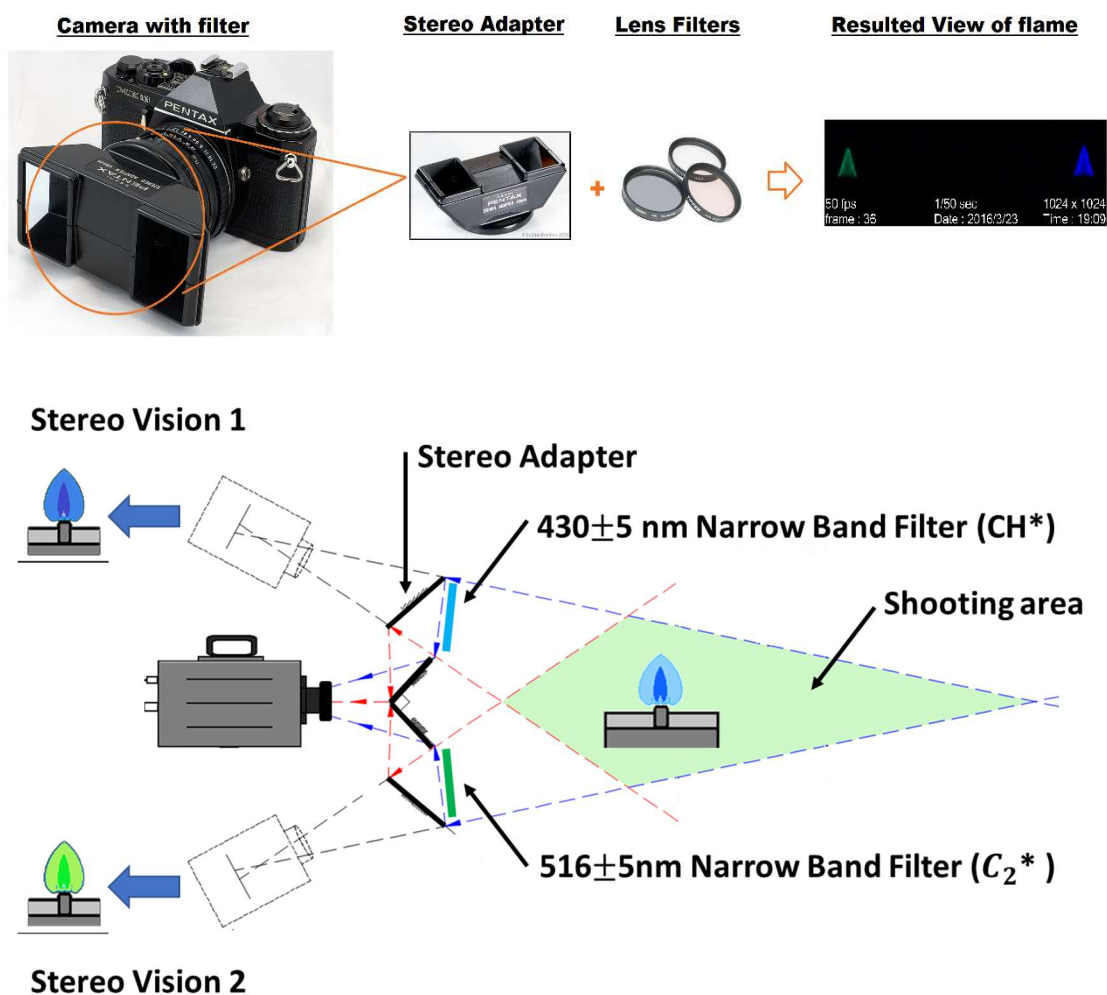


Figure 43 Principle and function of camera with the stereo adapter imaging system

The two bandpass filters mounted on the two view slots of the stereo adapter were 516 nm (greenish) and 430 nm (bluish) filters. This stereo imaging system allows one to determine the instantaneous CH*/C₂* ratio of the flame simultaneously. Because only light of a certain wavelength can pass the filter and the transparency rate of the filter can also block part of the light, a low frame rate was preferred to ensure adequate light was captured by the camera. Table. 3 shows the settings of the two cameras for different measuring methods.

Table. 3 Camera operation parameters

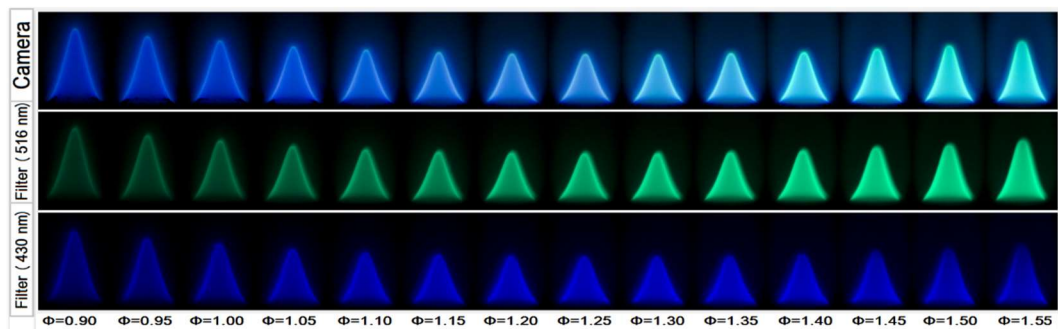
	Propane				Methane			
	High-Speed		Sony		High-Speed		Sony	
	Colour	Filter	Colour	Filter	Colour	Filter	Colour	Filter
Frame rate (fps)	125	50	50	10	125	50	50	1

The greyscale intensities of the CH* and C2* flame images were respectively calculated by a Matlab program. The CH*/C2* ratio can be simply defined as in Equation 25 and calculated for each equivalence ratio. The results are plotted against the equivalence ratio and compared with results of the colour model-based measurement.

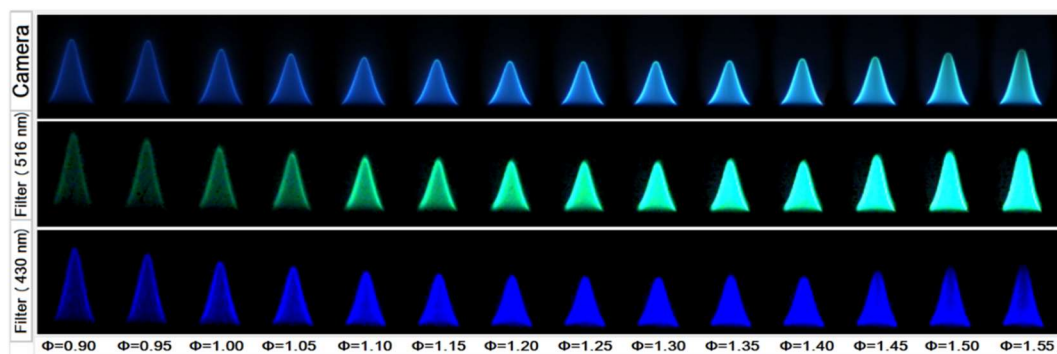
$$\frac{CH^*}{C_2^*} = \frac{\text{flame image intensity from 430nm filter}}{\text{flame image intensity from 516nm filter}} \quad \text{Equation 25}$$

4.5. Result and Discussion

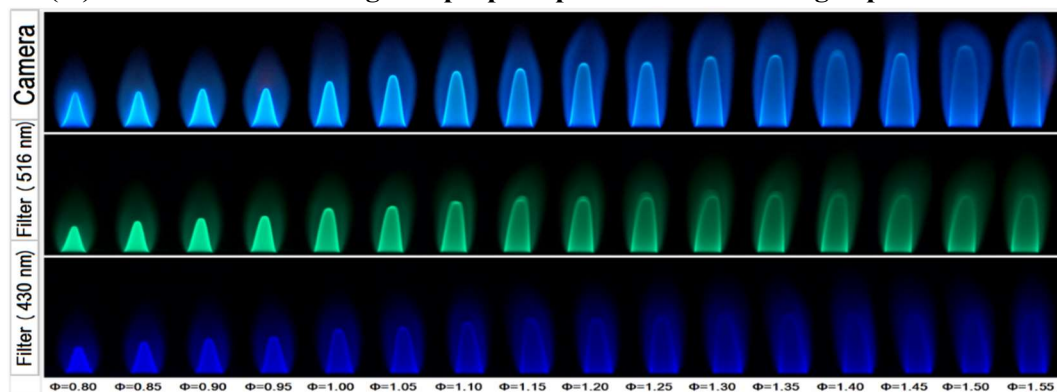
The flame images samples of different cameras and methods after de-noising and intensity enhancing are shown in Figure 44. The flame colour variation trend in the measured equivalence ratio range can be clearly noticed.



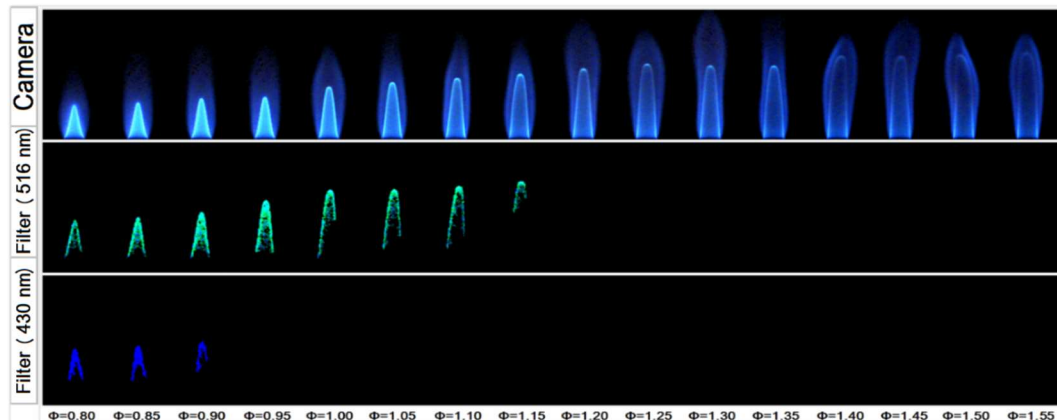
(a) Colour and filter images of propane premixed flame in Sony camera



(a') Colour and filter images of propane premixed flame in high-speed camera



(b) Colour and filter images of methane premixed flame in Sony camera



(b') Colour and filter images of methane premixed flame in high-speed camera

Figure 44 Samples of CH₄ and C₃H₈ premixed flame observed via different cameras and methods in the measured equivalence range

Figure 44 (a) and (a') illustrate the colour and filter images of propane premixed flame in the Sony and high-speed cameras for the equivalence ratio from 0.9 to 1.55. It

Chapter 4 Flame Chemiluminescence Measurements

can be evidently noticed by the naked eye from the colour images, that with the increase in the equivalence ratio, the colour of the premixed flame varied from blue to bright greenish-blue. In the filter images, the flame intensity of both the green filter (516 nm) images turn brighter with the increase in equivalence ratio and the change from the green filter is more noticeable.

For methane, Figure 44 (b) and (b') illustrate the colour and filter images of propane premixed flame in the Sony and high-speed cameras for the equivalence ratio from 0.8 to 1.55. As shown in the high-speed camera with narrowband filters at 516 nm and 430 nm, there is an incomplete trend owing to the signal drop-out at this frame rate of 50 fps, which is lowest flame rate level of the high-speed camera. The main reasons are the limited luminosity of the methane and that the filter blocks a certain amount of light. However, the trend of the methane flame can be captured by the Sony camera at frame rate 1 fps, because longer exposure time allows more light to reach the sensor.

It is noteworthy that in the methane premixed flame, a double flame structure with the inner primary reaction flame zone and outer secondary reaction flame can be obviously distinguished. With the increase in the equivalence ratio, after $\phi \geq 1.35$ the two flame zones gradually merge together, which is called a hybrid structure. The intermediate structure for methane always exists in the range $1.36 \leq \phi \leq 4.76$, as reported by Jeong et al. [91]. For $\phi \geq 4.76$, the luminous sooty region appears at the flame tips.

Measured Flame Region Effect

regions of the flame, (c) comparison of calculated CH^*/C_2^* ratio from different flame sections to equivalence ratio

The chemiluminescence of a local point is very useful for understanding the structure of the flame front. As mentioned in the previous section, in the lean premixed condition, the double flame structure can be clearly observed for both fuels. The inner flame is the primary combustion zone and the outer layer is the post-flame oxidation and radiation zone. The colour of both layers is determined by the chemical reaction. Therefore, to understand the effect of the equivalence ratio on the chemiluminescence behaviour in each section, the flame front has been segmented into two sections by Matlab imaging processing, as shown in Figure 45 (a) and analysed separately on the trend of the colour modelled CH^*/C_2^* intensity ratio against the equivalence ratio.

The corresponding colour map of the flame sections is shown in Figure 45 (b), which can offer a 2D local CH^*/C_2^* ratio distribution. The colour of the jet colourmap from blue to red indicates the colour-modelled CH^*/C_2^* ratio from 0 to 5. It can be obviously noticed that with the increase in equivalence ratio, the colour of the inner layer shows an evident change from red to blue, which indicates the equivalence ratio plays a predominant role on the CH^*/C_2^* intensity ratio at the inner layer. Furthermore, the colour distribution of the flame at a certain equivalence ratio is almost uniform, which demonstrates that the fuel and air are mixing well. On the contrary, there is no evident distinct tendency of colour change in the post-reaction zone with the variance in the equivalence ratio. At a certain equivalence ratio, the colour distribution of the outer layer flame is not uniform, and it randomly mixes the high, medium, and low ratio together. This indicates that the CH^*/C_2^* intensity ratio of the outer layer flame responds retardedly to the equivalence ratio.

A statistical investigation has been further analysed to assess the variation between

Chapter 4 Flame Chemiluminescence Measurements

the CH^*/C_2^* intensity ratio of different flame regions and the equivalence ratio, and the results are plotted in Figure 45 (c). The value of each point in the plot is the average value of the selected region from 500 images. In the figure, the blue and orange dotted lines indicate the results of the outer and inner flame layers, respectively. The black solid line refers to the results of the whole flame region. As shown by the results, all three lines begin with a high ratio value at the very lean premixed condition and show decreasing trends with the increase in the fuel proportion. The CH^*/C_2^* intensity ratio from the inner layer flame drops faster than the other two from above 4.5 to near 0.5 in the measured equivalence ratio range. As the decrement of the ratio value from the outer layers to within 0.5 and value of the whole flame (black line) is located in the centre of the inner and outer flame layers. The statistical results for the CH^*/C_2^* intensity ratio of the two sections are in agreement with the observation from the colour map.

As a consequence, the CH^*/C_2^* intensity ratio of the flame shows a linear relationship with the equivalence ratio, regardless the flame region. The decreasing trend of the results measured from the inner flame layer presents a clear linear correlation with the equivalence ratio. However, the result from outer flame does not have an obvious changing trend, which may reduce the accuracy and sensitivity in practical applications. Therefore, the inner layer is more suitable to be used as the equivalence ratio measurement and the entire flame can be a complementary option when the inner and outer flame layer are merged and difficult to segment. The following data analysis is based on the inner flame layer measuring in a lean premixed condition and the whole flame region in a partially premixed condition.

4.5.1. Results Comparison

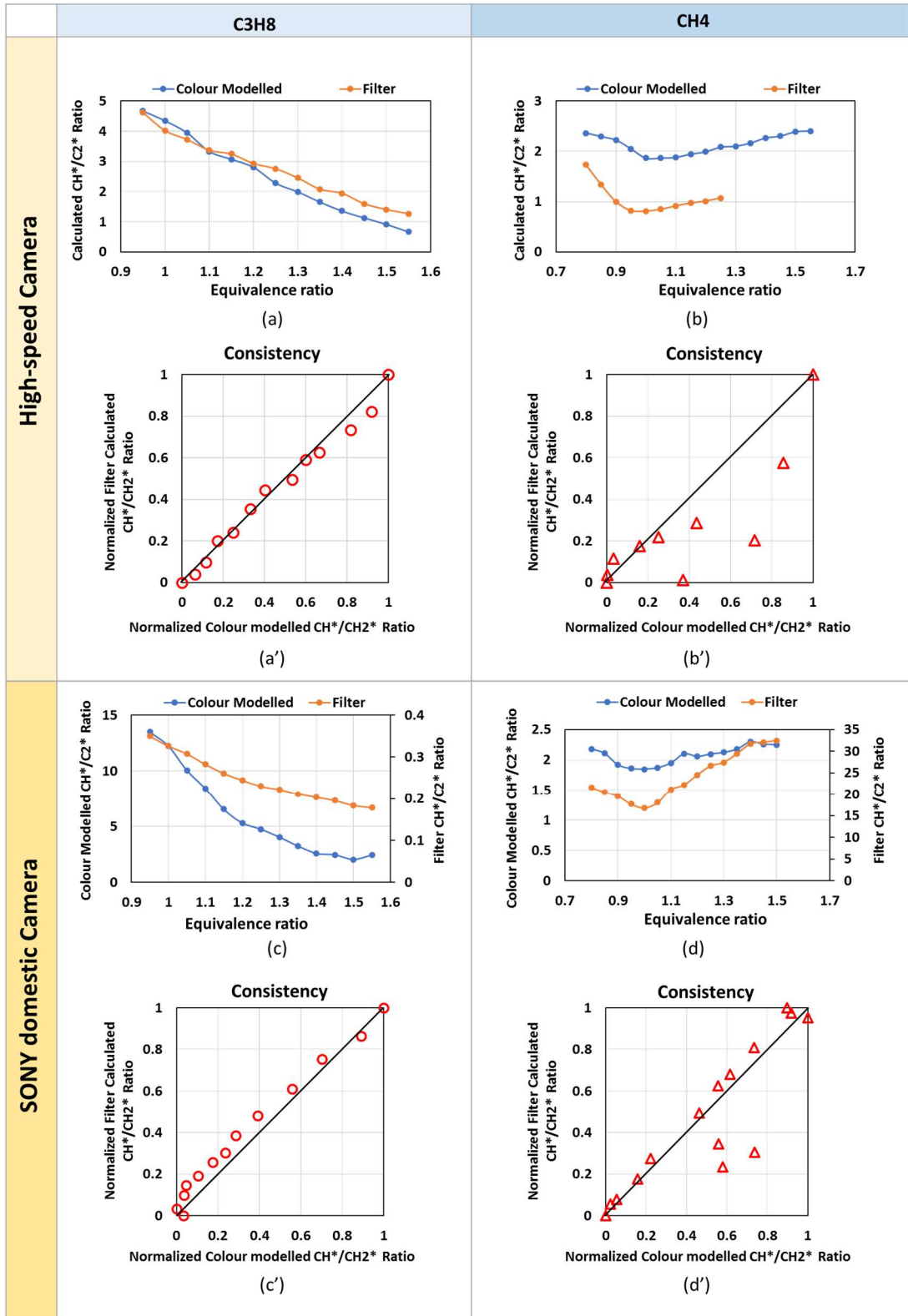


Figure 46 Analysis results of the CH^*/C_2^* based on colour-modelled and filter with two cameras;

(a)(a') Calculated CH^*/C_2^* of C3H8 flame with high-speed camera and the consistency of the two methods;

(b)(b') Calculated CH^*/C_2^* of CH4 flame with high-speed camera and the consistency of the two methods;

(c)(c') Calculated CH^*/C_2^* of C3H8 flame with SONY camera and the consistency of the two methods;

(b)(b') Calculated CH^*/C_2^* of CH4 flame with SONY camera and the consistency of the two methods;

In Figure 46, (a) (b) (c) (d) present the results of the calculated CH^*/C_2^* intensity ratio of propane and methane premixed flames measured by the novel colour-modelled method and conventional filter method with both the laboratory-grade high-speed camera and the commercial SONY camera. (a') (b') (c') (d') give an overall view of how the difference between proposed colour model and filter model varies with the equivalence ratio. For ease of comparison between the results from the two methods, they have been normalised the range from 0 to 1. The value of 0 indicates the lowest CH^*/C_2^* ratio in the measured equivalence ratio range, and the value of 1 indicates the highest value. The X-axis represents the results from colour-modelled method and the Y-axis represents those from the filter method. The solid black 45°-inclined line is the reference line. If the two sets of results were perfectly matched, all the data would be located exactly on the line. Instead, the more points deviate from the reference line, the larger the difference between the two sets of results.

As shown in the plots, the orange line refers to the results measured by filter and the blue line represents the colour-modelled results. In general, the results of the CH^*/C_2^* intensity ratio from the two methods exhibit similar trends. In the C3H8 tests, for the results from either camera, both lines decrease monotonically with the increase in

Chapter 4 Flame Chemiluminescence Measurements

equivalence ratio. From the consistency plots for both camera, most of the points are distributed along the reference line and the shifting of these points are in an acceptable range. The experimental errors should be taken into the consideration of the divergence, including the signal drop-out, transient changes of the flame, noise effects and so on. It is also worth noting that the divergence from the SONY camera is larger than that from the high-speed camera, which is mainly caused by the noncontiguous shooting, unstable sensor sensitivity, and lower instantaneity due to the longer exposure time.

In the CH₄ case, the CH*/C₂* intensity ratio shows an unexpected nonmonotonic tendency with the change in equivalence ratio. However, this outcome has been mutually reinforced via the two methods and two cameras. It is worth noting that the filter-measured result of the CH₄ from the high-speed camera only has the front end. The CH*/C₂* ratio for filter model only continued up to $\phi = 1.25$. Later, there is no adequate light passing through filter to support the calculation. Therefore, the intensity signals of the flame drop-out is an unavoidable drawback for filter-based measuring, especially in the restricted-exposure-time condition. The SONY camera with a lower shutter speed can capture the low-intensity light. The entire changing trend can be presented clearly, and the results show better consistency with the colour-modelled result.

As a result, in the equivalence ratio range 0.9 to 1.55, for the C₃H₈ premixed flame results have a monotonic linear trend with increasing equivalence ratio and are suitable for both measuring methods and cameras. However, matters are more complex for the CH₄ premixed flame. Apart from the nonmonotonic dependence on the equivalence ratio, there is a large error between the two sets of data.

In addition, certain considerations regarding the unexpected results tendency of the methane premixed flame have been proposed. First, as mentioned previously, the inner and outer flame layers of the methane flame gradually merge and become difficult hard

to calculate separately, which may affect the accuracy of the results. However, most previous studies report a correlation between the chemiluminescence with lean premixed flame and the approximately stoichiometric equivalence ratio. Therefore, further investigation should be done to determine the variation tendency of the CH^*/C_2^* intensity ratio with further increase in the equivalence ratio for both fuels.

4.5.2. Validated Range

It has been proven on countless occasions that the chemiluminescence ratio CH^*/C_2^* provides a good index of the equivalence ratio. The discussion above has also proved that the colour-modelled intensity ratio calculation are in good agreement with conventional filter measured method and it can be a powerful tool to measure the CH^*/C_2^* ratio.

In order to determine the validation range of the monotonic linear relationship between the chemiluminescence ratio (CH^*/C_2^*) and the equivalence ratio, an experiment was conducted on the hybrid and partially premixed of flames methane and propane. With the increase in the FAR, the sooty flame gradually appears on the flame tip. The yellowish colour of the sooty flame is dominated by black-body radiation. Therefore, for the chemiluminescence measuring, the sooty flame region needs be eliminated from the measure region before further calculations, according to the colour selection method introduced in Chapter 2.

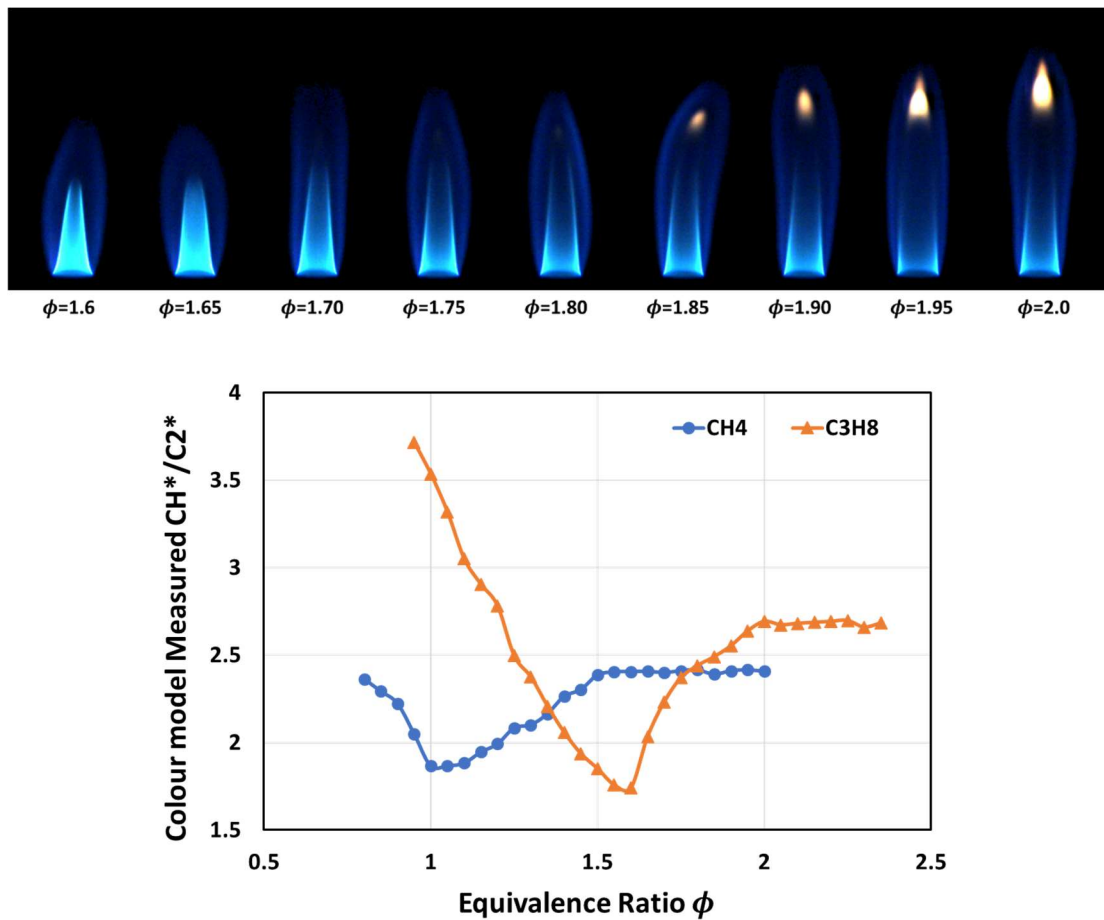


Figure 47 Relationship between the CH*/C2* intensity ratio and the equivalence ratio from lean premixed to partially premixed flame

The colour-modelled intensity ratio of CH*/C2* as function of the equivalence ratio is shown in Figure 47. In the present study, the correlations between the colour-modelled CH*/C2* and the equivalence ratio are nonmonotonic for both fuels.

As shown from the results, the behaviours of colour-modelled intensity ratio decrease gradually to the minimum value at approximately $\phi = 1$ for methane and $\phi = 1.55$ for propane. The colour model measured results show a similar trend as the results from Jeong et al. [91] measured via an intensified charge coupled device (ICCD) and photomultiplier tube (PMT), and the results reported by Migliorini et al. measured

by ICCD and interference filters on the flame of methane. The CH^*/C_2^* ratios and equivalence ratio are nearly linear, while ϕ is less than approximately 1 for methane and 1.55 for propane. However, at $\phi \geq 1$ for methane and $\phi \geq 1.55$ for propane, the CH^*/C_2^* ratios increase to a certain point and remain constant regardless of changes in the equivalence ratio. Therefore, it's impossible to evaluate the equivalence ratio for $\phi \geq 1$ in methane and $\phi \geq 1.55$ in propane. In other words, the chemiluminescence ratio of CH^*/C_2^* cannot be used to measure the equivalence ratio for hybrid premixed and partially premixed flame. The validation ranges of the flame chemiluminescence measurements are $\phi \leq 1$ in methane and $\phi \leq 1.55$ in propane.

4.6. Summary

In this experiment, the relationship between the chemiluminescence and equivalence ratio has been investigated the flame region effect, the fuels effect, camera sensors effect via two measuring methods. The conclusions from this study can be summarized as follows:

- The accuracy of the results in the employed cameras was largely affected by their sensors. Therefore, the camera sensitivity calibration is essential in the first step. Comparing with the domestic camera, the high-speed camera sensor can produce the intensity of each RGB channel more evenly for and perform much more reliably.
- For the propane flame, in equivalence ratio range $0.9 \leq \phi \leq 1.55$, the flame has easily distinguished double flame structure, inner and outer flame. The CH^*/C_2^* ratio of the inner layer shows best the linear correlation with equivalence ratio variation, followed by whole flame region. The results from outer post reaction zone is not sensitive to the equivalence ratio altering.
- In general, the results of the CH^*/C_2^* intensity ratio from the colour-modelled and

Chapter 4 Flame Chemiluminescence Measurements

filter exhibit similar trend for both fuels. The consistency is negligible for Propane cases, but there is considerable divergence in the methane tests. Furthermore, the filter method is not suitable for measuring at low-light situations.

- The CH^*/C_2^* intensity ratio of propane flame decrease monotonically with the increase of equivalence ratio within the range of $0.9 \leq \phi \leq 1.55$. While as the result of methane decrease firstly and then increase. The bottom point is located at about $\phi \approx 1$.
- For hybrid premixed and partially premixed flame, the chemiluminescence ratio of CH^*/C_2^* cannot be used to associate with the equivalence ratio. The validation range of the flame chemiluminescence measurements is $\phi \leq 1$ in methane and $\phi \leq 1.55$ in propane.

5. Acoustic Impact on Flame in An External Excited Chamber

5.1. Introduction

In practical combustion circumstances, the acoustic perturbation is unavoidable, triggered by self-driven and forced excitation. Many studies have been carried out to observe the flame/acoustic wave interaction on the flame dynamics, heat release rate, and dilution mixing [55,92–96]. Most of the random perturbation phenomena are undesirable in a combustion device, such as flame lift-off [55], thermoacoustic instabilities [97]. However, well-controlled acoustic excitation can be taken advantage of on the chemical reaction level, which may contribute to achieving the target of emission control [92]. Farhat et al. [98] noted that dramatic flame change occurred in the reaction zone of an acoustically excited diffusion flame, which can be changed into partial blue or completely blue. Jeongseog Oh's experimental investigation concluded that NO_x emission was reduced and minimised at the resonance frequency [99]. In the early 1980s, the character of dilution fuel and air by acoustic control was demonstrated and Vermeulen et al. [100] applied it to a gas turbine combustor to increase the combustion efficiency. Therefore, the acoustic forcing has been considered as an alternative approach to enhancing the fuel/air mixing and widely applied owing to its

ease of implementation and independent control of excitation frequency and amplitude [58].

To achieve the clear observation of the dynamic vortex structure, flame front wrinkle, dilution behaviour, and other instantaneous and complicated characteristics, researchers had to resort to technical equipment, including particle image velocimetry (PIV) laser [101], schlieren [102], photomultipliers [103] and so on. The optical-based imaging method is highly suitable for diagnosis and analysis of both flame colour and movement with reasonable spatial resolution. The data can be processed either in the frequency domain to illustrate the compounding effect of the acoustic perturbation and flame flicking frequency [103] or directly visualise the nonlinear diffusion flame structure evolution in a cycle [104]. Huang et al. introduced an image processing methodology, digital flame colour discrimination (DFCD), which has been successfully applied to several hydrocarbon flames. On the basis of the visible spectra of the electronically excited combustion radicals CH^* and C_2^* , the distribution over a range of equivalence ratios [105,106] and chemiluminescence emission behaviours under external excitation [107] have been studied.

Many studies were employed for investigations of diffusion flame, vortex on the flame boundary, flow velocity, and buoyancy effect. The flame front wrinkle is also one of the most significant features under acoustic excitation, which is associated with heat release [88,108,109]. Advanced visualisation approaches, such as schlieren, PIV, and numerical simulation have been applied to analyse the fluctuation characteristics. The flame instability induced by fuel flow oscillation has been studied theoretically and numerically by many researchers [58,110,111]. Few reports have mentioned the premixed flame front dynamics and the perturbation effect on fuel/air mixing, particularly the dynamic character of dilution behaviour in response to external

excitation. The objective of this research is to understand the wrinkle characteristics of laminar premixed conical flame in response to the various sound intensities under harmonically forced frequencies in a one-end open tube. The responses of laminar premixed flame shape and colour to acoustic modulation are determined by the fast Fourier transform (FFT) and DFCD methods. Here, we directly study the flame wrinkle front, local fuel/air mixture, and dilution dynamic principle, which have not been well explored to date.

5.2. Background Knowledge

5.2.1. Acoustic

Acoustics is an interdisciplinary science, concerned with vibrations propagated as a pressure wave in a transmission medium. Sound waves are longitudinal waves consisting of periodic compression and rarefaction of the medium in which the sound wave is traveling. Sound propagates by molecules passing the wave on to neighbouring molecules, and the coupling between molecules is the strongest in solids. In general, the speed of sound is the highest in solids, then liquids, then gases. The speed of sound in air is

$$v = 331 \text{ m/s} + 0.6 \text{ m/(s} \cdot \text{°C)} \times T_c \quad (T_c \text{ is temperature in } \text{°C}) \quad \text{Equation 26}$$

Humans are sensitive the frequencies ranging from 20 Hz to 20000 Hz. Whether you can hear a sound also depends on its intensity. In three dimensions, the intensity of a sound wave is its power/unit area,

$$I_s(r) = \frac{P}{A(r)} = \frac{P}{4\pi r^2} \quad \text{Equation 27}$$

Where

P: the sound power

r: the distance from the sound source

A(r): the area of a sphere of radius r

The sound intensity level described in the familiar expression is dB, which is the level relative to a reference value and defined as:

$$\beta = 10 \log_{10} \left(\frac{I_s}{I_0} \right) \text{ dB} \quad \text{Equation 28}$$

Where

I_s : the sound intensity;

I_0 : the reference sound intensity;

Every 10 dB represents a change of one order of magnitude in intensity. 120 dB, 12 orders of magnitude higher than the threshold of hearing, has an intensity of 1 W/m². A 60 dB sound has ten times the intensity of a 50 dB sound, and one-tenth the intensity of a 70 dB sound.

5.2.2. Standing Wave

A standing wave occurs when the two similar waves move in opposite directions. It most likely happens as a phenomenon of resonance due to the interference between the incident and reflected waves. To demonstrate the phenomenon in a mathematical method, the waves are simplified as sine waves in one dimension and the resonance is derived by adding the two equations together.

Incident wave is defined as:

$$y_{in}(x, t) = A \sin\left(\frac{2\pi}{\lambda}x + \omega t\right) \quad \text{Equation 29}$$

Reflected wave is defined as:

$$y_{re}(x, t) = A \sin\left(\frac{2\pi}{\lambda}x - \omega t\right) \quad \text{Equation 30}$$

Where

A: the wave amplitude

ω : the angular frequency

λ : the wavelength

x and t: longitudinal position and time

Hence, the resultant wave is

$$\begin{aligned} Y(x, t) &= y_{in} + y_{re} = A \sin\left(\frac{2\pi}{\lambda}x - \omega t\right) + A \sin\left(\frac{2\pi}{\lambda}x + \omega t\right) \\ &= 2A \cos(\omega t) \sin\left(\frac{2\pi x}{\lambda}\right) \end{aligned} \quad \text{Equation 31}$$

As result, any point on the x-axis constantly oscillated with $\sin\left(\frac{2\pi x}{\lambda}\right)$. Therefore, the amplitudes at the location of even multiples of a quarter wavelength,

$$x = -\frac{2n\lambda}{4}, \dots, -\frac{3\lambda}{2}, -\lambda, -\frac{\lambda}{2}, 0, \frac{\lambda}{2}, \lambda, \frac{3\lambda}{2}, \dots, \frac{2n\lambda}{4},$$

are always zero, which are called nodes.

the amplitudes at the location of odd multiples of a quarter wavelength,

$$x = -\frac{(2n-1)\lambda}{4}, \dots, -\frac{5\lambda}{4}, -\frac{3\lambda}{4}, -\frac{\lambda}{4}, \frac{\lambda}{4}, \frac{3\lambda}{4}, \frac{5\lambda}{4}, \dots, \frac{(2n-1)\lambda}{4},$$

are always the maximum value at that instant, which are called anti-nodes. These are illustrated in the Figure 48.

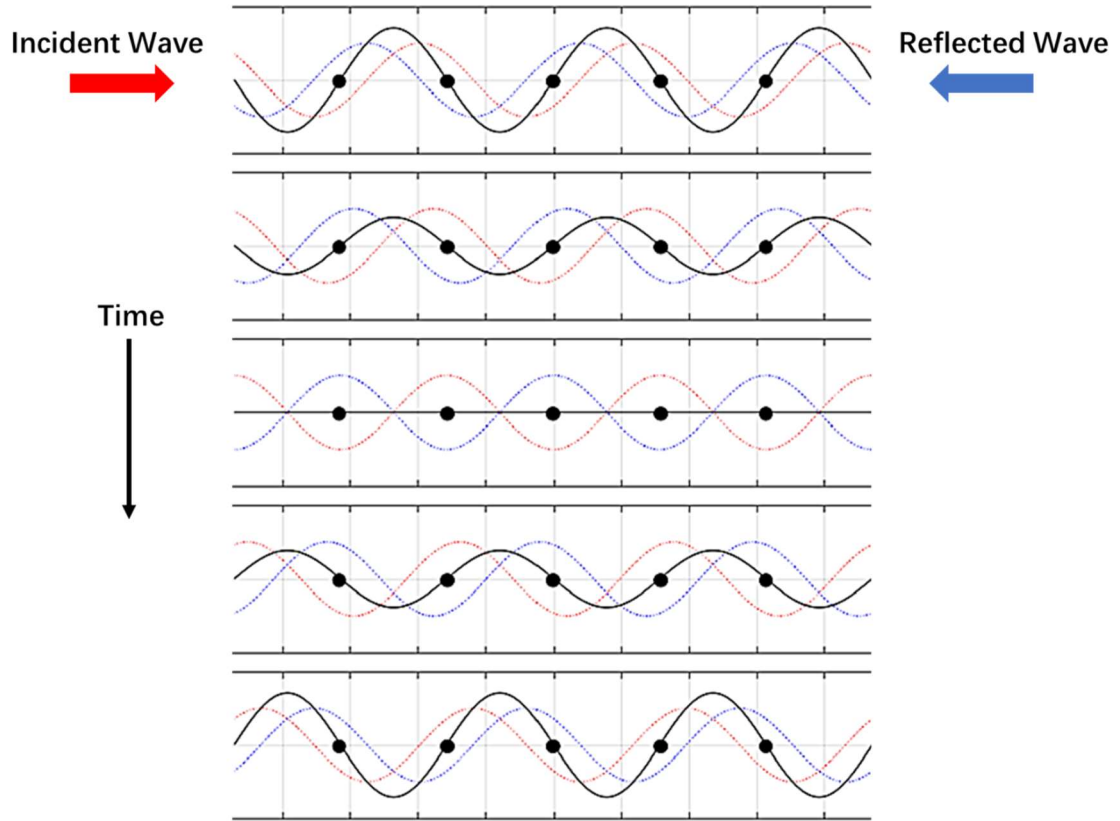


Figure 48 Two opposing waves combine to form a standing wave.

Whether the standing wave terminates in a node (minimum amplitude) or an antinode (maximum amplitude) depends on whether the other end of the tube is open or closed. There is a displacement node at the closed end, and an antinode at the open end. By analogy, consider a string fixed at one end (node) and free at the other (antinode). Arbitrarily make $x = 0$ the closed end, as shown in Figure 49

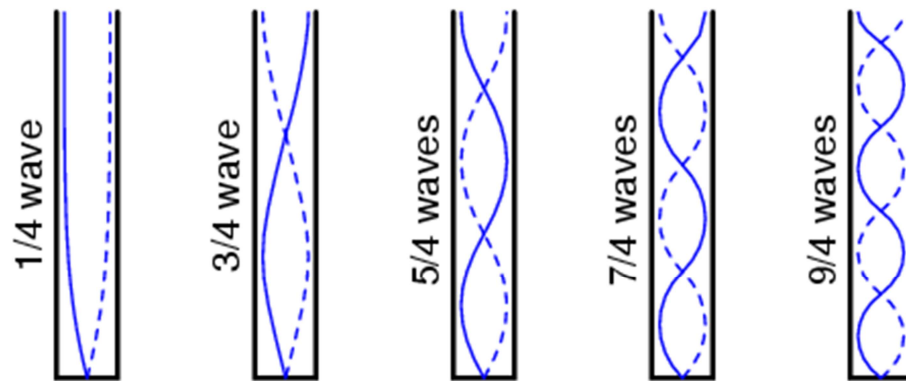


Figure 49. Standing sound waves in one end closed and one end open tube

The standing waves can resonate with the system at any frequency (wavelength) correlating to the node/antinode points of the system. In other words, there are multiple resonant frequencies for any system supporting standing waves. The resonance frequencies are given as:

$$f_n = \frac{(2n - 1)v}{4L}, (n \text{ can only be odd integers}) \quad \text{Equation 32}$$

where

L: the length of the tube

v: the velocity of sound in air

f: the frequency of sound

n: the integer for the nth harmonic

In the present study, the cross-section of the tube is square and non-constant. A pyramidal structure is designed in the lower half of the tube to fit the size of a loudspeaker. This acoustical system is more complex than that presented in Eq. 32. Hence, the microphone has been applied for the actual standing wave measurement presented in 6.2.3, and the following study is based on the experimental results.

5.2.3. Reynolds Number

$$\text{Re} = \frac{\rho_m V D}{\mu_m} \quad \text{Equation 33}$$

where

V, velocity of the mixture gas at the nozzle

D, the inner diameter of the nozzle

μ_m , the dynamic viscosity of the mixture gas

This is calculated from the Wilke equation as:

$$\mu_m = \frac{X_a \mu_a}{X_a + X_f \phi_{af}} + \frac{X_f \mu_f}{X_f + X_a \phi_{fa}} \quad \text{Equation 34}$$

where X denotes the mole fraction of a component and ϕ_{af} is defined by:

$$\phi_{af} = \frac{[1 + (\mu_a/\mu_f)^{1/2} (M_f/M_a)^{1/4}]^2}{[8 \times (1 + M_a/M_f)]^{1/2}} \quad \text{Equation 35}$$

and vice versa for ϕ_{fa}

ρ_m is the density of the mixture gas:

$$\rho_m = \frac{\rho_a v_a + \rho_f v_f}{v_a + v_f} \quad \text{Equation 36}$$

5.2.4. Flame Lifted Off

In most industrial applications, jet flame lifted off is always been regarded as the most undesirable instability performance, as it is unstable and easy to blow-off abruptly. Hence, the stabilisation and extinction mechanism has been subjected to numerical simulation and experimental investigation.

The jet flame has a tendency to lift off from the burner nozzle position when the jet

Chapter 5 Acoustic Impact on Flame

velocity of the flame reaches a critical value U_c [54]. With the increasing of the jet velocity, the lifted height will be increased beyond certain critical height [112]. Therefore, the stability of the lifted flame is an important parameter for basic combustor design. Scholefield and Garside's theory [113] claimed that the transition to turbulence is a prerequisite for the lifted flame stabilisation and the flame anchors at a point where the flow is turbulent. Gollahalli [114] argued that the flame will tend to stabilise at the position where the local flow velocity balances the normal flame propagation velocity. Navarro-Martinez and Kronenburg [115] determined that the excessive turbulent stretching at the nozzle leads to the lift-off, but they also claimed that the turbulent structure can be used to promote the flame sustainability. Recently, observations from Kiran and Mishra's [112] visual experiment proved that the flame lift-off height varies linearly with jet exit velocity. They presented a semi-empirical correlation between the normalised lift-off height and the global strain rate.

$$\frac{H_L}{D_f} = 1.8 \times 10^{-3} \frac{U_f}{D_f} \quad \text{Equation 37}$$

H_L : lift-off height

D_f : diameter of the fuel tube

U_f : fuel jet velocity

In addition to the velocity effect, the effect of stoichiometric burning on the physical mechanism blowout has been investigated by Broadwell et al. [116] and Pitts [117]. According to their study, the re-entrained gases are mixed with non-flammable jet gases, which cool down the hot products and hinder the continuous burning.

For the lifted flame, it has been proved by many research works that the rolling-up processes of vortex structures generated by the bluff body or acoustic perturbation will prevent the lifted flame from propagating downstream [55,56,118–120]. The flame

response to specific external excitation in the terms of frequency and amplitude was studied theoretically and experimentally by Demare and Baillet [121] They concluded that secondary vortices are sufficiently powerful to make the flame propagate oppositely. The study of flame stability mechanisms in the hysteresis region by acoustically exciting the unburned components has been investigated by Lin et al. [122] and the most significant effect was found when the acoustic frequency matched the fundamental frequency of the vortex. Chao et al. demonstrated that the acoustic excitation at certain frequencies could extend the blowout limit by more than 25% [119]. Moreover, the stability method of acoustic excitation on lifted flame was also proven to be feasible for soot suppression and emission control [58,123,124].

However, for a steady laminar flame, it is well-known that the external periodic acoustic forcing acts on both the flame jet and the surrounding air. Kim et al. [92] and Kartheekeyan et al. [95] observed that the flow oscillation varies the local strain rate at the shear layers, which contributes to fluctuations of the heat release rate and mixing rate. Additionally, the unsteady vortical structure pass-by can stretch and quench the flame [125]. Chen and Zhang experimentally investigated on the nonlinear coupling characteristics on different equivalence ratios of propane/air flame [103]. They showed the existence of complex nonlinear frequency components created by the coupling of buoyancy and excitation.

Although the acoustic excitation has been widely investigated from two aspects: namely, one where the acoustic stabilisation mechanism is studied and one where the flame oscillation response of the excitation is examined. The mechanism behind the transition of the flame lift-off and re-attachment procedures has not been clearly described. The present work is performed on conical laminar premixed flame in a rectangular tube excited by acoustic waves in different conditions. The oscillatory

behaviour of the laminar flame dynamic structure and lifted height are experimentally investigated with the high-speed image recording and contour line detection method.

5.2.5. Principle of Microphone

When the sound has been generated, the sound wave carries energy towards the microphone. The wave hits the diaphragm, which is a very thin plastic film located at the front side of the microphone. The coil, attached to the diaphragm and wound around a permanent magnet, vibrates with it. The back and forth movement of the coil intersects the magnetic field generated by the magnet. Hence, the electric signal can be generated and transmitted to the sound recorder device.

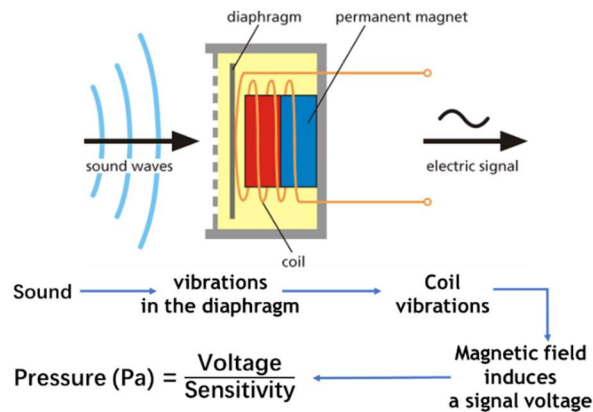


Figure 50. Principle of Microphone

High-sensitivity microphones are not always better than low-sensitivity microphones. The sensitivity refers to the characteristics of the microphone but not necessarily its quality. In near-field applications, such as cellular phones, where the microphone is close to the sound source, a microphone with higher sensitivity is more likely to reach the maximum acoustic input, clip, and cause distortion. A higher sensitivity may be desirable in far-field applications, such as conference phones and security cameras, in which the sound is attenuated as the distance from the source to the

5.3.1. Burner System

In the burner system, the gaseous fuel and air are supplied from a propane cylinder and air compressor. The flow rate is controlled by a rotameter. The fuel and air are connected to a mixing chamber to produce a premixed flame at the equivalence ratio of 1.4 (C_3H_8 0.12L/min, air 2.05/min). The inner diameter of the burner nozzle is 3 mm and the fuel was ignited with an electrical spark near the nozzle exit. The nozzle position relative to the tube could be adjusted through the 3D traverse system controlled by Labview. The tube is made with four glass panels and braced by four steel brackets with an open top end. The dimensions of the tube are 1000 mm in length and 120 mm in width of the square.

5.3.2. Sound Generating and Data Acquisition System

The sound generating system is used to produce the external acoustic excitation, including a Labview control panel, an audio amplifier and a loudspeaker. The output wave signal frequency is defined by Labview and the forcing amplitude is controlled by the audio amplifier, based on the output voltage (V). The loudspeaker (BUMPER model 0848 RF) converts the electrical signals to sound via an electromagnetic transducer.

In the data acquisition system, the sound pressure readings were collected by a microphone from PCB PIEZO model 377C10 (details shown in Appendix I). The microphone is mounted at the nozzle and recorded by a National Instruments DAQ card. The data acquisition card was an eight-slot NI cDAQ-9178 compact DAQ chassis with NI 9205 32 channel analogue input module and NI 9264 16 channel analogue output module. The maximum sampling rate of the card is 250 kHz. In this experiment, the sampling rate was set to 10,000 samples per second.

5.3.3. Standing Wave Measurement

The experimental measurements of the acoustic responses were made along the length of the tube using a microphone. The pressure value has been recorded at different position from 40 cm to 80 cm above the sound source with 2 mm intervals through the whole tube and the measurement point was in the centre of the tube. The range of excitation frequency was from 20 Hz to 600 Hz in increments of 5 Hz, with a voltage amplitude of 5 V. The experimental observation in Figure 52 indicates that the first four modes of the present rig are 90 Hz, 200 Hz, 380 Hz, and 500 Hz.

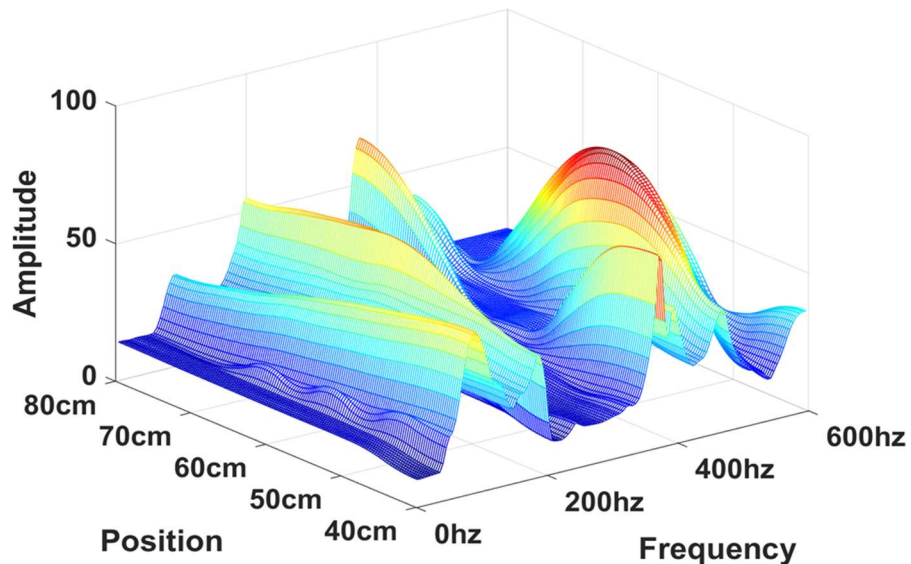


Figure 52 Experimental measurement of pressure response to position and frequency

5.3.4. Colour Imaging Setup

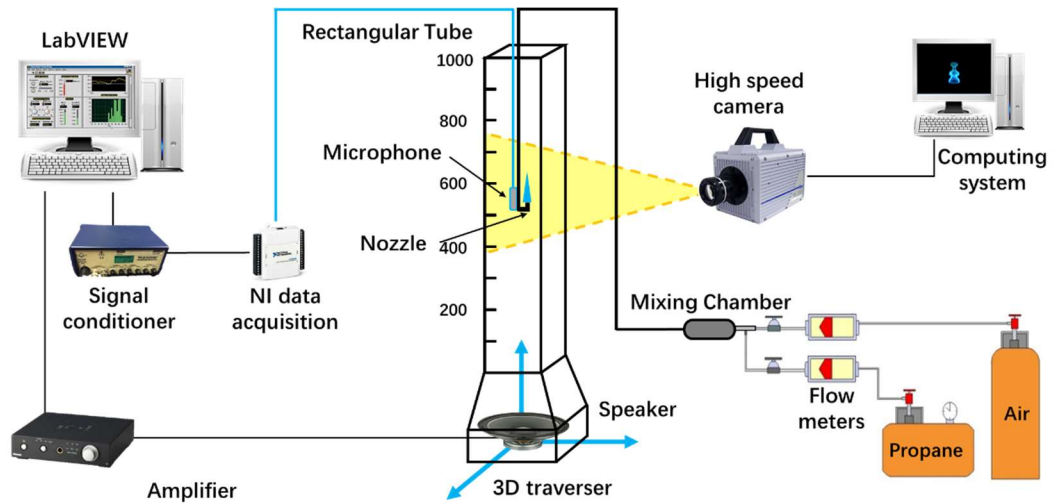


Figure 53 The schematic layout of the Colour imaging experimental apparatus setup

The optical colour imaging setup, shown in Figure 53, consists of a Photron-SA4 high-speed colour camera with a Sigma zoom 24–70 mm lens, as well as a computer control and recording system. Merely setting the brightness will increase the noise and other unwanted colour, which may increase the difficulty to acquire accurate analysis results. To avoid redundant noise signals affecting the weak signal detection, the experiments were carried out in completely dark room in addition to using a black background behind the flame. To ensure accuracy and generalisability, 2000 images were recorded at a frame rate of 2000 images per second for each condition. The data were quantitatively analysed by Matlab image processing.

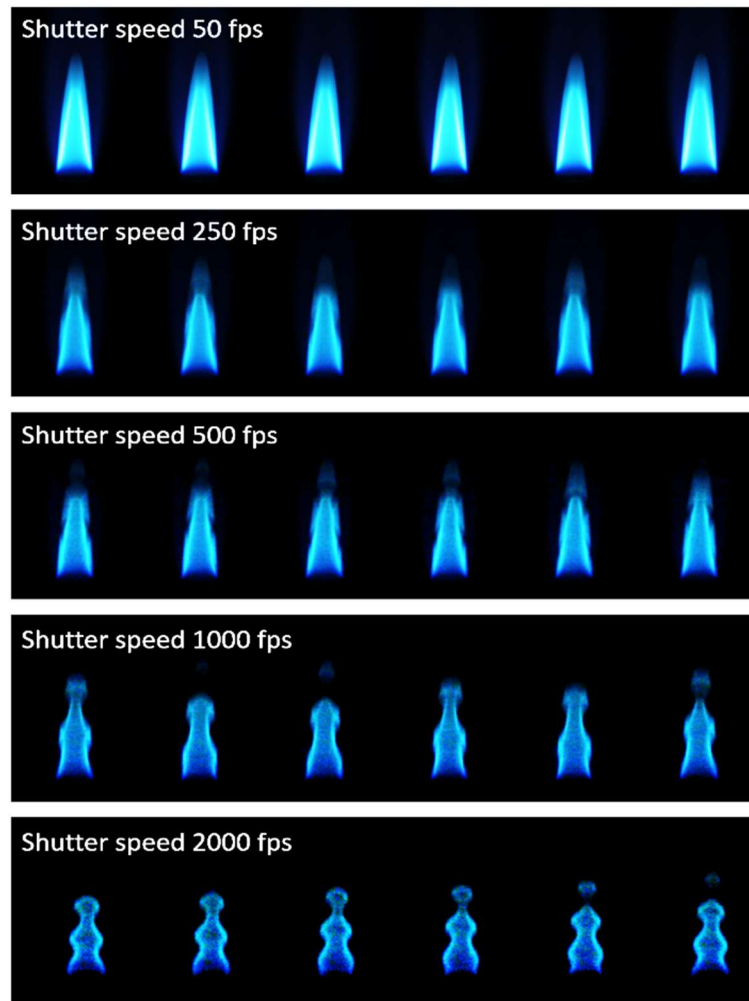


Figure 54. Shutter speed selection

In order to capture a precise image of the flame dynamic structure, a variety of shutter speeds were tested to choose the most suitable settings before collecting the data. In the test, the external excitation wave frequency was set to 385 Hz with pressure 40 Pa and the shutter speed was varied from 50 fps to 2000 fps. The results are shown in Figure 54. It is obvious that the flame boundary is blurry and there is no clear difference between the flame structures at low shutter speeds. Chen [126] claimed in his previous study that under the same acoustic excitation, a premixed flame is more stable than a diffusion flame. This view is compatible with observations of the flame under the low

shutter speed, shown in the first line. However, as the shutter speed increases, the boundary line is sharper, and more details of the flame dynamic structure can be identified. The higher shutter speed leads to poor visualisation on the bluish flame and creates a barrier to further analysis due to the restriction of exposure time at the instantaneous flame capture condition. Therefore, 2000 fps is selected for the following imaging capture and study.

5.3.5. Single Schlieren System

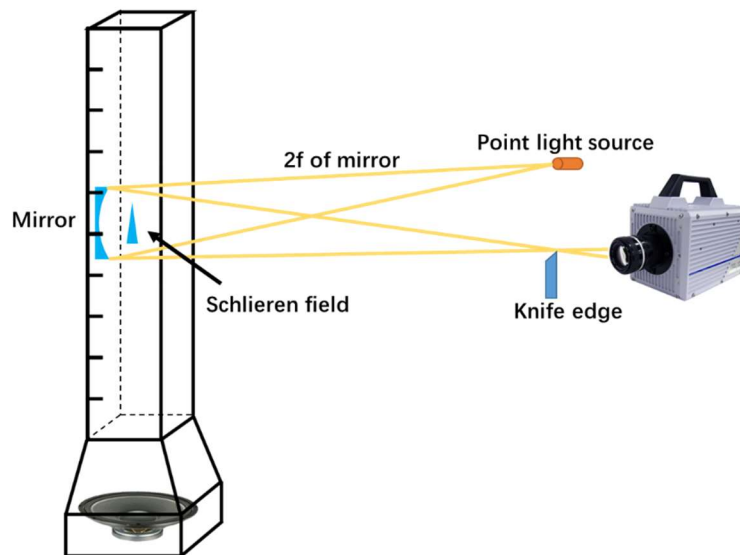


Figure 55 Experimental setup of schlieren system

The experimental setup for the schlieren system is shown in Figure 55. A single schlieren system has been applied to visualise the flow dynamic and vortex structure. The single schlieren has a higher sensitivity than the Z-type system, because the light passes through the density gradients object twice. Taking advantage of this, vortices in both the hysteresis region and the self-illuminated flame are clearly shown in the schlieren image. The schlieren system consists of a point light source and one $\lambda/10$

parabolic mirror with 75 mm diameter and 75 cm focal length. A knife edge was placed at the focal point, just in front of camera, to adjust the brightness and contrast. The schlieren images were recorded by a SA4 high-speed camera at the full frame resolution of 1024×1024 pixels.

5.4. Results

5.4.1. Flame Flicking

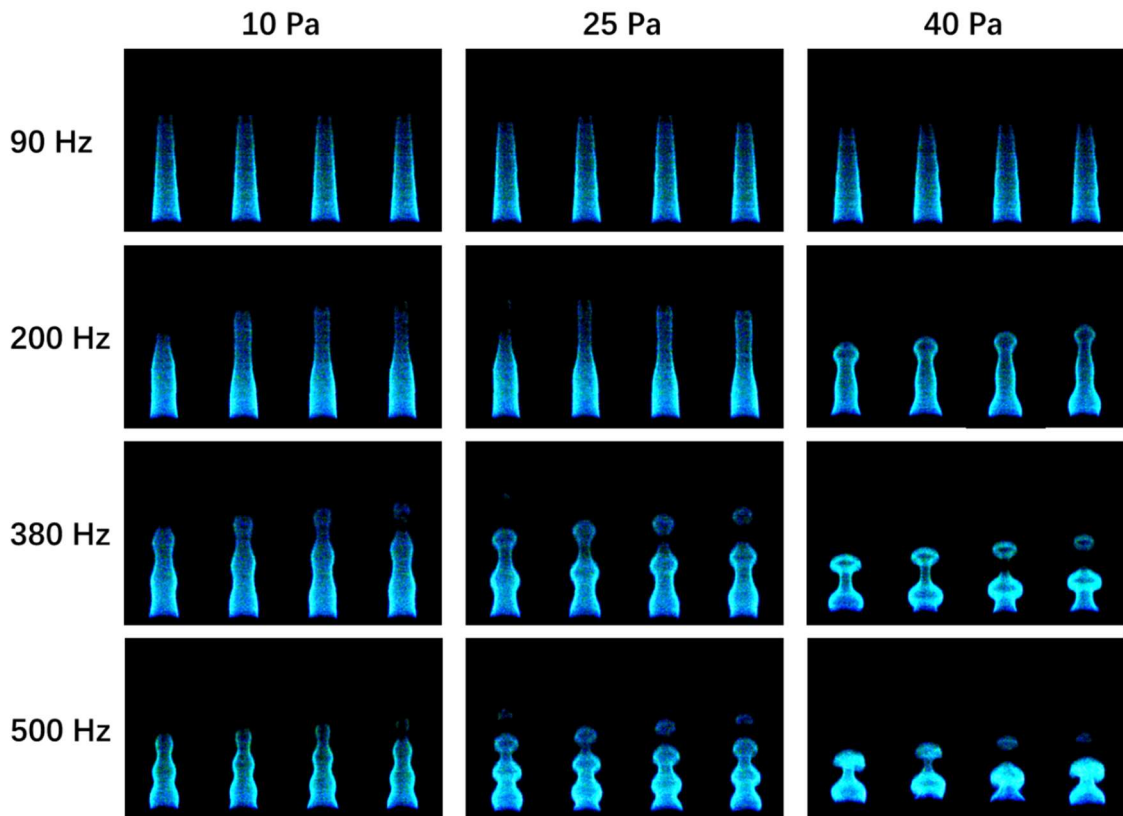


Figure 56. The sample of series images under various excitation groups

Examples of sets of four consecutive images in $4/2000$ s are shown in Figure 56, The results show the changing trend of the shape of the flame front with sound pressure

Chapter 5 Acoustic Impact on Flame

at 10 Pa, 25 Pa, and 40 Pa and at an external excitation frequency according to the first four harmonic frequencies. It is clearly demonstrated that, at each external excitation frequency, the flame front generated more evident wrinkles and separated flame bubbles with increasing sound amplitude. For the lower-excitation-frequency case, the wave on the flame front can barely be perceived in the 4/2000 s duration. With the increase in the frequency, the wavelength on the flame front is shorter and the amplitude is larger. It is also noteworthy that, in the low-frequency and high-pressure case, such as 90 Hz and 220 Hz under 40 Pa, more than one type of combined waves are exhibited on the flame front. Moreover, severe deformation and flame lift-up can be noticed in the picture of the flame under high sound pressure in the 500 Hz group. These phenomena on the flame front have never been observed on a diffusion flame. In other words, the premixed flame is prone to be disturbed by the external excitation. Further analysis of the flame dynamics, wrinkle, acoustic dilution, and lifted flame are discussed in the following section.

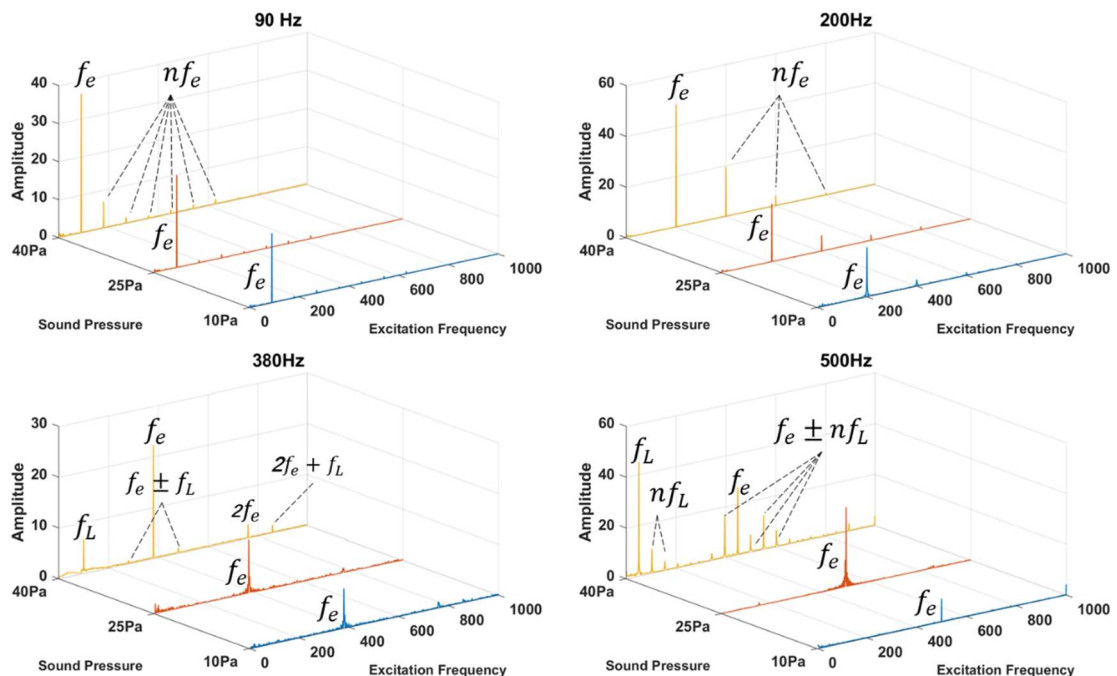


Figure 57 Intensity frequency under the four harmonic frequencies and three sound pressures

Figure 57 illustrates the dynamics of flame intensity under the various acoustic excitations corresponding to those in Figure 56. The frequency components are very different at the different external excitation frequencies and intensities. For all the cases, the excitation frequencies f_e dominate the flame dynamics. No buoyancy-forced flame flicking frequency can be determined, which indicates that the external perturbation is sufficiently powerful to overshadow the buoyancy-induced flame flicker. At the low excitation frequencies, 90 Hz and 200 Hz, several peaks of the harmonic frequencies nf_e can be clearly observed. With the increase in the pressure, the frequency components are similar, but the amplitude of the harmonic response is more evident. Under severe excitation condition, as shown in the cases of 380 Hz and 500 Hz, the chaotic front exhibits an asymmetrically irregular geometry and leads to unexpected periodic motion, which is similar to the results reported by Bourehla et al. [127]. By observing the result, the nonconstant value of peaks f_L have been seen at in the range 20–40 Hz, which are caused by the flame lifted-off phenomenon. The sets of the fore and aft peaks that accompany the dominant and harmonic frequencies $f_e \pm nf_L$ have also been detected. The particular frequencies are induced by the acoustic lift-up phenomenon [128], which can be observed in the corresponding flame images in Figure 56. The flame bottom partially lifted and gradually propagated downward and attached to the nozzle in the following images. This acoustic induced flame lift-up behaviour will be thoroughly analysed in Section 5.4.3.

5.4.2. Flame Configuration

A Matlab-based contour detection algorithm has been employed to define the conical flame front. By carefully tuning the threshold and denoising process, the bright primary reaction zone can be separated from the post-reaction zone and the boundary line can be extracted. Figure 58 presents the three sequential samples of the flame front

contour lines with 1/2000 s intervals for each of the external excitation frequency and sound intensity groups.

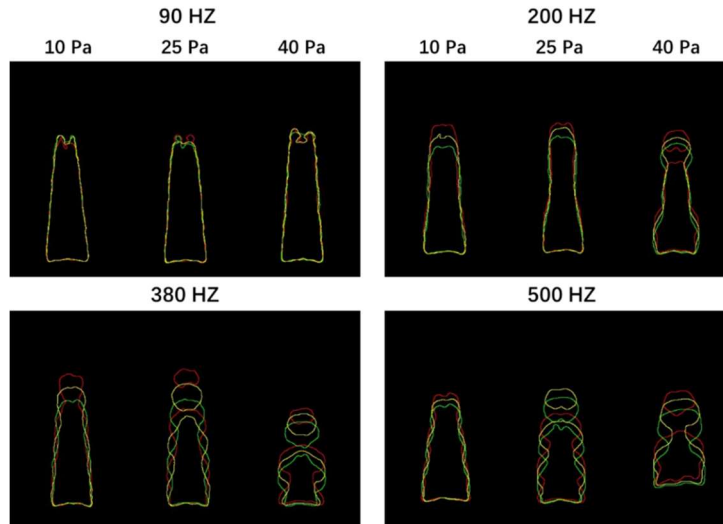


Figure 58 Samples of boundary lines of the instantaneous flame

The contour lines exhibit that the amplitude of fluctuation keeps growing with the increase in the excited sound intensity and resonance frequencies. The higher forcing amplitudes, for all forcing resonance frequencies, restrain the height of the flame, which is consistent with the observation of Karimi et al. [129]. Under severe excitation condition, as shown in the group of 40 Pa at 500 Hz, the chaotic front exhibits an asymmetrically irregular geometry and leads to unexpected periodic motion, which is similar the results of Bourehla et al. [127]. The root segment of the front shows noticeable a lift-off trend and the lift height oscillates, which can also be observed in other excitation groups. With the increase in the perturbation level, the amplitude of the lift-off oscillation is increased until blow-off finally occurs. Another noteworthy phenomenon is that the separated flame bubble is formed on the top of the flame under high forcing perturbation level, which considerably increases the flame front surface and prompts the fresh mixture changing.

5.4.2.1. Fluctuation of Single Point on Flame Wrinkle

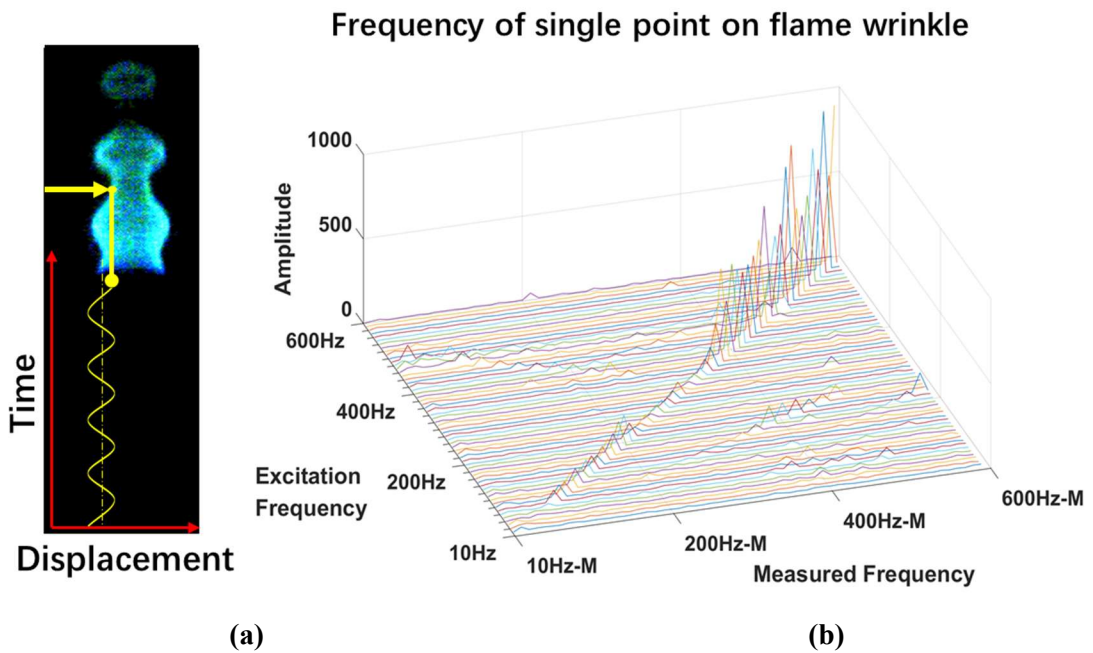


Figure 59. Schematic of the single-point displacement on the flame wrinkle

Figure 59 (a) shows the time trace of the disturbing displacement for a single point on the sample flame under three different forcing amplitudes at an excitation frequency of 380 Hz. It is clear from this figure that the response of any picked-up single point on the surface of the flame front to the acoustic excitation includes regular oscillation in the time scale. Increasing the forcing pressure enlarges the wave amplitude of the flame disturbance, but does not alter the wavelength, which results in a more wrinkled flame with same frequency. In the following discussion of the single point, the selected point is at the location of 200 pixels above the nozzle.

The following section aims at extending the identification of the excited flame parameters submitted to FFT response to the excitation frequencies ranging from 10 Hz to 600 Hz, the single point disturbed response amplitude of flame wrinkling, the surface area disturbance under excitation along the standing wave, and the line configuration of

the forcing flame wrinkle.

Apart from the displacement amplitude of the wrinkle changing with the excitation, the wrinkle also shows different oscillation frequency peaks under the different excitations. To examine the general relationship between the measured wrinkle point displacement frequency and the excitation frequency, the flame images were captured under a range of excitation frequencies from 10 Hz to 600 Hz in increments of 10 Hz, with a voltage amplitude of 3 V. The nozzle was fixed at the position of 50 cm in the transparent glass tube, regardless of the standing wave effect.

As shown in Figure 59 (b), the measured response frequencies exactly match excitation frequencies f_e , which indicates that the flame wrinkling correlates well with the acoustic disturbance. Additionally, the frequency peaks become more prominent when the excitation frequency increases. The buoyancy-driven flame flicking effect is difficult to observe on the premixed flame front wrinkle fluctuation. This result matches with the result of the nonlinear coupling flame intensity frequencies studied by Chen and Zhang [103].

The standing wave has a non-negligible effect on the flame wrinkle amplitude. To confirm this prediction, flame images of the acoustic responses were recorded along the whole measurable length of the tube under a range of excitation frequencies from 10 Hz to 600 Hz with 10 Hz intervals. The voltage of the acoustic excitation signal was fixed at 3 V. The nozzle location was in the centre of the tube cross-section, and was varied from 40 cm to 80 cm in increments of 5 cm.

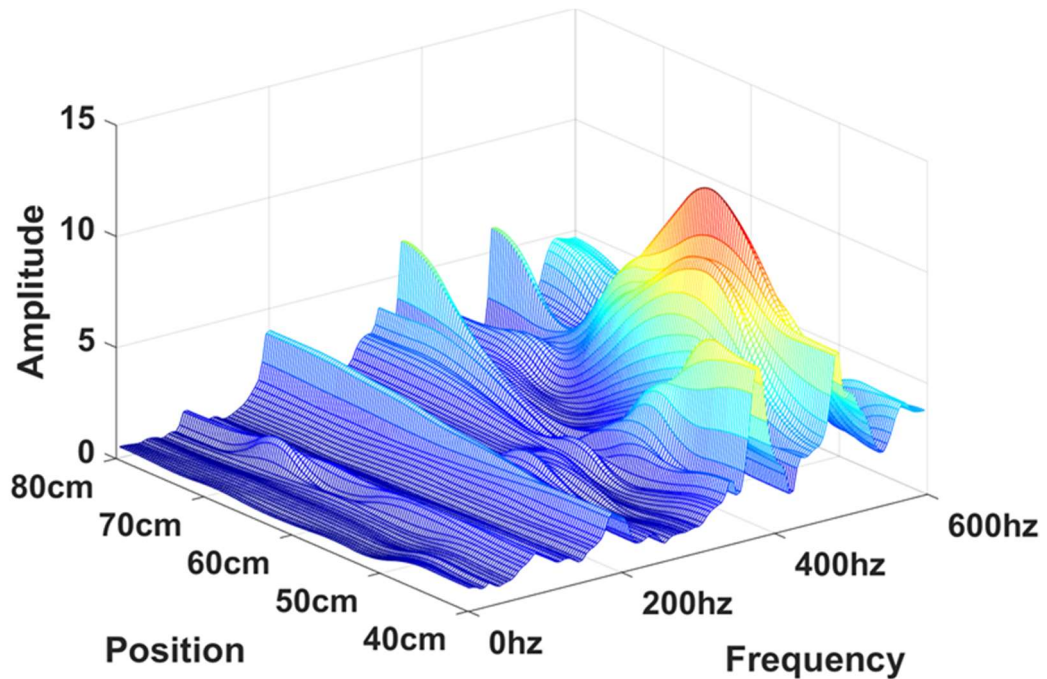


Figure 60 Amplitude of the point displacement along the tube under various excitation frequencies

The amplitude results of the single point on the flame wrinkle under various excitation frequencies along the tube are shown in Figure 60. The amplitude of the flame wrinkling has a similar fluctuation trend to the acoustic pressure field measured by microphone in the tube. However, similar results also show a disagreement between the results of the microphone and flame response. From the observations, the disturbance amplitude is less evident at lower frequencies. Combined with the evidence of the measured flame frequency results in Figure 59, the flame configuration parameters are more likely to sensitive to the higher frequency excitation.

5.4.2.2. Fluctuation of Flame Wrinkle Line

Axisymmetric premixed laminar conical flames submitted to harmonically external acoustic excitation are investigated in this study. The geometry is a 2D flame captured

by high-speed camera with the selected enhancement technique by image processing shown in Figure 61 (a). The coordinate system in Figure 61 (b) is chosen to be in alignment with the laminar flame at stable condition, as per the method introduced by Shim and Lieuwen [110]. The i -axis is tangential to the stable flame edge and the j -axis is perpendicular to it. The ξ_i^+ and ξ_i^- represent the displacement of perturbation of the flame front to the steady position at the location of i -axis and the $+/-$ symbols indicate the direction. Owing to the vertical axial symmetry structure of the flame, only one side will be calculated, in the following analysis.

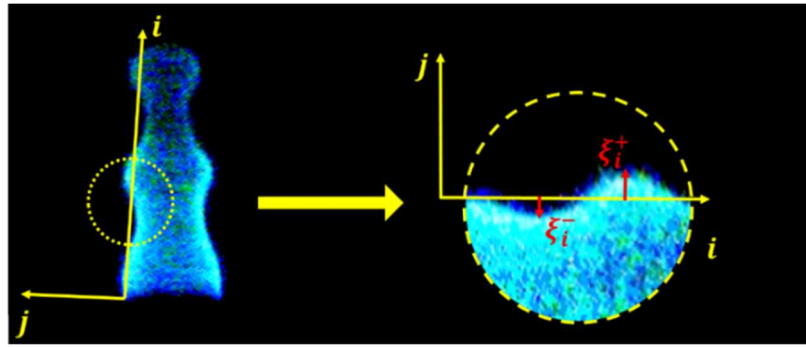


Figure 61. Schematic of the flame front configuration (a) and the wrinkle coordinates (b)

Figure 62 plots the instantaneous flame wrinkle spatial variation along the i/L_{stable} axis at four forcing conditions with sound pressures 10 Pa, 25 Pa, and 40 Pa, where L_{stable} is the unperturbed flame length. A clear expression for ξ_i^\pm is obtained in a normalised form by Equation 38. The plot clearly shows the displacement is growing with the sound pressure in each frequency excitation and more evident fluctuation is observed in the high forcing frequency group. Moreover, the fluctuation grows with the downstream distance.

$$\widetilde{\xi}_i^\pm = \frac{\xi_i^\pm}{|\xi_{max} - \xi_{min}|} \quad \text{Equation 38}$$

To achieve a clear view of the wrinkle perturbation and the propagation character, the results will be analysed from two aspects: the amplitude of the oscillation along the downstream direction and the frequency of wrinkle displacement at point 0.5 of the i/L_{stable} axial position under the four forcing frequencies.

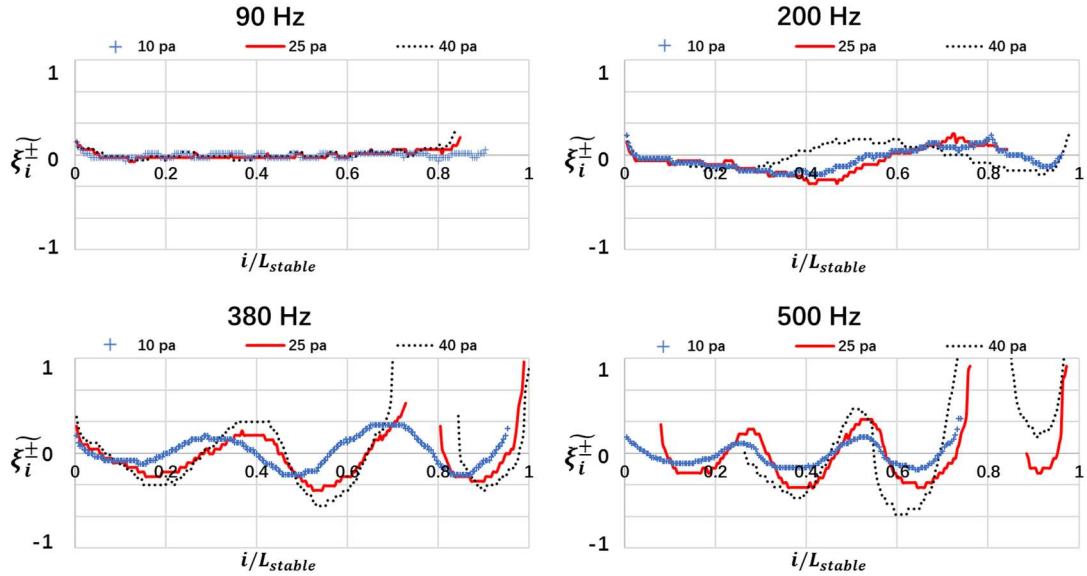


Figure 62. Instantaneous fluctuation magnitude of the sample flame front from each excitation group along the normalized i -axis

Figure 63. presents the fluctuation amplitudes of the flame wrinkle under each excitation condition, where the average amplitude of 2000 images in 1 s for each position on the downstream direction is calculated as the standard deviation by Equation 39.

$$\sigma_{\xi_i} = \sqrt{\frac{\sum_{n=1}^N (\xi_{ni} - \bar{\xi}_i)^2}{N-1}}, \quad (N = 2000) \quad \text{Equation 39}$$

The wrinkle amplitude on the vertical coordinate is given in a normalised form $\sigma_{\xi_i} / \bar{\sigma}_{max}$, showing that the perturbation effect grows with the axial position. The solid

lines calculated by linear curve-fitting for these points present a direct view of the amplitude growing trend. The result from the external excitation is opposite to wrinkle destruction behaviour when the flame wrinkle is induced by the flame base oscillation, as studied by Shin and Lieuwen [110]. The wrinkle size growth mechanism can be explained by the nature of coherent structures raised by Brown and Roshko in 1974 [130]. The value of the slope k is the indication of the wrinkle expansion rate. As can be obviously noticed from the graph, the increase rate of the wrinkle is not only promoted by the external induced sound pressure at the action point, but also the harmonic frequency value. In addition, under the higher forcing frequency, the growth rate of k with the sound pressure is more remarkable than those under the lower frequencies.

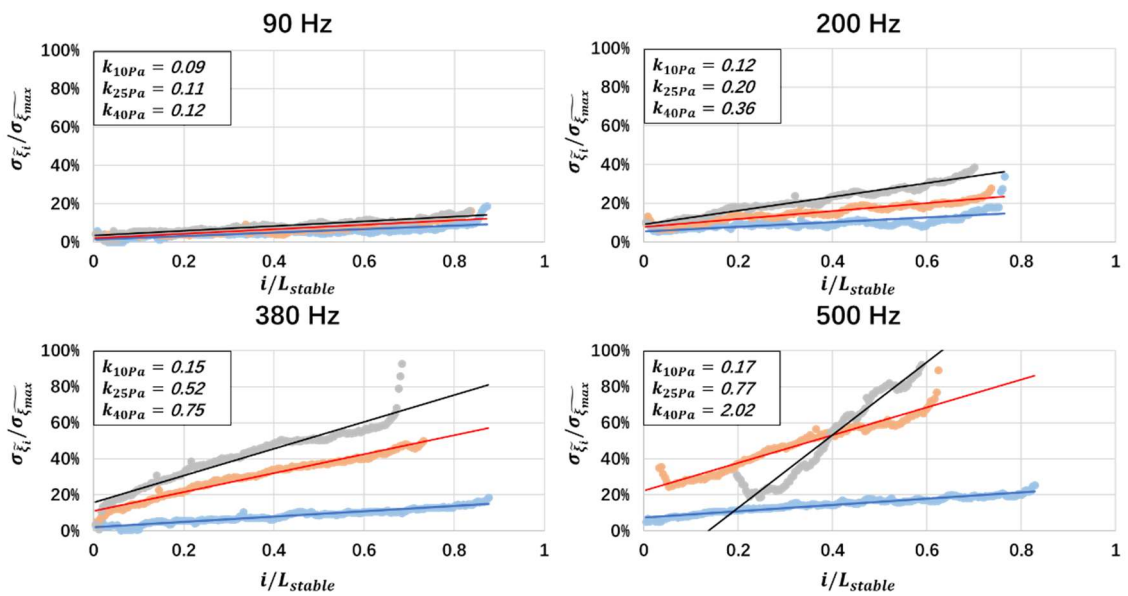


Figure 63. Fluctuation magnitude on downstream direction at different excitation cases

5.4.2.3. Flame Surface Area to Volume Ratio

The excited flame wrinkling line disturbance will be certainly bound by the flame

front volume and surface area. This phenomenon was mentioned in the previous study by Karimi et al. [94,129]. The method they used was to divide the entire flame into 10 equal segments. Assuming axisymmetry in each of the flame segments, the flame surface area was calculated through numerical integration, in which the rotation of each row of pixels bounded by the flame surface about the burner centre line generates a flame surface area element and a rectangular integration method is used to calculate the total flame surface area. Their result revealed that the time trace of this surface area disturbance under different forcing amplitudes closely resembles sine wave after 10th-order polynomial curve fitting.

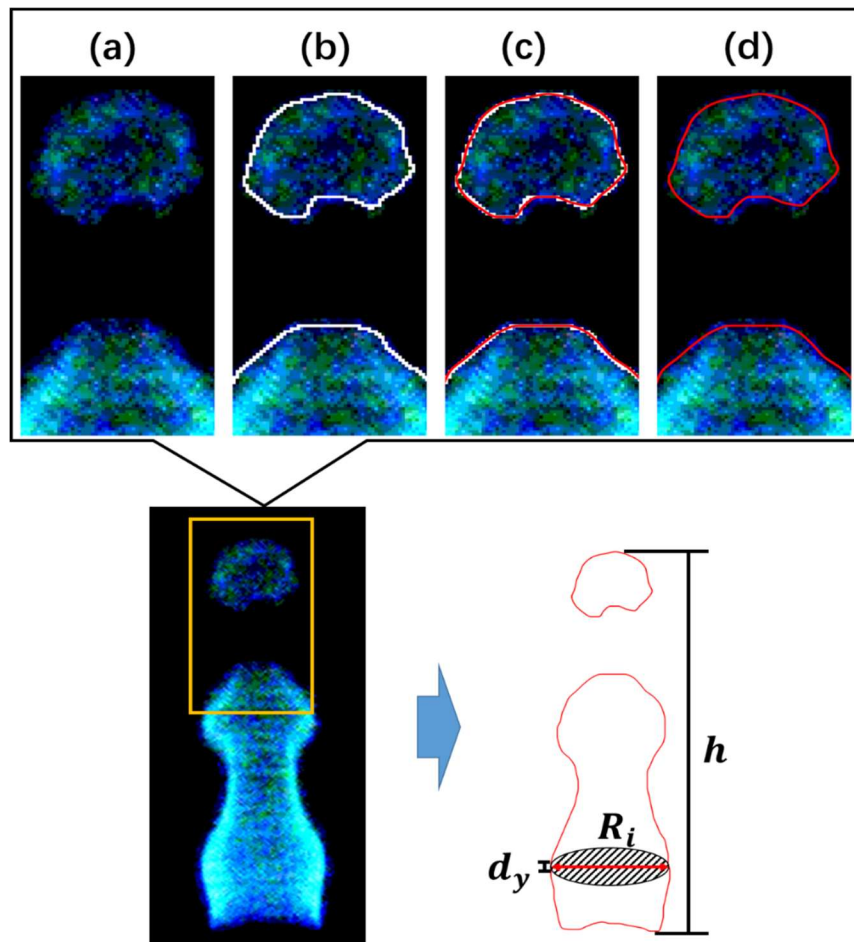


Figure 64 The refine perimeter of the excited flame front

Chapter 5 Acoustic Impact on Flame

However, the accuracy of the 10 equal segments was deemed insufficient to calculate the complex wrinkled flame front configuration. In this study, a more precise boundary detection program is applied. Figure 59 shows the refined perimeter of the complex wrinkled flame front and the discrepancy between the tentative and refined ones. The refinement, characterised by a smoothing of the boundary, gained through the application of the 10-point interpolation principle is clearly evident for the smooth boundary. Therefore, the following calculation will be more than 100 times precise than the results of Karimi [94]. The following discussion of the volume and surface area ratio is based on the refined perimeters.

The burning rate at a specific location increasing through flame wrinkling is simply due to the increase in the surface area mentioned in Law's book [130]. However, the flame envelop does not continually enlarge with the increase in sound pressure in the high-frequency range. This is mainly caused by the severe flame front volume shrinkage. Hence, the consequence indicated by Law can be described more reasonably by the surface area per unit volume.

$$a_{unit} = \frac{A}{V} \quad \text{Equation 40}$$

where

$$A = \int_0^h d_L = \int_0^h 2\pi r d_y = \int_0^h \pi R_i d_y \quad \text{Equation 41}$$

$$V = \int_0^h d_A = \int_0^h \pi r^2 d_y = \int_0^h \pi \left(\frac{R_i}{2}\right)^2 d_y \quad \text{Equation 42}$$

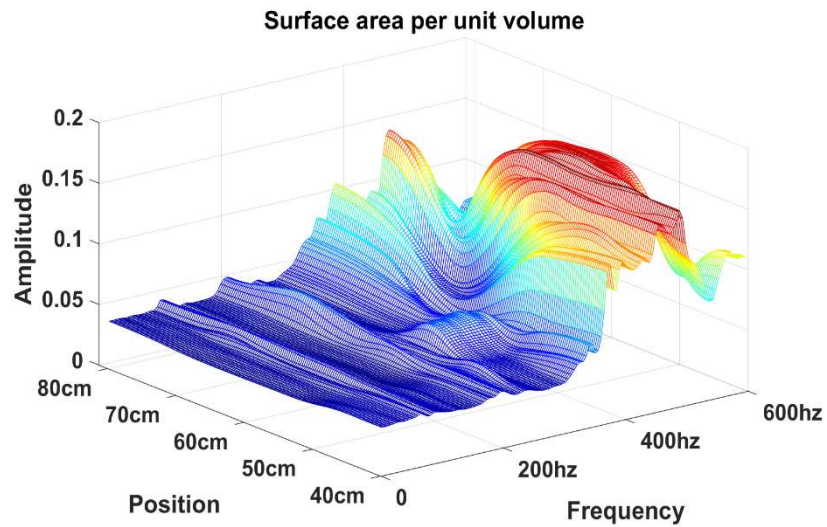


Figure 65. Surface area per unit volume along the tube under various excited frequencies

In Figure 65, shows a basic similarity between the value of the surface area per unit volume and the acoustic sound pressure level inside the tube Figure 52. Even at the first harmonic frequency, the embossment can be easily distinguished. The anomalous wave profile occurs at the 4th harmonic. Under these conditions, the flame was on the verge of extinction owing to the violent disturbance. The surface area per unit volume has expanded to the maximum limitation. Additionally, this shows evidently that at the low frequency, the flame surface area per unit volume does not have distinctive peaks, even at the high-sound-pressure locations. However, the effect at high frequency is obvious, even in the trough region.

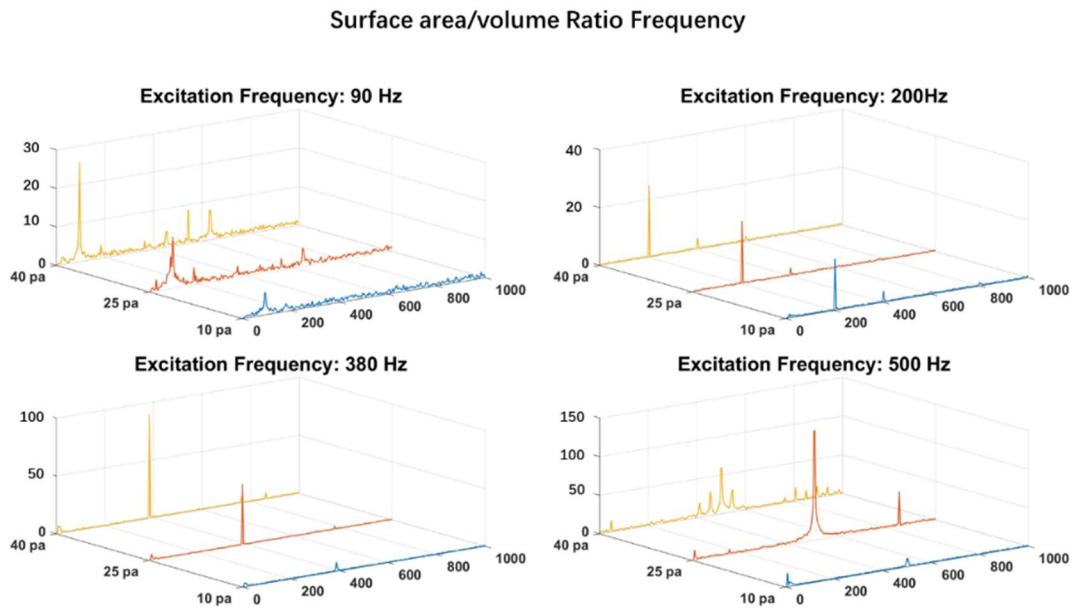


Figure 66 Surface area to volume ratio FFT

Figure 66 exhibits the distribution of the surface area to volume ratio in the frequency domain. Generally, the vibration of the surface area to volume ratio expressed great profile similarity to the flame intensity frequency. This denotes that the external acoustic excitation has a straightforward impact on the vibration of reaction surface area and volume character. In accordance with the previous study by Birbaud et al. [96], the vortices can promote the external air to entrain into the fresh mixture and the burnt gas in the quartz tube, which can contribute on diluting the fuel/air mixture and changing the equivalence ratio. The further analysis on the dynamics of the dilution behaviour and the changed equivalence ratio ϕ^* based on DFCD will be discussed in next section.

5.4.3. Flame Lifted Behaviour

External acoustic excitation induced lifted premixed jet flame is often observed in the combustion chamber and produces undesirable instability, including reattachment to the nozzle, lift-off flame, and hydrodynamic instabilities. The flame chemiluminescent

emission fluctuations and the vortex structure of the lifted jet flame under acoustic excitation were extensively studied in this investigation. By employing high-speed visualisation and the DFCD image processing method, the fluctuation of the instantaneous mixture fraction has been found to be highly correlated with the lifted height variation. Vortices in both the hysteresis region and the self-illuminated flame were clearly shown in the schlieren image. This clearly demonstrates that the highest stabilised position is most probable at the top of the second pairing of the coherent vortices. This behaviour can be further explained by analysing the velocity fluctuation of the symmetric vortices in the shear layer. The measurements show that the high velocities generated by the excitation lead to the flame lift-off. However, the vortices play a key role in preventing flame lift-off and diluting the flame, because they are able to roll-in more fresh air. The frequency of the reattachment and instantaneous mixture fraction fluctuation increase with the external excitation frequency. However, the excessive external acoustic excitation leads to blow-off due to over-dilution and increased lifted height.

5.4.3.1. Hysteresis Behaviour

The stabilisation mechanism that governs the dynamics at the flame base of lifted flames has been subject to numerical simulation and experimental investigation. When the jet velocity of the flame reaches a critical value U_c , the jet flame has a tendency to get lifted off from the burner rim and stabilise above it. This is a typical ‘pure liftoff’ phenomenon. The lifted height is called the hysteresis region. The lifted flame is unstable and can blow-off or extinguish at any time if the velocity is further increased, and the lift-off height increases beyond certain critical height. Thus, flame stability of the lifted diffusion flame is an important parameter for basic combustor design. Van Quickenborne and van Tiggelen [131] investigated the stability characteristics of lifted

Chapter 5 Acoustic Impact on Flame

methane jet diffusion flames in terms of lift-off height, HL, and found that the fuel and air are fully premixed at the base of a lifted diffusion flame. They presumed that the flame gets stabilised at the position where the mean flow velocity is equal to the burning velocity of a stoichiometric premixed turbulent flame.

Figure 67 (a) presents a sequence of photographs from the single-mirror schlieren setting at excitation frequency of 380 Hz and forcing intensity of 40 Pa to show the hysteresis region and the self-illuminated flame with a shutter speed 1/50 s at equal intervals. Under violent excitation, the periodic lift-off and reattachment process of the premixed flame can be clearly observed in the visible flame area. The motion is concurrent with the activity of the hot gas region.

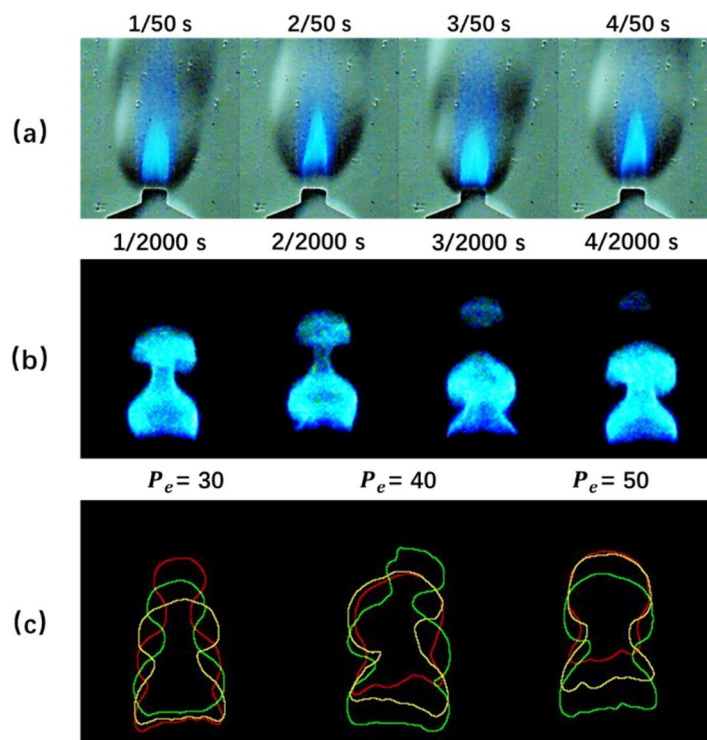


Figure 67 (a) Sequence of photographs from the single-mirror schlieren at shutter speed 1/50 s; (b) The samples of series colour images in successive 4/2000 s; (c) Three sequential samples of the flame front contour lines with 1/2000 s interval

To obtain a better observation of the periodically lifted flame behaviour, a higher shutter speed of 1/2000 s was used out for the visible flame imaging, as shown in Figure 67 (b). The samples of sets images in successive 4/2000 s display the visible flame front structure in the transition between lift-off and reattachment. Under the acoustic forcing, the flame front exhibits severe deformation with evident wrinkle fluctuation, separated flame bubbles and lifted-up flame base.

A Matlab-based contour detection algorithm was employed to define the conical flame front, and the extracted boundary lines are shown in Figure 67(c). The three sequential samples of the flame front contour lines with 1/2000 s interval from the 380 Hz frequency excitation case are drawn in each of the forcing pressure conditions, 30 Pa, 40 Pa, and 50 Pa. The root segment of the front exhibits a noticeable position shifting in the vertical direction. The contour lines illustrate that the fluctuating amplitude of lifted height continues to grow with the increasing perturbation pressure. In addition, the flame front exhibits an asymmetrically irregular geometry, which is similar to that mentioned by Bourehla et al. [127] and Gollahalli et al.[114]. These observations demonstrate that the lifted-off behaviour of premixed flame is sensitive to external excitation. The formation of hysteresis and reattachment processes are investigated and identified by its dominant flow characteristic in this experimental study.

The diagrammatic geometry of a 2D flame captured by the high-speed camera at a shutter speed of 1/2000 s with the selected colour enhancement technique by image processing is shown in Figure 68 (a). The red line presents the smoothing of the boundary gained through the application of the interpolation principle. The centre point (0, 0) of the coordinate system is located at the middle top of the nozzle, x is horizontal and increases to the right, and y is vertical and increase upward. The flame length H_f is defined as the nondimensional distance between the top point and the bottom point,

calculated by the number of pixels in y -axis direction, as shown Figure 68 (a). The lift-off height H_l is defined by the distance in the y -axis direction between the bottom point and the nozzle. The values of visible flame length H_f and the lift-off height H_l are the average of the 500 relevant images for each under forcing frequencies 380 Hz and 500 Hz and a variety of external acoustic forcing intensities, as shown in Figure 68 (b). The measurement of sound amplitude ranges from the initial sign of lift-off to the blow-off point. Therefore, the amplitude ranges for the forcing frequencies 380 Hz and 500 Hz depended on their resistance to blow-off, 22–50 Pa and 2–30 Pa, respectively. The flame lengths H_f exhibit a descending trend for both frequency groups. The error bars represent the standard deviation of flame length fluctuation amplitude.

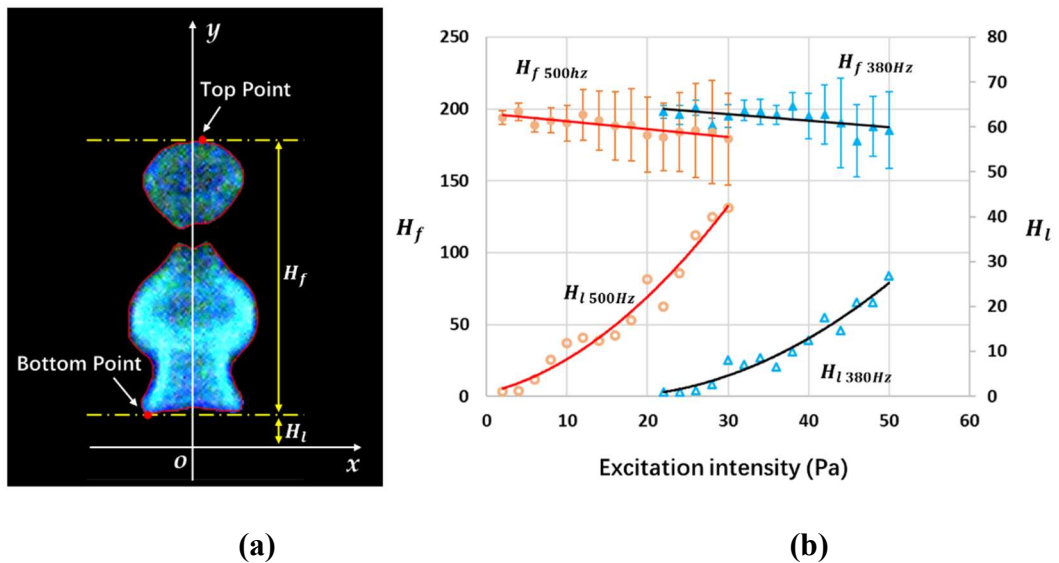


Figure 68 Variation of flame height H_f and lift-off height H_l of acoustically excited flame

As can be obviously noticed from the graph, the external sound pressure promotes the flame length fluctuation. This is mainly caused by the growing flame lifted height combined with the generation of separated flame bubbles. Moreover, the growing rate of flame lifted height from 500 Hz frequency excitation is higher than that from 380 Hz

frequency excitation, which indicated the premixed flame is prone to be disturbed and quenched suddenly under the condition of high-frequency acoustic perturbation. The observation is in contrast to the results of the non-premixed flame reported by Chen [103].

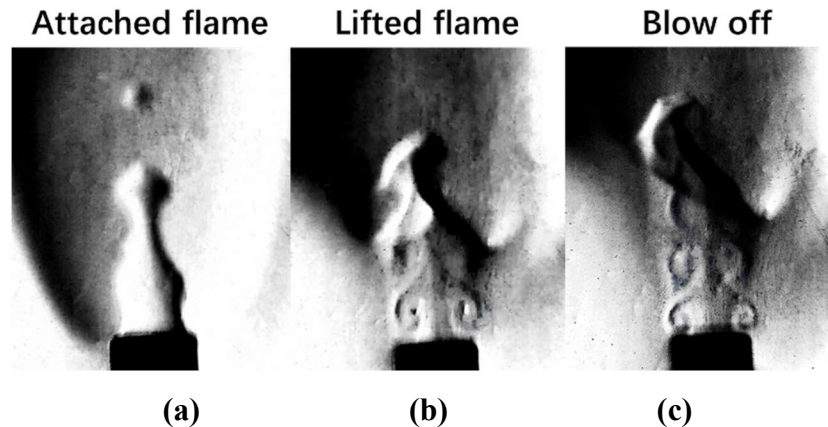


Figure 69 Sample schlieren pictures for three perturbation conditions

Figure 69 presents the sample schlieren pictures at the salient feature point for each of three sound perturbation conditions at 380 Hz, including attached flame (20 Pa), lifted flame (35 Pa), and blow-off (50 Pa). Although the vertical orientation of the knife edge is only sensitive to the radial density gradients, the vortex structure caused by the Kelvin–Helmholtz instabilities become visible on the unburn jet shear layer near the nozzle.

At the low-sound-amplitude level, the configuration of the flame front presents as a wavy boundary before flame is lifted. With the increase in the external perturbation, the waves overturn the are in the vicinity and grow into billows in the unburning hysteresis region, which leads to the intermittent flame holding. In the burning flame part, the convolution structure becomes distorted and gradually dissipates. This is because the formation of the vortices structure is suppressed by the presence of the flame according to the studies by Gollahalli [114] and Chao [119]. The observations of the massive

schlieren pictures demonstrate that the highest stabilised position is most probable at the top of the second pairing of the coherent vortices. Further increasing the sound pressure level causes severe interference of the surrounding air and fuel. The excessive re-entrained cold fresh air from the vortices cools down the hot products, which results in hinderance of sustainable burning, reduction in heat release [132] and eventually flame extinction. During the blow-off procedure shown in Figure 69 (c), the organised streamwise vortex pair gradually spreads to larger-scale structure further downstream, which is in accordance with the observation by Demare et al. [56].

5.4.3.2. Nonlinear Coupling of Lifted Flame and Acoustic Wave

Figure 70 (a) shows a sequence of colour images for the flame in the transition cycle process of attachment, lift-off, and reattachment. The successive frames are at equal intervals 2 ms. According to the coordinate system established in Figure 68, the trajectories of the visual flame lifted height, showed in Figure 70 (b), was recorded at 2000 fps over 100 ms. As obviously shown in the graph, apart from the oscillations between lift-off and reattachment, there was another high-frequency oscillation throughout the period.

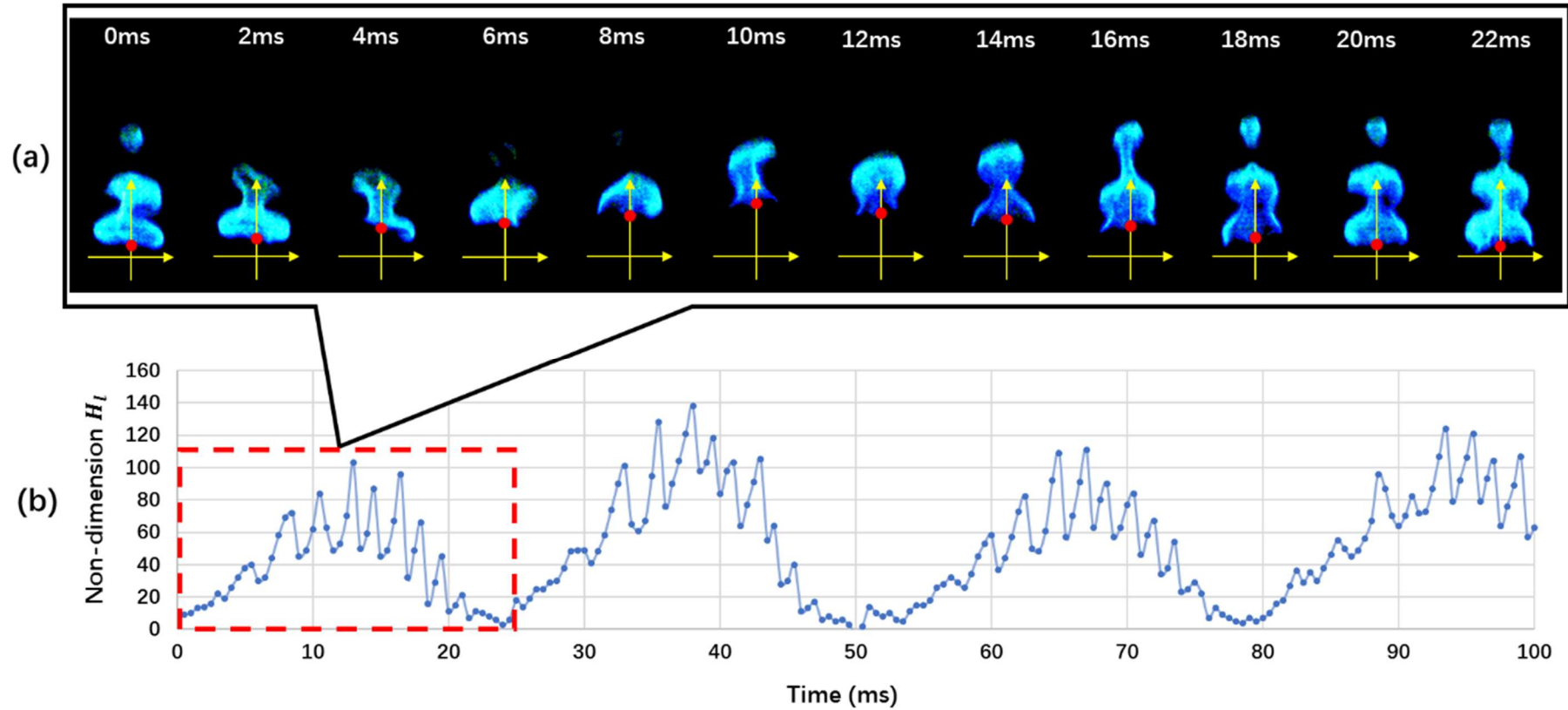


Figure 70 (a) Colour images for cycle of attachment, lift-off and reattachment; (b) The trajectories of the flame lifted height

Chapter 5 Acoustic Impact on Flame

To determine the principle of the oscillations, a low-pass FFT filter was applied to the data of various acoustic intensities from the two frequency cases, as shown in Figure 71. The FFT graph illustrates the dynamics of lifted height under various acoustic perturbations. The frequency components perform differently at the different external excitation frequencies and intensities. Demare and Baillot [56] claimed that the lifted-off height fluctuated randomly despite being subjected to periodic forcing. However, as shown in the results, generally for all the cases, the nonconstant value of lift-off frequency f_L dominates the flame dynamic in the range 20–40 Hz. This indicates that the fluctuation of the lifted height is not random, but it is difficult to determine the discipline for the exact frequency, which relates to the formation conditions of the Kelvin–Helmholtz vortices and flame burning speed. The excitation frequencies f_e show more evident peaks under the lower acoustic forcing intensity. No natural flame flicking frequency can be detected, which indicates that the buoyancy driving force does not have an effect on the flame lifted fluctuation at this low jet velocity ($Re = 557$).

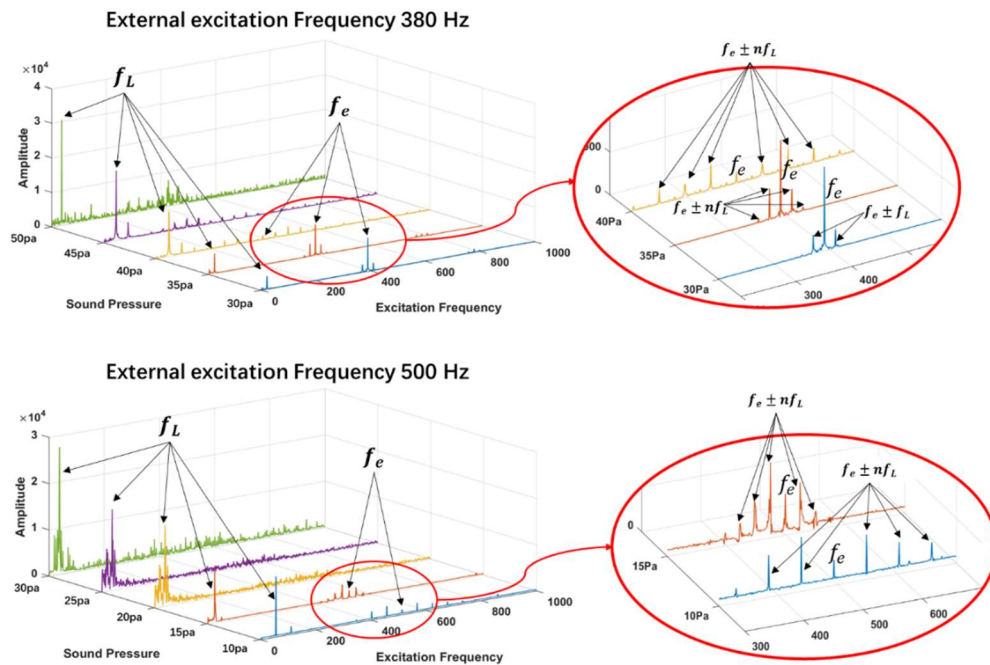


Figure 71 Frequency of the lifted height for various acoustic excitation conditions

At the mild excitation amplitude in both cases of 380 Hz and 500 Hz, the sets of the fore and aft peaks that accompany the dominated and harmonic frequencies $f_e \pm nf_L$ have been detected. The sets of accompanied fore and aft peaks $f_e \pm nf_L$ are explained by nonlinear coupling theory, which was recently reported by Chen and Zhang [103]. The two frequency components can be simplified into wave signals, as shown below:

$$Y_{Excitation}(t) = x_e \sin(w_e t) \text{ and } Y_{Lifted}(t) = x_L \sin(w_L t) \quad \text{Equation 43}$$

The nonlinear coupling results in the creation of the frequency component as:

$$Y_{coupling}(t) = k \sin(w_e t) \sin(w_L t) \quad \text{Equation 44}$$

This can then be broken down into the following equation:

$$Y_{coupling}(t) = \frac{k[\cos(w_e - w_L) t] - [\cos(w_e + w_L) t]}{2} \quad \text{Equation 45}$$

Hence, this is the main explanation for the nonlinear coupling relationship of $f_e \pm nf_L$. Therefore, the flame oscillated in both the i-axis and j-axis directions and the result illustrates the coupling frequency of both directions.

The stabilisation mechanism of the vortices has been reported by many researches [133,134]. These researchers noticed that for the lifted flame, at the hysteresis region, the vortices play an important role for the flame stabilisation and reattachment. It is well-known that when the jet velocity U_{jet} is higher than the burning velocity U_{burn} , the flame detaches itself from the nozzle and stabilises at the position where $U_{jet} \approx U_{burn}$ in the downstream region. The lifted height is unstable, as the hysteresis zone is

vulnerable to the external interference. Contrary to the weakly excited case, after the flame lifted off, the relative velocity field condition reversed, the velocity of the unburned jet flow is much higher than that of the ambient air, and the velocity disparity results in the formation of Kelvin–Helmholtz vortices. This observation agrees with the results of Chao [119] and Demare [121]. Chao et al. claimed that the local velocity of the vortex core region is higher than the natural jet, but the outer edge of the layer and the mean velocity of the travelling wave has been dramatically decreased. Therefore, the rolling-up vortices effectively prevent the lifted flame from propagation upstream. Demare and Baillet presented the velocity field of both the vertical and the horizontal views. They found that the vortex radial velocity of the excited jet is nearly half of the natural jet and the root-mean-square value is 25% lower. Therefore, the Kelvin–Helmholtz ring structure provides a suitable circumstance for the flame reattachment. Moreover, these vortex structures not only minimise the velocity disparity at the shear layer, but also promote the further mixing between the fuel and the ambient air. The mixture fraction will be further analysed by the DFCD image processing method applied to flame chemiluminescence.

5.4.4. Flame Chemiluminescent Radiations Measurement

The bottom of the tube is not sealed, and fresh air can continually enter the tube, although it is considered to be acoustically closed. Based on Chen’s previous study [6], the evidence shows that the circulated fresh air is sufficient to keep the pure diffusion flame burning continuously.

The behaviour of the acoustic perturbation diluting the fuel/air mixture has been mentioned and verified by many researchers. In the laminar premixed condition, the flame front colour changes from greenish blue to pure blue, as can be clearly noticed

directly by eye from the sequence of the dynamic flame images under different external acoustic excitation conditions in Figure 56. This is because the C_2^* radicals, perceived as green colour by human eyes, would be more likely to be generated under fuel-rich mixing conditions. In this section, a quantitative parametric investigation based on the DFCD approach will be presented.

The experimental data measured by Gu [135] proved that burning velocity for premixed flame reaches its maximum value when the equivalence ratio is approximately 1. In addition, Walchshofer concluded that the lifted flame is stabilised close to the surface stoichiometric mixing conditions [136]. In other words, the premixed flame at the equivalence ratio 1.4 preferably drifts towards the relatively fuel-leaner side. Hence, the DFCD method has been implemented in the present work to evaluate the distribution of fuel concentration, which was introduced in Huang's previous studies [106] and applied to both gaseous [137] and liquid combustions [138].

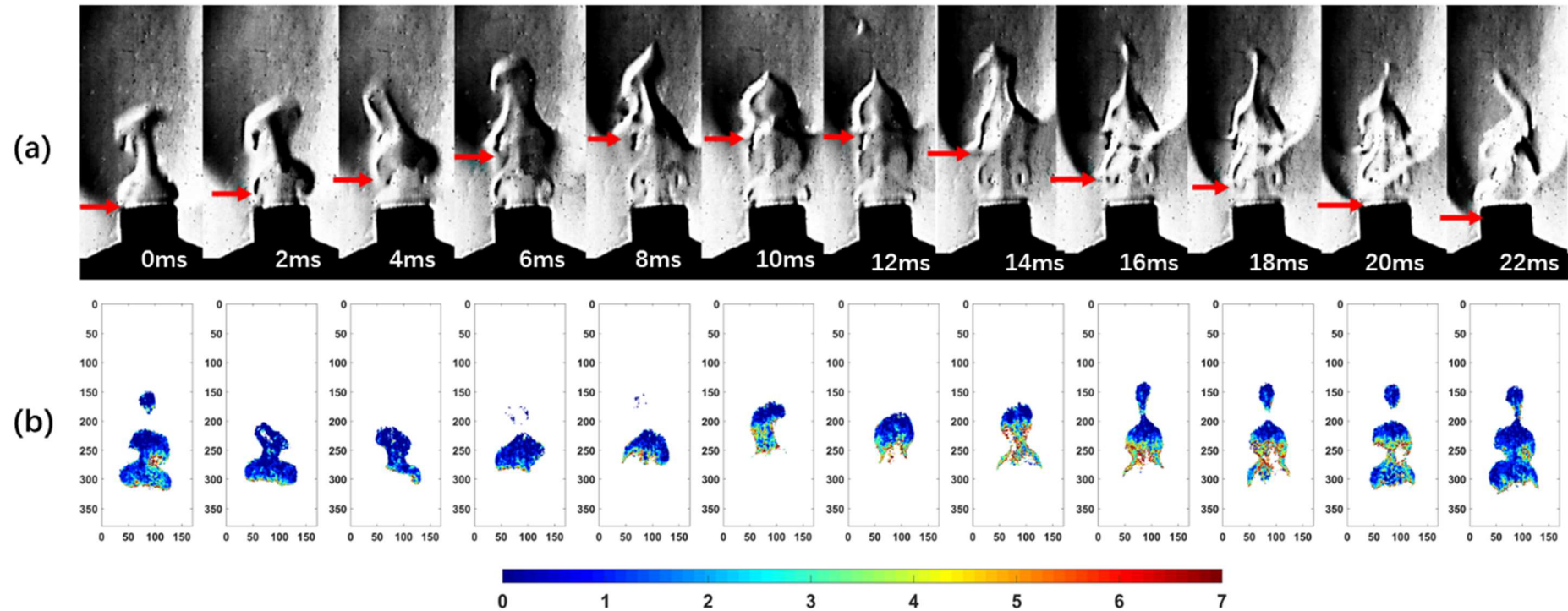


Figure 72 (a) Schlieren images for flame and jet flow structure during the lifted and reattached process; (b) Instantaneous calculated $CH^*/C2^*$ ratio colour map

The CH^*/C_2^* ratio has been proved to have a linear relation with the equivalence ratio. It can be regarded as an indicator to reveal the fuel mixing fraction level, in which the fuel-lean flame has higher CH^*/C_2^* ratio and high-fuel concentration flame has a lower CH^*/C_2^* ratio. Figure 72 (a) shows the sequence of schlieren images for the flame lifted and reattached cycle process with 2 ms intervals. The Kelvin–Helmholtz rolling-up structure can be clearly recognised in the unburn jet region above the nozzle when the flame lifted. Figure 70 (b) presents the instantaneous colour map of the calculated CH^*/C_2^* ratio of the corresponding images. The ratio ranges from 0 to 7 and displays the colour from dark blue to red. As the flame propagates downstream, the flame area gradually decreases, but there is no evident change in the fuel concentration and most of the flame area is exhibited as dark blue. As soon as the flame lifted to the highest position, the reddish and yellowish colour gradually emerges at the bottom section, which indicates that the vortex-up configuration enhances the mixing between the fuel and the surrounding air.

The dilution effect of the vortex structure has been reported by many others' studies [139–141]. During the falling period, the lifted flame propagates upstream as a result of vortices-induced local lower mixture fraction, which is consistent with flame propagation preference. It is worth noting that, apart from the predominant distribution zone of the reddish and yellowish points at the bottom region of the flame, it also occurs at the core of the vortex. Therefore, based on the discussion above, the upstream propagation behaviour of the acoustic excited lifted flame could be explained by the rolling-up vortices stabilisation mechanism and local mixing enhancement.

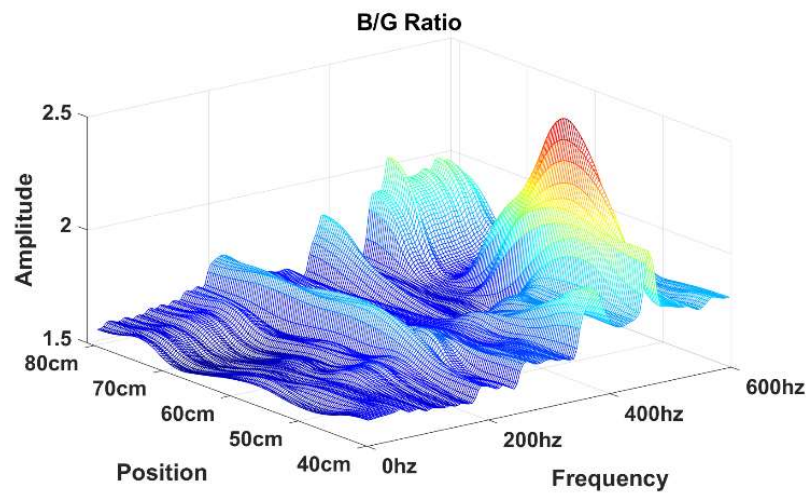


Figure 73 CH^*/C_2^* ratio along the tube under various excited frequencies

Hence, according to its similar feature as the Figure 65, the dilution effect is mainly contributed by the enlarged surface area to fresh air. The wave profile of the B/G ratio has a similar trend to the acoustic response in the tube, especially at the third and fourth harmonic frequency. In other words, under the 380 Hz and 500 Hz external acoustic excitations, the mixture of the flame has been diluted strongly in accordance with the local sound pressure. However, at the low-frequency range, the effect can be barely identified. This indicates that the mixture disturbance behaviour is not sensitive to the sound pressure fluctuation at low frequency.

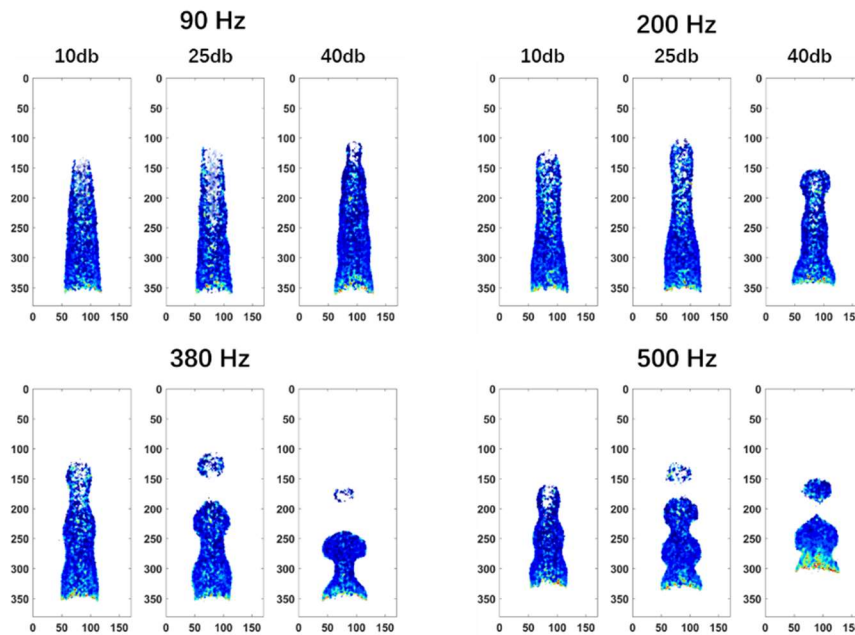


Figure 74 Sample of post-processed images to give CH^*/C_2^* ratio distribution at the various sound intensities condition of each frequency group

The calculated CH^*/C_2^* ratio instantaneous distribution provides a better view to understand the performance of acoustic impact on the flame. In the colour map shown in Figure 74, one flame sample image has been randomly chosen from each circumstance, with the ratio ranging from 0 to 10 and displaying the colour from dark bluish to red. At the low-disturbance condition, dark blue is uniformly distributed over the whole flame area. With the increase in the intensity and resonance frequency, yellow and red spots appear at the bottom of the flame, which spread out the area in the high-frequency group, and the subgenerated flame bubble is more likely to turn to a greenish colour. This provides particularly local insight into the fuel/air dilution behaviour trend.

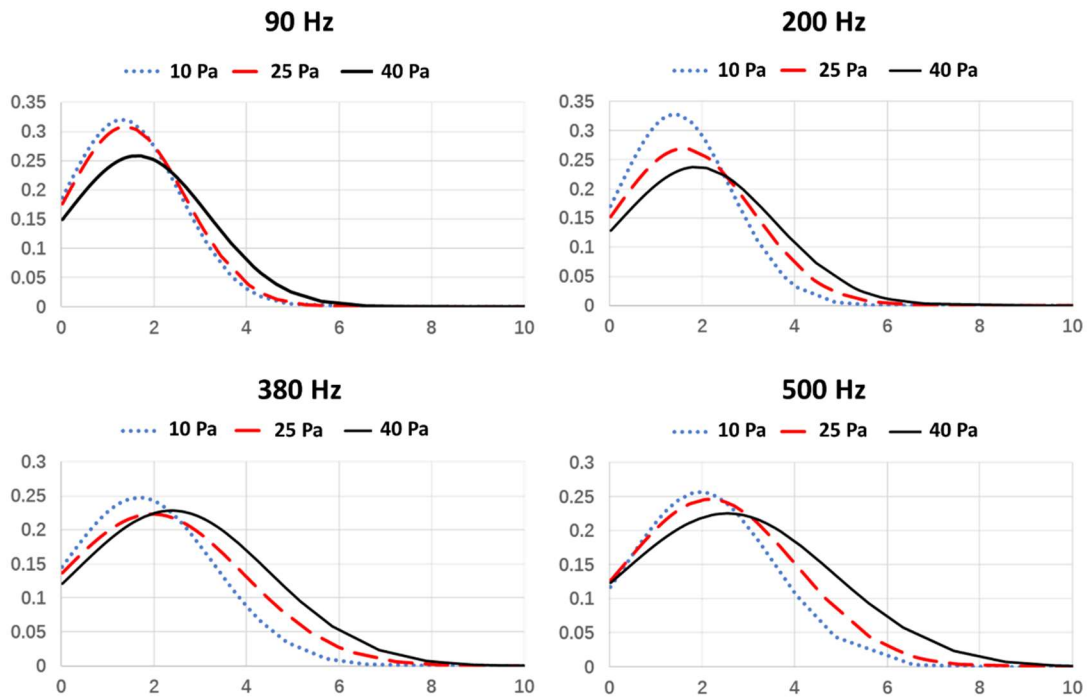


Figure 75 6th order polynomial curve fit Gaussian distribution CH*/C₂* ratio for various acoustic excitations

Referring to the previous study by Yang on the B/G ratio Gaussian distribution calculation, with the increase in the equivalence ratio, the peak gradually moves to higher B/G ratio [78]. As the plot in Figure 75 shows, in each external excitation group, the wave moves to higher B/G ratio with the increase in the sound intensity. Comparing the plot in the column by the acoustic frequency group, the waves show the left-moving trend towards higher B/G ratio. This presents a clear variation tendency induced by the acoustic perturbation, which means both the sound pressure and the exciton frequency contribute evidently to the mixture dilution caused by the external acoustic excitation.

As the colour contour map distribution is conducted with a single image, avoiding the overgeneralisation errors, the average of CH*/C₂* ratios of 4000 images in 2 s at the nozzle under each acoustic condition were calculated and compared in Figure 76. The

Chapter 5 Acoustic Impact on Flame

dotted, dashed, dash-dotted, and solid lines represent the external excitation frequencies of 90 Hz, 200 Hz, 380 Hz, and 500 Hz respectively, and the error bar indicates the standard deviation of the ratio of the 4000 images. All four lines present a growing trend with the increasing the sound volume, but with various growth rates. The solid line is constantly above the other three and the dotted line at the bottom barely increases during the whole operation. This indicates that the frequency plays a substantial role in the fuel/air dilution. The ratios of the two low-frequency cases grow slightly when the sound intensity continually increases, whereas the solid line and the dash-dotted line maintain their growth rates. The growth rate bends from 25 Pa to 40 Pa, which indicates that the dilution trend is nonlinear.

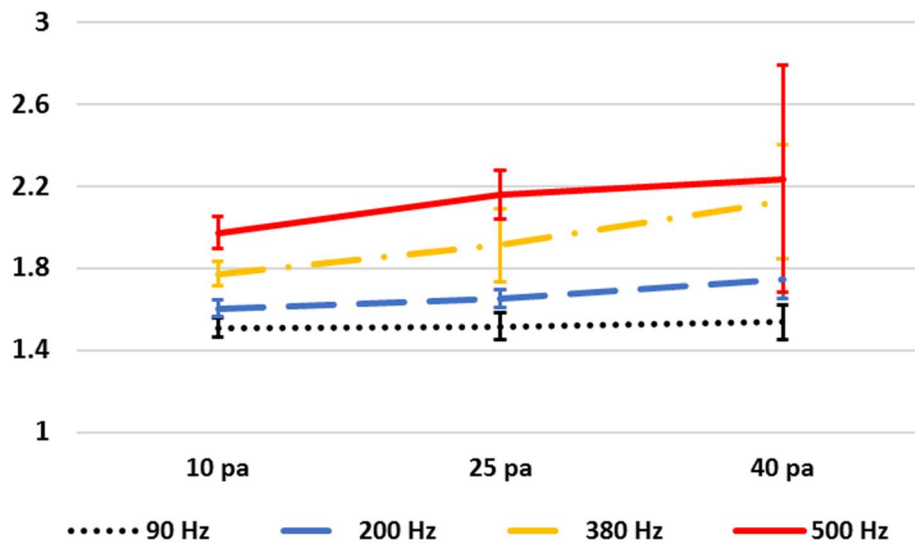


Figure 76 Comparison of the average CH^*/C_2^* ratio

By combining these results with the previous analysis, the reasons for the dilution can be inferred. For the lower forcing frequencies 90 Hz and 220 Hz, the calculated CH^*/C_2^* ratio and the surface area to volume ratio share the same trend, which indicates the mixture changing is mainly owing to the larger reaction area with fresh air induced by the vortices. This principle is also applicable to the case of 500 Hz at the low sound

amplitude of 10 Pa. However, for the high sound amplitude, the large standard deviation is not only caused by the shrinkage or expansion of the flame front area resulting in a less linear increase rate, but also from the lift up phenomenon providing the opportunity for the fresh air to enter into the unbound zone and keep the CH^*/C_2^* ratio at a relatively high level.

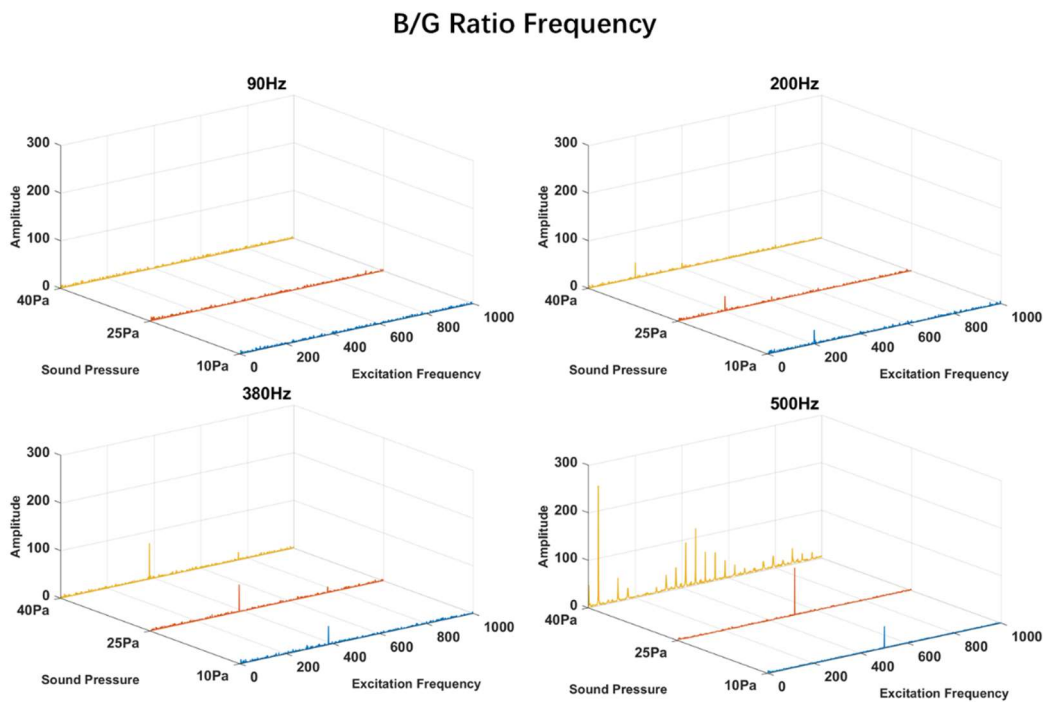


Figure 77 CH^*/C_2^* ratio FFT

Another phenomenon that must be mentioned is that the increase in the standard deviation with the magnification of the sound intensity can be noticed evidently. That means that the vibration range of mixing level has been enlarged by the sound intensity. Further study will concentrate on the fluctuation of the ratio to determine the ratio changing characteristics influenced by the acoustics.

Figure 77 demonstrates the changing principle of the fuel/air dilution level. At the low excitation condition, no evident peak can be identified as the primary frequency.

However, under the excitation condition, the peak frequency is obvious, and the dominant frequency and secondary generated frequencies are identified with the excitation frequency. A comparison with the results in Figure 57 shows that the frequency profile obtained from the CH^* / C_2 ratio resembles that from flame intensity and the observation of harmonic behaviour investigation remained consistent. In particular, the complementary frequencies peak at $f_e \pm n f_f^*$ at intensive excitation condition are also very evident. This indicates that the flame lifted-up behaviours contribute significantly to the fuel/air mixture changing. Nevertheless, the external excitation frequency not only dominates the flame intensity frequency, but also exerts a noteworthy impact on the frequency of flame fuel/air proportion level.

5.5. Conclusion

This study has shown that a premixed flame is sensitive to the frequency of acoustic perturbation. The investigated flame features include the flame wrinkle fluctuation frequency, amplitude, surface area to volume ratio, and acoustically induced dilution behaviour.

- On the whole, it has been observed that the frequencies of the measured properties match exactly with excitation frequencies, and their amplitudes show a similar trend to the sound pressure standing wave in the tube. This indicates that the various features of the flame correlate well with the acoustic disturbance.
- Furthermore, the lower excitation frequency has less impact on the all analysed aspects of flame features, regardless of the sound pressure. The higher excited frequency will induce more severe disturbance and produce more evident changes, especially with respect to the surface area to volume ratio and dilution behaviour. Under the intensive perturbation condition, the nonlinear frequency response can be

explained by the involvement of the lift-off behaviour.

- For flame configuration, the wrinkle amplitude shows an increasing trend along the downstream direction under external excitation condition. Both the external forcing frequency and the sound pressure on the action point have a positive effect on the flame wrinkle amplitude growth rate. The growth rate presents a linear trend with respect to the axial distance.
- For the lifted flame features, the premixed flame is prone to be disturbed and can be extinguished suddenly under high-frequency acoustic perturbation. The fluctuating amplitude of the lifted height continues to grow with the increasing forcing pressure.
- The external forcing pressure promotes the flame height fluctuation owing to the appearance of the separated flame bubbles.
- The Kelvin–Helmholtz ring structure forms at the unburnt jet boundary near the nozzle when the flame lifts off, thereby intermittently stabilising the flame. However, the flame will blow off eventually under the severe turbulence stretching, because the excessive re-entrainment of the cold fresh air cools down the hot products and the flame fails to be sustained.
- Under the low forcing sound pressure, the nonconstant value of lift-off frequency f_L is nonlinearly coupled to the external excitation frequencies, whereas under the low forcing sound pressure, the vortices dominated the lifted height oscillation.
- Before the flame lift-off, the relative velocity in the flame shear layer increases with the increase in the sound amplitude. After the flame lift-off, the intensive vorticity region concentrates in the Kelvin–Helmholtz rolling-up region, thereby reducing the velocity disparity and providing a suitable environment for flame reattachment.
- A moderate fresh air entrainment along with the Kelvin–Helmholtz vortex structures dilutes the mixture fraction. The premixed-flame burning speed and propagation preference drag the flame back to the nozzle.
- For flame dilution behaviour, both the surface area per unit volume expansion and

Chapter 5 Acoustic Impact on Flame

flame lift-off can promote the further mixing of the fuel and air. However, the surface expansion has a limitation and excessive lifted height will quench the flame.

6. Gas Turbine Combustion of Fuels Evaluation

6.1. Introduction

The tremendous expansion of the aviation demand, combined with the energy crisis and the stringent environmental pollution limitations, has been the challenge and the driving force for the aeronautic combustion research. Therefore, revolutions in both the modern aeronautical gas turbine and alternative fuels are ongoing. New aircraft designs have been investigated by many research programmes [142]. However, it is difficult to achieve the low emission goal in the short term, owing to the long research and development cycle and slow replacement rate of older inefficient aeroplanes with newer models [143]. Alternative fuels offer the potential to provide immediate benefits.

Towards the widespread application of the alternative fuels, the test campaign aimed to guarantee that reliable combustion performance and acceptable emission profiles of the alternative fuels are compatible with infrastructure and operating conditions.

The University of Sheffield's Low Carbon Combustion Centre (LCCC) is an allied partner in the National Jet Fuels Combustion Program (NJFCP), which is a US multi-agency program led by the Federal Aviation Administration (FAA). The project aims to gain a better understanding of the effect of alternative jet fuel on engine combustion with

collaborations between universities, governmental research agencies, and engine manufacturers. [144]

6.2. Background Knowledge

6.2.1. Flame Stability in Jet Engine

Most of the modern civil aviation aircraft are powered by the gas turbine engine with turbofans, and some use turboprops. In a gas turbine engine, the fuel is ejected from the nozzle into the combustor chamber and the nozzle is surrounded by a compressed air vent. The air has been compressed in a compressor before reaching the vent. At the moment when the fuel is injected into the chambers, the fuel has been atomised into millions of small droplets by the strong impact force of the compressed air flow. The atomised fuel burns in the chamber and releases hot gases to power a turbine shown, as in Figure 78[145].

In petrol or diesel engines, the fuel needs to be periodically lighted, whereas the flame in a jet engine is continuously burning in the combustor, as shown in Figure 79. Therefore, the flame stability is an extremely crucial factor for the fuel evaluation because once the flame is extinguished, the aircraft is flying without power, which is the last thing we may expect. This scenario can lead to power loss and fatal consequences, especially if the engine cannot be re-lighted in time. All modern jet engines have been designed to be suitable to operate with conventionally sourced fuel. Hence, the new candidate fuels have to be proven safe enough for use in conventional engines and their performance in terms of flame stability must be well studied.

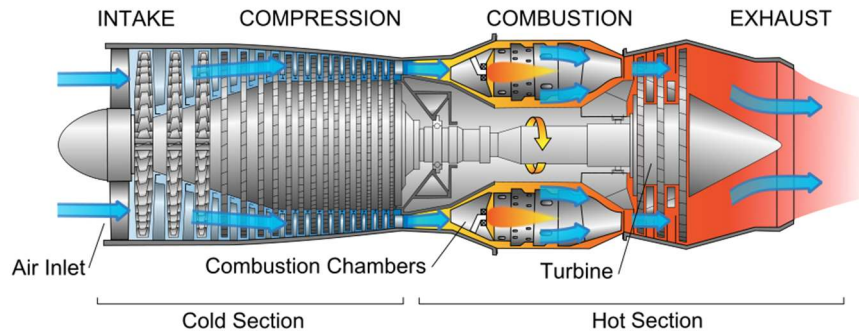


Figure 78. Basic components of a gas turbine engine

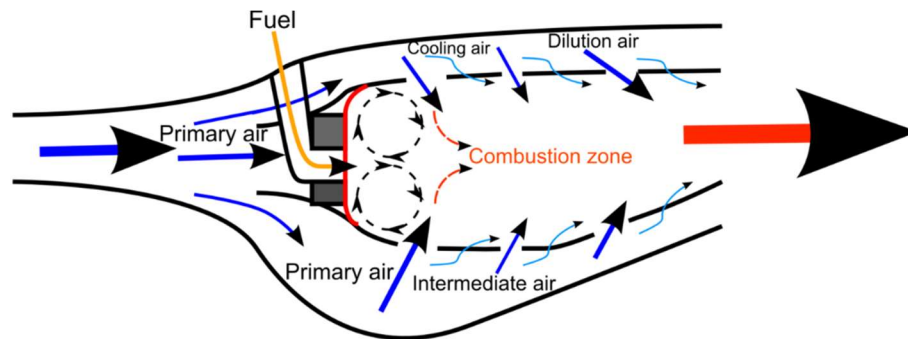


Figure 79. Diagram of air flow paths in a gas turbine combustor[146]

In a premixed combustible gas mixture in a chamber, most of the fuel is only combustible in a limited range of equivalence ratios, from approximately 0.5 to 3, because the flame cannot propagate well if the mixture is too lean or too rich [147]. However, the range is not very restricted. The limitation of the flammability varies with the operating pressure and temperature in the chamber. For the liquid fuel combustion, volatility, which is the vaporisation tendency of the fuel, is affected by the fuel composition, and temperature are important factors determining the flammability limits, because they directly alter the fuel–air mixing.

According to the measured mass flow rate of air and fuel into a jet engine combustor, the given air/fuel ratio for the whole rig can be calculated, but practically the liquid fuel

and air will not be mixed as perfectly as the gaseous fuel and air do. Therefore, the realistic results vary significantly for different fuels throughout the combustor [147]. As candidate fuels are developed to control the particulate emissions and improve combustion efficiency and reducing NO_x and particles emission, this leads to greater concerns regarding the LBO performance.

6.2.2. Lean Blowout Detection Method

In the aviation sector, there are far greater restrictions on any candidate fuel to provide high-level reliability and stable combustion during operation [147]. In order to reduce pollutant emissions, it has to narrow the stability limits and attain a satisfactory LBO performance. The blow-off events increase engine maintenance cost and may even be fatal in an aircraft engine, particularly during landing [148]. Accordingly, the LBO performance is one of the major considerations for the evaluation of fuels [6–8].

The parameters related to the combustor configurations and burning condition have large impacts on the LBO limit [149], including inlet flow velocity, equivalence ratio, bluff body geometry, inlet temperature, and stratification [152]. Based on Lefebvre's theory [153], , the LBO fuel/air ratio is mainly dependent on the combustor geometric, thermo-fluidic, and fuel property terms, as shown in Equation 46. The effects of the candidate fuel properties on the combustion performance are investigated in this study.

$$\text{LBO fuel/air ratio} \propto \left[\frac{f_{pz}}{V_{pz}^{(1+x)}} \right] \left[\frac{\dot{m}_A^{(1+x)}}{P_3^{(1+nx)} \exp(xT_3/300)} \right] \left[\frac{D_0^2}{\lambda_{effLCV}} \right]$$

Geometrical
Term

Thermo-Fluidic Term

Fuel Property
term

Equation 46

Owing to the intrinsic transient nature of the LBO process, many complicated

diagnostic systems have been exploited to provide real-time monitoring of these quantifiable dynamic characteristics. The preliminary LBO prediction relied on pressure drop or fluctuation in the combustion chamber as claimed by Snyder et al. [154] and Lucenko et al. [155]. Lee and Santavicca [156] used Piezo-electric transducers to diagnose the heat release. Li et al. developed a novel tuneable diode laser temperature sensor to acquire the temperature fluctuations [157]. The most common methods are based on the acoustic detection and optical emission measurements [158–161]. Nair and Lieuwen demonstrated the feasibility of acoustic monitoring with a fast diagnostic technique on the LBO' signature description [162].

The optical approach through narrow or broadband, filter, high-speed colour imaging based on emission is a suitable alternative nonintrusive diagnostic method to determine valuable dynamic combustion parameters [75,108,163,164]. Flame luminosity is one of the easily observable main features, and each flame has its own spectrum of luminosity that can be used to characterise combustion process [66]. An infrared sensing high-speed camera has been utilised to determine the thermo-instability of LBO [165]. Planar laser induced fluorescence (PLIF) has been applied as a tracer for fuel-mixing oscillations [118]. The simultaneous stereo-PIV and OH-PLIF measurements have been implemented by Stöhr et al. [166] to observe the unstable vortex and gas mixing near LBO. An OH* chemiluminescence LBO prediction technique based on UV high-speed imaging has been implemented on the active safe-operation control system [167–169]. In the visible spectrum range, flame luminosity is attributed to the spectra emitted from the electronically excited radicals CH* and C₂* [170,171], in addition to the soot continuous spectrum. Chaudhari et al. proposed a LBO prediction strategy according to the flame colour change from reddish to bluish. In experimental work conducted by Fujino et al. [50] and Jiotode et al. [49], visualisation techniques provide time-resolved imaging data in the combustion chamber to analyse

flame temperature distribution and combustion efficiency. Botero [172] correlates the visual sooty flame height with soot particles mass to analyse the paraffin impact on soot tendency. Later, he also studied optical soot formation induced by aromatic fractions via luminous temperature and particles size number [173]. Witkowski [174] provides an experimental diffusion flame soot propensity model by combining the LII and soot profile, collected using transmission electron microscope (TEM) imaging.

The digital flame colour discrimination (DFCD) approach developed by Huang and Zhang [105,106,175,176] shows that the instantaneous flame mixture condition can be directly represented in flame colour. The optical detection method and imaging post-processing provide a non-intrusive and alternative approach for monitoring the instantaneous soot formation behaviour of liquid fuel combustion [138,177].

In this context, this chapter aims to investigate LBO limit with alternative fuels and their characteristic flame properties on a Rolls-Royce Tay combustor rig. High-speed colour imaging has been applied to capture flame features of various fuels. The DFCD post-processing methodology was implemented via Matlab for the analysis of flame features based on the soot concentration ratio via visible colour segregation method.

6.2.3. Alternative Fuels

Population and economic growth have boosted air traffic markedly; in Europe, increases of approximately three times in the number commercial flights and eight times in the volume of passengers by are expected by 2050 compared to 2011 [178]. The Advisory Council for Aviation Research and Innovation in Europe (ACARE) has established goals to reduce the Greenhouse gas (GHG) emissions, noise and other pollutants for the civil aviation industry. This policy targets a 75% reduction in CO₂

emissions and a 90% reduction in NO_x emissions per passenger kilometre by 2050, with respect to 2000.

The investigations of new aircraft designs are concerned with payload capabilities, alternative fuels, and new engine powering methods to achieve drastic decreases in civil aviation emissions; the electrical and hybrid-electrical engines have been implemented in the aviation industry. However, currently, the alternative energy is mainly applied to the ancillary systems to ensure the competitiveness and sustainability of the light aircraft. The other new generation of air vehicles, including hybrid airships, blended wing aircraft, and new aircraft engines powered by liquid hydrogen fuel, solid oxide fuel cells, solar cells, and nuclear power are still at low levels of technological readiness. It is difficult to achieve the low emission goal in the short term, owing to the long research and development cycle and slow replacement rate of older inefficient aeroplanes with newer versions [143].

Developing new types of aviation fuel not only mitigates climate change and air quality effects, but also contributes to national security with a stable, low-cost, and diversified supply of energy. These candidate fuels should not only meet the airworthiness requirements in flight and on the ground, but also require rigorous assessment to ensure their safety, operability, durability, stability, etc.

In the aviation sector, there are much greater restrictions on any candidate fuels to provide high-level reliability and stable combustion during operation, including[147]:

1. A high specific energy or high energy density to provide high heat content for payload.
2. Fine atomisation.
3. High evaporation rate.
4. Good relight capability and resistance blow-off.

5. Low explosion risk.
6. High specific heat capacity.
7. No potentially harmful contaminants.
8. Minimum unburned carbon formation.
9. Low viscosity and high lubricity (e.g. low freezing point) for easy storage, pumping and facilitation for altitude operation.
10. Good thermal stability.
11. Easy acquisition and reasonable cost.
12. Environmentally friendly.
13. Facilitation for ground storage and transportation.

Obviously, it is impossible to meet all these requirements at the same time. Some requirements are even mutually contradictory. Of these, the ignition and LBO are the two major processes for the fuel performance evaluation. The ignition instability and blow-off events increase engine maintenance cost [179] and even result in fatalities in an aircraft engine, particularly for landing operations[148].

6.2.4. Fuel Physical Properties

The fuel properties and composition have been theoretically studied for high thermal stability and applicability to jet fuel design and evaluation. It was observed that not all fuel compositions/properties have the same effects on combustion performance. Unfortunately, insufficient data were provided in the publication to compare the different hydrocarbon distributions over a wide range of properties.

Density:

Fuel density is the most basic property of the fuel. It concerns the energy density,

the storage, and transportation. The higher the fuel density means the greater the mass of fuel that can be stored in a given tank. Fuel density generally increases with increasing molecular weight of the fuel molecules, and the weight of the component atoms of the fuel molecules. It has been proved that with the increase in fuel density, the overall performance of rockets improves, especially under the heavy load and in the high-pressure condition. Fuel density is also the parameter to calculate fuel volume ratio and tank mass [180].

Viscosity:

Viscosity describes the resistance of the fuel to flow. Viscosity is generally measured in units of Pascal-seconds (Pa•s). It is a main factor that affects the atomisation, evaporation rate, and pumping. A high viscosity is always undesirable for the fuel. In an engine, fuel is delivered to the chamber from the fuel tank via a fuel system. The major components of the fuel supply system include the fuel container, pipes, pump, filter, and injectors. It can be assumed that a fuel with very high viscosity, with a honey-like consistency, is impossible to inject into the combustion chamber through the thin pipe and to atomise by compressed air when the engine starts. Viscosity is subject to three major factors:

- Intermolecular forces

The bonds between molecules resist the flow of the fuel; in other words, a more viscous the fuel has stronger bonds.

- Molecular size

Smaller molecules facilitate flowing past each other more than the bigger ones.

- Molecular shape

The shape does not play a decisive role in the viscosity. Linear molecules, branched molecules, and the ring-shape molecules all have unique effects on the flowability, which depend on their flow patterns.

Aromatics:

Aromaticity describes a hydrocarbon molecule with a circular shape, with bonds between carbon atoms. The simplest configuration is the well-known benzene ring, consisting of six carbon atoms. This type of geometric structure exhibits more stability than other connective arrangements.

Derived Cetane No.

The cetane number rate for aviation fuel is similar to that seen on a retail gasoline dispenser, which is used to indicate the fuel's quality of ignition. The derived cetane number (DCN) possesses an inverse function of ignition delay in the engine. The time period of delay is counted as from the initial fuel injection to the first time when identifiable pressure can be detected by a sensor during ignition. According to previous experience, especially for diesel engines, fuels with higher cetane number will have shorter ignition delay time than lower-Cetane fuels [181]. Burger [182] advocated that the DCN have noticeable influence on blowout because of the covariance of fuel properties with ignition delay. Colket et al. [183] also report that the fuel with higher DCN can have better capability of resistance to blowout and the experimental result shown in Figure 80. The research work done by Won et al. [184] is in agreement with this observation. He claimed that there is a relevance between the DCN and the gas turbine combustion and extinction behaviour.

Studies have shown that the DCN of fuel alters when they are blended with alternative jet fuels or additives are introduced [185,186], which is mainly caused by the shifting of n-paraffin/iso-paraffin ratio. Braun-Unkhoff claimed, owing to the natural of reactivity, the cetane numbers of n-paraffin are higher than those of iso-paraffin.

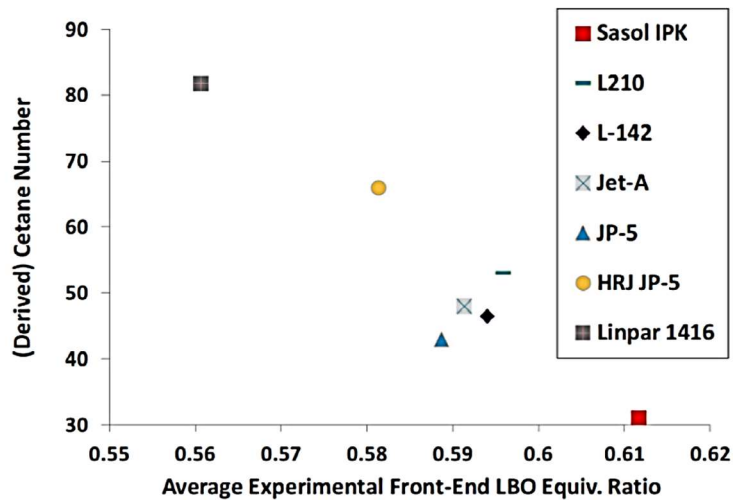


Figure 80 Derived cetane number against equivalence ratio at LBO[183]

Flash Point

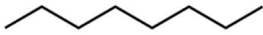
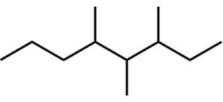
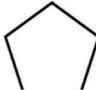
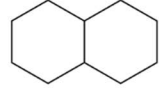

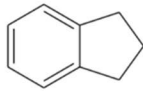
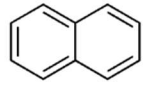
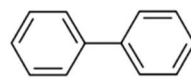
The flash point is the lowest temperature required for a material to volatilise enough flammable vapor, which can be ignited when subjected to an ignition source. The flash point is regarded as a descriptive characteristic to distinguish flammable liquids and combustible liquids. It is also a main factor to determine the level of fire hazard [187], which is closely related to the fuel storage and transportation. Generally, the flash point increases with carbon number and a higher flash point indicates a lower fire hazard level of the fuel.

Net Heat of Combustion

The heat of combustion is the overall energy released as heat when a specified amount fuel undergoes complete combustion. The chemical reaction is usually the hydrocarbon reacting with excessive oxygen at constant pressure. This is a main character to quantify the performance of a fuel to power the engine, turbines, and motors.

6.2.5. Chemical Composition

Table 4 Typical Chemical Families in Aviation Fuel

Chemical Groups	Chemical components	Chemical Structure
N-paraffins	Normal alkane (linear, normal paraffin)	
	Long-chained Unbranched Alkanes Formula: C_nH_{2n+2}	
Iso-paraffins	Iso alkane	
	Long-chained, Branched Alkanes Formula: C_nH_{2n+2}	
Cyclo-paraffins	Cyclo (Naphthenes) Formula: C_nH_{2n+2}	
	Di-cyclo alkane (di-naphthene) Formula: C_nH_{2n-2}	
Aromatics	Mono-aromatic /Alkyl Benzenes (+alkyl substitution) Formula: C_nH_{2n-6}	
	Naphthenic mono-aromatic (+cyclo alkane ring) Formula: C_nH_{2n-8} ($C_x \geq 9$)	
	Di-aromatic Formula: C_nH_{2n-12} ($10 \leq C_x \leq 12$)	
	Formula: C_nH_{2n-12} ($C_x > 12$)	

A typical jet fuel consists of hundreds or even thousands of different hydrocarbons, depending on the crude oil source and/or processing techniques employed, which significantly influence the fuel composition. Accordingly, sometimes the fuels have same specification but with high variation in hydrocarbon composition. Fuels refined from non-traditional sources, such as oil sands, biomass oils, or produced using

alternative techniques may vary in terms of chemical composition and carbon distribution.

The chemical species of the kerosene from conventional crude oil can be grouped into four types: n-paraffins, iso-paraffins, cyclo-paraffins, and aromatics, and the chemical structures are shown in Table 4. No sufficient knowledge has been obtained in terms of how these chemical components of the alternative fuel impact on the gas turbine LBO, emission, supply, operation, and safety.

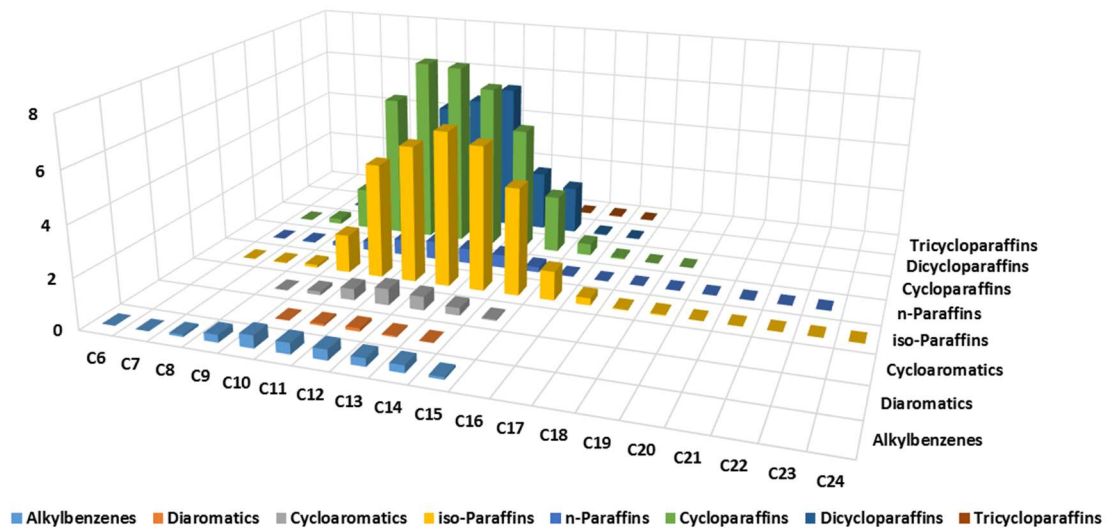


Figure 81 Chemical compositions of C-7

The objective of this part is to understand how variation in fuel chemical composition affects gas turbine LBO performance. In order to attribute performance variation to fuel chemistry, gas chromatography flame ionisation/mass spectrum was employed to quantify the amount and type of chemical components and calculate the fuel formulation data, including the formula, molecular weight, carbon ratio, etc. The chemical composition results of sample alternative fuel C-7 is shown in Figure 81.

Similar to the conventional fuel, the composition only contains hydrocarbons [188],

but the size and number distribution of the chemical groups are considerably different. As reported by Marina, a gas to liquid (GtL) is aromatics-free and only has three chemical groups, which evidently reduces the emission and increases environmentally friendly performance compared to crude oil kerosene. This demonstrates that the composition of the alternative fuel can significantly affect the combustion performance and operating suitability.

6.3. Experiment Setup

This section presents the experimental hardware and setup design. The instruments used in the system and method application are expounded in detail. These instruments have different roles of measurement including: PM mass, vibration, and noise measuring. A detailed description of the experiment procedure and data post processing method are provided. The chapter then proceeds with the description of tested candidate fuels, including blending proportion, properties, and compositions.

6.3.1. Combustor Rig and Alternative Fuels Test Campaign

The results shown in this chapter are part of a large test campaign, which has been carried on at Low Carbon Combustion Centre (LCCC). The main aim of the test campaign is to better understand the operability and the performance of the candidate fuels on jet engines from Rolls Royce. This combustor is fitted with an air blast atomiser. The six candidate fuels are sponsored by the Ministry of Defence (MoD) and the Federal Aviation Authority (FAA).

In the test campaign, the part of the whole investigation I took responsibility for was to detect the visualised combustion performance at the ignition and LBO of the six alternative fuels provided by the FAA, benchmarked against Jet A-1. The overall aims of the test campaign are to evaluate the fuel properties based on the combustion

performance before they are certified for flight, to test the applicability of alternative fuels to existing engines designed for Jet A-1, and to develop new models for the alternative fuels evaluation of combustor performance.

6.3.2. Tay Combustor Experimental Apparatus

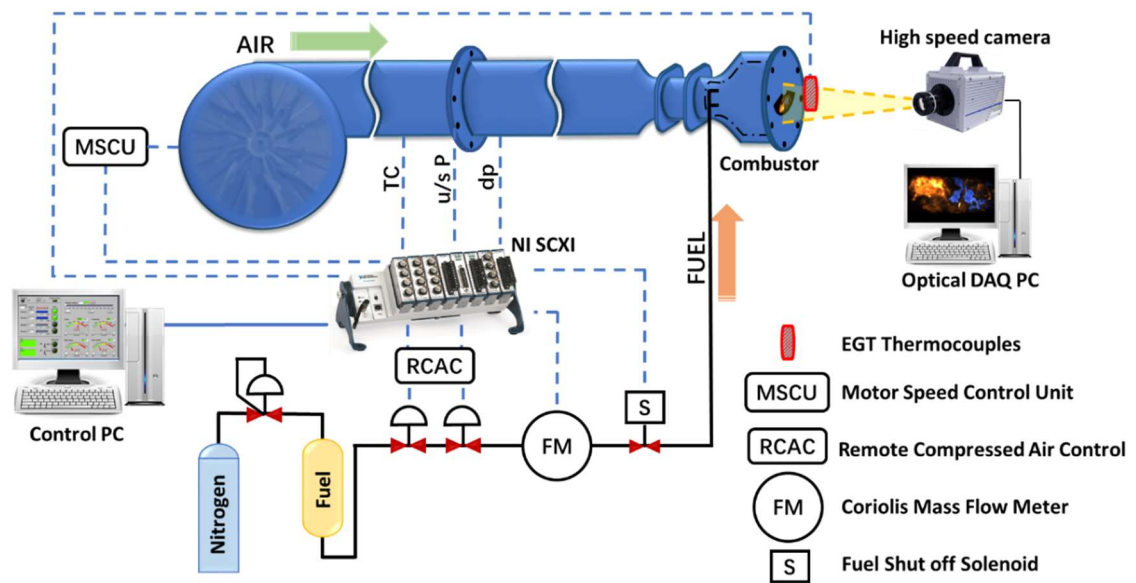


Figure 82. Tay Combustor experimental apparatus

A schematic of the experimental rig design for the Tay Combustor test is shown in Figure 82. It contains an air supply system, a fuel supply system, and an optical data acquisition system. In the air supply system, air is delivered to the combustor from an atmospheric pressure fan through a 6" process line, which has been designed and manufactured according to industrial design standard BS:5167. This line is capable of measuring flow to a total uncertainty of $\pm 2\%$ of the measured value. The atmospheric pressure fan drive motor is controlled by a speed controller, which provides analogue control of the fan speed when controlled by in-house LabVIEW (LV) Code.

The main part of the combustor test rig is a Tay gas turbine engine sponsored by

Chapter 6 Gas Turbine Combustion

Rolls-Royce, an overview of which shown in Figure 83. This ring of annular combustor cans was first designed in 1964, and has been substituted by new-generation engines, a single annular combustor. This tubular engine is now mainly used in the laboratory for test purposes. Compared with new engines, this rig operates with lower air and fuel flow rates.

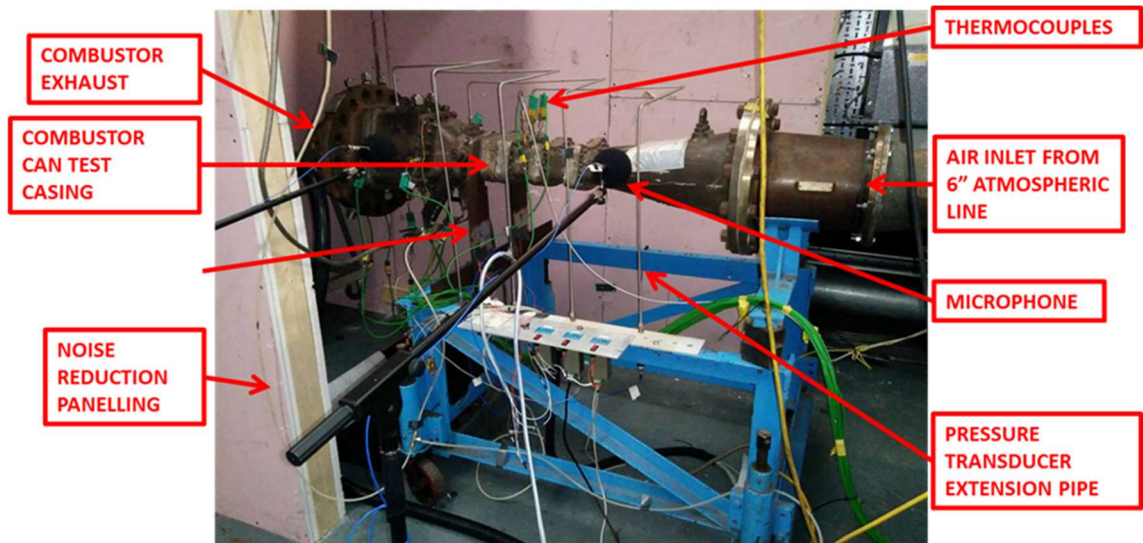


Figure 83. Overview of the combustor test rig

Fuel is supplied to the combustor by means of an electronically controlled fuel system. The fuel supply bomb is pressurised using a regulated head of nitrogen, which provides a steady fuel pressure with an air-assist pressure of 1 bar, as shown in Figure 84. Fuel exiting the bomb is then controlled by twin series (coarse and fine) air-actuated needle valves and an air-actuated fuel shut-off solenoid.

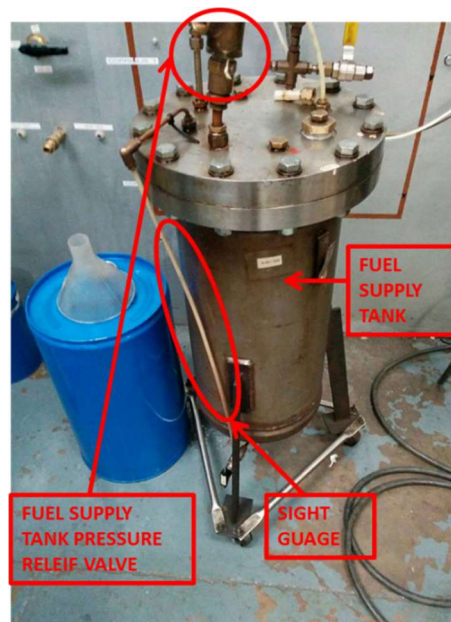


Figure 84 Fuel supply system

Each of the air-actuated fuel control valves, and the air fan motor speed controller are controlled using a LV analogue voltage controller at a frequency of approximately 5 Hz via the NI SCXI chassis and control PC (C PC). Data from the atmospheric pressure airline orifice flow meter and fuel flow Coriolis meter is read into this low-speed system and displayed to the screen, as shown in Figure 85, to be monitored by the test engineer. Table. 5 shows the operating parameters for the LBO condition.

Table. 5 Operating parameters for the LBO condition

Condition	Fuel pressure	Air-mass flow	Atomisation pressure	Fuel flow rate
LBO	150 kPa	0.2 kg/s	40 kPa	Real time
Stable	300 kPa	0.2 kg/s	80 kPa	1.8 g/s

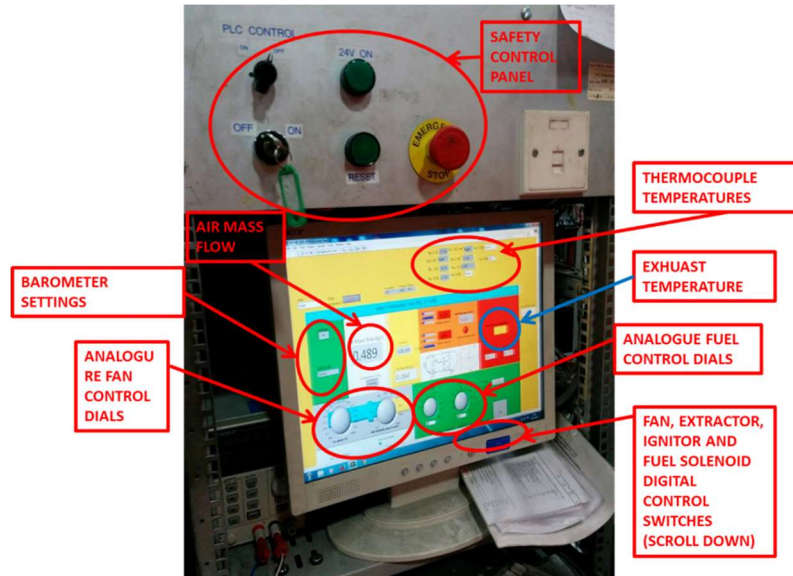


Figure 85. NI SCXI chassis and control PC

The optical setup consists of a Photron-SA4 high-speed colour camera with a full frame resolution of 1024×1024 pixels. A sigma 24–70 mm lens is applied to the camera. The aperture is set as $f/2.8$ in all the cases and the shutter speed is $1/2000$ s. The camera was positioned at the exhaust end of the combustion chamber and the images were taken at the tail of the flame through the exhaustion vent.

6.3.3. Experimental Procedures

The experimental variables are presented in Table. 6. Prior to each test, the atmospheric line heater set the combustor inlet air to 50 °C. The air mass flow was set to 200 g/s using a LV PID control code. The fuel flow was then increased whilst continually firing the surface discharge ignitor at 1 s intervals until ignition was observed for each fuel air mixture. A recessed surface discharge ignitor and high-voltage ignition unit provided the ignition source. During ignition imaging, a constant fuel flow of 1.5 g/s was delivered. Ignition images were recorded between the spark firing and the stable combustion.

Table. 6 Operating conditions and measurement uncertainty during LBO.

	Air Mass Flow (g/s)	Air Inlet Temperature (°C)	Steady exhaust gas temperature (°C)	Fuel mass flow reduction rate (g/s)	Fuel mass flow at LBO (g/s)
Target Value	200	50	400	0.00001	?
Measurement Uncertainty	±2	±3	±3	±0.005	±0.005

Once the combustor had reached a steady exhaust temperature of 400°C, the fuel flow was reduced gradually in steps of 0.2 g/s. With each reduction, constant fuel supply was maintained to insure steady-state operation at that particular equivalence ratio. This was determined by careful observation of the exhaust gas temperature. The process was iterated once a stable exhaust gas temperature was obtained.

In order to increase the stability of the system close to LBO, the final fuel reduction rate was controlled with a PID-controlled fuel flow reduction ramp. The fuel flow rate was reduced at 0.0001 g/s for the final 0.2 g/s above the experimentally determined LBO fuel flow rate. This was found to increase the experimental reliability with respect to manual control of the valves. The fuel flow stability was seen to be susceptible to fuel bomb nitrogen supply pressure. Small changes in the fuel pressure lead to variations in the fuel flow, which could cause LBO errors. This was thought to be due to the difference between the regulator cracking pressure and the desired supply pressure as the fuel volume in the fuel bomb reduced. As a result, the fuel bomb was partially filled (<40%) to dampen the effect of regulator pressure variations with a larger nitrogen head volume.

This process was repeated for the next ignition condition for every fuel investigated. Meanwhile, the control computer recorded all the parameters. To identify the blow out, the combustor upstream pressure and exhaust gas temperature were observed to spot any sudden drop. Once the LBO point was identified, the above procedures were repeated at

least four more times to obtain five consistent points. For blow-out imaging, the camera used the end trigger mode. The camera was set to record continuously until the trigger was pressed at LBO, whereupon imaging data of the flame before that point was saved.

Once each test was complete, the fuel supply was switched off, and the fuel bomb was cleaned using isopropanol. Isopropanol was then used to purge the fuel line. After the line and bomb had been cleaned, they were both purged using compressed air in order to clean any residue from their walls before the next fuel was filled into the fuel bomb for the following test.

All the acquired imaging data have been quantitatively analysed by Matlab image processing. The blue flame signals are quite weak compared to the orange soot emission. For the facilitation of visual observation of the flame propagation at the initial of ignition and LBO flame character, 10 times selective digital image enhancement of the blue pixels was carried out via the approach introduced by Huang and Zhang [77,105], in the following flame figures.

6.3.4. Fuels Matrix

All the properties and chemical compositions information of the candidate fuels is provided by FAA. Some information is protected as confidential materials. Thus, the original fuel data sheets cannot be attached in this work. The necessary data for analysis has been selectively presented in this section.

Table 7 Conventional Fuel Selection

Fuel CODE	Composition	Key aspects for combustion testing
A1	JP8	Best
A2	Jet A	Average
A3	JP5	Worst
C1	Gevo ATJ fuel (100%), 2,2,4,6,6 - Pentamethylheptane	Extremely low cetane, unusual boiling range, C12 and C16 iso-paraffins
C3	JP-5 64 vol% /farnesane 36 vol% blend, Kerosene&2,6,10 Trimethyl dodecane	Bio-Jet, high viscosity fuel
C4	Sasol IPK 60%vol/Gevo ATJ 40% vol blend, 2,2,4,4,6 - Pentamethylheptane	Low cetane fuel, but broader, more conventional boiling range
C5	Isoparaffin 73% vol /trimethyl benzene 27% vol	Narrow boiling fuel c10, extremely “flat” boiling range, fuel boils at same temperature
C7	RP-2 (75 vol%), A-3 (23 vol %), Penn State high decalin (2%)	High cycloparaffin
C8	Jet A + Exxon aromatic blend	High aromatic

Table 8 Conventional Fuel Properties Matrix

	Ave Molecular Formula	Ave Molecular Weight	Density	Viscosity	Derived Cetane No.	Net Heat of Combustion	Flash Point+	Aromatics	n-paraffins	i-paraffins	c-paraffins
		g/mole	@15°C (kg/m ³)	@ 20 °C (cSt)		(MJ/kg)	(°C)	(wt%)	(wt%)	(wt%)	(wt%)
A1	C10.8H21.8	152	779.9	3.5	40.4	43.1	42	13.41	26.82	39.69	20.08
A2	C11.4H22.1	159	803.2	4.5	47	43	48	18.66	20.03	29.45	31.86
A3	C11.9H22.6	166	826.8	6.5	47.9	43	60	20.59	13.89	18.14	47.38
C1	C12.6H27.2	178	759.7	5	17.1	43.82	49.5	0	0	100	0
C3	C12.8H25.3	180	807.7	8	47	43.29	66	13.61	9.17	45.19	31.72
C4	C11.4H24.8	162	759.2	3.87	28	43.81	46	0.39	0.23	98.94	0.43
C5	C9.7H18.7	135	768.9	1.96	39.6	43.01	44	30.68	17.66	51.58	0.07
C7	C12.1H23.9	170	817	6.53	42.6	43.3	64	4.88	3.3	29.51	62.31
C8	C11.6H21.4	160	823	4.84	42.6	42.9	56	27.31	13.72	20.99	37.97
CN 31 Jet A	C11.7H23.6	163.83	777	4.33	31	43.668	50	9.52	10.45	69.23	10.8
CN 44 Jet A	C11.4H23.0	160.18	786	4.6	44	43.6	49	8.91	16.37	42.17	32.55
CN 54 Jet A	C11.7H24.1	165.05	786	5	54	42.8	56	5.3	26.33	37.56	30.82

Table 9 Data of the Fuels with Cetane additives

Fuel Base	% Di-tert-butyl peroxide [by volume]	DCN
ATJ-8	0.1	17.93882
ATJ-8	0.3	19.26446
ATJ-8	0.5	20.5901
ATJ-8	0.6	21.25292
ATJ-8	0.7	21.91574
Banner solvent	0.035	79.91825
Banner solvent	0.07	82.0165
Banner solvent	0.105	84.11475
Banner solvent	0.14	86.213
Banner solvent	0.175	88.31125
Banner solvent	0.21	90.4095
Banner solvent	0.245	92.50775
Banner solvent	0.28	94.606
Banner solvent	0.315	96.70425
Banner solvent	0.35	98.8025

6.4. Results and Discussion

In this section, nine conventional jet fuels are tested under LBO conditions. The combustion performance of the candidate fuels is analysed from three aspects (LBO equivalence ratio, sooty flame ratio, and blow-off resistance). The results inform the relationship between the fuel properties and their performance. All the candidate fuels performance are benchmarked against Jet A (A2).

6.3.5. Fuel Physical Property Effect on LBO Performance

6.3.5.1. LBO Equivalence Ratio

The equivalence ratio for the LBO of each fuel was directly measured by the FM (Coriolis mass flow meter) at the blow-off point. The value of each point plotted in Figure 86 is the average of five times recording to ensure reliability and repeatability. From the column graph, C1 (Gevo ATJ fuel) blows off at the highest ϕ_{LBO} of all of the candidate fuels. However, A3 and C7 are located at the lowest ϕ_{LBO} in the graph. A3 can resist to blow-off until the ϕ_{LBO} reduced below 0.02.

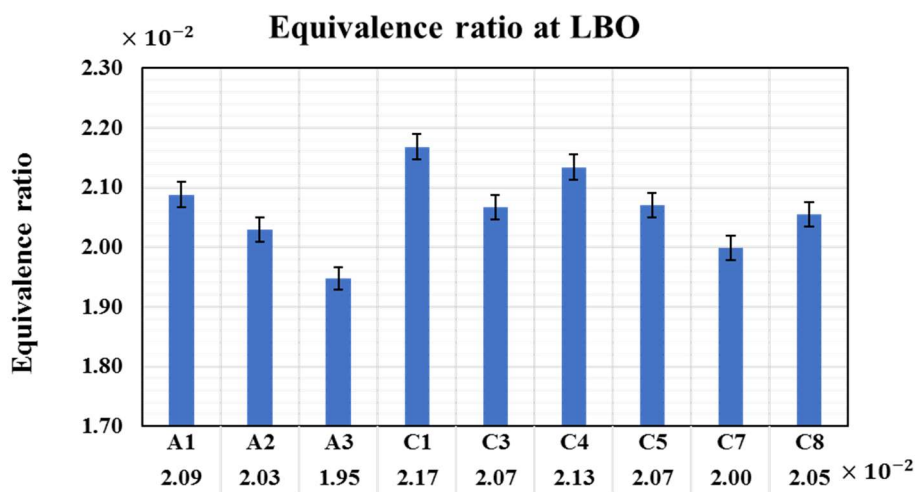


Figure 86 Equivalence ratio of candidate fuels at LBO

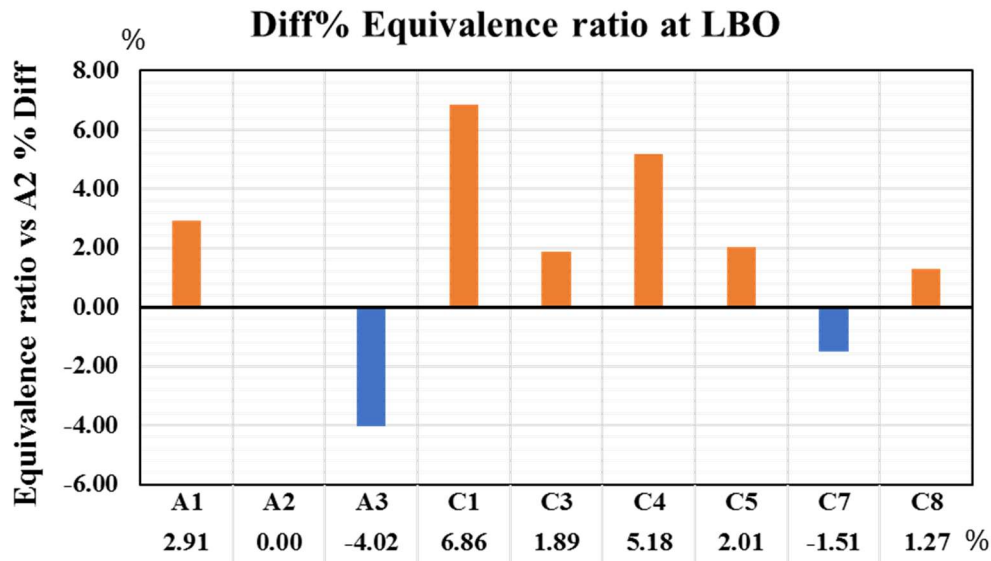


Figure 87 Equivalence ratio of candidate fuels at LBO

To have a better view of the LBO behaviour of alternative fuels, the equivalence ratios of all the fuels have been compared with A2 with the calculation through Equation 47 and the results are shown in Figure 87. The positive value indicates the fuel blowout at a higher ϕ_{LBO} than A2 (Jet A), which means it exhibits worse LBO behaviour than A2. The negative value direction indicates the fuel blowout at a lower ϕ_{LBO} than Jet A (A2), which means it has a better LBO performance. As the results shown in the bar graph, only A3 and C7 can sustain burning at a lower equivalence ratio than A2 and the ϕ_{LBO} of C1 reaches nearly 7% higher than Jet A.

$$\%Diff = \frac{\phi (LBO_{fuel}) - \phi (LBO_{A2})}{\phi (LBO_{A2})} \quad \text{Equation 47}$$

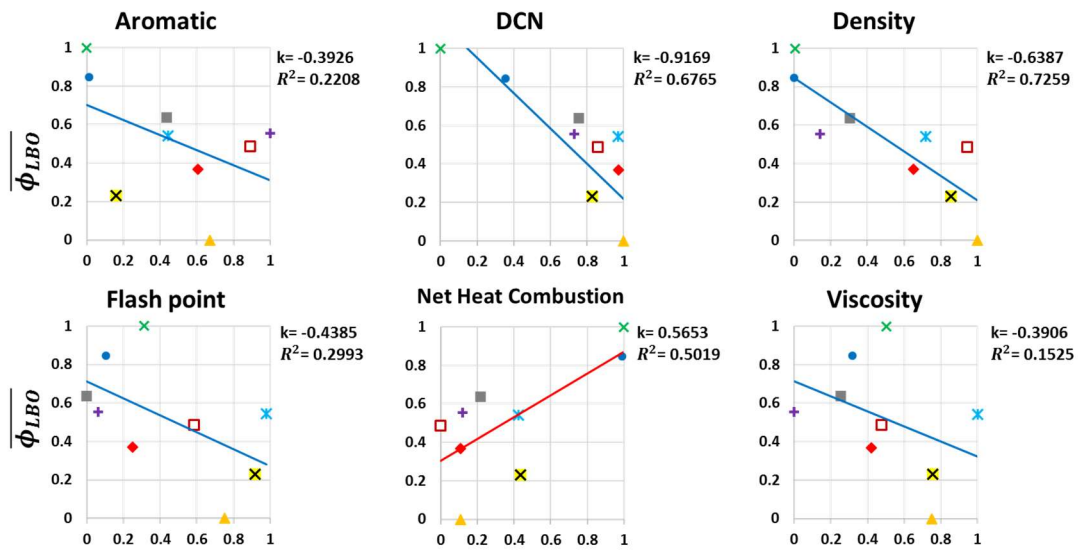


Figure 88 Plot of the normalised equivalence ratio against normalised fuel properties

For ease of comparison of the fuel property effects on the LBO equivalence ratio, Figure 88 shows plots of measured ϕ_{LBO} against the property of the fuels, including: density/engine cetane/viscosity/aromatics, etc. They have been normalised in the range of 0 to 1. 0 in the X-axis which means the lowest value of the property and 1 means the highest value of the property of all the candidate fuels. In each of the plots, the Y-axis shows the normalised measured combustion characters. A linear trend line has been added to each plot, assuming linear regression on each set of data. The gradient of the linear trend line is k and the value of each plot has been presented at left of the graph. The ‘-’ symbol means the equivalence ratio decreases with the increase in the fuel properties values and the trend line is presented in blue. On the contrary, the ‘+’ symbol means the equivalence ratio increases and the trend line in is shown in red.

It is clearly shown in the plot that only the increment of net heat of combustion will lead to high blow out equivalence ratio. In contrast, fuels with high values of density, viscosity, DCN, flash point, and aromatic have a good effect on the LBO equivalence

ratio.

The coefficient of determination (R^2) is a statistical measure of how powerfully the property dominated the LBO. The rank of the feature importance for LBO is shown in Figure 89. The density and DCN are the most dominant two factors for LBO performance, whereas the aromatic content and viscosity do not have considerable effect on the LBO.

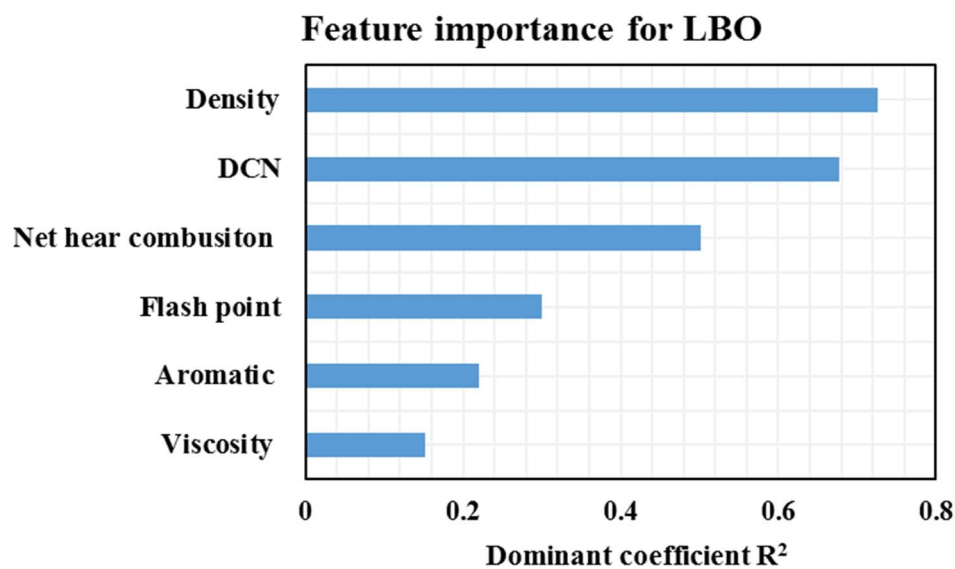


Figure 89 Feature importance for LBO

6.3.5.2.LBO Sooty Flame Concentration

Soot emission is one of the main parts of the fuels evaluation of the air pollution control. Sooty flame consists of unburned impure carbon particles, which has been heated up and exhibit the bright yellow colour, due to incomplete combustion. Hence, the sooty flame concentration performance is a direct indicator for the soot emission of the fuel character.

In this section, this study investigates the flame performance at the LBO point in a gas turbine combustion chamber. Visual images were recorded by a high-speed camera to give further details of the flame behaviour of various fuels near the LBO condition.

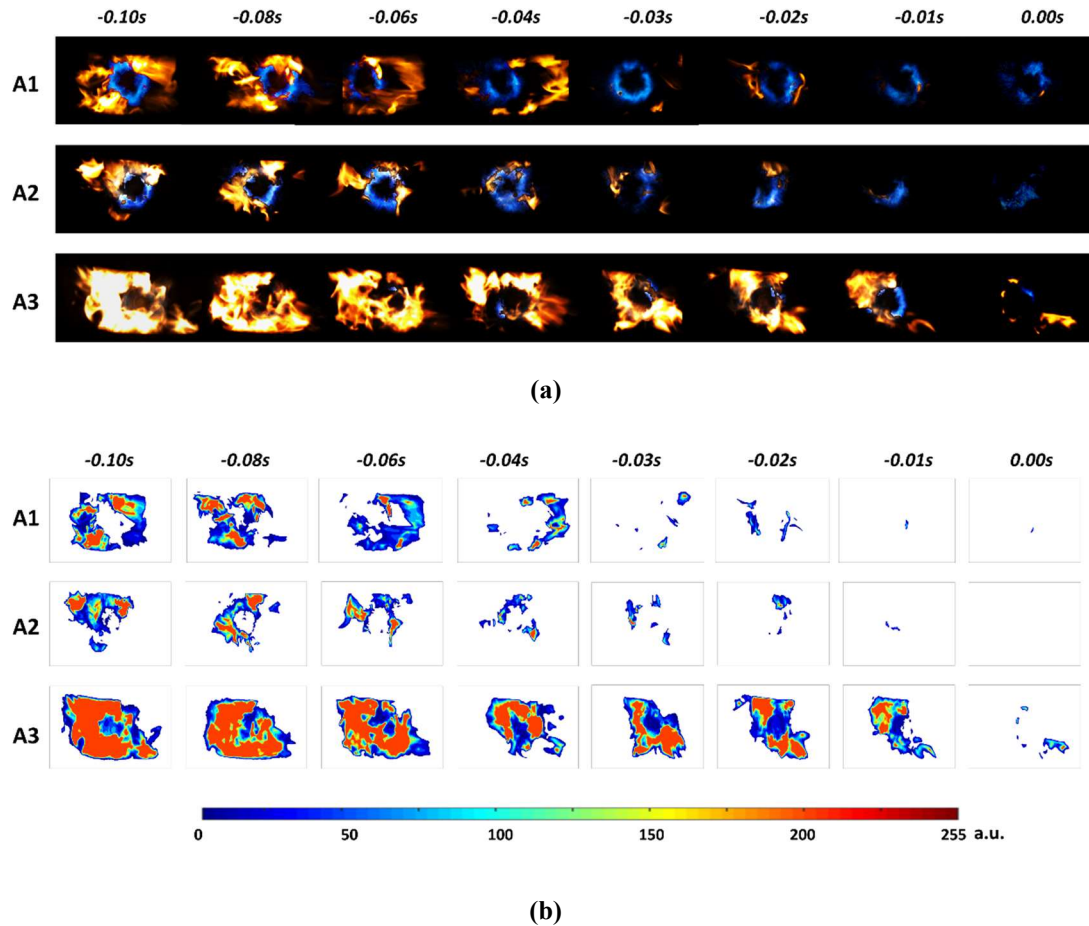


Figure 90 (a) Flame visualisation and (b) soot concentration contour plot of different types of sample fuels at last 0.1s of LBO;

Figure 90 (a) presents the sample images of the LBO behaviour of three different jet fuels in the last 0.1s, in which set the moment of the last appearance of flame as the 0 s and before that are counted as negative seconds. The LBO images for all the other fuels is shown in Appendix II. The two-dimensional flame image can be considered the integration of flame luminosity, along the axis of the combustion chamber. For each fuel, the flow pattern of the bluish and yellowish luminosity generally exhibited highly

complex turbulence in a ring shape, with a clockwise-swirl motion encircling the central recirculation zone. More dynamic flame details of the blends at blow-out point can be observed in this video [189]

As shown in Figure 90 (a), at the end of five consecutive images before LBO, most of the fuels burned sufficiently and presented a pure bluish colour. However, for different candidate fuels, the sooty flame appearance varies, which indicates the fuels still cannot have clean and sufficient burn even at the very lean combustion condition. The combustion performance is based on the properties and compositions of the fuels. The further quantitative analysis will be conducted on the Sooty flame concentration ratio.

Soot emission is the one of the main parts of the fuel evaluation in terms of the air pollution control. As discussed in the previous results, the colour of the sooty flame region is mainly contributed by the flame heating sooting particles. Hence, the sooty flame is a considerable indicator for soot emission at LBO conditions. Owing to the limitation of the imaging position, the spatial distribution of the sooty flame cannot be detected. But, the soot radiation concentration based on the integrated luminosity can be analysed via the method introduced by Huang and Zhang [77], which was successfully applied to various combustion performance evaluations [49,190]. They suggested that the 'R intensity' in the hue rang of 0° to 70° can express the soot-induced digital coloration and represents the local distribution of the soot concentration. The 2D contour plot of soot concentration result is shown in Figure 90 (b). The soot concentration rate displayed in the colour bar ranges from 0 to 255, in arbitrary units, and varied colour from dark blue to red. The red regions in a contour represent the highest soot concentration.

According to the recorded images, the sooty flame concentration ratio is defined

by Equation 48 and calculated through MATLAB. The results shown in Figure 91 are the average of the 2048 relevant images for each fuel.

$$\begin{aligned}
 \text{SCR} &= \sum_{hue=0^{\circ}}^{70^{\circ}} R_{hue} \times \frac{\text{Sooty flame region}}{\text{Whol flame region}} \\
 &= \sum_{hue=0^{\circ}}^{70^{\circ}} R_{hue} \times \frac{\text{Pixel No. of sooty flame}}{\text{Pixel No. of Whole flame area}}
 \end{aligned}
 \tag{Equation 48}$$

Figure 91 shows Sooty flame concentration ratio performance of the tested fuels in the LBO condition. It clearly shows that A3 blowout with the highest soot area ratio, followed by C8. However, C4 had the lowest sooty area ratio and C1 was second lowest. Both fuels blowout with a Sooty flame concentration ratio less than 10%, which indicates the best performance of sufficient burning.

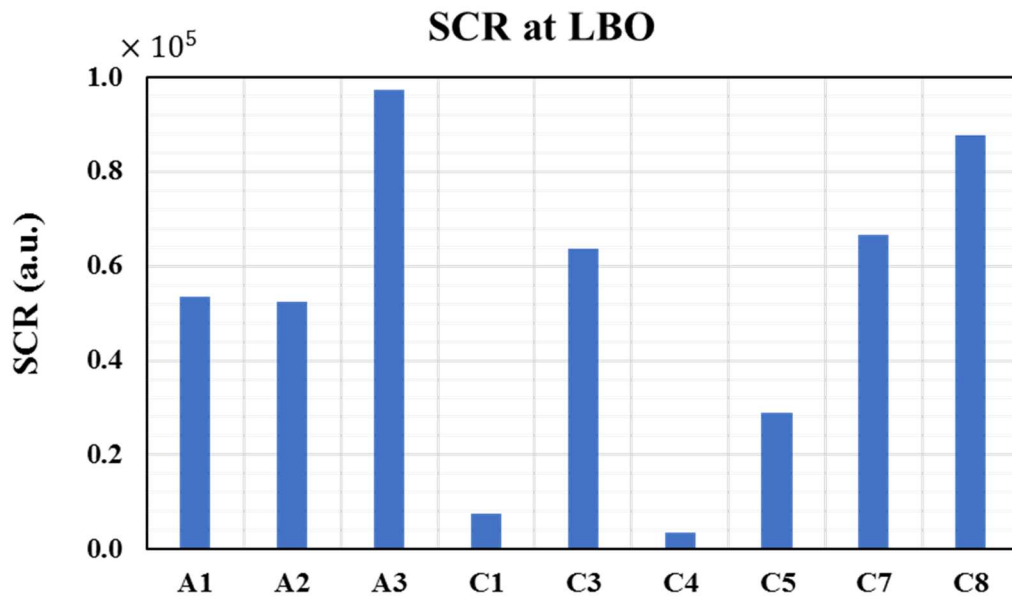


Figure 91 Sooty flame concentration ratio of candidate fuels at LBO condition

To have a better view of the sooty emission behaviour of alternative fuels, the sooty

Chapter 6: Gas Turbine Combustion

area ratios of all the fuels have been compared with fuel A2, calculated using Equation 49. and results are shown in Figure 92. A positive value indicates the fuel burns with more soot than A2, whereas a negative value means the better sufficient burning performance.

$$\%Diff = \frac{SCR (LBO_{fuel}) - SCR (LBO_{A2})}{SCR (LBO_{A2})} \quad \text{Equation 49}$$

It can easily be observed that A3, C3, C7, and C8 blowout with more sooty flame than Jet A. A1 exhibited similar performance as Jet A. The remaining three candidate fuels burn cleaner than Jet A. Moreover, the Sooty flame concentration ratio of C1 and C4 show 80% less than Jet A.

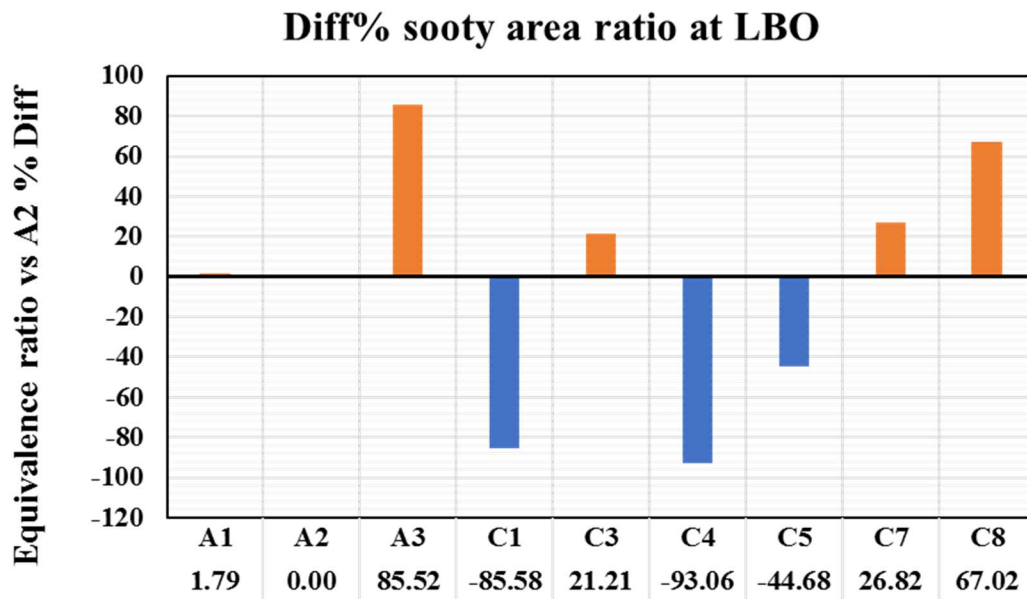


Figure 92 Sooty flame concentration ratio of the candidate fuels comparing with the A2

For ease of comparison between the fuel properties effects on the sooty flame concentration ratio, Figure 93 shows plots of the calculated SCR against the properties

Chapter 6: Gas Turbine Combustion

of the fuels, including density/DCN/viscosity/aromatics, etc. They have been normalised in the range of 0 to 1.0 in the X-axis, as in the method introduced in the previous section. In each of the plots, the Y-axis shows the normalised sooty area ratio. A linear trend line has been added to each plot, assuming linear regression of each set of data. The gradient of the linear trend line is k and the value has been presented beside each plot. The ‘-’ symbol means the sooty area percentage has a downward tendency with the increase in the fuel property values and the trend line is presented in blue. On the contrary, the ‘+’ symbol means it has an upward trend and the trend line is shown in red.

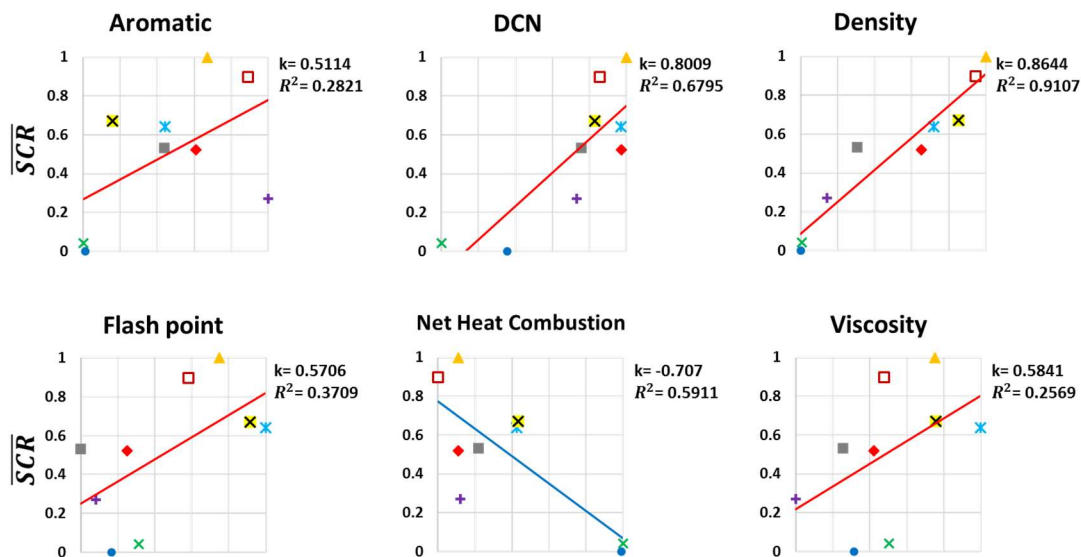


Figure 93 Plot of the normalised sooty area ratio against normalised fuel properties.

It's clear shown in the plots, the fuel with high value of Density, Viscosity, Derived Cetane No., flash point Aromatic will lead to more sooty flame at LBO. In contrast, Net Heat of Combustion have positive impact on the sufficient burning at very lean condition.

The coefficient of determination (R^2) is a statistical measure of how powerfully the property dominated the SCR performance. The rank of the feature importance for SCR is shown in Figure 94. It's interesting to note that it shares the same ranking as the feature importance for LBO, which means the density and DCN are the most dominant factors for combustion performance at LBO condition, whereas the aromatic content and viscosity do not have considerable effect.

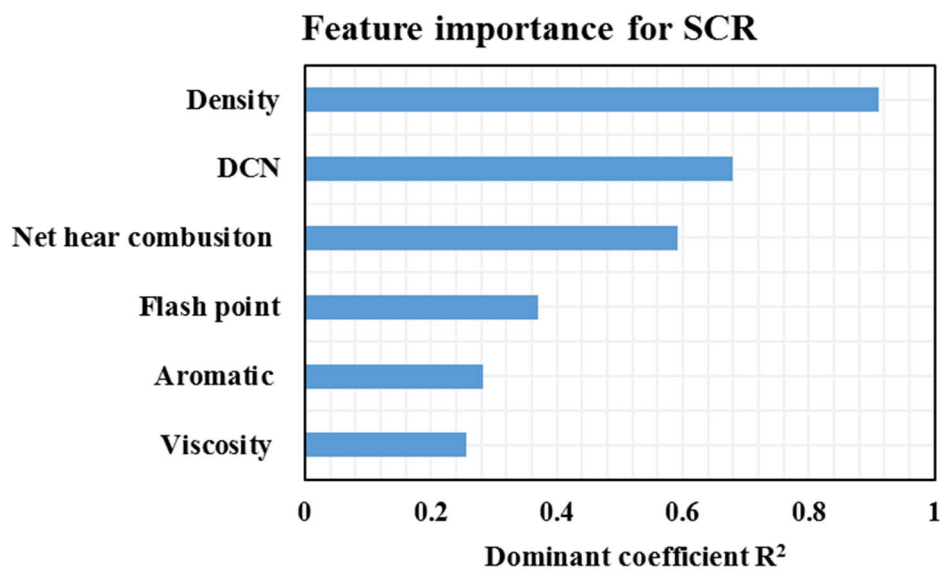


Figure 94 Feature importance for SCR

6.3.5.3. Summery

The gradient k indicated the fuel properties effect on combustion performance with increasing the value of the property. The large absolute k value indicates great effect of the property on the combustion character. The '+' and '-' symbol present the up and down tendency of the effect on the performance. As discussed above, beside of the effect factor, the different importance index of these properties should be taken into consideration. Therefore, the integrated effect of each fuel property has been calculated by Equation 50. The integrated effect index of the fuel properties on the combustion

performance has been incorporated in Figure 95

$$Effect\ index = k \times R^2 \quad \text{Equation 50}$$

As clear shown in the column diagram, with increasing the value of the fuel properties, they have different levels of impacts on the LBO equivalence ratio and soot formation tendency.

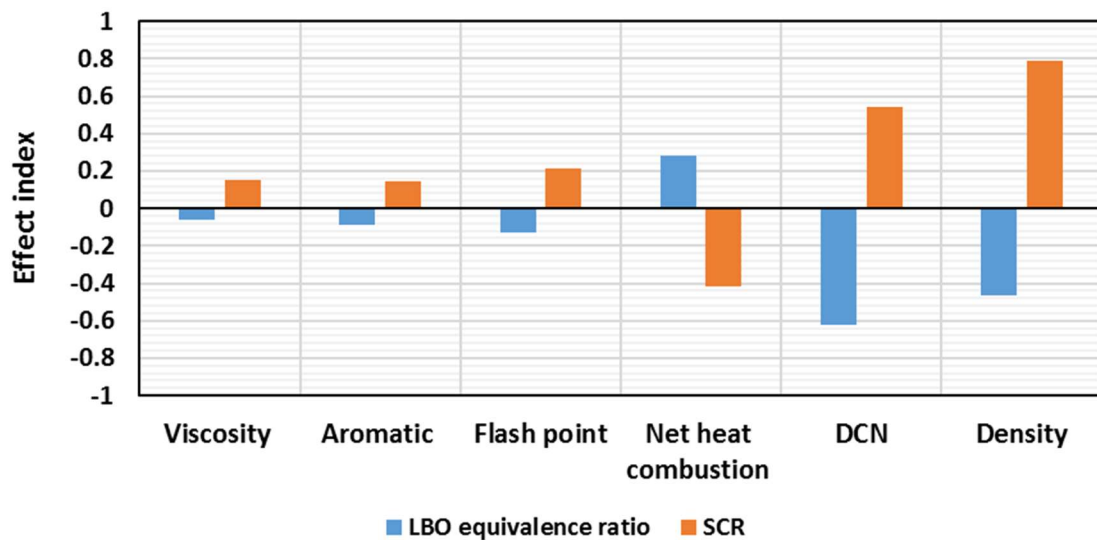


Figure 95 Incorporated effects index of fuel properties on the combustion performance at LBO condition

For all the studied fuel properties, the LBO equivalence ratio and the soot area ratio always have the opposite performance, which means good blow-out resistance capacity and low soot formation tendency cannot be achieved at the same time and a compromise should be made. The density and the DCN are dominant factors for the combustion performance at LBO. High density may induce large degree increase of sooty tendency and resist the lean blowout to same extent. The fuel with high DCN has the best effect to strengthen blow-out resistance capacity, but it may generate more soot. Comparing

with other properties, adjusting DCN can be the most considerable method to optimise the LBO performance.

6.3.6. Fuel Composition Effect on LBO Performance

Single kerosene is not available because its composition is dependent on the origin of the crude oil, processing, and storage duration. Profound knowledge of the candidate alternative jet fuel with respect to how the specific composition might impact on engine performance and emissions is needed [188].

Figure 96 (a) shows the fuel distribution 3D ternary diagram for aromatic, normal-, iso-, and cyclo-paraffin as a fraction of the whole fuel content by mass. Each corner of the ternary represents 100% of one content and 0% of the other three contents. The following 2D contour plots of fuel performance take the top view of this 3D ternary plot and the aromatic content is not be presented. As in the method introduced in the previous section, the combustion performance character has been normalised in the range of 0 to 1. In the contour plot, the highest value of character 1 presented in red and the lowest value 0 is in blue.

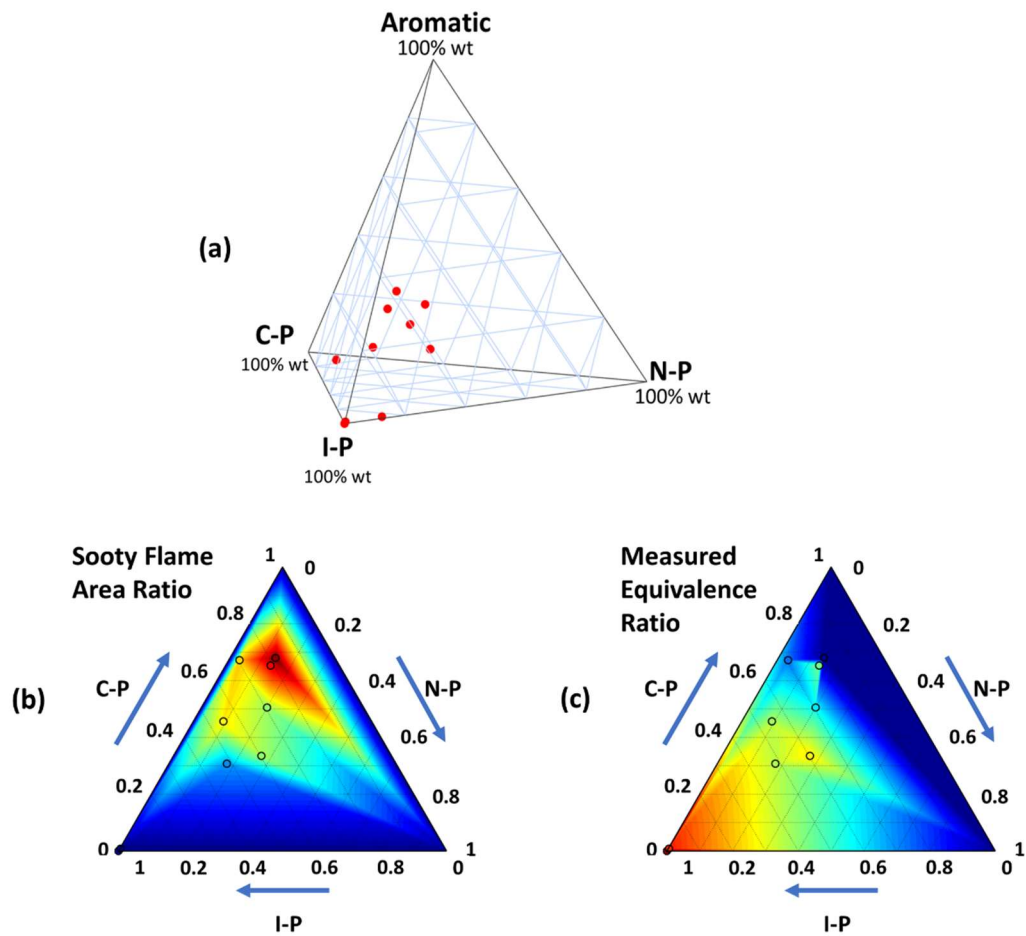


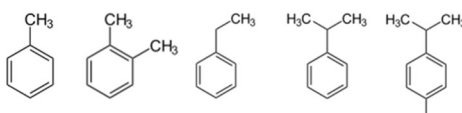

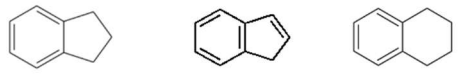
Figure 96 Ternary diagram for fuel composition effect on combustion performance

Most of the candidate fuels are concentrated close to the iso-paraffin axis and there is no fuel with high normal-paraffinic content by mass. Therefore, Figure 96 (b) provides a clear view of the fuel composition effect on the Sooty flame concentration ratio. As shown in the result, the high ratio concentrates at the high-cyclo-paraffins corner, which means the fuels with high cyclo-paraffin content are prone to generate more soot, even at extreme fuel-lean condition. In terms of the available data analysis results shown in Figure 96 (c), the high ϕ_{LBO} concentrates at the high-iso-paraffins corner, which means the fuels with high iso-paraffin content are prone to blow out with high fuel/air ratios.

Chapter 6: Gas Turbine Combustion

According to recent literature, the process of soot formation mainly involves the following procedures [191–194]: fuel oxidation, free radicals generation, initial aromatic formation, coalescent growth that forms larger and more complex aromatics, molecular expansion and agglomeration, and oxidised particle formation. As such, the aromatic content of fuels is primarily responsible for the generation of soot formation [195]. However, not all aromatics produce the same levels of smoke and emissions. As mentioned by Zheng [196], all the concerned fuel properties have the consistent effect on Sooty flame concentration ratio measured at LBO condition and PM concentration measured at stable condition. This indicates the results from high-speed imaging and DMS 500 can correlate well with each other. Therefore, the fuel composition effect on the soot formation can be presented by the Sooty flame concentration ratio.

Table 10 Aromatics groups description

Aromatics groups name	Feature	Examples
Alkyl benzenes	<ul style="list-style-type: none"> Derivatives of benzene. One or more hydrogen atoms are replaced by alkyl groups of different sizes A subset of the aromatic hydrocarbons. The simplest member is toluene, in which a hydrogen atom of the benzene was replaced by a methyl group. 	 <p>Toluene Xylene Ethylbenzene Cumene p-Cymene</p>
Diaromatic Alkyl naphthalenes	<ul style="list-style-type: none"> Derivative of naphthalene present in crude oil. Structure consists of a fused pair of benzene rings Simplest polycyclic aromatic 	 <p>Naphthalenes Biphenyl</p>
Cyclo aromatics	<ul style="list-style-type: none"> Derivatives of benzene. One or more hydrogen atoms are replaced by series of atoms in the compound is connected to form a ring. Similar to the naphthalene chemical structure but one ring is unsaturated. 	 <p>Indan Indene Tetralins</p>

According to chemical structure, the aromatic species can be roughly grouped into three types, alky-benzenes, di-aromatics and cyclo-aromatics, and the details are shown in Table 10. Table 11 provides the content by mass of the aromatics types for each

candidate fuel.

Table 11 Aromatic types content of each candidate fuel

Aromatics Group	A1	A2	A3	C1	C3	C4	C5	C7	C8
Alkylbenzenes (wt%)	10.859	12.896	10.369	0	6.841	0.271	30.676	2.458	18.191
Diaromatics (wt%)	1.059	2.332	1.335	0	0.966	0.014	0.000	0.274	1.982
Cycloaromatics (wt%)	1.490	3.434	8.883	0	5.805	0.104	0.000	2.148	7.141

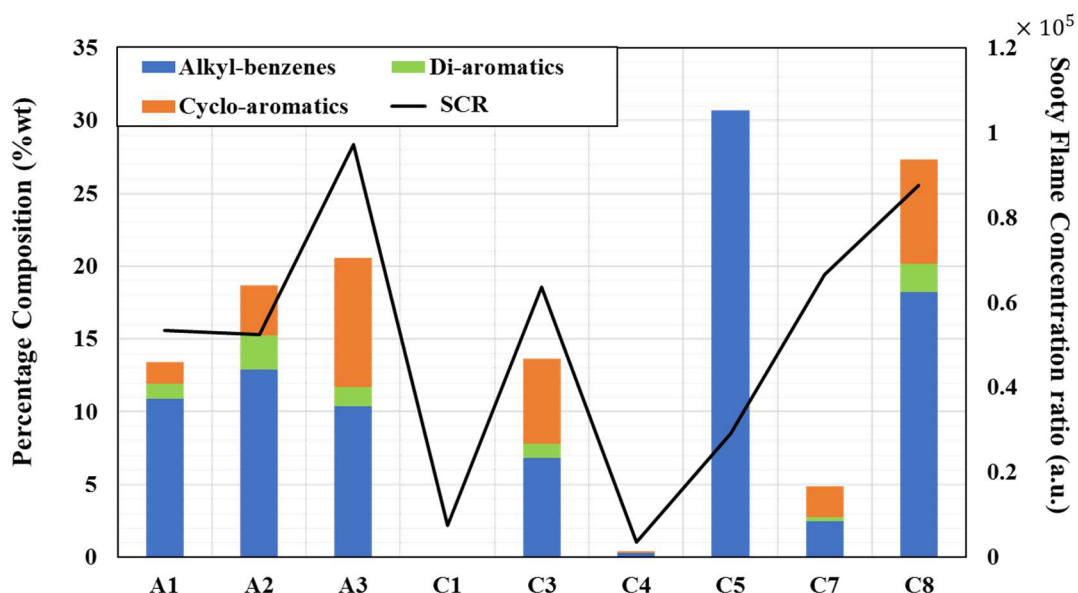


Figure 97 Aromatics composition effect on sooty flame concentration ratio

Figure 97 shows combined results of a line plot of sooty area ratio and column graph of aromatics percentage composition for different fuels. The results confirm the influence of aromatic contents on soot from gas turbines. As the results show, the fuels C1 and C4 that barely contain aromatics undoubtedly produce the least amount of soot. However, the fuels A3 and C8 generate the highest sooty flame but their aromatic

contents are lower than C5. It is interesting to notice that C5 has the highest aromatic content, but the soot area ratio is relatively low. This phenomenon is mainly because the aromatic in C5 principally composed of alkylbenzenes, whereas the aromatics of A3 and C8 are comprised of a plurality of structures. This indicates comparing with di-aromatics and cyclo-aromatics, alkylbenzenes are not the major contributors to large amounts of soot formation. Owing to their inherently complex and stable chemical structure, di-aromatics and cyclo-aromatics are relatively hard to decompose effectively and result in the formation of soot.

6.3.7. Air Flow Rate Effect

In addition to the fuels' natural physical and chemical properties, according to Lefebvre's theory shown in Equation 46, the thermo-fluidic properties are also a decisive factor in determining the LBO performance. An increment of air flow rate can be used as method to increase the thermodynamic efficiency and control the soot emission. However, it increases the instability of the combustion and increases the tendency of the flame to blow out. This section investigated the combustion performance at LBO of the six alternative fuels conducted on three air flow conditions. It aims to evaluate the air flow rate effect on the LBO combustion performance from the perspective of imaging monitoring and the sensitivity of different candidate fuels to the air flow rate.

Figure 98 presents sample images of the LBO behaviour of A3 at three air flow rate conditions in the last 50/2000 s, in which the moment of the last appearance of flame is set as 0 s and the period before that counted as negative seconds. More images for all the other fuels are shown in appendix III. The beginning of the 0.025 s of recorded time, the sooty flame appearance varies in the fuels and air flow rates shown in the left

column of the graph. This indicates that burning performances are relative to both the properties of the fuel and operating conditions.

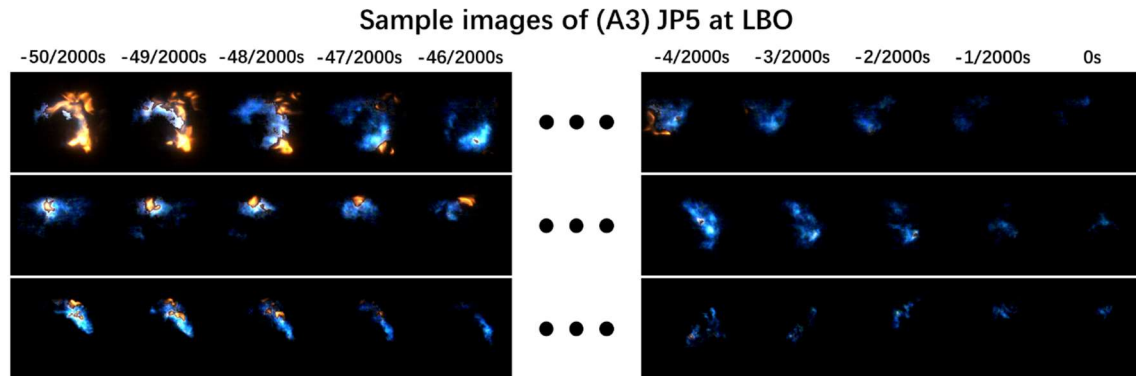


Figure 98. Sample images for seven fuels burning in the last 50/2000s at LBO

The sooty flame concentration ratio results in Figure 99 are the average of the 1000 relevant images for each fuel and each air flow rate condition. It shows the sooty flame emission performance of the seven tested fuels at three air flow rate conditions. It shows downward trend of the ratio with the increasing air flow, which indicates that all the fuels produced less soot emission with the higher air flow rate at the LBO point.

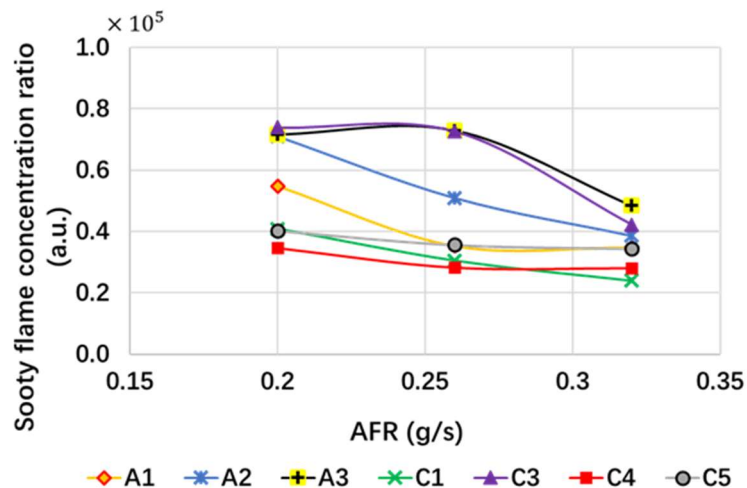


Figure 99 Sooty flame concentration ratio for seven fuels at three air flow conditions

In Figure 99, for the fuels A3 and C3, the sooty emission conditions are not alleviated with the increasing air flow at first. After continually increasing the air to 0.32 g/min, they exhibit an evident drop. However, they remain at the highest level of soot emission around 50% compared with the others. C1, C4, and C5 are always located at the bottom of the soot emission rate and present a slow descending tendency with the increase in air flow, in which C1 hits the lowest ratio of 24% at the highest air flow rate. The soot emission of A2 is very sensitive to the air flow rate. It shows a steady decline when adding more air and the sooty flame concentration ratio has been cut in half at the end. A1 shows a similar decline rate as A2 at the first stage. However, the trend is bent when adding more air. A discrepancy of only 4% of the sooty flame concentration ratio has been shown when burning at the air flow rate of 0.26 kg/s and 0.32 kg/s.

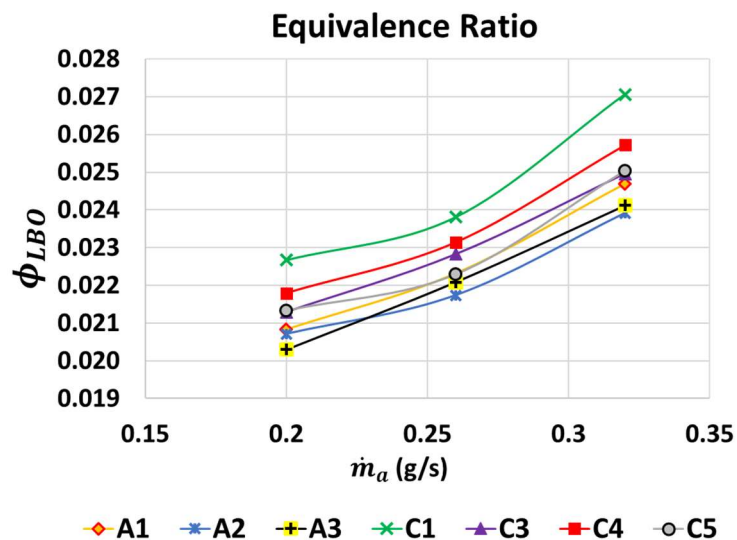


Figure 100 Equivalence ratio for seven fuels at three air flow conditions

The equivalence ratio for the LBO of each fuel was directly measured by the FM (Coriolis mass flow meter) at the blow-off point. The value of each point plotted in Figure 100 is the average of five times recording to ensure reliability and repeatability. From the line graph, each of the fuel blew off at a higher equivalence ratio under higher

air flow rate. In other words, when the air flow rate is high, the fuel more easily blows off. However, this does not mean that the lower air flow rate is better and safer. This will be further analysed in the following graphs. C1 blows off at the highest ϕ_{LBO} for all three air-flow rates, followed by C4, whereas the lines of A2 and A3 are located at the lowest ϕ_{LBO} in the graph. A3 can resist to blow-off until the ϕ_{LBO} is reduced to nearly 0.02 at the air flow rate 0.2 kg/s.

The higher AFR promotes the atomization and mixture, which leads to more fuel participated in the reaction instead of converting into soot particles. This is obviously shown in Figure 101, in which the soot flame concentration ratio is drops continually with the increase in the equivalence ratio.

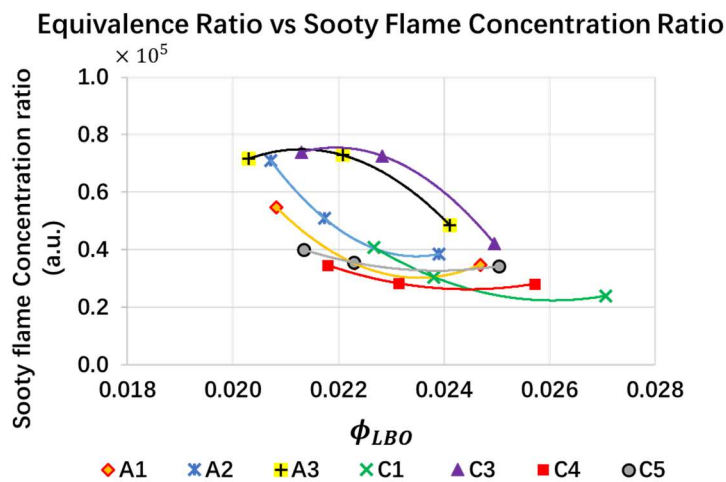


Figure 101 Sooty flame concentration ratio vs the LBO equivalence ratio at three flow rate conditions

6.3.8. Cetane Additives Effect

As in the results and discussion in the previous section, a high DCN will result in a lower LBO equivalence ratio with acceptable soot formation. The DCN of the fuel

Chapter 6: Gas Turbine Combustion

can be easily manipulated by introducing additives, which means, by taking advantage of this, the LBO condition of the alternative fuels can be optimised by use of additives without impacting emissions and other properties. This is as expected, because cetane improvers promote easier combustion, but this study is the first to demonstrate the benefits for gas turbine LBO performance. In this chapter, the DCN effect on the fuel performance will be analysed on the two kinds of fuels with adding various proportions of di-tert-butyl peroxide (DTBP), and the details are shown in Table 9.

As shown in Figure 102, the DCN of ATJ-8 has slightly increased by 3.98 from 17.94 to 21.92 with adding DTBP from 0.1% to 0.7%. However, the DCN of banner sol has been increased by 18.9 from 79.91 to 98.8 with adding 0.35% of DTBP by volume.

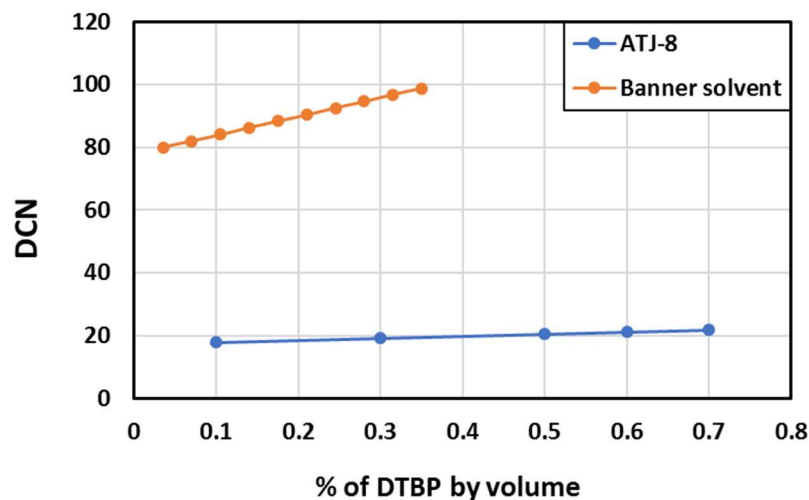


Figure 102 DCN result of the Fuels with DTBP

In this section, this study investigates the combustion performance of the Cetane additive blends at or near the LBO point from the aspects of FAR and sooty area ratio.

Figure 103 shows the LBO FAR results for the ATJ-8 and banner solvent with

different proportions of DTBP. The LBO FAR results for both of the fuel cases show decreasing tendency with increased Cetane additive proportion. The slope of the banner solvent case is larger than the ATJ-8 case, which is cause by the difference in DCN for each of the base fuels. ATJ-8 DCN is less sensitive to the DTBP proportion, but, according the results, the LBO FAR has been improved by nearly 10%.

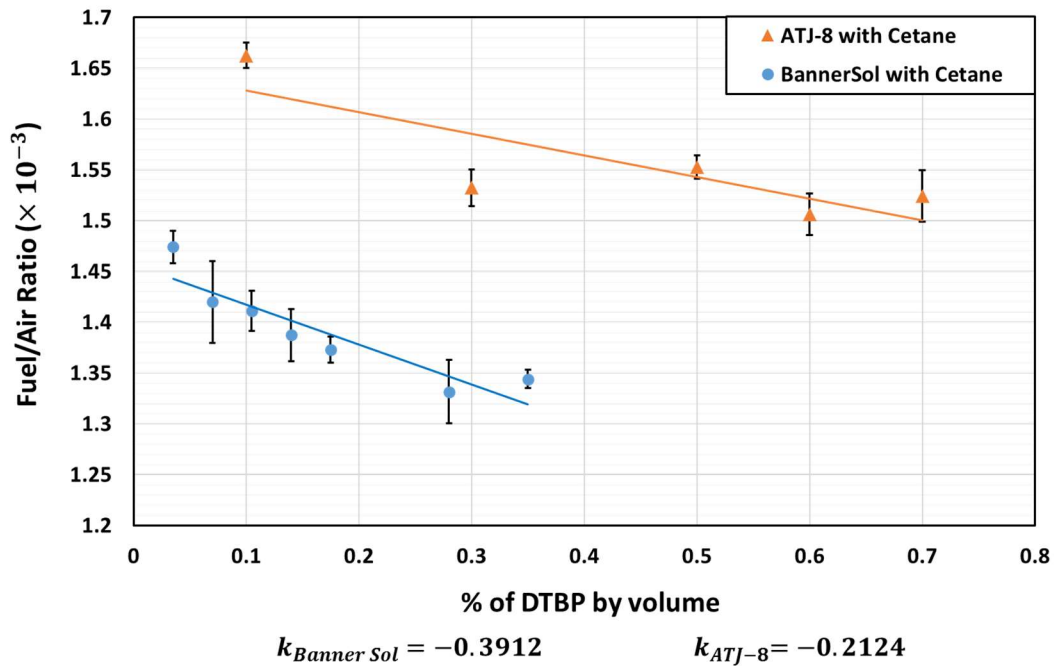


Figure 103 LBO Fuel/Air Ratio results for two fuels with different proportions of DTBP

The Sooty flame concentration ratio results for the two fuels with different proportion of DTBP are shown in Figure 104. For both of the fuels, the results show upward trend with increased Cetane additives. The slope of the banner solvent case is steeper than ATJ-8 case. Accordingly, the DCN of banner solvent is more susceptible to the DTBP additives, which leads to more soot flame formation. The results are in good accordance with those of the previous section. Therefore, adding cetane additives to a jet fuel is a feasible approach to achieve better, more stable combustion

performance at LBO condition.

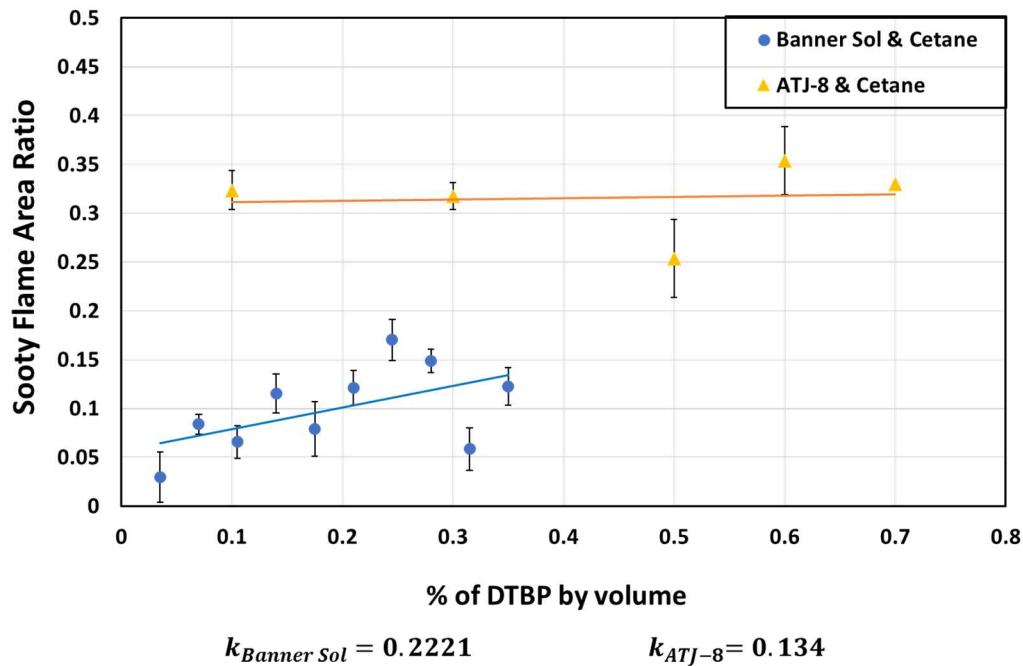


Figure 104 Sooty flame concentration ratio results for the two fuels with different proportions of DTBP

6.5. Conclusion

An experimental investigation has been carried out to evaluate the fuel properties and composition effects on the transient LBO and stable combustion condition on a small spray gas turbine combustor. This study focused on a comparative analysis of how powerfully the property dominated the combustion performance. Prior to performing individual additives blending, investigations were conducted to characterise the effects of the physical and chemical properties on LBO equivalence ratio and soot flame formation. These investigations showed that:

- The sooty flame formation largely depends on the aromatics and is not sensitive to

viscosity.

- Aromatics, DCN, density, flash point, and viscosity exhibit positive effect to extend the LBO limit to different degrees. However, they have a potential negative effect on the soot particles control and efficient burning. The high value of these properties also leads to insufficient burning and heavier soot formation
- Fuel with a high percentage content of i-paraffinic are prone to blow out at high equivalence ratio and high cyclo-paraffinic contribute to heavy soot formation.
- With the increasing of the AFR, all the candidate fuels are prone to blow off at higher equivalence ratio.
- For the LBO, the Sooty flame concentration ratios of all seven fuels show an obvious drop with the increase in \dot{m}_a , in spite of blowing out at a higher equivalence ratio, which means increasing \dot{m}_a is one of the most effective means of soot emission control.
- Cetane additives the blends at serial proportions to provide a better understanding of the impacts of the physical properties on LBO performance. Upon addition of DTBP, the LBO equivalence ratio had been notably improved with a marginally increased sooty flame ratio.

7. Summary and Future Work

7.1. Summary

In the present work, the schlieren, DFCD method, self-developed denoise, boundary detection methods and flame chemiluminescence measuring methods have been applied to gaseous fuel and liquid fuel combustion to acquire quantitative analysis of the combustion performance. By integrating these optical monitoring findings with their inherent nature, physical insights of these combustion phenomena have been achieved.

7.1.1. Visualisation Monitoring Techniques

- The accuracy of the results in the employed cameras were largely affected by their sensors. Therefore, the camera sensitivity calibration is an essential first step. Compared with the domestic camera, the high-speed camera sensor can produce the intensity of each RGB channel more evenly for and perform much more reliably.
- For the propane Bunsen flame, in the equivalence ratio range $0.9 \leq \phi \leq 1.55$, the flame has an easily distinguished double-flame structure, with an inner and outer flame. The CH^*/C_2^* ratio of the inner layer shows best the linear correlation with equivalence ratio variation, followed by whole flame region. The results from the

outer post-reaction zone are not sensitive to the equivalence ratio altering.

- In general, the results of the CH^*/C_2^* intensity ratio from the colour-modelled and filter exhibit similar trends for both fuels. The consistency is negligible for propane Bunsen flame cases, but there is considerable divergence in the methane tests. Furthermore, the filter method is not suitable for measuring in low-light situations.
- The CH^*/C_2^* intensity ratio of propane flame decrease monotonically with the increase in the equivalence ratio within the range of $0.9 \leq \phi \leq 1.55$, whereas the results of methane decrease first and then increase. The bottom point is located at approximately $\phi \approx 1$.
- For hybrid premixed and partially premixed flame, the chemiluminescence ratio of CH^*/C_2^* cannot be associated with the equivalence ratio. The validation range of the flame chemiluminescence measurements is $\phi \leq 1$ for methane and $\phi \leq 1.55$ for propane.

7.1.2. Application on Acoustic Induced Gaseous Fuel

Monitoring

This study has shown that the premixed combustion is sensitive to the frequency of acoustic perturbation. The investigated flame features include the flame wrinkle fluctuation frequency, amplitude, surface area to volume ratio, and acoustically induced dilution behaviour. It also presented a quantitative experimental observation of the acoustic-excitation-induced lifted flame. The investigated lifted flame features include the fluctuation of flame length and lifted height, vortex structure, premixed flame fuel/air mixing ratio, and propagation behaviour. It has been observed that:

- On the whole, it has been observed that the frequencies of the measured properties match exactly with excitation frequencies, and their amplitude have a similar trend

Summary and Future Work

to the sound pressure standing wave in the tube. This indicates that the various features of the flame correlate well with the acoustic disturbance.

- Furthermore, the lower excitation frequency has less impact on all the analysed aspects of flame features, regardless of the sound pressure. The higher excited frequency will induce more severe disturbance and produce more evident changes, especially for the surface area to volume ratio and dilution behaviour. Under the intensive perturbed condition, the nonlinear frequency response can be explained by the involvement of the lift-off behaviour.
- For the flame configuration, the wrinkle amplitude shows an increasing trend along the downstream direction under external excitation condition. Both the external forcing frequency and the sound pressure on the action point have a positive effect on the flame wrinkle amplitude growth rate. The growth rate presents a linear trend with respect to the axial distance.
- For the lifted flame features, the premixed flame is prone to be disturbed and can be extinguished suddenly under the condition of high-frequency acoustic perturbation. The fluctuating amplitude of the lifted height keeps growing with the increasing forcing pressure.
- The external forcing pressure promotes the flame height fluctuation owing to the appearance of the separated flame bubbles.
- The Kelvin–Helmholtz ring structure forms at the unburnt jet boundary near the nozzle when the flame lifts off, thereby intermittently stabilising the flame. However, the flame will blow off eventually under the severe turbulence stretching, because the excessive re-entrainment of the cold fresh air cools down the hot products and the flame fails to be sustained.
- Under low forcing sound pressure, the nonconstant value of lift-off frequency f_L is nonlinearly coupled to the external excitation frequencies, whereas under the low forcing sound pressure, the vortices dominated the lifted height oscillation.

- Before the flame lift-off, the relative velocity in the flame shear layer increases with the increase in the sound amplitude. After the flame lift-off, the intensive vorticity region concentrates in the Kelvin–Helmholtz rolling-up region, thereby reducing the velocity disparity and providing a suitable environment for flame reattachment.
- A moderate fresh air entrainment along with the Kelvin–Helmholtz vortex structures dilute the mixture fraction. The premixed-flame burning speed and propagation preference drag the flame back to the nozzle.
- For flame dilution behaviour, both the surface area per unit volume expansion and flame lift-off can promote the further mixing of the fuel and air. However, the surface expansion has a limitation and excessive lifted height will quench the flame.

7.1.3. Application on Gas Turbine Liquid Fuel Monitoring

An experimental investigation has been carried out to evaluate the effects of fuel properties and composition on the transient LBO and stable combustion condition on a small spray gas turbine combustor. This study focused on a comparative analysis of how powerfully the property dominated combustion performance. Prior to performing individual additives blending, investigations were conducted to characterise effects of the physical and chemical properties on LBO equivalence ratio, Sooty flame concentration percentage, and emissions. These investigations showed that:

- The sooty flame formation largely depends on the aromatics and is not sensitive to viscosity.
- Aromatics, DCN, density, flash point, and viscosity exhibit positive effects to extend the LBO limit to different degrees. However, they have potential negative effects on the soot particles control and efficient burning. The high value of these properties also leads to insufficient burning and heavier soot formation.

Summary and Future Work

- Fuel with high percentage content of i-paraffinic are prone to blow out at high equivalence ratio and high cyclo-paraffinic contribute to heavy soot formation.
- With the increasing AFR, all the candidate fuels are prone to blow off at higher equivalence ratio.
- For the LBO, the Sooty flame concentration ratios of all seven fuels exhibit an obvious drop with the increase in \dot{m}_a , in spite of blowing out at a higher equivalence ratio, which means increasing \dot{m}_a is one of the most effective means of achieving soot emission control.
- Cetane additives the blends at serial proportions to provide a better understanding of the impacts of the physical properties on LBO performance. Upon addition of DTBP, the LBO equivalence ratio had been notably improved with a marginally increased sooty flame ratio.

7.2. Future Work

The suggestions for future work are summarized as follows:

For the image colour-based flame chemiluminescence measurement:

- For the current measurement method, only B and G channels have been employed to calculate the mixture status. This method only can provide validated chemiluminescence calculation at fuel lean condition and the validation range is varied from different fuels. Therefore, the correlation between the flame colour and fuel/air mixture status for the partial premixed condition should be established to develop a more general measuring method.
- Then the chemiluminescence diagnose method can be effectively used to monitor the complex combustion performance at ignition, dilution and other indeterminate mixture status conditions.

Summary and Future Work

For the interaction between the acoustics excitation and flame oscillation:

- For the current experimental work, only one burning condition has been tested. The response of the flame pattern with different equivalence ratios and Reynolds numbers to acoustics excitation can be investigated more.
- The PIV method can be employed to provide further explanation of the lifted-off and interaction behaviour by analysing the velocity fluctuation of the vortices in the shear layer
- The different geometry and size of the tube can be manufactured to have a further experimental investigation.
- Only single flame front has been tested in this work, the thermal interaction between the two or several flame fronts with acoustic perturbation can be further studied.
- As the tested flame is fixed in this study, the acoustic perturbation effect on the flame propagation in the open / close tube can be an interesting topic for further study. According the flame propagation test done by Yang [137], the suggested setup is shown in Figure 105. The loudspeaker can be put at either side of the tube to generate the excitation forward or opposite to the flame propagation direction.

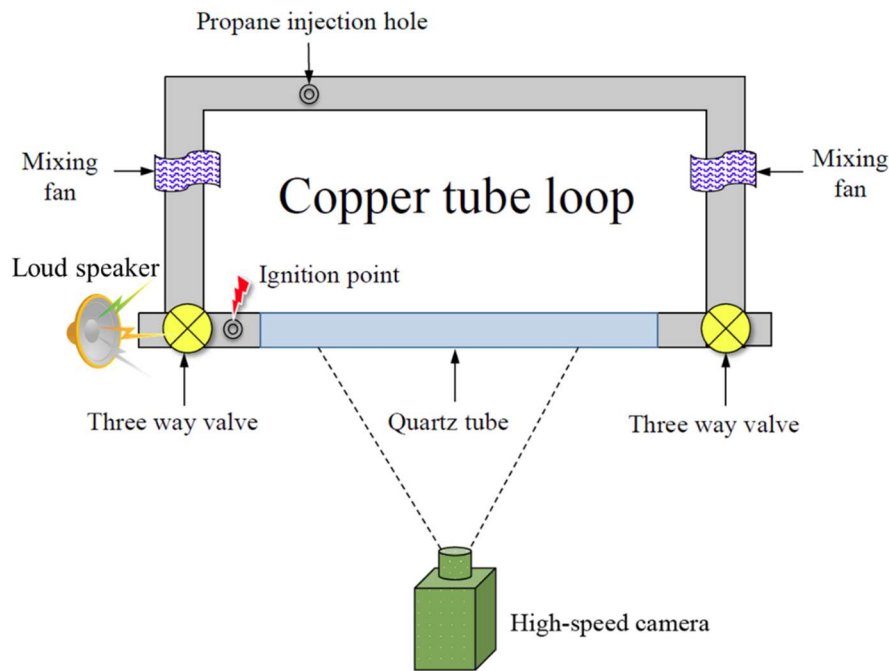


Figure 105 Suggested setup for the acoustic perturbation effect on the flame propagation in open/close tube

For the flame optical monitoring in gas turbine combustor

- As for current experimental setup, a quartz window was mounted on the exhaust duct, facing the combustor chamber axially. The images were acquired at the tail of the flame plume through the exhaustion vent. Sometimes, the entire shape of the ring could not be captured due to the shape of the exhaust vent, particularly at the stable burning condition. Therefore, the dynamic information of the highly complex turbulence in a ring shape cannot be effectively collected. New imaging direction or the shape and size of the exhaust vent should be adjusted for comprehensive flame investigation.
- Side optical window for combustion chamber monitoring is suggested to be designed and a deal sample instrument has been designed by Esclapez et al. [197] and shown in Figure 106. With the side window, the lift-off behaviour,

the colour distribution, and the swirl dynamics of the flame at the transient blow-out process can be further understood.

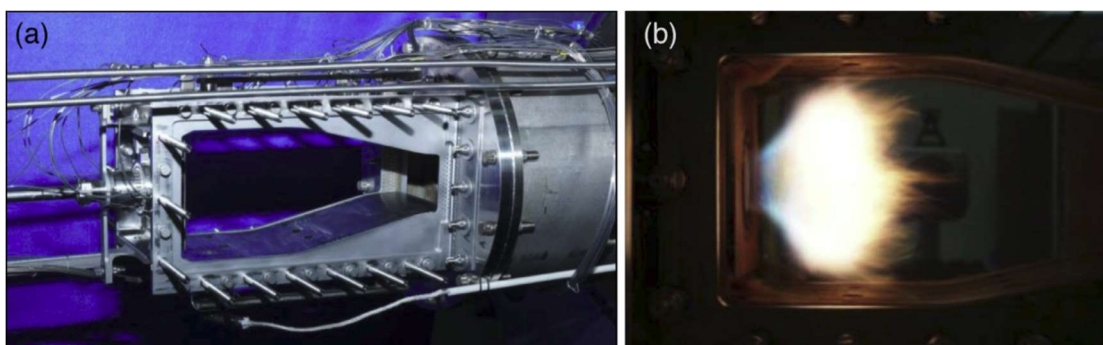



Figure 106 Deal sample instrument for side combustion chamber optical monitoring

- In the current investigation, it only provided a general concept that comparing with Di-aromatics and Cyclo-aromatics, Alkykenzenes is not the major contribution for large amounts of soot formation. But the details of performance and combustion processes of different aromatic types and content remain insufficient for fuel development.
- In this work, only the relation between the PM and SCR at LBO condition has been linked for the sooting propensity investigation. At the stable burning condition, not bluish flame can be detected, thereby a new correlation of the sooty flame at the stable condition and the PM emission should be established.
- Beside of the soot formation tendency, the consecutive flame images contain more information on flame dynamics. These performances can provide an integrated view on the combustion thermal dynamics information, if combining the noise and vibration data of the combustion chamber.

Appendix

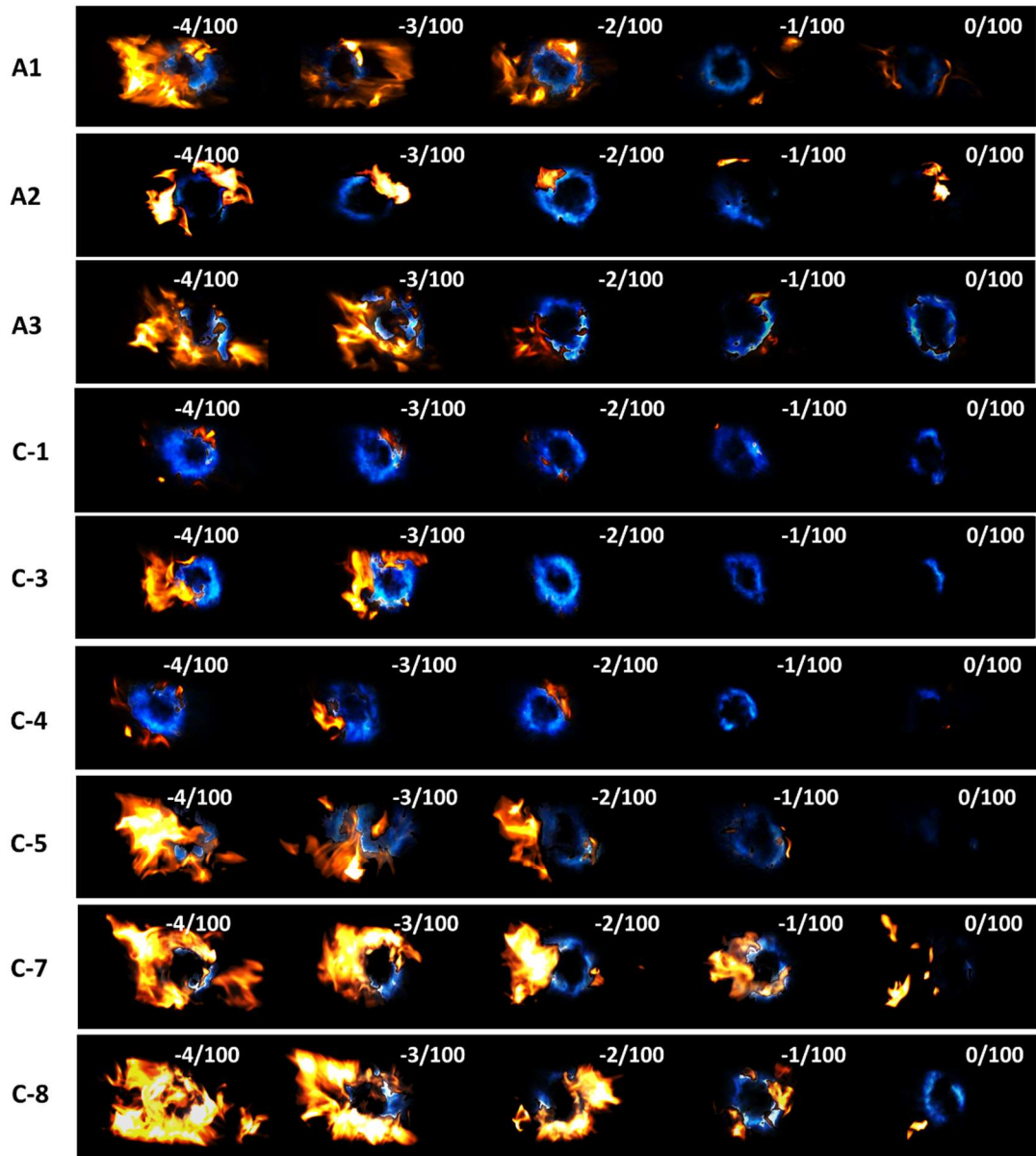
Appendix I: Microphone Specification

Model Number 377C10		PRECISION CONDENSER MICROPHONE		Revision: J ECN #: 47338
		<u>ENGLISH</u>	<u>SI</u>	
Performance	Nominal Microphone Diameter	1/4"	1/4"	
	Frequency Response Characteristic	1.0 mV/Pa	1.0 mV/Pa	
	Open Circuit Sensitivity	-60 dB re 1 V/Pa	-60 dB re 1 V/Pa	[3]
	Open Circuit Sensitivity(± 3 dB)	4 to 70,000 Hz	4 to 70,000 Hz	[3]
	Frequency Range(± 2 dB)	0.25 to 3.0 Hz	0.25 to 3.0 Hz	[1]
	Lower Limiting Frequency(-3 dB)	65 kHz	65 kHz	[1]
	Resonant Frequency(90° Phase Shift)	<35 dB(A) re 20 µPa	<35 dB(A) re 20 µPa	[1]
	Inherent Noise	178 dB re 20 µPa	178 dB re 20 µPa	[1]
	Dynamic Range(3% Distortion Limit)			
Environmental	Temperature Range(Operating)	-40 to +248 °F	-40 to +120 °C	[1][3]
	Temperature Coefficient of Sensitivity(+14 to +122°F (-10 to +50°C))	0.004 dB/°F	0.007 dB/°C	[1][3]
	Static Pressure Coefficient	-0.003 dB/kPa	-0.003 dB/kPa	[1][3]
	Humidity Coefficient of Sensitivity(0 to 100%, non-condensing)	± 0.0012 dB/%RH	± 0.0012 dB/%RH	[3]
	Influence of Axial Vibration(0.1g (1 m/s ²))	66 dB re 20 µPa	66 dB re 20 µPa	[1]
Electrical	Capacitance(Polarized)	5 pF	5 pF	[1]
	Polarization Voltage	0 V	0 V	[2]
Physical	Housing Material	Stainless Alloy	Stainless Alloy	
	Venting	Rear	Rear	
	Mounting Thread(Preamplifier)	0.2244 - 60 UNS	5.7 mm - 60 UNS	
	Mounting Thread(Grid)	0.25 - 60 UNS	6.35 mm - 60 UNS	
	Size (Diameter x Height)(with grid)	0.28 in x 0.41 in	7.0 mm x 10.5 mm	
	Size (Diameter x Height)(without grid)	0.25 in x 0.36 in	6.4 mm x 9.1 mm	
	Weight	0.06 oz	1.8 gm	[1]
<p>OPTIONAL VERSIONS</p> <p>Optional versions have identical specifications and accessories as listed for the standard model except where noted below. More than one option may be used.</p> <p>NOTES:</p> <p>[1] Typical [2] Prepolarized [3] re 250 Hz [4] See PCB Declaration of Conformance PS167 for details.</p>				
<p>SUPPLIED ACCESSORIES:</p> <p>Model ACS-20 Calibration of Precision Condenser Microphones (1)</p>				
Entered: LK	Engineer: MT	Sales: MW	Approved: MT	Spec Number: 40215
Date: 10/17/2017	Date: 10/17/2017	Date: 10/17/2017	Date: 10/17/2017	
 <p>PCB PIEZOTRONICS[™]</p> <p>3425 Walden Avenue, Depew, NY 14043</p>		<p>Phone: 716-684-0001 Fax: 716-684-0987 E-Mail: info@pcb.com</p>		

All specifications are at room temperature unless otherwise specified.
In the interest of constant product improvement, we reserve the right to change specifications without notice.
ICP® is a registered trademark of PCB Group, Inc.

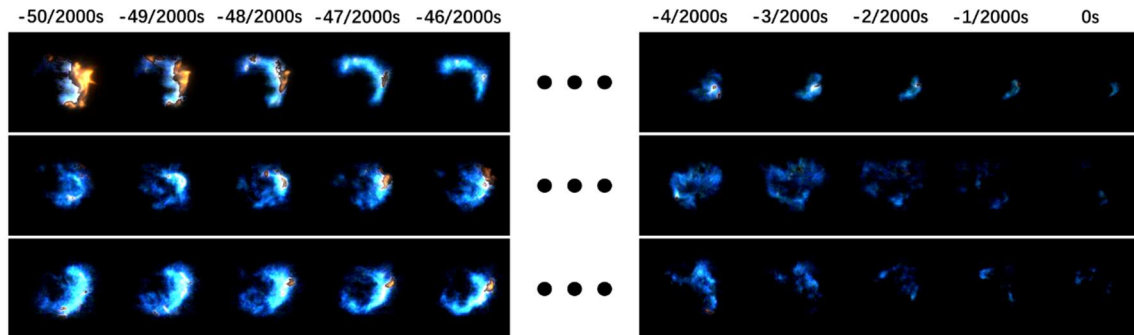


Appendix II: LBO Images for All the Fuels

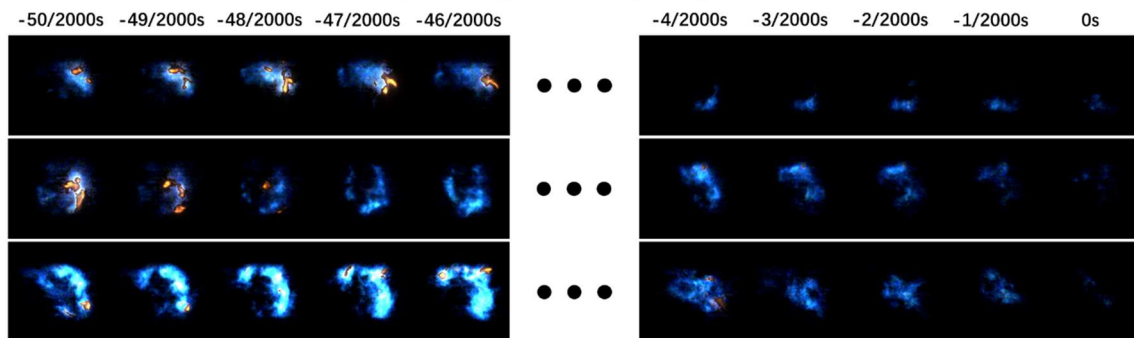


Appendix III: Sample LBO Images for Seven Fuels Burning at Three Operating Conditions

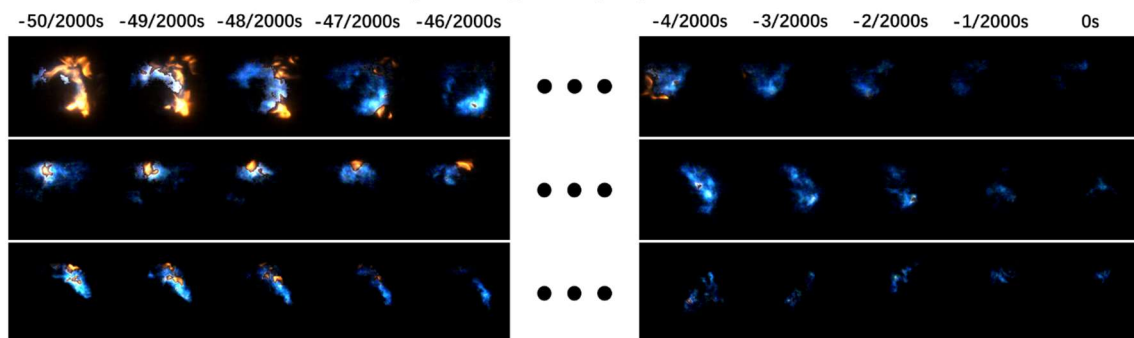
Sample images of A1 (JP8) at LBO



Sample images of A2 (Jet A) at LBO

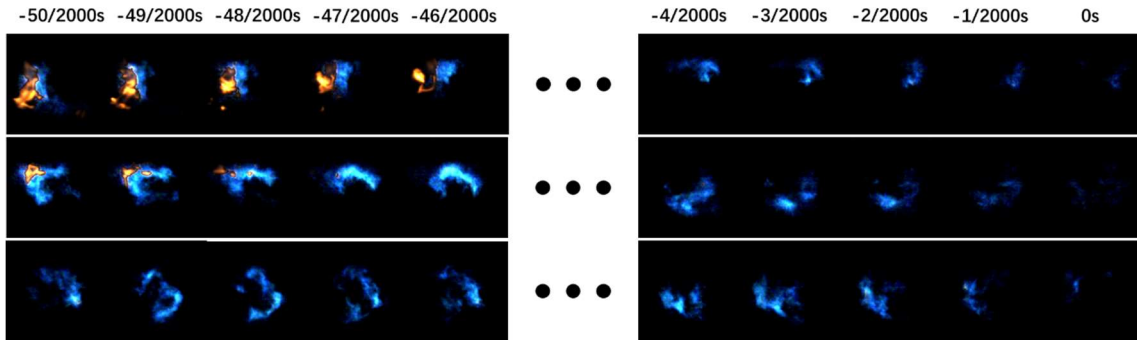


Sample images of (A3) JP5 at LBO

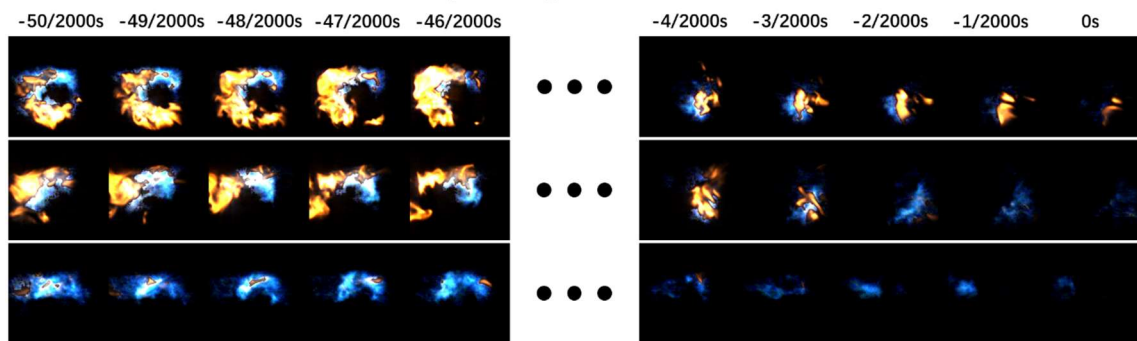


Appendix

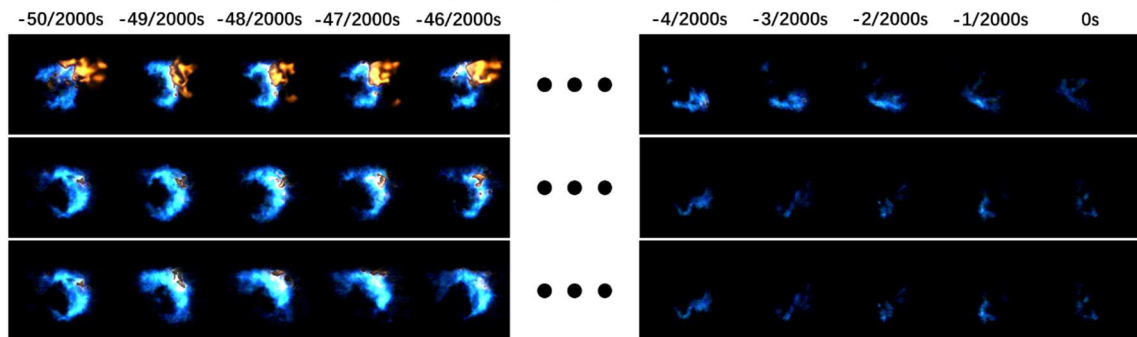
Sample images of C1 at LBO



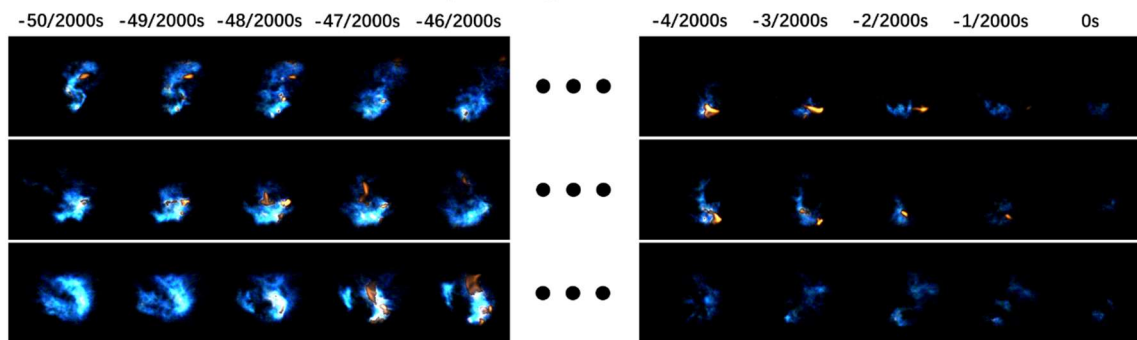
Sample images of C3 at LBO



Sample images of C4 at LBO



Sample images of C5 at LBO



Reference

- [1] K.K. Kuo, Principles of combustion, (1986).
- [2] W.B. Jensen, The Origin of the Bunsen Burner, *J. Chem. Educ.* 82 (2005) 518. doi:10.1021/ed082p518.
- [3] S. Freese, The structure of soot influences the optical effects seen in fires, (n.d.). <https://www.pinterest.co.uk/pin/673991900457285755/> (accessed January 16, 2018).
- [4] C.E. Polymeropoulos, S. Das, The effect of droplet size on the burning velocity of kerosene-air sprays, *Combust. Flame.* 25 (1975) 247–257.
- [5] H. Sarv, A.A. Nizami, N.P. Cernansky, Droplet size effects on NOX formation in a one-dimensional monodisperse spray combustion system, in: 1982 Jt. Power Gener. Conf. GT Pap., American Society of Mechanical Engineers, 1982: p. V001T01A010-V001T01A010.
- [6] C. Baumgarten, Mixture formation in internal combustion engines, Springer Science & Business Media, 2006.
- [7] F.B. and Q.C. and S.C. and J.G. and K.J. and Q. Du, Experimental investigation on the spray characteristics of power-law fluid in a swirl injector, *Fluid Dyn. Res.* 49 (2017) 35508. <http://stacks.iop.org/1873-7005/49/i=3/a=035508>.
- [8] R. Payri, J. Salvador, J. Gimeno, J. De la Morena, Analysis of diesel spray atomization by means of a near-nozzle field visualization technique, *At. Sprays.* 21 (2011).
- [9] G.A.E. Godsave, Combustion of Droplets in a Fuel Spray, *Nature.* 164 (1949) 708.
- [10] G.A.E. Godsave, Studies of the combustion of drops in a fuel spray—the burning of single drops of fuel, in: *Symp. Combust.*, Elsevier, 1953: pp. 818–830.
- [11] G.A.E. Godsave, Combustion of Fuel Droplets, *Nature.* 166 (1950) 1111.
- [12] D.B. Spalding, Combustion of liquid fuels, *Nature.* 165 (1950) 160.
- [13] D. Segawa, H. Yamasaki, T. Kadota, H. Tanaka, H. Enomoto, M. Tsue, Water-coalescence in an oil-in-water emulsion droplet burning under microgravity, *Proc. Combust. Inst.* 28 (2000) 985–990.

Reference

- [14] Y. Onuma, M. Ogasawara, Studies on the structure of a spray combustion flame, in: Symp. Combust., Elsevier, 1975: pp. 453–465.
- [15] S.R. Turns, An introduction to combustion, McGraw-hill New York, 1996.
- [16] Electro Magnetic Spectrum and light, (2017). <http://9-4fordham.wikispaces.com/Electro+Magnetic+Spectrum+and+light> (accessed December 6, 2017).
- [17] AZoSensors, A Guide to Optical Flame Detection – How UV, IR and Imaging Detectors Work, (2017). <https://www.azosensors.com/article.aspx?ArticleID=815> (accessed December 11, 2017).
- [18] M.M. Tripathi, S.R. Krishnan, K.K. Srinivasan, F.Y. Yueh, J.P. Singh, Chemiluminescence-based multivariate sensing of local equivalence ratios in premixed atmospheric methane-air flames, *Fuel*. 93 (2012) 684–691. doi:10.1016/j.fuel.2011.08.038.
- [19] S.K. Friedlander, Smoke, dust and haze: Fundamentals of aerosol behavior, New York, Wiley-Interscience, 1977. 333 P. (1977).
- [20] U.S. Epa, Air quality criteria for particulate matter, US Environ. Prot. Agency, Res. Triangle Park. (2004).
- [21] W.F. Rogge, L.M. Hildemann, M.A. Mazurek, G.R. Cass, B.R.T. Simoneit, Sources of fine organic aerosol. 4. Particulate abrasion products from leaf surfaces of urban plants, *Environ. Sci. Technol.* 27 (1993) 2700–2711.
- [22] J.A. Sarnat, J. Schwartz, H.H. Suh, Fine particulate air pollution and mortality in 20 US cities, *N Engl J Med.* 344 (2001) 1253–1254.
- [23] H.-E. Wichmann, A. Peters, Epidemiological evidence of the effects of ultrafine particle exposure, *Philos. Trans. R. Soc. London A Math. Phys. Eng. Sci.* 358 (2000) 2751–2769.
- [24] G. Polichetti, S. Cocco, A. Spinali, V. Trimarco, A. Nunziata, Effects of particulate matter (PM 10, PM 2.5 and PM 1) on the cardiovascular system, *Toxicology.* 261 (2009) 1–8.
- [25] D.W. Dockery, Health effects of particulate air pollution, *Ann. Epidemiol.* 19 (2009) 257–263.
- [26] R.D. Brook, J.R. Brook, A road forward to improve public health, (2011).
- [27] F.J. Kelly, J.C. Fussell, Size, source and chemical composition as determinants of toxicity attributable to ambient particulate matter, *Atmos. Environ.* 60 (2012) 504–526.

Reference

- [28] J. Heyder, Deposition of inhaled particles in the human respiratory tract and consequences for regional targeting in respiratory drug delivery, *Proc. Am. Thorac. Soc.* 1 (2004) 315–320.
- [29] G. Settles, E.E. Covert, Schlieren and Shadowgraph Techniques: Visualizing Phenomena in Transport Media, *Appl. Mech. Rev.* 55 (2002) B76. doi:10.1115/1.1483362.
- [30] W. Merzkirch, *Flow visualization.*, 2nd ed., Orlando , Orlando , 1987.
- [31] R.J.H. Klein-Douwel, P.J.M. Frijters, L.M.T. Somers, W.A. De Boer, R.S.G. Baert, Macroscopic diesel fuel spray shadowgraphy using high speed digital imaging in a high pressure cell, *Fuel.* 86 (2007) 1994–2007.
- [32] R. Castrej, Review: The shadowgraph imaging technique and its modern application to fluid jets and drops, 57 (2011) 266–275.
- [33] A. Adam, M. Rizalman, T. Yatsufusa, Analysis of Diesel Spray Droplets Behavior Using Shadowgraph Technique Images, *Int. J. Mater. Mech. Manuf.* 3 (2015) 60–64. doi:10.7763/IJMMM.2015.V3.167.
- [34] M.J. Hargather, G.S. Settles, Retroreflective shadowgraph technique for large-scale flow visualization., *Appl. Opt.* 48 (2009) 4449–4457. doi:10.1364/AO.48.004449.
- [35] G. Settles, T. Grumstrup, Full-scale high-speed “Edgerton” retroreflective shadowgraphy of explosions and gunshots, *Proc. 5th Pacific Symp. Flow Vis. Image Process.* (2005) 7 pages. <http://www.me.psu.edu/psgdl/Pubs/2005-Settles-PSFV.pdf>.
- [36] Andrew Davidhazy, *Supersonic Bullet*, (2007). https://www.nasa.gov/mission_pages/galex/20070815/f.html (accessed January 31, 2018).
- [37] An experimental study on the combustion of a fuel droplet, *Symp. Combust.* 5 (1955) 141–148. doi:10.1016/S0082-0784(55)80021-5.
- [38] S. Lehmann, S. Lorenz, E. Rivard, D. Brüggemann, Experimental analysis and semicontinuous simulation of low-temperature droplet evaporation of multicomponent fuels, *Exp. Fluids.* 56 (2015) 1871.
- [39] G.S. Settles, *Schlieren and shadowgraph techniques: visualizing phenomena in transparent media*, Springer Science & Business Media, 2012.
- [40] J. Rienitz, Optical inhomogeneities: schlieren and shadowgraph methods in the seventeenth and eighteenth centuries, *Endeavour.* 21 (1997) 77–81.
- [41] B.E. Richards, K.J. Badcock, G. Barakos, M. Woodgate, J. Henderson, D. Feszty,

Reference

- M. Allan, R. Menzies, Computational Modelling of Unsteady Aircraft Aerodynamics Flows, in: 2nd World Eng. Congr., 2002: pp. 22–25.
- [42] Combustion of fuel droplets in a falling chamber, *Symp. Combust.* 6 (1957) 726–731. doi:10.1016/S0082-0784(57)80100-3.
- [43] R. Reichenbach, D. Squires, S. Penner, Flame propagation in liquid-fuel droplet arrays, *Symp. Combust.* 8 (1961) 1068–1073. doi:10.1016/S0082-0784(06)80602-8.
- [44] S. Okajima, S. Kumagai, Further investigations of combustion of free droplets in a freely falling chamber including moving droplets, *Symp. Combust.* 15 (1975) 401–407. doi:10.1016/S0082-0784(75)80314-6.
- [45] M. Jain, R.S. Prakash, G. Tomar, R. V. Ravikrishna, Secondary breakup of a drop at moderate Weber numbers, *Proc. R. Soc. A Math. Phys. Eng. Sci.* 471 (2015) 20140930–20140930. doi:10.1098/rspa.2014.0930.
- [46] Y.C. Liu, Y. Xu, M.C. Hicks, C.T. Avedisian, Comprehensive study of initial diameter effects and other observations on convection-free droplet combustion in the standard atmosphere for n-heptane, n-octane, and n-decane, *Combust. Flame.* 171 (2016) 27–41. doi:https://doi.org/10.1016/j.combustflame.2016.05.013.
- [47] M. Mikami, H. Oyagi, N. Kojima, Y. Wakashima, M. Kikuchi, S. Yoda, Microgravity experiments on flame spread along fuel-droplet arrays at high temperatures, *Combust. Flame.* 146 (2006) 391–406. doi:https://doi.org/10.1016/j.combustflame.2006.06.004.
- [48] A. Ambekar, A. Chowdhury, S. Challa, D. Radhakrishna, Droplet combustion studies of hydrocarbon-monopropellant blends, *Fuel.* 115 (2014) 697–705. doi:https://doi.org/10.1016/j.fuel.2013.07.056.
- [49] Y. Jiotode, A.K. Agarwal, Endoscopic Combustion Visualization for Spatial Distribution of Soot and Flame Temperature in a Diesohol Fueled Compression Ignition Engine, *Energy and Fuels.* 30 (2016) 9850–9858. doi:10.1021/acs.energyfuels.6b01585.
- [50] R. Fujino, Y. Aoyagi, H. Osada, T. Yamaguchi, S. Mizuno, Direct Observation of Clean Diesel Combustion using a Bore Scope in a Single Cylinder HDDE, (2009).
- [51] M. Tanahashi, S. Murakami, G.-M. Choi, Y. Fukuchi, T. Miyauchi, Simultaneous CH–OH PLIF and stereoscopic PIV measurements of turbulent premixed flames, *Proc. Combust. Inst.* 30 (2005) 1665–1672.
- [52] J. Hult, U. Meier, W. Meier, A. Harvey, C.F. Kaminski, Experimental analysis of

Reference

- local flame extinction in a turbulent jet diffusion flame by high repetition 2-D laser techniques and multi-scalar measurements, *Proc. Combust. Inst.* 30 (2005) 701–709.
- [53] M. Reeves, N.J. Lawson, Evaluation and correction of perspective errors in endoscopic PIV, *Exp. Fluids*. 36 (2004) 701–705.
- [54] D. Demare, F. Baillot, The role of secondary instabilities in the stabilization of a nonpremixed lifted jet flame, *Phys. Fluids*. 13 (2001) 2662–2670. doi:10.1063/1.1386935.
- [55] F. Baillot, D. Demare, Physical Mechanisms of a Lifted NonPremixed Flame Stabilized in an Acoustic Field, *Combust. Sci. Technol.* 174 (2002) 73–98. doi:10.1080/713713066.
- [56] D. DEMARE, F. BAILLOT, Acoustic enhancement of combustion in lifted nonpremixed jet flames, *Combust. Flame*. 139 (n.d.) 312–328. <http://cat.inist.fr/?aModele=afficheN&cpsidt=16363812> (accessed February 23, 2017).
- [57] Y. Chao, M. Jeng, Behavior of the lifted jet flame under acoustic excitation, *Symp. Combust.* (1992) 333–340.
- [58] M. Kim, Y. Choi, J. Oh, Y. Yoon, Flame-vortex interaction and mixing behaviors of turbulent non-premixed jet flames under acoustic forcing, *Combust. Flame*. 156 (2009) 2252–2263. doi:10.1016/j.combustflame.2009.08.004.
- [59] Film structure and photochemical chemistry, (n.d.). http://www.360doc.com/content/17/1226/05/51349688_716311937.shtml (accessed December 25, 2017).
- [60] J.H. Bear, What Is the HSV Color Model?, (2017). <https://www.thoughtco.com/what-is-hsv-in-design-1078068> (accessed December 25, 2017).
- [61] R.C. Gonzalez, *Digital image processing using MATLAB*, 2nd ed., New Delhi : McGraw Hill Education India, c2010, New Delhi, 2010.
- [62] A.R. Smith, Color gamut transform pairs, *Proc. 5th Annu. Conf. Comput. Graph. Interact. Tech. - SIGGRAPH '78.* (1978) 12–19. doi:10.1145/800248.807361.
- [63] K.I. Svensson, A.J. Mackrory, M.J. Richards, D.R. Tree, Calibration of an RGB, CCD Camera and Interpretation of its Two-Color Images for KL and Temperature, *SAE Technical Paper*, 2005.
- [64] H. Zhao, N. Ladommatos, Optical diagnostics for soot and temperature measurement in diesel engines, *Prog. Energy Combust. Sci.* 24 (1998) 221–255.

Reference

- [65] J. Yang, Z. Ma, Y. Zhang, A Novel Flame Chemiluminescence Measurement using a Digital Colour Camera, 25th ICDERS. 6 (2015) 7.
- [66] V. Nori, J. Seitzman, Evaluation of Chemiluminescence as a Combustion Diagnostic under Varying Operating Conditions, 46th AIAA Aerosp. Sci. Meet. Exhib. (2008) 1–14. doi:10.2514/6.2008-953.
- [67] T.P. Clark, Studies of OH, CO, CH, and C (sub 2) Radiation from Laminar and Turbulent Propane-air and Ethylene-air Flames, (1958).
- [68] B.D. Stojkovic, T.D. Fansler, M.C. Drake, V. Sick, High-speed imaging of OH* and soot temperature and concentration in a stratified-charge direct-injection gasoline engine, Proc. Combust. Inst. 30 (2005) 2657–2665.
- [69] R.W. Schefer, Flame sheet imaging using CH chemiluminescence, Combust. Sci. Technol. 126 (1997) 255–279.
- [70] J.G. Lee, K. Kim, D.A. Santavicca, Measurement of equivalence ratio fluctuation and its effect on heat release during unstable combustion, Proc. Combust. Inst. 28 (2000) 415–421.
- [71] B.D. Bellows, Q. Zhang, Y. Neumeier, T. Lieuwen, B.T. Zinn, Forced response studies of a premixed flame to flow disturbances in a gas turbine combustor, AIAA Pap. 824 (2003).
- [72] Y. Hardalupas, M. Orain, Local measurements of the time-dependent heat release rate and equivalence ratio using chemiluminescent emission from a flame, Combust. Flame. 139 (2004) 188–207.
- [73] N. Docquier, F. Lacas, S. Candel, Closed-loop equivalence ratio control of premixed combustors using spectrally resolved chemiluminescence measurements, Proc. Combust. Inst. 29 (2002) 139–145.
- [74] T.M. Muruganandam, B.H. Kim, M.R. Morrell, V. Nori, M. Patel, B.W. Romig, J.M. Seitzman, Optical equivalence ratio sensors for gas turbine combustors, Proc. Combust. Inst. 30 (2005) 1601–1608. doi:10.1016/j.proci.2004.08.247.
- [75] J.U.N. Kojima, Y. Ikeda, T. Nakajima, SPATIALLY RESOLVED MEASUREMENT OF OH *, CH *, AND C * CHEMILUMINESCENCE IN THE REACTION ZONE OF LAMINAR METHANE / AIR PREMIXED FLAMES, 28 (2000) 1757–1764.
- [76] J. Kojima, Y. Ikeda, T. Nakajima, Basic aspects of OH (A), CH (A), and C 2 (d) chemiluminescence in the reaction zone of laminar methane–air premixed flames, Combust. Flame. 140 (2005) 34–45.
- [77] H.W. Huang, Y. Zhang, Dynamic application of digital image and colour processing in characterizing flame radiation features, Meas. Sci. Technol. 21

Reference

- (2010) 085202--. doi:10.1088/0957-0233/21/8/085202.
- [78] J. Yang, Z. Ma, Y. Zhang, A Novel Flame Chemiluminescence Measurement using a Digital Colour Camera, 25th ICDERS. (2015) 1–6.
- [79] N. Docquier, S. Candel, Combustion control and sensors: a review, *Prog. Energy Combust. Sci.* 28 (2002) 107–150.
- [80] J. Reyes, U. States, K. Ahmed, Simultaneous Spectral Imaging of C₂^{*}/CH^{*} at Low-to-High Pressure Combustion, (2017) 1–7. doi:10.1115/GT201763722.
- [81] T.M. Muruganandam, B. Kim, R. Olsen, M. Patel, B. Romig, J.M. Seitzman, Chemiluminescence based sensors for turbine engines, *AIAA Pap.* (2003). <http://www.aric.or.kr/treatise/journal/content.asp?idx=52744%5Cnhttp://arc.aiaa.org/doi/pdf/10.2514/6.2003-4490>.
- [82] T. García-Armingol, J. Ballester, A. Smolarz, Chemiluminescence-based sensing of flame stoichiometry: Influence of the measurement method, *Meas. J. Int. Meas. Confed.* 46 (2013) 3084–3097. doi:10.1016/j.measurement.2013.06.008.
- [83] T. García-Armingol, Y. Hardalupas, A.M.K.P. Taylor, J. Ballester, Effect of local flame properties on chemiluminescence-based stoichiometry measurement, *Exp. Therm. Fluid Sci.* 53 (2014) 93–103. doi:10.1016/j.expthermflusci.2013.11.009.
- [84] N. Kawahara, A. Inoue, E. Tomita, Time-series Spectra Measurements from Initial Flame Kernel in a Spark-Ignition Engine, 17th Int. Symp. Appl. Laser Tech. to Fluid Mech. (2014) 7–10.
- [85] Q. Wang, Y. Zhang, C.Y. Zhao, Experimental investigation of coflow effect on the ignition process of a methane jet diffusion flame, *Exp. Therm. Fluid Sci.* 91 (2018) 184–196. doi:10.1016/j.expthermflusci.2017.10.016.
- [86] M. Takeuchi, T. Kubono, A spectroscopic detecting system for measuring the temperature distribution of silver breaking arc using a CCD color camera, *IEEE Trans. Instrum. Meas.* 48 (1999) 678–683. doi:10.1109/19.772195.
- [87] S. Simonini, S.J. Elston, C.R. Stone, Soot temperature and concentration measurements from colour charge coupled device camera images using a three-colour method, *Proc. Inst. Mech. Eng. Part C J. Mech. Eng. Sci.* 215 (2001) 1041–1052. doi:10.1177/095440620121500905.
- [88] F. Migliorini, S. Maffi, S. De Iuliis, G. Zizak, Analysis of chemiluminescence measurements by grey-scale ICCD and colour digital cameras, *Meas. Sci. Technol.* 25 (2014) 55202. doi:10.1088/0957-0233/25/5/055202.
- [89] Y. Jin, Y. Song, X. Qu, Z. Li, Y. Ji, A. He, Three-dimensional dynamic measurements of CH^{*} and C₂^{*} concentrations in flame using simultaneous chemiluminescence tomography, *Opt. Express.* 25 (2017) 4640–4654.

Reference

- doi:10.1364/OE.25.004640.
- [90] F. Carranza, Y. Zhang, Study of drag and orientation of regular particles using stereo vision, Schlieren photography and digital image processing, *Powder Technol.* 311 (2017) 185–199.
- [91] Y.K. Jeong, C.H. Jeon, Y.J. Chang, Evaluation of the equivalence ratio of the reacting mixture using intensity ratio of chemiluminescence in laminar partially premixed CH₄-air flames, *Exp. Therm. Fluid Sci.* 30 (2006) 663–673. doi:10.1016/j.expthermflusci.2006.01.005.
- [92] K.T. Kim, J.G. Lee, B.D. Quay, D.A. Santavicca, Response of partially premixed flames to acoustic velocity and equivalence ratio perturbations, *Combust. Flame.* 157 (2010) 1731–1744. doi:10.1016/j.combustflame.2010.04.006.
- [93] C.T.N. In, PERFORMANCE OF COMBUSTOR WITH ACOUSTIC AUGMENTATION OF PRIMARY ZONE AIR-JET MIXING P. J. Vermeulen, J. Odgers, V. Ramesh and B. Sanders Department of Mechanical Engineering The University of Calgary, 114 (1992) 31–32.
- [94] N. Karimi, M.J. Brear, S.H. Jin, J.P. Monty, Linear and non-linear forced response of a conical, ducted, laminar premixed flame, *Combust. Flame.* 156 (2009) 2201–2212. doi:10.1016/j.combustflame.2009.06.027.
- [95] S. Kartheekyan, S.R. Chakravarthy, An experimental investigation of an acoustically excited laminar premixed flame, *Combust. Flame.* 146 (2006) 513–529. doi:10.1016/j.combustflame.2006.04.014.
- [96] A.L. Birbaud, D. Durox, S. Ducruix, S. Candel, Dynamics of confined premixed flames submitted to upstream acoustic modulations, *Proc. Combust. Inst.* 31 I (2007) 1257–1265. doi:10.1016/j.proci.2006.07.122.
- [97] D. Zhao, Z.H. Chow, Thermoacoustic instability of a laminar premixed flame in Rijke tube with a hydrodynamic region, *J. Sound Vib.* 332 (2013) 3419–3437. doi:10.1016/j.jsv.2013.01.031.
- [98] S.A. Farhat, W.B. Ng, Y. Zhang, Chemiluminescent emission measurement of a diffusion flame jet in a loudspeaker induced standing wave, *Fuel.* 84 (2005) 1760–1767. doi:10.1016/j.fuel.2005.03.020.
- [99] M. Saitoar, Soot suppression by acoustic oscillated combustion, *Fuel.* 77 (1998) 973–978. doi:10.1016/S0016-2361(97)00286-X.
- [100] P. ~J. Vermeulen, J. Odgers, V. Ramesh, Acoustic control of dilution-air mixing in a gas turbine combustor, *J. Eng. Power.* 104 (1982).
- [101] L.W. Chen, Application of PIV measurement techniques to study the characteristics of flame-acoustic wave interactions, *Flow Meas. Instrum.* 45

Reference

- (2015) 308–317. doi:10.1016/j.flowmeasinst.2015.07.013.
- [102] L.W. Chen, Q. Wang, Y. Zhang, Flow characterisation of diffusion flame in a standing wave, *Exp. Therm. Fluid Sci.* 41 (2012) 84–93. doi:10.1016/j.expthermflusci.2012.03.014.
- [103] L.W. Chen, Y. Zhang, Experimental observation of the nonlinear coupling of flame flow and acoustic wave, *Flow Meas. Instrum.* 46 (2015) 12–17. doi:10.1016/j.flowmeasinst.2015.09.001.
- [104] Q. Wang, H.W. Huang, H.J. Tang, M. Zhu, Y. Zhang, Nonlinear response of buoyant diffusion flame under acoustic excitation, *Fuel*. 103 (2013) 364–372. doi:10.1016/j.fuel.2012.08.008.
- [105] H. Huang, Y. Zhang, Flame colour characterization in the visible and infrared spectrum using a, 85406 (n.d.). doi:10.1088/0957-0233/19/8/085406.
- [106] H.W. Huang, Y. Zhang, Imaging based chemiluminescence characterisation of partially premixed syngas flames through DFCD technique, *Int. J. Hydrogen Energy*. 38 (2013) 4839–4847. doi:10.1016/j.ijhydene.2013.01.142.
- [107] H.W. Huang, Q. Wang, H.J. Tang, M. Zhu, Y. Zhang, Characterisation of external acoustic excitation on diffusion flames using digital colour image processing, *Fuel*. 94 (2012) 102–109. doi:10.1016/j.fuel.2011.12.034.
- [108] J. Li, D. Durox, F. Richecoeur, T. Schuller, Analysis of chemiluminescence, density and heat release rate fluctuations in acoustically perturbed laminar premixed flames, *Combust. Flame*. 162 (2014) 3934–3945.
- [109] A. Cuquel, D. Durox, T. Schuller, Comptes Rendus Mecanique Impact of flame base dynamics on the non-linear frequency response of conical flames, *Comptes Rendus Mec.* 341 (2013) 171–180. doi:10.1016/j.crme.2012.11.004.
- [110] D.H. Shin, T. Lieuwen, Flame wrinkle destruction processes in harmonically forced, laminar premixed flames, *Combust. Flame*. 159 (2012) 3312–3322. doi:10.1016/j.combustflame.2012.06.015.
- [111] H.Y. Wang, C.K. Law, T. Lieuwen, Linear response of stretch-affected premixed flames to flow oscillations, *Combust. Flame*. 156 (2009) 889–895. doi:10.1016/j.combustflame.2009.01.012.
- [112] D.Y. Kiran, D.P. Mishra, Experimental studies of flame stability and emission characteristics of simple LPG jet diffusion flame, *Fuel*. 86 (2007) 1545–1551. doi:10.1016/j.fuel.2006.10.027.
- [113] D.A. Scholefield, J.E. Garside, The structure and stability of diffusion flames, in: *Symp. Combust. Flame, Explos. Phenom.*, Elsevier, 1948: pp. 102–110.

Reference

- [114] S.R. Gollahalli, Ö. Savaş, R.F. Huang, J.L. Rodriguez Azara, Structure of attached and lifted gas jet flames in hysteresis region, *Symp. Combust.* 21 (1988) 1463–1471. doi:10.1016/S0082-0784(88)80379-5.
- [115] S. Navarro-Martinez, A. Kronenburg, Flame stabilization mechanisms in lifted flames, *Flow, Turbul. Combust.* 87 (2011) 377–406.
- [116] J.E. Broadwell, W.J.A. Dahm, M.G. Mungal, Blowout of turbulent diffusion flames, *Symp. Combust.* 20 (1985) 303–310. doi:10.1016/S0082-0784(85)80515-4.
- [117] W.M. Pitts, Assessment of theories for the behavior and blowout of lifted turbulent jet diffusion flames, *Symp. Combust.* 22 (1989) 809–816. doi:10.1016/S0082-0784(89)80090-6.
- [118] S. Chaudhuri, S. Kostka, M.W. Renfro, B.M. Cetegen, Blowoff dynamics of bluff body stabilized turbulent premixed flames, *Combust. Flame.* 157 (2010) 790–802. doi:10.1016/j.combustflame.2009.10.020.
- [119] Y.-C. Chao, J. Ming-Shan, Behavior of the lifted jet flame under acoustic excitation, *Symp. Combust.* 24 (1992) 333–340. doi:10.1016/S0082-0784(06)80044-5.
- [120] J. Oh, Q.S. Khan, Y. Yoon, Acoustic excitation effect on NO_x reduction and flame stability in a lifted non-premixed turbulent hydrogen jet with coaxial air, *Fuel.* 89 (2010) 1492–1498. doi:10.1016/j.fuel.2009.10.001.
- [121] D. Damare, F. Baillot, The role of secondary instabilities in the stabilization of a nonpremixed lifted jet flame, *Phys. Fluids.* 13 (2001) 2662–2670. doi:10.1063/1.1386935.
- [122] C.K. Lin, M.S. Jeng, Y.C. Chao, The stabilization mechanism of the lifted jet diffusion flame in the hysteresis region, *Exp. Fluids Exp. Methods Their Appl. to Fluid Flow.* 14 (1993) 353–365. doi:10.1007/BF00189494.
- [123] J. Oh, Q.S. Khan, Y. Yoon, Nitrogen dilution effect on flame stability in a lifted non-premixed turbulent hydrogen jet with coaxial air, *Fuel.* 89 (2010) 1492–1498. doi:10.1016/j.fuel.2009.10.001.
- [124] Y. Chao, D. Wu, C. Tsai, Effects of Acoustic Excitation on the Combustion and Pollution Emission Characteristics of a Jet Flame, 0 (2000) 1–13.
- [125] J.S. Kistler, C.J. Sung, T.G. Kreut, C.K. Law, M. Nishioka, Extinction of counterflow diffusion flames under velocity oscillations, in: *Symp. Combust.*, Elsevier, 1996: pp. 113–120.
- [126] L. Chen, A theoretical and experimental study on flow characterisation in an acoustically excited chamber, *Wave Motion.* 58 (2015) 68–76.

Reference

- doi:10.1016/j.wavemoti.2015.07.003.
- [127] A. Bourehla, F. Baillot, Appearance and stability of a laminar conical premixed flame subjected to an acoustic perturbation, *Combust. Flame*. 114 (1998) 303–318. doi:10.1016/S0010-2180(97)00323-4.
- [128] L. Zheng, S. Ji, Y. Zhang, Experimental Investigation on the Flame Wrinkle Fluctuation under External Acoustic Excitation, in: *Int. Colloq. Dyn. Explos. React. Syst.*, Boston, 2017: pp. 2–7.
- [129] N. Karimi, Response of a conical, laminar premixed flame to low amplitude acoustic forcing: A comparison between experiment and kinematic theories, *Energy*. 78 (2014) 490–500. doi:10.1016/j.energy.2014.10.036.
- [130] C.K. LAW, *COMBUSTION PHYSICS*, 2006.
- [131] L. Vanquickenborne, A. van Tiggelen, The stabilization mechanism of lifted diffusion flames, *Combust. Flame*. 10 (1966) 59–69. doi:10.1016/0010-2180(66)90028-9.
- [132] D.M.H.-P. & K.C.S. E. GUTMARK, T. P. PARR, Stabilization of a Premixed Flame by Shear Flow Excitation, *Combust. Sci. Technol.* 73 (1990) 521–535. doi:10.1080/00102209008951668.
- [133] A. Onder, J. Meyers, Modification of vortex dynamics and transport properties of transitional axisymmetric jets using zero-net-mass-flux actuation, *Phys. Fluids*. 26 (2014). doi:10.1063/1.4890242.
- [134] J. Lee, S.H. Won, S.H. Jin, S.H. Chung, Lifted flames in laminar jets of propane in coflow air, *Combust. Flame*. 135 (2003) 449–462. doi:10.1016/S0010-2180(03)00182-2.
- [135] X.J. Gu, M.Z. Haq, M. Lawes, R. Woolley, Laminar burning velocity and Markstein lengths of methane–air mixtures, *Combust. Flame*. 121 (2000) 41–58. doi:10.1016/S0010-2180(99)00142-X.
- [136] C. Walchshofer, H. Steiner, Computational investigation of the stability of a lifted strongly buoyant jet flame, *Combust. Flame*. 162 (2015) 613–627. doi:10.1016/j.combustflame.2014.09.007.
- [137] J. Yang, F.M.S. Mossa, H.W. Huang, Q. Wang, R. Woolley, Y. Zhang, ScienceDirect Oscillating flames in open tubes, *Proc. Combust. Inst.* 35 (2015) 2075–2082. doi:10.1016/j.proci.2014.07.052.
- [138] L. Zheng, A. Faik, Y. Zhang, Flame colour analysis for the droplet combustion of water-in-diesel emulsions, in: *12th Int. Conf. Heat Transf. Fluid Mech. Thermodyn.*, Malaga, Spain, 2016: pp. 212–217. <https://edas.info/web/hefat2016/titles.html#F>.

Reference

- [139] Z.G. Wang, M.B. Sun, H.B. Wang, J.F. Yu, J.H. Liang, F.C. Zhuang, Mixing-related low frequency oscillation of combustion in an ethylene-fueled supersonic combustor, *Proc. Combust. Inst.* 35 (2015) 2137–2144. doi:10.1016/j.proci.2014.09.005.
- [140] S.D. Terry, K.M. Lyons, Turbulent Lifted Flames in the Hysteresis Regime and the Effects of Coflow, *J. Energy Resour. Technol.* 128 (2006) 319. doi:10.1115/1.2358147.
- [141] B.J. Lee, J.S. Kim, S.H. Chung, Effect of dilution on the liftoff of non-premixed jet flames, *Symp. Combust.* 25 (1994) 1175–1181. doi:10.1016/S0082-0784(06)80756-3.
- [142] R. Parker, M. Lathoud, Green aero-engines: technology to mitigate aviation impact on environment, *Proc. Inst. Mech. Eng. Part C J. Mech. Eng. Sci.* 224 (2010) 529–538. doi:10.1243/09544062JMES1515.
- [143] E. Torenbeek, *Synthesis of subsonic airplane design: an introduction to the preliminary design of subsonic general aviation and transport aircraft, with emphasis on layout, aerodynamic design, propulsion and performance*, Springer Science & Business Media, 2013.
- [144] T. Edwards, M. Colket, N. Cernansky, F. Dryer, F. Egolfopoulos, D. Friend, E. Law, D. Lenhart, P. Lindstedt, H. Pitsch, A. Sarofim, K. Seshadri, M. Smooke, W. Tsang, S. Williams, Development of an Experimental Database and Kinetic Models for Surrogate Jet Fuels, in: *45th AIAA Aerosp. Sci. Meet. Exhib.*, American Institute of Aeronautics and Astronautics, 2007. doi:10.2514/6.2007-770.
- [145] Jeff Dahl, Diagram of a typical gas turbine jet engine, *FAA Handb.* (2007). https://commons.wikimedia.org/wiki/File%3AJet_engine.svg (accessed March 8, 2017).
- [146] Henderson and Blazowski, Combustor, (n.d.) 110. <https://en.wikipedia.org/wiki/Combustor> (accessed March 23, 2017).
- [147] S. Blakey, L. Rye, C.W. Wilson, Aviation gas turbine alternative fuels: A review, *Proc. Combust. Inst.* 33 (2011) 2863–2885. doi:10.1016/j.proci.2010.09.011.
- [148] R.R. Chaudhari, R.P. Sahu, S. Ghosh, A. Mukhopadhyay, S. Sen, Flame color as a lean blowout predictor, *Int. J. Spray Combust. Dyn.* 5 (2013) 49–65. doi:10.1260/1756-8315.5.1.49.
- [149] A. Mukhopadhyay, R.R. Chaudhari, T. Paul, S. Sen, A. Ray, Lean Blow-Out Prediction in Gas Turbine Combustors Using Symbolic Time Series Analysis, *J. Propuls. Power.* 29 (2013) 950–960. doi:10.2514/1.B34711.

Reference

- [150] R.B.K. Meor, Evaluating Effects of Fuel Properties on Smokes, 1 (2016) 1–18.
- [151] B. Khandelwal, S. Roy, C. Lord, S. Blakey, Comparison of Vibrations and Emissions of Conventional Jet Fuel with Stressed 100% SPK and Fully Formulated Synthetic Jet Fuel, *Aerospace*. 1 (2014) 52–66. doi:10.3390/aerospace1020052.
- [152] S.R. Chakravarthy, R. Sampath, V. Ramanan, Dynamics and Diagnostics of Flame-Acoustic Interactions, *Combust. Sci. Technol.* 189 (2015) 1–20. doi:10.1080/00102202.2016.1202938.
- [153] A.H. Lefebvre, Fuel Effects on Gas Turbine Combustion - Ignition, Stability, and Combustion Efficiency., *J. Eng. Gas Turbines Power*. 107 (1985) 24–37. doi:http://dx.doi.org/10.1115/1.3239693.
- [154] T.S. Snyder, T.J. Rosfjord, Active gas turbine combustion control to minimize nitrous oxide emissions, (1998).
- [155] M. Lucenko, R.E. Vanderleest, K.J.S. Onge, Method and apparatus for detecting burner blowout, (1996).
- [156] J.G. Lee, D. a Santavicca, Experimental diagnostics of combustion instabilities, *Prog. Astronaut. Aeronaut.* 210 (2005) 481–529.
- [157] H. Li, X. Zhou, J.B. Jeffries, R.K. Hanson, Active control of lean blowout in a swirl-stabilized combustor using a tunable diode laser, *Proc. Combust. Inst.* 31 II (2007) 3215–3223. doi:10.1016/j.proci.2006.07.006.
- [158] M.G. De Giorgi, A. Sciolti, S. Campilongo, A. Ficarella, Image processing for the characterization of flame stability in a non-premixed liquid fuel burner near lean blowout, *Aerosp. Sci. Technol.* 49 (2016) 41–51. doi:10.1016/j.ast.2015.11.030.
- [159] T. Muruganandam, S. Nair, Y. Neumeier, T. Lieuwen, J. Seitzman, Optical and Acoustic Sensing of Lean Blowout Precursors, in: 38th AIAA/ASME/SAE/ASEE Jt. Propuls. Conf. Exhib., American Institute of Aeronautics and Astronautics, 2002. doi:doi:10.2514/6.2002-3732.
- [160] S. Prakash, S. Nair, T.M. Muruganandam, Y. Neumeier, T. Lieuwen, J.M. Seitzman, B.T. Zinn, Acoustic Based Rapid Blowout Mitigation in a Swirl Stabilized Combustor, (2005) 443–451. http://dx.doi.org/10.1115/GT2005-68589.
- [161] A. Singh, J. Zhou, Y. Yang, P. Wu, M. Shah, A. Taware, Acoustics Based Prognostics for DLE Combustor Lean Blowout Detection, (2006) 493–496. http://dx.doi.org/10.1115/GT2006-90231.
- [162] S. Nair, T. Lieuwen, Acoustic Detection of Blowout in Premixed Flames, J.

Reference

- Propuls. Power. 21 (2005) 32–39. doi:10.2514/1.5658.
- [163] J.-M. Samaniego, F.N. Egolfopoulos, C.T. Bowman, CO₂* Chemiluminescence in Premixed Flames, *Combust. Sci. Technol.* 109 (1995) 183–203. doi:10.1080/00102209508951901.
- [164] T. Trindade, A. Ferreira, E. Fernandes, Characterization of Combustion Chemiluminescence: An Image Processing Approach, *Procedia Technol.* 17 (2014) 194–201. doi:10.1016/j.protcy.2014.10.228.
- [165] D. Allgood, S. Murugappan, S. Acharya, E. Gutmark, Infrared measurements of thermoacoustic instabilities in a swirl-stabilized combustor, *Combust. Sci. Technol.* 175 (2003) 333–355. doi:10.1080/00102200302398.
- [166] M. Stöhr, I. Boxx, C. Carter, W. Meier, Dynamics of lean blowout of a swirl-stabilized flame in a gas turbine model combustor, *Proc. Combust. Inst.* 33 (2011) 2953–2960. doi:10.1016/j.proci.2010.06.103.
- [167] S. Zhu, S. Acharya, An Experimental Study of Lean Blowout With Hydrogen-Enriched Fuels, *J. Eng. Gas Turbines Power.* 134 (2012) 41507–41510. <http://dx.doi.org/10.1115/1.4004742>.
- [168] T. Yi, E.J. Gutmark, Real-Time Prediction of Incipient Lean Blowout in Gas Turbine Combustors, *AIAA J.* 45 (2007) 1734–1739. doi:10.2514/1.25847.
- [169] T.M. Muruganandam, S. Nair, D. Scarborough, Y. Neumeier, J. Jagoda, T. Lieuwen, J. Seitzman, B. Zinn, Active Control of Lean Blowout for Turbine Engine Combustors, *J. Propuls. Power.* 21 (2005) 807–814. doi:10.2514/1.7254.
- [170] Gaydon, *The spectroscopy of flames*, (1974) 487–488.
- [171] J. Krabicka, G. Lu, Visualisation and Characterisation of Flame Radical Emissions through Intensified Spectroscopic Imaging, 178 (2009) 1–5. doi:10.1088/1742-6596/178/1/012041.
- [172] M.L. Botero, S. Mosbach, M. Kraft, Sooting tendency of paraffin components of diesel and gasoline in diffusion flames, *Fuel.* 126 (2014) 8–15. doi:10.1016/j.fuel.2014.02.005.
- [173] M.L. Botero, S. Mosbach, J. Akroyd, M. Kraft, Sooting tendency of surrogates for the aromatic fractions of diesel and gasoline in a wick-fed diffusion flame, *Fuel.* 153 (2015) 31–39. doi:10.1016/j.fuel.2015.02.108.
- [174] D. Witkowski, K. Kondo, G. Vishwanathan, D. Rothamer, Evaluation of the sooting properties of real fuels and their commonly used surrogates in a laminar co-flow diffusion flame, *Combust. Flame.* 160 (2013) 1129–1141. doi:10.1016/j.combustflame.2013.01.027.

Reference

- [175] H.W. Huang, Y. Zhang, Digital colour image processing based measurement of premixed CH₄ + air and C₂H₄ + air flame chemiluminescence, *Fuel*. 90 (2011) 48–53. doi:10.1016/j.fuel.2010.07.050.
- [176] H.W. Huang, Y. Zhang, Dynamic application of digital image and colour processing in characterizing flame, 85202 (n.d.). doi:10.1088/0957-0233/21/8/085202.
- [177] W.B. Ng, E. Clough, K.J. Syed, Y. Zhang, The combined investigation of the flame dynamics of an industrial gas turbine combustor using high-speed imaging and an optically integrated data collection method, *Meas. Sci. Technol.* 15 (2004) 2303–2309. doi:10.1088/0957-0233/15/11/016.
- [178] H. Group, *Flightpath 2050*, Isbn 978-92-79-19724-6. (2011) 28. doi:10.2777/50266.
- [179] S. Nair, T.M. Muruganandam, R. Olsen, A. Meyers, J. Seitzman, B. Zinn, T. Lieuwen, T. Held, H. Mongia, Lean blowout detection in a single nozzle swirl cup combustor, *AIAA Pap.* (2004).
- [180] Isidoro Martinez, *Fuel Property*, (1996) 1–18.
- [181] Growmark, *Diesel Fuel Cetane Number*, (2011) 1–2. <http://www.gofurtherwithfs.com/Whitepapers/Forms/AllItems.aspx>.
- [182] V. Burger, *The influence of fuel properties on threshold combustion in aviation gas turbine engines*, (2017).
- [183] M. Colket, S. Zeppieri, Z. Dai, D. Hautman, Fuel research at UTRC, in: *Multi-Agency Coord. Counc. Combust. Res. 5th Annu. Fuel Res. Meet.* Livermore, California, Sept., 2012: pp. 17–20.
- [184] S.H. Won, P.S. Veloo, S. Dooley, J. Santner, F.M. Haas, Y. Ju, F.L. Dryer, Predicting the global combustion behaviors of petroleum-derived and alternative jet fuels by simple fuel property measurements, *Fuel*. 168 (2016) 34–46. doi:10.1016/j.fuel.2015.11.026.
- [185] X. Hui, K. Kumar, C.J. Sung, T. Edwards, D. Gardner, Experimental studies on the combustion characteristics of alternative jet fuels, *Fuel*. 98 (2012) 176–182. doi:10.1016/j.fuel.2012.03.040.
- [186] N. Jeyashekar, D. Ph, P. Muzzell, E. Sattler, N. Hubble, S. Antonio, *LUBRICITY AND DERIVED CETANE NUMBER MEASUREMENTS OF JET FUELS , ALTERNATIVE FUELS AND FUEL BLENDS INTERIM REPORT* by Force Projection Technologies, 53 (n.d.).
- [187] NFPA 30: *Flammable and Combustible Liquids Code*, 2012 Edition, (2017). <http://catalog.nfpa.org/>.

Reference

- [188] M. Braun-Unkhoff, T. Kathrotia, B. Rauch, U. Riedel, About the interaction between composition and performance of alternative jet fuels, *CEAS Aeronaut. J.* 7 (2016) 83–94. doi:10.1007/s13272-015-0178-8.
- [189] Lukai Zheng, Flame visualization of Toulene, Indene and Methylnaphthalene blending with base solvent at LBO, 2018. <https://youtu.be/XOp1FZOdhTI>.
- [190] H. Mortazavi, Y. Wang, Z. Ma, Y. Zhang, The investigation of CO₂ effect on the characteristics of a methane diffusion flame, *Exp. Therm. Fluid Sci.* 92 (2018) 97–102. doi:<https://doi.org/10.1016/j.expthermflusci.2017.11.005>.
- [191] M. Frenklach, Reaction mechanism of soot formation in flames, *Phys. Chem. Chem. Phys.* 4 (2002) 2028–2037. doi:10.1039/b110045a.
- [192] K. Siegmann, K. Sattler, H.C. Siegmann, Clustering at high temperatures: carbon formation in combustion, *J. Electron Spectros. Relat. Phenomena.* 126 (2002) 191–202. doi:[https://doi.org/10.1016/S0368-2048\(02\)00152-4](https://doi.org/10.1016/S0368-2048(02)00152-4).
- [193] C.S. McEnally, L.D. Pfefferle, B. Atakan, K. Kohse-Höinghaus, Studies of aromatic hydrocarbon formation mechanisms in flames: Progress towards closing the fuel gap, *Prog. Energy Combust. Sci.* 32 (2006) 247–294. doi:<https://doi.org/10.1016/j.pecs.2005.11.003>.
- [194] D. Chen, Z. Zainuddin, E. Yapp, J. Akroyd, S. Mosbach, M. Kraft, A fully coupled simulation of PAH and soot growth with a population balance model, *Proc. Combust. Inst.* 34 (2013) 1827–1835. doi:<https://doi.org/10.1016/j.proci.2012.06.089>.
- [195] M. Saffaripour, P. Zabeti, M. Kholghy, M.J. Thomson, An experimental comparison of the sooting behavior of synthetic jet fuels, *Energy and Fuels.* 25 (2011) 5584–5593. doi:10.1021/ef201219v.
- [196] L. Zheng, E. Ubogu, J. Cronly, I. Ahmed, Y. Zhang, B. Khandelwal, Effects of Fuel Properties on LBO and Emission Characteristics of Gas Turbine Combustor, 2017.
- [197] L. Esclapez, P.C. Ma, E. Mayhew, R. Xu, S. Stouffer, T. Lee, H. Wang, M. Ihme, Fuel effects on lean blow-out in a realistic gas turbine combustor, *Combust. Flame.* 181 (2017) 82–99. doi:10.1016/j.combustflame.2017.02.035.